Final Report

MITNRL–067

DOE/ER/75859--T1

An Analysis of the Proposed MITR-III Core to Establish Thermal-Hydraulic Limits at 10 MW

by

Otto K. Harling and David D. Lanning

with

John A. Bernard, John E. Meyer, and Allan F. Henry

Submitted to

U.S. Department of Energy

Contract No. DE-FG02-93ER75859

AN ANALYSIS OF THE PROPOSED MITR-III CORE TO ESTABLISH THERMAL-HYDRAULIC LIMITS AT 10 MW

The 5 MW Massachusetts Institute of Technology Research Reactor (MITR-II) is expected to operate under a new license beginning in 1999. Among the options being considered is an upgrade in the heat removal system to allow operation at 10 MW. The purpose of this study is to predict the Limiting Safety System Settings and Safety Limits for the upgraded reactor (MITR-III). The MITR Multi-Channel Analysis Code was written to analyze the response of the MITR system to a series of anticipated transients in order to determine the Limiting Safety System Settings and Safety Limits under various operating conditions. The MIT Multi-Channel Analysis Code models the primary and secondary systems, with special emphasis placed on analyzing the thermal-hydraulic conditions in the core. The code models each MITR fuel element explicitly in order to predict the behavior of the system during flow instabilities. The results of the code are compared to experimental data from MITR-II and other sources.

New definitions are suggested for the Limiting Safety System Settings and Safety Limits. An acceptable steady-state operating region is identified by analyzing the response of the system to loss of flow, loss of heat sink, and reactivity insertion transients. From operation within this envelope, the Limiting Safety System Settings are defined to be the reactor trip points at which a scram signal must initiate in order to prevent nucleate boiling from occurring anywhere in the core prior to the scram. Similarly, the Safety Limits are defined as the trip points necessary to avoid reaching critical heat flux anywhere in the core.

MITR Limit Diagrams are included for three different heat removal system configurations. It is concluded that safe, year-round operating at 10 MW is possible, given that the primary and secondary flow rates are both increased by approximately 40%.

Table of Contents

List of Figures

List Of Tables

1. Introduction

1.1 General

The Massachusetts Institute of Technology Research Reactor (MITR-II) is a $5MW_{th}$ facility that is used by MIT for research and education. Its predecessor, MITR-I, began operation in 1958. The MITR-I was cooled, moderated, and reflected by heavy water. In the 1970s the Institute initiated a project to increase the available neutron flux from the core. This study led to the replacement of the MITR-I core with a compact core designed to be cooled by and moderated by H_2O, and reflected by D_2O.

The MITR-II began operation in 1976 and has operated successfully for 19 years. Because its license will expire in 1999 the MIT Nuclear Engineering Department and the Nuclear Reactor Laboratory (NRL) are examining several options for the future of the reactor. The most promising is to upgrade the reactor coolant system and to raise the authorized power to 10 MW_{th}. This would roughly double the neutron flux available in the beam ports without requiring any major changes to the overall reactor design.

The new reactor, generically referred to as MITR-III, must meet Nuclear Regulatory Commission (NRC) licensing guidelines for research reactors. This requires that a Safety Analysis Report (SAR) be prepared that analyzes possible safety issues and clearly defines the limits of reactor operation.

1.2 Description of the MITR

A block diagram of the major components in the MITR coolant system is shown in Figure 1.2.1. During normal operation the heat generated in the core is transferred to the primary coolant by forced convection. In the main heat exchangers (HX), the primary coolant transfers its heat to the secondary coolant. The secondary coolant flows to the cooling towers where the heat is ultimately rejected to the atmosphere.

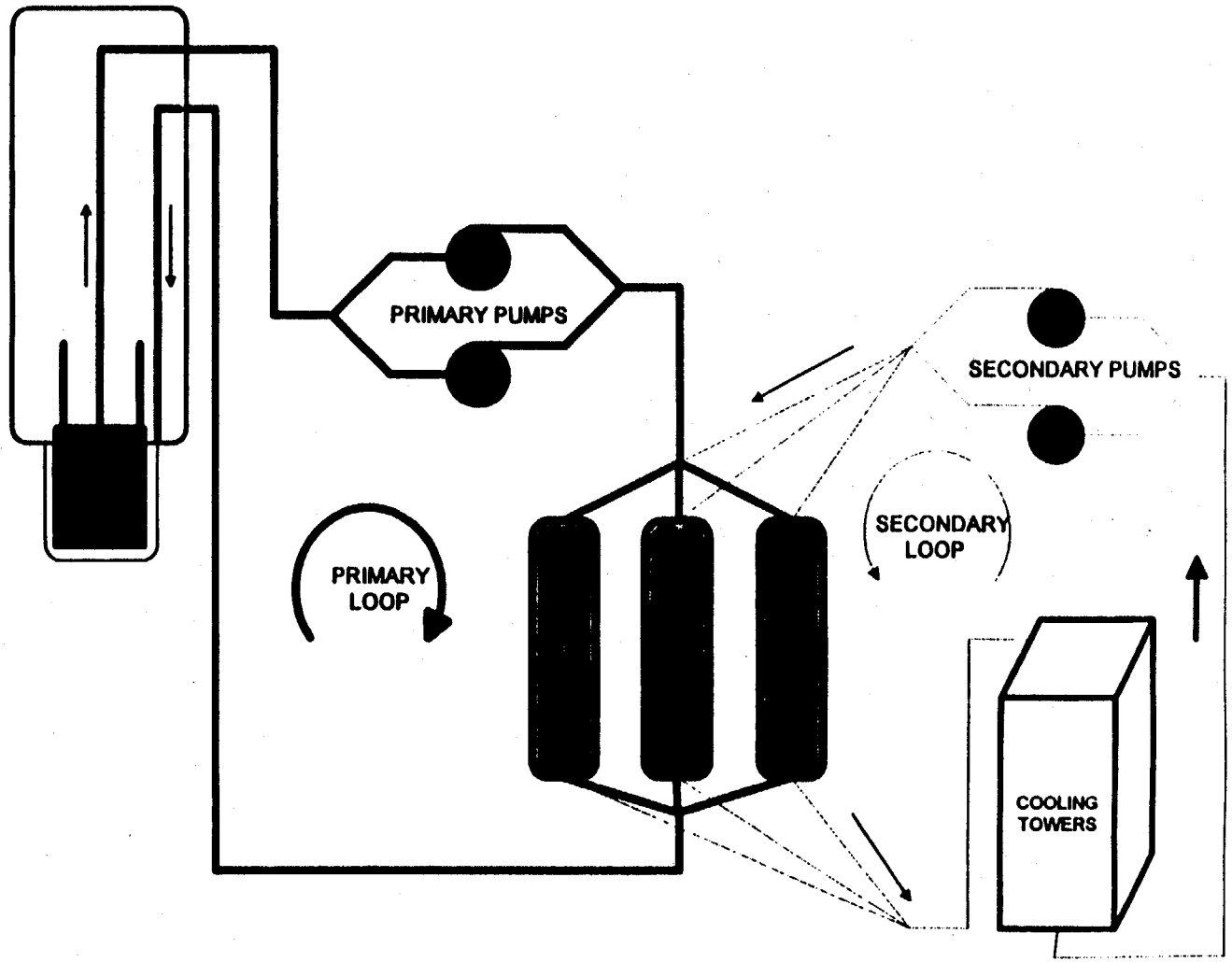

Figure 1.2.1. MITR primary and secondary loops. Diagram of MITR heat removal system showing major components of primary and secondary loops.

1.2.1 Primary Loop

The primary loop is a closed H_2O system driven by two primary pumps that operate in parallel. The pumps provide a nominal flow rate of 127 kg/s, which is sufficient to remove in excess of 5 MW of heat. The coolant discharged from the primary pumps enters the primary side of a bank of three heat exchangers. Depending on the operating conditions, either one or two of the heat exchangers will receive flow. Upon exiting the heat exchangers the coolant flows through a single 190 mm pipe (the cold leg) towards the base of the core tank, where it travels upward through the thermal column towards the core inlet nozzles.

Figure 3.2.1 shows the flow path of the primary coolant within the core tank under conditions of forced flow. From the inlet nozzle the coolant enters the downcomer between the mixing area and the core tank. At the bottom of the core tank the flow is directed up to the fuel and dummy elements in the core. The primary flow splits and flows through the core in up to twenty-seven non-communicating fuel elements, where the heat from fission is added to the coolant. The flow exiting each fuel element enters the region above the core within the flow shroud. The flow from all fuel elements mixes in the shroud region and the mixing area and then exits the core at the outlet nozzles.

The pipe leaving the core (the hot leg) roughly parallels the cold leg as it leads from the core and back into the equipment room where the pumps are located. Although not shown in Figure 1.2.1, several auxiliary systems interact with the primary system.

1.2.2 Secondary System

The secondary system, outlined in Figure 1.2.2, is an open H_2O loop that connects the heat exchangers to the cooling towers. Cool water is drawn from the cooling tower basins by two secondary pumps. Flow from the pump outlets is combined into a single pipe that runs from the cooling towers, through the containment, and into the equipment room. The secondary flow feeds the secondary sides of the heat exchangers and then merges into a single pipe for return to the cooling towers. At full power the secondary water is normally pumped to the top of the cooling towers and sprayed down onto the tower fill matrix while large fans draw ambient air up through the tower. The tower fill matrix increases the rate of heat transfer in the cooling towers by adding a large surface area for convection to take place. The secondary water, cooled by convection and evaporation, returns to the basin.

The secondary coolant loop also receives heat from three auxiliary systems. These are the shield coolant, D_2O reflector, and air conditioning systems, which transfer heat to the secondary system through separate heat exchangers.

1.2.3 Reactor Control System

Startup of the MITR-II and major power changes are achieved by the movement of six stainless steel control blades that contain boron to absorb neutrons. In addition, there is one aluminum-clad cadmium regulating rod that is used for fine adjustments of power. The control system permits the movement of the regulating rod and one blade at a time. During normal operation constant speed motors are used; however, variable speed motors are available for special applications. The control system has built-in interlocks and safety features that limit the potential for criticality accidents and excessive reactivity insertions.

In the event of an unplanned transient or component failure the reactor will be automatically scrammed if any one of many instrument signals exceeds its programmed limit. In addition, the operator may initiate a scram from the control room at any time.

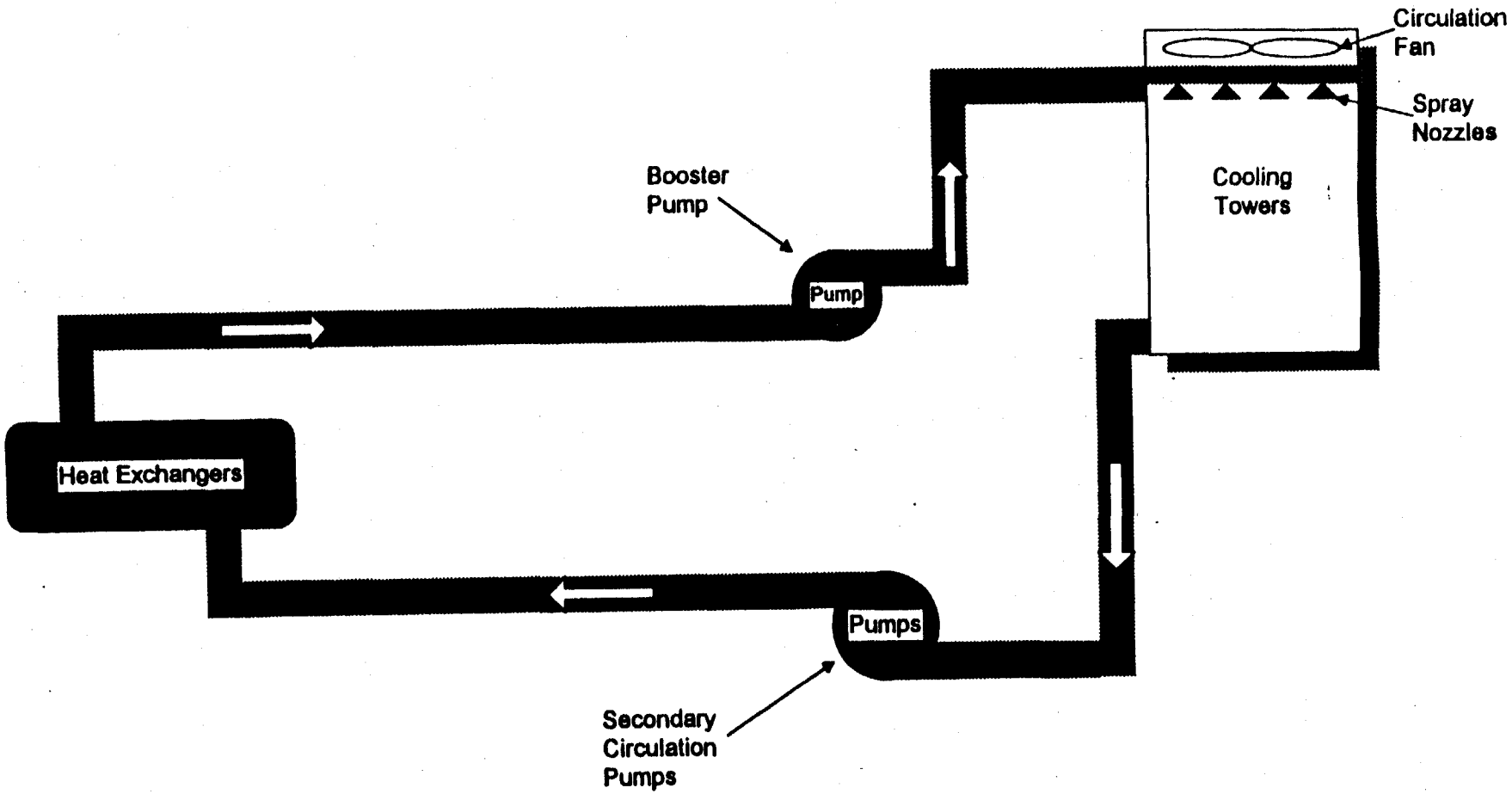

Figure 1.2.2. MITR secondary system components.

When an instrument registers a condition that exceeds a setpoint, current to the control blade magnets is cut off (following a short instrumentation delay time). The control blades then drop into their full-in positions adjacent to the core by gravity, and the control rod drives are subsequently run to their full-in limit. In the event of a failure of the scram system, the operator may dump the D_2O reflector to bring the reactor to a subcritical condition.

1.3 Objectives and Scope of Research

The primary objective of this research is to develop methods that can be used to establish the Limiting Safety System Settings (LSSS) and Safety Limits for safe operation of MITR-III. This method is used to define an envelope of acceptable steady-state operation, and to determine LSSS and Safety Limits for MITR-III based on current information and on anticipated hardware upgrades. The LSSS are designed to prevent nucleate boiling in the core, while the Safety Limits are chosen to prevent critical heat flux and its associated excessive clad temperatures.

Inherent in this task is the analysis of MITR-III under various transient scenarios that may approach the LSSS and Safety Limits. The study of these transients and the predicted response of the MITR provides a basis to determine the values at which the LSSS and Safety Limits should be set for a particular set of operating conditions. This requires detailed knowledge of key core variables as a function of space and time.

Onset of Nucleate Boiling In the Core:

The onset of nucleate boiling (ONB) is defined as the point in time and space at which the first vapor bubbles begin to form on the walls of the fuel elements. The occurrence of ONB is important because it was used to define the LSSS for the MITR-II, and it will be used to set the them for the MITR-III. The point of ONB is a function of several local properties including: pressure, clad temperature, subcooling, heat flux, and channel flow rate. Accurate knowledge of these variables at each point in the core is complicated by the fact that each channel is subject to a different set of operating conditions (heat flux distribution, flow rate), and each channel's conditions are dependent upon the conditions in every other channel.

In determining the Safety Limits, knowledge of ONB is important because it is the first point at which the true quality and void fraction of the coolant exceed zero. A nonzero void fraction may lead to a greater pressure drop in a channel, which may cause that channel to be deprived of flow.

Flow Instability and Critical Heat Flux In MITR:

When a rising void fraction leads to flow reduction in a channel, the potential for a flow instability is present. Flow instability is irrelevant to calculation of LSSS because it occurs after ONB; however, its prediction is required to set Safety Limits. Parallel channel flow instabilities of the type predicted to occur in the MITR core may result in a rapid loss of flow to the hottest elements. During this flow excursion the mass flux in a single fuel element may drop off rapidly while the other channels receive slightly more flow. The channel experiencing the flow excursion is likely to approach critical heat flux (CHF) because of its extreme local conditions. Determining the point in time and the channel where the onset of flow instability (OFI) occurs is not enough to set the Safety Limits. The behavior of the core during and after OFI is necessary to monitor the approach to CHF in each channel. The parallel channel instability described here is considered a static instability because it leads to the establishment of a new (and much lower) mass flux in the hot channel. Dynamic flow instabilities that cause large fluctuations in channel flow may occur during situations such as channel blockage.

The onset of flow instability in an MITR channel is not necessarily a Safety Limit itself, but it represents a key path to CHF. In the absence of OFI, the Safety Limits are still set based on the occurrence of CHF, but in this case the mechanism may be different because the channel is still operating at its normal flow rate. Knowledge of the state of each flow channel as a function of time is necessary to determine where and when OFI occurs, and whether or not it leads to CHF.

The approach developed to set the LSSS and Safety Limits for MITR-III is based on a computer simulation of the MITR system with emphasis on the core. Prediction of OFI and post-OFI behavior requires that each channel be treated explicitly and that the interdependence of the channels be accurately modeled. The computer model was written specifically for the purpose of setting limits for MITR. Therefore, it uses correlations and component models that are optimized for this reactor and its systems. Because MITR-II and its successor will share much of the same structure, it is possible to use this code to reexamine the conservative limits set for MITR-II and to verify parts of the code by comparison with MITR-II experimental data. Although some of the components for the upgraded reactor (pumps, heat exchangers, cooling towers) have not yet been selected, it is possible to model these components based upon their design specifications.

. In the past, calculations such as those presented here were done by conservative assumptions designed to yield a "worst-case" type of answer. The intent was that these solutions would represent a bounding limit to the true solution. The use of conservative assumptions allowed for simplified models and analytic solutions to complex problems, but this approach has two shortcomings [1]:

1) A final result based on overly-conservative calculations will yield a very pessimistic result. Such a result may cause designers or operators to take improper actions.

2) When conservatism is included at many levels, the conservatism of the final solution is difficult to evaluate. Scaling effects and uncertainties can cause initial conservatism to grow or shrink by large amounts.

The objective of this work is to yield accurate limits for the MITR-III based on best-estimate calculations. This philosophy allows for greater confidence in the final output, but the user must be careful to consider that the result does not contain the built-in conservatism of the previous types of calculations. *It is therefore the user's responsibility to take the results of these calculations (LSSS and Safety Limits), consider uncertainties, and add a factor of safety between them and the operating limits used in MITR-III.*

The "best-estimate plus uncertainty" approach does not guarantee any given level of accuracy, but it does allow for an estimate of the uncertainty in the solution. The use of a "best-estimate plus uncertainty" approach is believed to provide the most useful information for reactor operators and engineers who have a solid understanding of the system being analyzed.

In cases where a choice of calculational methods or correlations is necessary, the one that is proven to be the most accurate over the range of parameters being considered is chosen. When several methods or correlations are believed to be equally reliable, the more conservative one is chosen and its limitations are noted.

1.4 Organization of Report

Chapter 2 of this report provides background on the derivation of limits used in the Safety Analysis Report for MITR-II. Proposed definitions of the Limiting Safety System Settings and Safety Limits for MITR-III are also presented. The method for finding these limits is included in Chapter 2 as well.

Chapter 3 describes the models used to represent the MITR primary and secondary systems in the Multi-Channel Analysis Code that is used to evaluate the limits for MITR-III. The mathematical models for the major components and methods for solution of the momentum, mass, and energy conservation equations for the systems are outlined. The choice of empirical correlations is also included in Chapter 3.

Chapter 4 presents calculations using the Multi-Channel Analysis Code and compares these results with previous calculations and experimental data, where available. In particular, the ability of the code to accurately predict the onset of flow instabilities in the reactor core is evaluated and compared with theory and experiment.

The Multi-Channel Analysis Code is applied to the MITR system in Chapter 5. The results of several key transient simulations are. Chapter 5 contains Limit Diagrams of the proposed MITR-III Limiting Safety System Settings and Safety Limits based on the approach outlined in this report.

Conclusions and recommendations for future work in this area are included in Chapter 6.

2. Approach For Calculation of MITR-III Limits

2.1 *Present MITR-II Limit Definitions*

This section describes the derivation of the LSSS and Safety Limits for the MITR-II as expressed in the current SAR. This report proposes different definitions of these limits for MITR-III. Therefore, a direct comparison between the MITR-II limits discussed in this section and the new limits suggested in Chapter 5 of this report is not possible.

The limits for MITR-II are based on a series of margins between the reactor operating point and the point of fuel clad failure. Figure 2.1.1 shows the relationship between the various limits and reactor variables in MITR-II. The safety criterion is that the temperature of the hottest spot on the hottest fuel plate should not exceed 450°C. The Safety Limit is defined to prevent operation near the point of OFI, as predicted by empirical correlations for flow instability in a heated channel. The CHF resulting from OFI is considered to be the most limiting form of CHF for the reactor [2]. The SAR is based on the assertion that operation below OFI conditions will prevent CHF and the resulting excessive clad temperature, thereby meeting the Safety Limit criterion. Subsequent studies have supported the assertion that OFI is the most limiting case [3].

The LSSS for the MITR-II was set to prevent operation near the Safety Limit. The LSSS was determined by preventing ONB anywhere in the core during critical operation (i.e., prior to a scram during a transient). An Operating Limit was included to prevent operation near the LSSS. The margin between the Operating Limit and the LSSS is included to account for instrument delay time between receiving a scram signal and the insertion of the control blades, and for the physical response time of the system to the control blade insertion. The Operating Limit also represents the set points for the reactor scram. Normal operation of MITR-II takes place below the operating limits.

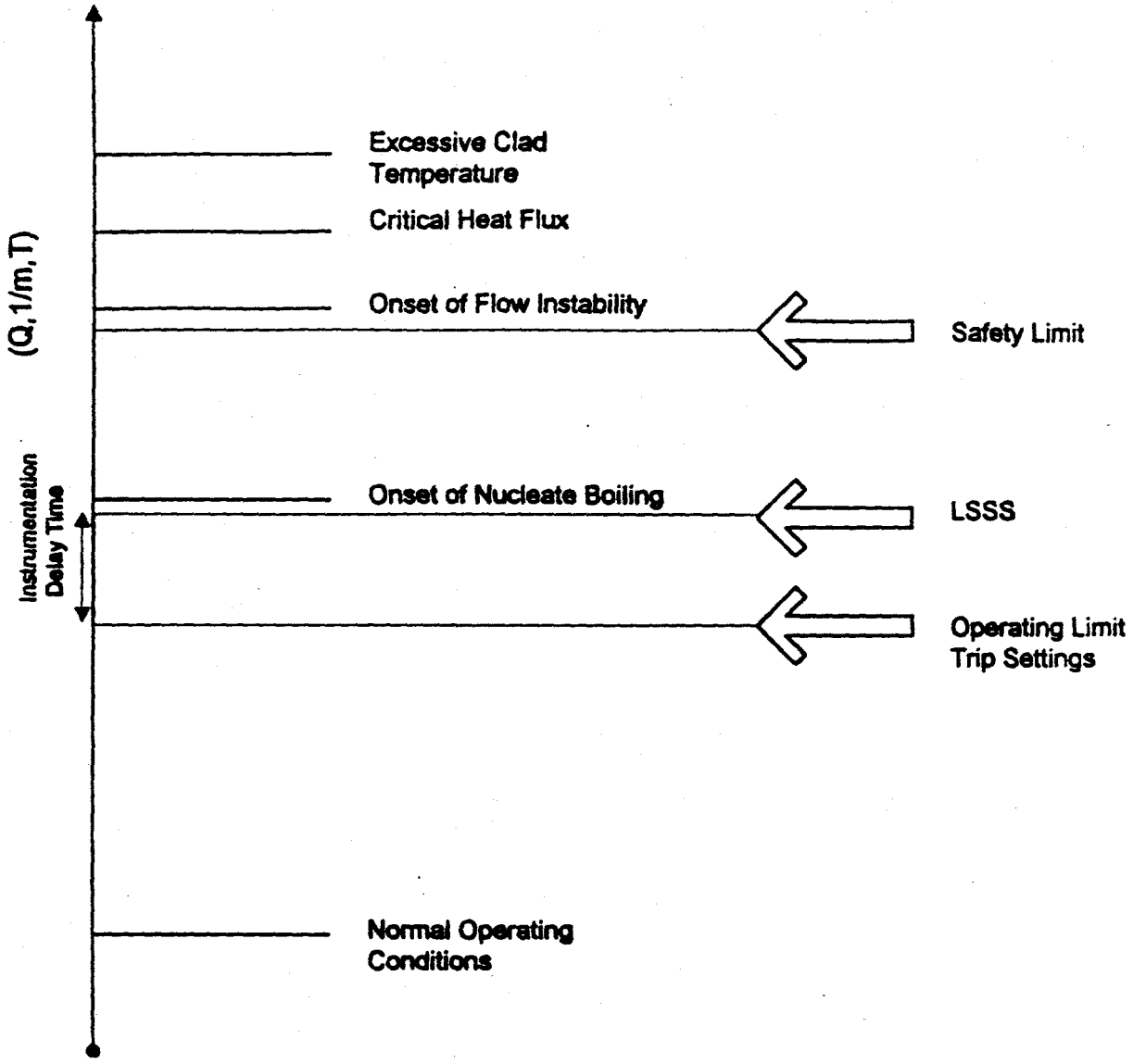

Figure 2.1.1. MITR-II limits. Based on the current definitions of LSSS and Safety Limits, conservative calculations are used to determine limits for MITR-II.

During the derivation of the limits for MITR-II there were limited computational tools available for analyzing the response of the system to transients. Because of this fact, the OFI, CHF, and excessive clad temperature limits shown in Figure 2.1.1 could not be distinguished from one another. If OFI was predicted to occur then it was assumed that the maximum clad temperature would be exceeded. There was no calculated margin between these events. To include a margin, the LSSS was defined to separate ONB from OFI.

The MITR-II limits were based on very conservative, steady-state calculations with large margins to account for the possibility of transients. The LSSS shown in the left side of Table 2.1.1 represent a steady-state operating point at which the reactor could operate without experiencing ONB. These limits are found by setting the LSSS power at 120% of maximum power (maximum power is 5 MW with both pumps running), and the LSSS hot leg temperature at 60°C. The LSSS flow rate is then calculated to be that lowest possible steady-state flow rate that can be achieved without nucleate boiling in the core. In the event of a transient, however, ONB would likely occur if the scram signal was sent based on the LSSS. This is the reason for including the operating limits for MITR-II.

The Safety Limits, given on the right side of Table 2.1.1, *do not* represent a steady-state operating point. They are defined such that if one of the three parameters is moved to its Safety Limit while the other two remain at their LSSS values, there will be no OFI. The MITR-II SAR states that, "Because of the conservative nature of the calculations used to establish these limits it is believed that it would be possible for the reactor to be operated with any one of these variables at the safety limit and all other parameters within their normal operating limits without serious consequences to the reactor core." Since the writing of the SAR, this statement has been supported by further calculations [3,4].

Table 2.1.1. LSSS and Safety Limits for MITR-II [2,3]

	Limiting Safety System Settings		Safety Limits	
	One Pump	**Two Pumps**	**One Pump**	**Two Pumps**
Core Power (MW)	3	6	4.1	8.2
Primary Flow Rate (kg/s)	56.8	113.5	40.7	81.4
(gpm)	(900)	(1800)	(657)	(1314)
Outlet Temperature (°C) (Measured In Hot Leg)	60.0	60.0	72.6	72.6

Initial studies for MITR-III have determined LSSS and Safety Limits for 10MW operation based on the same limit definitions that are in the MITR-II SAR. Table 2.1.2 shows the results of studies by Parra and Trosman. Because of more precise knowledge of reactor parameters and analysis tools, these calculations are closer to "best-estimate" calculations than the original MITR-II SAR. The LSSS represent steady-state operating conditions that would avoid ONB in the core. The Safety Limits derived by Parra do not represent a safe steady-state operating point. Trosman also proposed operating limits that took into account the instrumentation delay time [4].

Table 2.1.2. Previous calculations of LSSS and Safety Limits for MITR-III At 10 MW (Two Pumps)[3,4]

	Limiting Safety System Settings [4]	Safety Limits [3]
Core Power (MW)	12	19.2
Primary Flow Rate (kg/s)	155	34.2
(gpm)	(2502)	(552)
Outlet Temperature (°C) (Measured In Hot Leg)	69	93.3

It must be emphasized that the limits presented in the above tables are provided as background information. The definitions for the LSSS and Safety Limits presented in this report are different than those used in the current MITR-II SAR, although the limiting criteria are the same.

2.2 *Objectives of Present MITR-III Limit Definitions*

The objective of this study is to propose new definitions for LSSS and Safety Limits that are clearly defined, logically developed, and easily applied to reactor operation. The limits should be expressed in terms of the total core power, Q (MW), primary loop mass flow rate, m (kg/s), and a reference temperature, T (°C) (the choice of where to measure the reference temperature is described in Section 2.6. Regardless of what temperature is chosen, the approach is the same). These parameters are chosen because they define a state-space that represents three independent operating variables that can be measured by the current MITR instrumentation system. These three variables are currently used to initiate reactor trips and include redundant instruments.

Furthermore, the limits should include the delay time for detecting an abnormal signal, initiating a reactor scram, and dropping the control blades by gravity into the core. This implies that possible transients should be analyzed to determine which ones present the most serious limits to reactor safety. Three possible transients have been identified as "limiting transients" for the purposes of setting limits on reactor operation. Less severe transients will present less of a threat to the reactor, so designing for the limiting transients will encompass the more minor ones as well. More severe transients are beyond the design basis of the reactor and are not expected to occur. The limiting transients are: Loss of Primary Flow (LOF), Loss of Heat Sink (LOHS), and Reactivity Insertion.

Loss of Primary Flow:

A loss of electrical power or an electrical failure within the pump causes torque to the pump rotor to go to zero. The primary loop flow begins to "coast down" from its initial value towards zero. The rotational inertia of the pump and the inertia of the primary flow give the pump coastdown an exponential shape. Due to the possibility of common mode failure, a loss of both primary pumps is believed to be plausible.

The core inlet pressure gauges MP-6 and MP-6A will detect any loss in core inlet pressure that results from a loss in primary flow. In addition, the primary loop flow is measured by a flow nozzle in the primary loop and the signal is used to send a low-level trip during a loss of flow event. A loss of both pumps will lead to a rapid drop in primary flow rate. A gradual drop in the primary mass flow rate could require a reactor trip to be initiated at a higher mass flow rate. Three loss of flow transients will be examined:

Limiting LOF Transients: (1) From operation at steady-state, both primary pumps trip and the flow coasts down in accordance with measured or predicted flow coastdown curves; and, (2) From operation at steady-state, one primary pump trips and the flow coasts down in accordance with measured or predicted flow coastdown curves; and, (3) The primary mass flow rate is reduced from full flow to zero flow over an infinite time interval.

Loss of Heat Sink:

The reactor could lose access to its ultimate heat sink (the atmosphere) as a result of several initiating events. The most serious, plausible event is the loss of flow in the secondary system leading to decreased heat transfer from the primary loop. The flow in the secondary loop would coast down as described for the primary loop, above.

The secondary flow is monitored by measuring the pressure drop across a flow orifice at the inlet to each heat exchanger. A low secondary flow rate would initiate a reactor trip. If this was not initiated, the rise in core outlet temperature measured at the inlet to the hot leg would initiate a trip. Because of the large volume of the mixing area and the turbulent mixing within this region, there is a substantial time delay between the loss of secondary flow and the detection of a temperature rise at the hot leg sensor.

Limiting LOHS Transient: From operation at steady-state, both secondary pumps trip and the flow coasts down in accordance with measured or predicted flow coastdown curves.

Reactivity Insertion:

Reactivity may be inserted into the core by various mechanisms. Limits set on the reactivity worth of experimental assemblies reduce the risk of a reactivity insertion from these facilities. During normal operation at full power, one plausible event would be the inadvertent withdrawal of a single control blade and the regulating rod from the core at their maximum rates of withdrawal. This transient would lead to a rapid rise in surface heat flux, while the coolant temperature would be slow to respond to the increasing power.

At the other extreme, an infinitesimally small reactivity insertion would cause the power to begin to rise very slowly. The core would reach a steady-state at each new power level. Although this type of reactivity insertion transient leads to lower heat fluxes, it does result in higher coolant temperatures. Both of these transients are examined to determine power limits.

The reactor power is monitored by a set of neutron detectors that determine the neutron flux. High power level detectors and low power level detectors (below 100kW) can initiate reactor trips based on excessive neutron flux measurements. In addition, the reactor period is measured and it is used to initiate a reactor trip if the power changes too rapidly.

Limiting Reactivity Insertion Transients: (1) From operation at steady-state, the control blade with the highest worth and the regulating rod are withdrawn from the core at a rate of 1.8 mm/s (4.25 in/min); and, (2) From operation at steady-state, the power begins to rise slowly enough that a new steady-state is achieved at each power level.

The MITR-III LSSS and Safety Limit definitions are based on operation within a steady-state operating envelope in (Q,m,T) space such that initiation of any of the limiting transients from within that envelope will not lead to a condition that exceeds that safety criteria.

2.3 *Definition of the Limiting Safety System Settings (LSSS) for MITR-III*

The criteria for the LSSS is that no nucleate boiling is to occur anywhere in the core prior to a scram. The corresponding definition is:

> *For a given acceptable, steady-state operating point (Q,m,T), ONB will not occur anywhere in the core prior to a scram following the initiation of a transient, given that the reactor trip signal is sent at or before the LSSS is reached.*

In other words, the LSSS for a given steady-state operating condition (Q,m,T) represent the ultimate possible trip points to avoid ONB prior to a scram. If the reactor is operating at (Q_o, M_o, T_o) and the corresponding LSSS are at $[Q_l, m_l, T_l]$ then a transient initiated at time zero will proceed until one of the following occurs:

1) Core power, Q, rises until it equals Q_l;
2) Primary flow, m, drops until it equals m_l;
3) Coolant reference temperature, T, rises until it equals T_l.

Although all three of the variables will be changing with time, one will reach its limit before the others. When one of these conditions is met, a reactor trip signal is initiated. After an instrumentation delay time has elapsed, the control blades are released and begin to drop by gravity. Based on the definition of the LSSS, no nucleate boiling occurs in the core until the reactor is scrammed. For this study, the reactor is considered to be scrammed when the blades have reached 80% of full insertion. The current MITR-II SAR requires that the time from the initiation of the scram signal to the time of 80% insertion be less than 1.0 s.

After the blades have reached 80% insertion, nucleate boiling is permitted to occur in the core. Boiling is allowed to occur in the core following the scram because the decay power is not high enough to cause Critical Heat Flux in the system.

This definition of LSSS refers to only three mechanisms for a reactor trip: excessive core power, deficient primary flow, and excessive coolant temperature. As pointed out earlier, there are reactor trips based on other operational parameters that may scram the reactor sooner for a given transient. Reliance on only these three trips reduces the system's dependence on additional engineered safeguards. The additional trip mechanisms should remain in place to detect abnormal events and initiate a scram, but these definitions and the corresponding calculations do not require their function in order to ensure safe operation of MITR-III.

The envelope of acceptable steady-state operating points represent the limitations on where the reactor can operate. The LSSS are found by initiating transients from the operating envelope. For operation outside the operating envelope, the LSSS are undefined. The LSSS represent a set of values of power, flow, and temperature that correspond to the extreme limits of the trip points. If the reactor did not trip until after one of the LSSS limits was reached, nucleate boiling may occur prior to the scram.

From this proposed definition of MITR-III LSSS, the reactor could conceivably operate with the reactor trip points exactly at their LSSS values. Such operation would be inadvisable for several reasons:

1) Steady-state operation with the trip points at their LSSS implies that there is no margin between the operating limits and the LSSS.

2) Any perturbation to the system is likely to cause a reactor scram.

3) Calculation of the LSSS yields a best estimate, but there is an uncertainty associated with this LSSS. Operating with trip settings exactly at the LSSS would be neglecting this uncertainty.

Although it is beyond the scope of this report, it is suggested that operating limits be developed that place a margin between the calculated LSSS and reactor operating conditions. This margin should include, as a minimum, the following:

1) The uncertainty in calculation of LSSS

2) Any changes in reactor hardware or configuration that would impact the location of the LSSS (new pumps, procedures, experiment loading, etc.)

In reality, the operating limits will probably be determined by licensing and operational considerations. Although the operating envelope presented in this report may allow for operation above 10 MW for a given set of conditions, the operating license for the reactor will specify that power is not to exceed 10 MW (10 MW is the upper limit on authorized power for a research reactor). The operating limits should represent the trip points for power, flow, and temperature. In this sense, the LSSS represents an upper bound for the choice of reactor trip points.

2.4 *Definition of the Safety Limits for MITR-III*

The criteria for the Safety Limits is that there be no critical heat flux anywhere in the core. The corresponding definition is:

> *For a given acceptable, steady-state operating point (Q,m,T), CHF will not occur anywhere in the core following the initiation of a transient, given that the reactor trip signal is sent at or before the Safety Limits are reached.*

The physical meaning of this definition is that if a transient is initiated from a steady-state operating point (Q_o, M_o, T_o) and the reactor trip points are set at the Safety Limits (Q_2, M_2, T_2), CHF will not occur in the reactor. The Safety Limits, unlike the LSSS definitions, do not state that the limiting criteria (in this case, CHF) is allowed to occur after the scram. Immediately following a scram, the heat flux drops to a small fraction of its steady-state power (about 7%). Studies by Parra indicate that critical heat flux will not occur in MITR-III at decay heat power levels [3].

It is obvious that the reactor would never be operated with the reactor trip points set at the Safety Limits. Defining the Safety Limit in a manner analogous to the LSSS allows the margin between the two to be easily calculated and provides a physical meaning to the Safety Limits.

The Safety Limits will also be calculated using a best-estimate approach. In this case, however, the uncertainties associated with two-phase flow and heat transfer and the applicable CHF correlations are much greater than for the LSSS calculations. In addition there is far less experimental data for the performance of the MITR system (or similar systems) under two-phase conditions than for single-phase operation. Therefore, the Safety Limits are not as well-defined as the LSSS. For practical purposes, however, the LSSS are far more important because they have an operational purpose: to provide an upper bound for setting reactor operating limits.

Figure 2.4.1 shows a two-dimensional plot of Q versus T showing the relationship between the reactor operating point (T_o, Q_o), the LSSS (T_1, Q_1), and the Safety Limits (T_2, Q_2). For simplicity, the steady-state mass flow rate, m_o, is not shown in this 2-D projection of (Q, m, T) space. The operating point is shown to be within the operating envelope. In a loss of heat sink transient, the operating point will move to the right, along the $Q = Q_0$ line until it intersects the LSSS line. At this point, where $T = T_1$, the reactor trip signal is initiated. The primary system temperature continues to rise, but the core power is now only a fraction of Q_0. By the definition of the LSSS, no nucleate boiling occurred in the core prior to the control blades reaching 80% insertion. In reality, there would be another limit line below the LSSS where the reactor trip points would be.

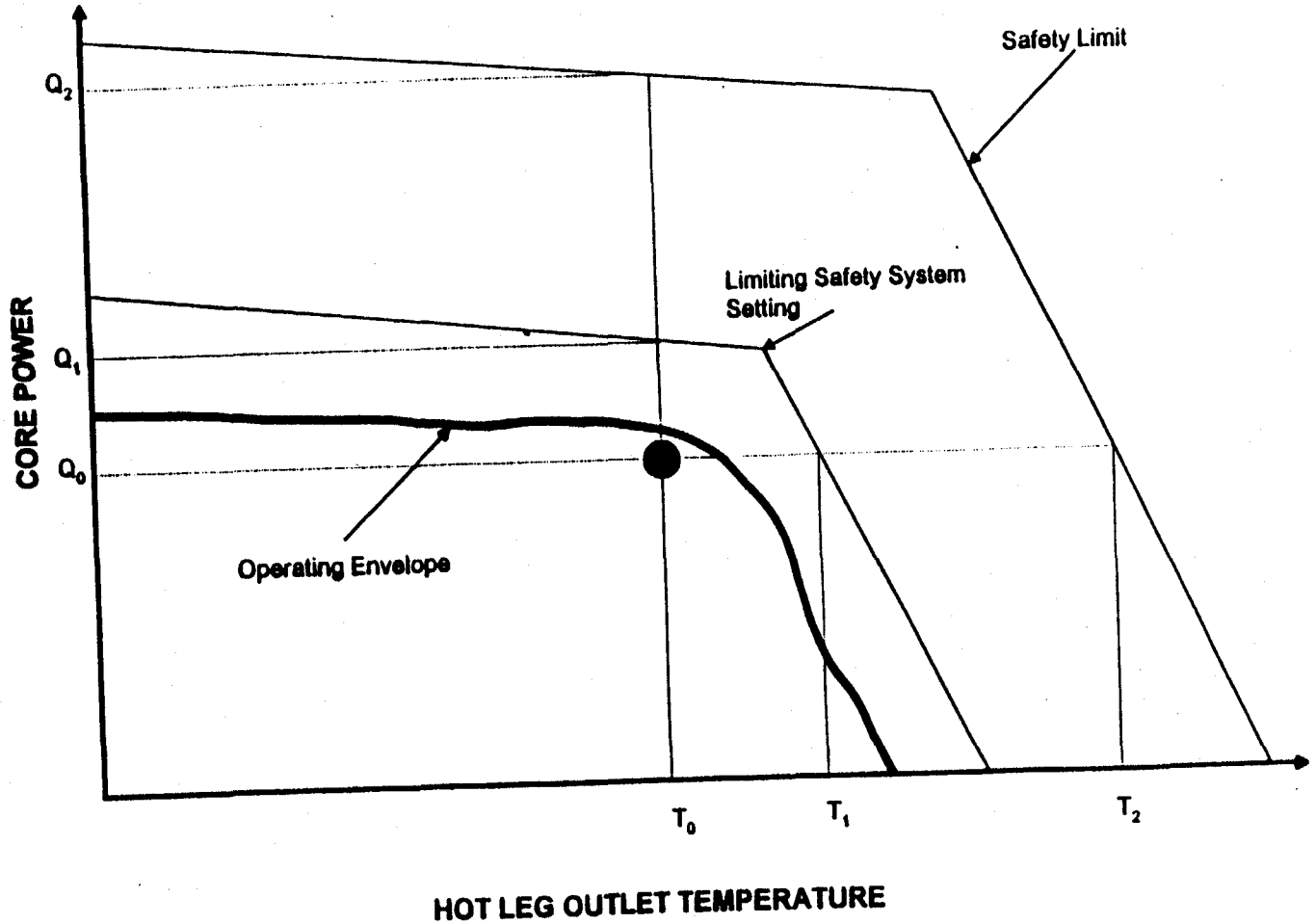

Figure 2.4.1. Proposed LSSS and Safety Limit definitions for the MITR-III. New Limiting Safety System Setting and Safety Limit definitions are proposed for MITR-III. A two-dimensional projection of (Q,m,T) space with a constant primary flow rate is shown. From operation within the operating envelope, ONB will be avoided if the reactor trips at or before $T = T_1$, or $Q = Q_1$. Similarly, CHF will not occur if the reactor trips when $T = T_2$, or $Q = Q_2$

To illustrate the meaning of the Safety Limits, consider operation at (T_o, Q_o) with reactor trip points set at the Safety Limits (T_2, Q_2). During the loss of heat sink transient, the operating point of the reactor would move past (T_1, Q_0) on the $Q = Q_0$ line. By the time the Safety Limit is reached at (T_2, Q_0) nucleate boiling will have begun, and one or more channels may be experiencing a flow excursion. Critical heat flux is being approached. If the reactor is not shut down by the time the flow reaches m_2, critical heat flux is predicted to occur. Note that CHF will not necessarily have occurred by the time flow equals m_2, but the reactor system has passed the point where it can be assured that CHF will not occur sometime in the near future.

Similar examples can be given for reactivity insertion transients, or loss of primary flow transients.

The new definitions for LSSS and Safety Limits defined above are different from the definitions outlined in the MITR-II SAR. The different definitions make it impossible to directly compare the limits derived using the MITR-II definitions and those derived using the definitions presented here. The LSSS shown in Tables 2.1.1 and 2.1.2 give a steady state operating point beyond which operation is not permitted. This operating point could be plotted on the limit diagram presented in this report. The point would lie on the edge of the operating envelope (assuming that similar calculational methods were used in both cases). The old LSSS give a steady state operating point, while the new LSSS give a set of trip points that doe not represent an acceptable steady state operating point.

The Safety Limits given in Tables 2.1.1 and 2.1.2 are inconsistent with the new Safety Limit definitions. The old Safety Limits predicted how far one variable could deviate from its LSSS value while the others stayed at their LSSS limits. The new Safety Limits, defined in a manner analogous to the new LSSS, give a set of trip points that must be adhered to in order to avoid CHF.

2.5 Approach Used To Find Limits

Because the LSSS and Safety Limits are defined analogously, the methods used to evaluate them are similar. Both sets of limits are defined for transients initiated from an operating envelope. The goal is to produce a two-dimensional surface (an "envelope") in the three-dimensional (Q,m,T) space under which it can be assured that all points represent acceptable steady-state operating conditions. For each operating point within this envelope, there exists a set of correseponding LSSS and Safety Limit values. The objective of this report is to find these limits. The LSSS and Safety limits are further restricted such that if the steady-state operating point moves to a more conservative operating point (lower power, higher flow rate, or lower temperature), the LSSS and Safety Limits do not need to change.

The surest way to find these limits would be to build a large number of identical MITR-IIIs and operate each one at a different steady-state operating point (Q_o,M_o,T_o). In each reactor, each of the limiting transients would be initiated. The trip points would be moved further from the operating point in each trial until the limit criteria were reached. The last acceptable trip point would represent the correct value of the limit.

Because such an experiment is not feasible, the method developed here uses a computer simulation of the MITR to determine the limits from each steady-state operating point. In order to present the three limit variables in a two-dimensional format, the limits are shown for a constant primary flow rate.

The first step is to find the envelope of acceptable steady state operation. A steady-state point is determined to be unacceptable if there is any nucleate boiling in the core. The steady-state envelope is restricted further by determining if any of the limiting transients would cause ONB prior to a scram.

Once the steady-state envelope has been determined, a loss of heat sink transient is simulated and a temperature trip point is found that avoids ONB prior to the scram. Next, various reactivity insertion transients are simulated to find the core power trip point that would just avoid ONB. Finally, a mass flow rate trip point is determined by simulating loss of flow transients from within the operating envelope. A similar procedure is used to find the Safety Limits.

2.6 *Choice of Characteristic Temperature*

In the definition of the LSSS and Safety Limits there was no definition given for the characteristic temperature, T. Three different options are available for selecting the temperature used to define the limits.

1) Core Outlet Temperature. The core tank outlet contains redundant temperature sensors that are used to measure the temperature of the primary coolant leaving the core tank and entering the hot leg. This temperature is currently used to scram the reactor, and it is the temperature referred to in Tables 2.1.1 and 2.1.2. The advantage of using this temperature is that it reflects any changes in core power. In case of a failure to scram on excessive power or low flow, this sensor would initiate a scram. The disadvantage of using the hot leg temperature is that it does not give a direct indication of core outlet temperature because the mixing area above the core. Hot coolant exiting the fuel elements during a transient mixes with cooler water in the mixing area. Studies are currently underway to determine the characteristics of this turbulent mixing process [5]. It takes several seconds for a rise in core outlet temperature to be detected at the hot leg sensor, and the temperature rise at the hot leg is not necessarily indicative of the change in core outlet temperature. Therefore, the hot leg temperature sensor is inadequate to detect a primary pump trip or reactivity insertion in time to prevent ONB. It would, however, be acceptable for detecting a loss of heat sink that raises the core inlet temperature.

2) Core Inlet Temperature. Temperature sensors located near the inlet to the core tank give the temperature of the coolant exiting the cold leg and entering the core tank. This temperature is much quicker to respond to a loss of heat sink transient than the hot leg sensor would be. However, it does not provide any information about the heat added in the core. The core mixed outlet temperature is related to the core inlet temperature at steady-state by an energy balance,

$$T_{out} = T_{in} + \frac{Q_{core}}{m_{core} c_p} \qquad (1)$$

where, Q_{core} = Total core power (W),

m_{core} = Core mass flow rate (kg/s),

c_p = Specific heat of coolant (J/kg°C).

Another disadvantage of using core inlet temperature as the basis for MITR-III limits is that the reactor instrumentation would have to be modified to trip the reactor on excessive inlet temperature.

3) Ambient Wet-Bulb Temperature. At steady-state, the core power and the primary and secondary loop flow rates determine the range of coolant temperatures on the primary and secondary sides. The endpoint temperature on the secondary side is related to the ambient wet-bulb temperature and the cooling tower effectiveness. With these quantities known, the secondary temperatures into and out of the heat exchangers can be determined. These temperatures in turn dictate the primary loop inlet and outlet temperatures. The wet-bulb temperature is useful for setting LSSS and Safety Limits because it is an easily measured quantity that can be found prior to reactor startup. The wet-bulb temperature would give no relevant information concerning any events within the reactor systems.

This study uses the hot leg temperature to set LSSS because of the hardware currently in place and the operating experience that has been gained using this practice. Reliance on the hot leg temperature to detect loss of heat sink transients lowers the LSSS because of the long time delay between the initiation and detection of the transient. The relatively gradual rise in system temperatures makes this delay acceptable.

It is recommended that the core inlet temperature be monitored to initiate a trip signal when the cold leg temperature begins to rise, but the limits presented here do not rely on a cold leg temperature trip.

3. MITR-III Multi-Channel Analysis Code

A FORTRAN code developed as part of this research is used to evaluate the response of the MITR system to a series of transients in order to determine whether a given steady-state operating point meets the criteria outlined in sections 2.3 and 2.4 above.

3.1 Objectives of the MITR-III Multi-Channel Analysis Code

Given the ultimate objective of predicting LSSS and Safety Limits, the code must model all major systems involved in the removal of energy from the core to the ultimate heat sink. Any component whose failure would hinder the removal of heat from the core must be accurately modeled.

Because the LSSS and Safety Limits are based on thermal-hydraulic conditions in the fueled region of the core, this region deserves the most attention. The possibility of a flow instability in the core, and the need to model the behavior of individual fuel elements after the Onset of Flow Instability (OFI) prohibits the use of a lumped-parameter core model. The core model must be capable of explicitly treating each fuel element in order to account for variations in power shape, flow disparity, and pressure loss. Because of the discrete nature of computer models, however, it is not possible to consider continuous variations in these properties within a channel. Nevertheless, some effort must be made to account for the continuous variations in channel properties in a discrete code.

The high computational effort required to model each fuel element explicitly makes the use of a true three-dimensional model unfeasible. A one-dimensional model of flow through the primary and secondary system piping will be adequate to describe its behavior, while a quasi-2-D treatment of the core is required. This model for the core ignores variations in variables in the width and thickness directions. In order to avoid under-predicting extreme values, a three-dimensional shape can be imposed on the core model through the use of peaking factors when key limits are evaluated.

The code should be capable of modeling two-phase flow within the core in order to predict the Safety Limits. A single-phase model for the rest of the system is acceptable because of the long period of time required to boil off the water in the above-core mixing area. The core two-phase model should use the best available empirical correlations for two-phase heat transfer coefficients because these will determine whether OFI has occurred or not. Similarly, two-phase pressure drop is important in predicting the OFI and post-OFI behavior in the fuel elements.

The MITR-III has several features that deserve special attention. First, its low pressure makes prediction of flow quality and void fraction critical. A void fraction model is required for atmospheric pressure systems which is applicable to the MITR-III and other low-pressure systems. Secondly, the presence of small, vertical fins on the surface of each fuel plate must be considered. The fins are present to improve the heat transfer characteristics of the fuel. Without the use of a fully 3-D coolant channel model, some system must be developed to account for the effects of the fins. Finally, the unique design of the MITR core tank and the presence of four natural circulation valves must be modeled properly to predict the behavior of the system during a loss of primary flow.

3.2 General Models of MITR-III

Figure 3.2.1 shows a block diagram of the flow path and control volumes used for forced flow in MITR-III. Relatively large nodes are used to represent regions where coolant properties vary slowly (secondary loop, parts of the primary loop), while much smaller volumes are used to represent regions where properties can change rapidly (spatially and temporally) and where the most accuracy is required (the fueled region of the core). The control volume scheme used for the primary system (excluding the fuel elements) is based on models used by Kao and Trosman [4,6]. Data concerning the physical dimensions of the volumes is given in Table 3.2.1.

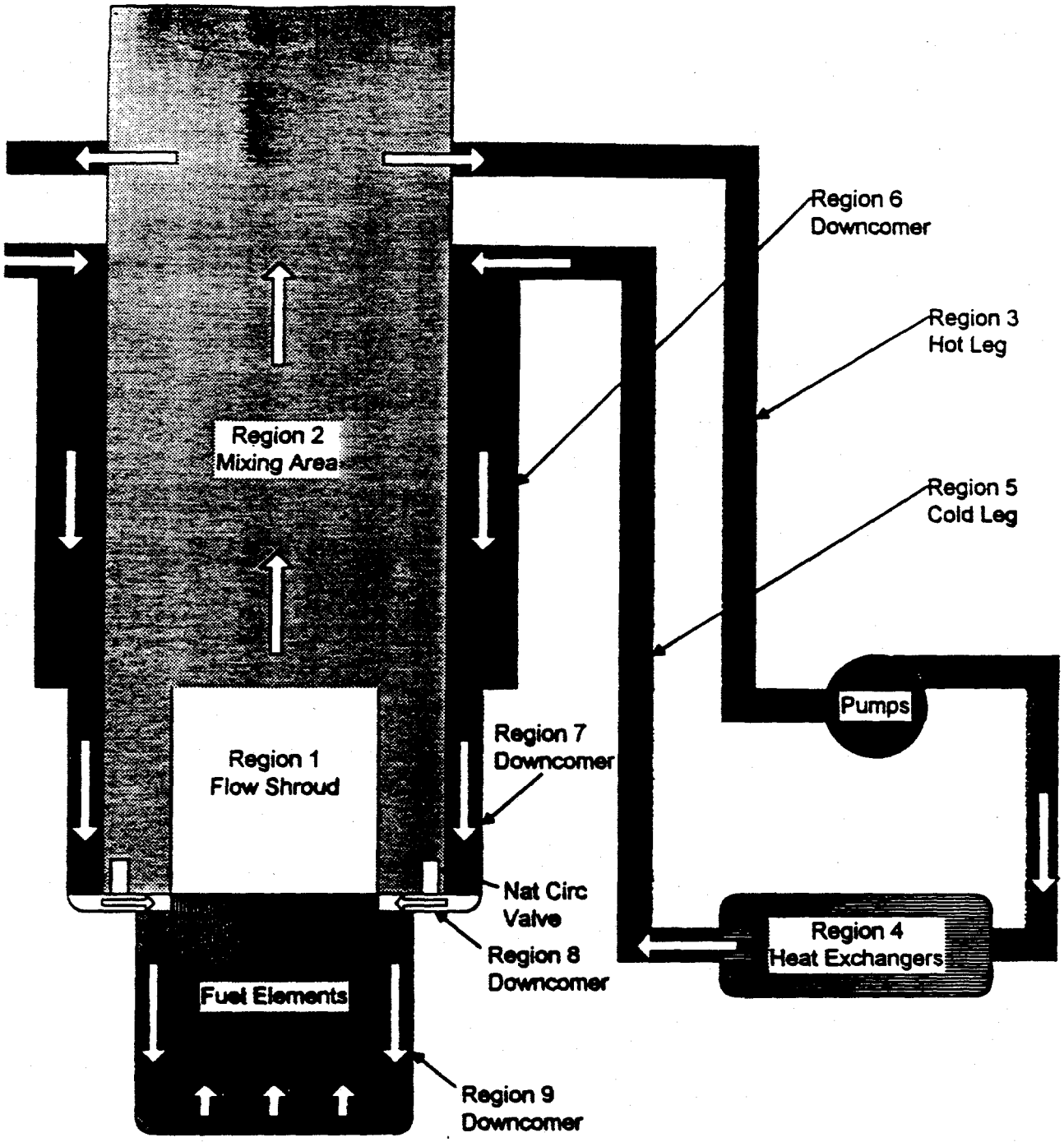

Figure 3.2.1. Primary loop control volumes. During forced convection, the nine regions shown above are used to calculate coolant properties. The fuel elements are further divided into axial and radial control volumes to provide more detailed information.

Table 3.2.1. Major component parameters for primary loop.

Region (See Figure 3.2.1)	Flow Area (m^2)	Volume (m^3)	D_e (m)	$Z_{out} - Z_{in}$ (m)	K Factor
Flow Shroud	0.130	0.099	0.387	0.76	0.0
Mixing Area	0.923	1.920	1.084	1.32	0.0
Hot Leg	0.032	0.427	0.203	-7.08	4.58
Heat Exchangers (Primary Side)	0.0689	0.297	0.00704	0.0	7.30
Cold Leg	0.032	0.468	0.203	6.97	2.17
Downcomer 6	0.339	0.413	0.180	-1.22	0.0
Downcomer 7	0.111	0.076	0.063	-0.69	0.30
Downcomer 8	0.0044	0.016	0.220	-.01	0.18
Downcomer 9	0.029	0.018	0.040	-0.61	0.0

Figure 3.2.2 shows the reactor core which contains 27 rhomboidal elements. The letters and numbers indicate the in-core position. The A-ring includes the innermost three positions. The B-ring contains the intermediate positions, while the C-ring holds the 15 outer positions adjacent to the control blades. The numbers are ordered clockwise, starting at the position of the regulating rod. Each position may be occupied by a fuel element, a dummy element, or an in-core experiment. Six 1.1% boron-impregnated control blades are placed at the hexagonal periphery of the fueled core.

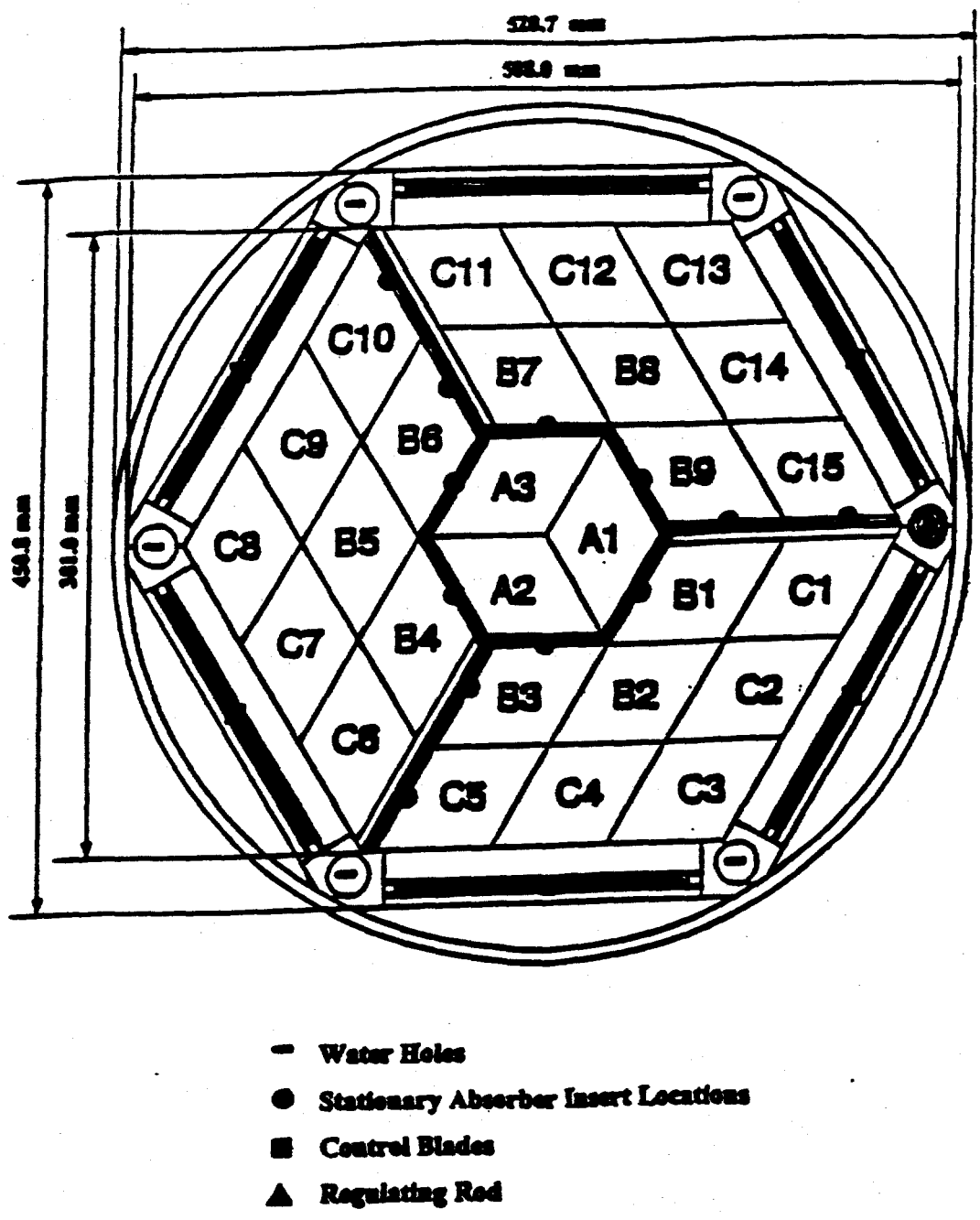

Figure 3.2.2. Horizontal cross-section of the MITR core. A horizontal cross section of the MITR core shows the 27 fuel element positions [3]. During normal operation, up to five fuel elements may be replaced with dummy elements or experimental facilities.

A close-up view of an individual fuel element is given in Figure 3.2.3. Each element contains 15 finned fuel plates. Each plate contains approximately 0.510 kg of U^{235} in a 93% enriched, uranium-aluminide fuel meat. The fuel is covered on both surfaces by aluminum cladding. The cladding, averaging 0.508 mm thick, is covered with 110 rectangular, longitudinal fins on each side. The fins are 0. 254 mm in height and width, and run the length of the fuel plate. Figure 3.2.4 shows the geometry of a single MITR coolant channel, drawn to scale.

Each fuel element is modeled as a collection of its 14 subchannels (plus two "half-channels" on the ends) lumped together. The code is capable of modeling each subchannel individually, but this is not done for several reasons. First, this creates up to 432 individual channels that each have different properties. The solution of the momentum and mass conservation equations for this many coupled subsystems would be a computationally prohibitive task. Second, all subchannels within a fuel element share a common inlet and outlet nozzle and a common position within the core. During normal operation these two factors combine to determine the flow to each fuel element. Within a fuel element, the subchannel with the highest power input, where total power input to a channel is given by Q_l,

$$Q_l = \int_0^L q'(z')dz' = \sum_{z=1}^{Z} q''(i,z)P_h\Delta z \qquad (2)$$

where, $q'(z')$ = Channel linear heat generation rate (W/m),

L = Channel heated length (m),

$q''(i,z)$ = Heat flux in channel i, axial node z (W/m^2),

Z = Number of axial nodes,

P_h = Heated perimeter (m),

Δz = Length of axial node (m).

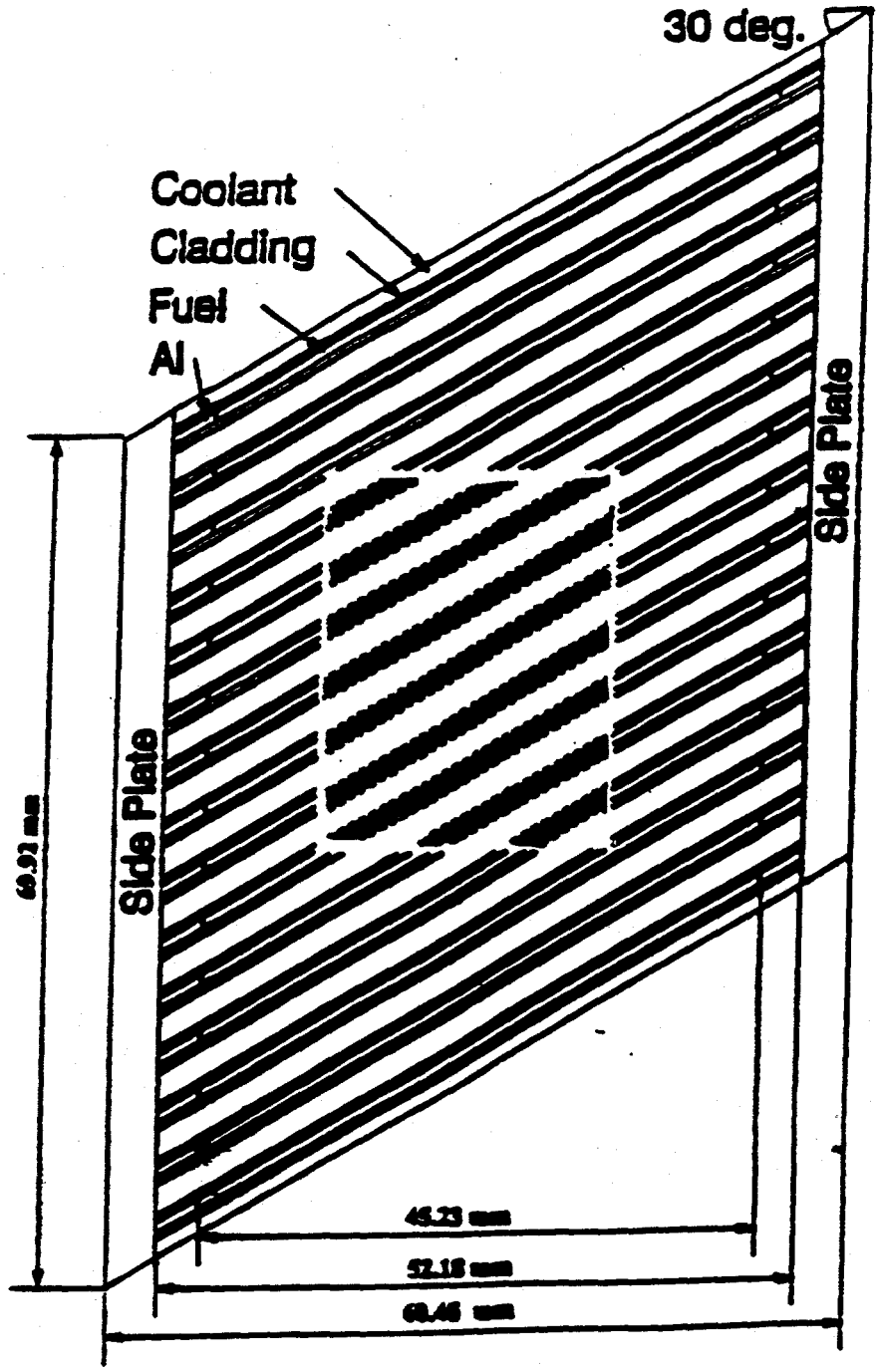

Figure 3.2.3. Horizontal cross-section of an MITR fuel element. A Cross-sectional view of a single MITR fuel element shows the finned surfaces [3].

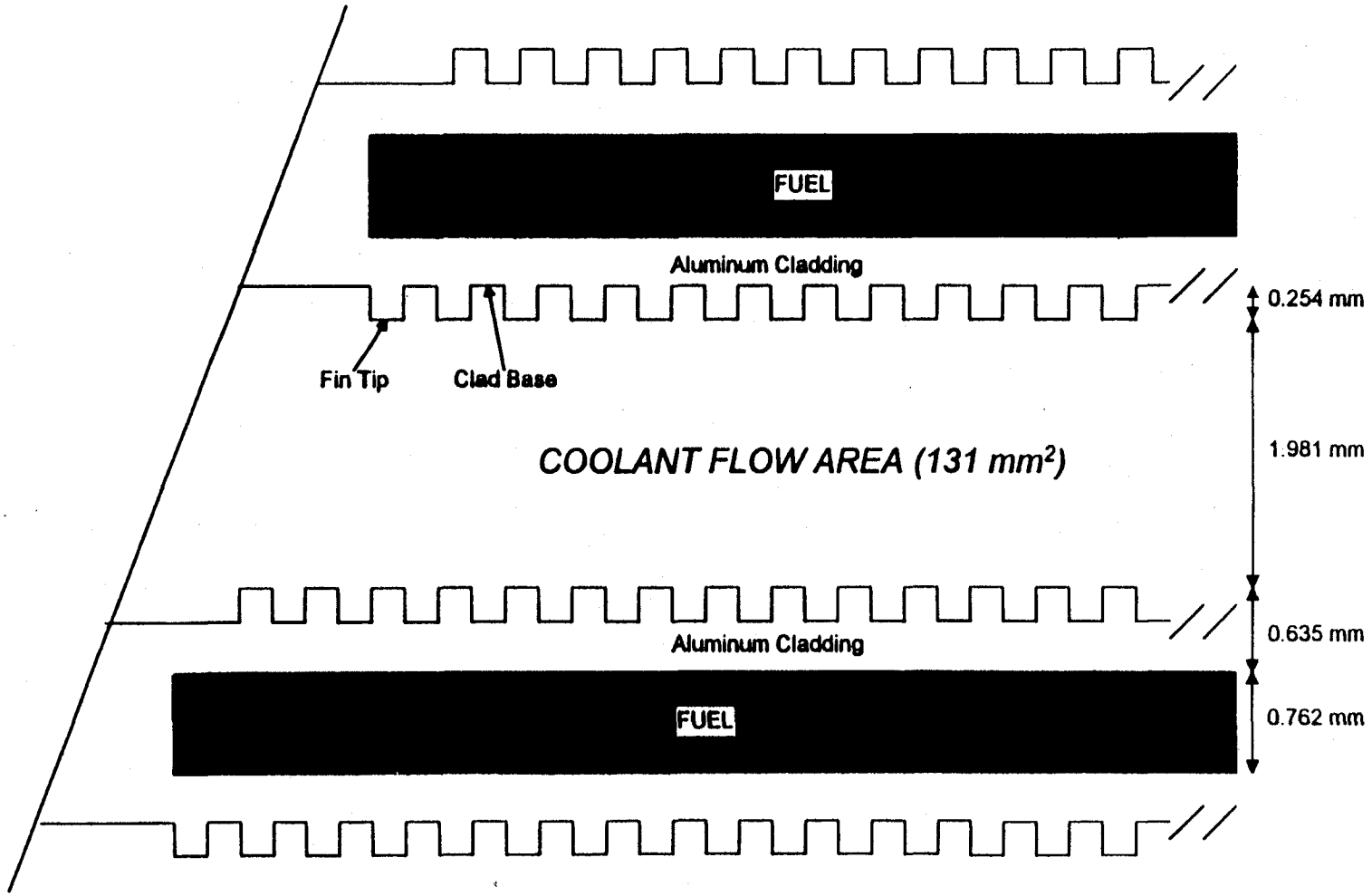

Figure 3.2.4. Flow area between two MITR finned fuel plates. The size of the fins and coolant channel are shown to scale. On an MITR fuel plate, there are 110 longitudinal fins (0.254 mm x 0.254 mm) on each side.

will receive the highest flow rate for single phase flow. The higher average coolant temperature in the hot channel leads to less frictional losses (density and viscosity decrease with increasing temperature). Because the losses per unit flow are less, and the pressure drop across each channel must be the same, the hot channel receives more flow than the colder channel during single-phase flow.

The point with the highest heat flux may have the highest clad temperature, despite the increased flow. To account for this, and to predict the onset of nucleate boiling at the hot spot, requires some method to consider the hot spot while still preserving the overall heat balance in the core. Considering the entire node to be at the "hot spot" or "hot stripe" conditions will lead to an inaccurate overall heat balance. The approach used here is to treat the whole node as being at the nodal-average heat flux, while checking for ONB at a hot spot using a series of peaking factors. This method, described in detail in section 3.10, is also used to allow for variations in surface heat flux and wall temperatures due to fin effects.

The following sections describe the key component and system models used in the MITR-III Multi-Channel Analysis Code.

3.3 Momentum Equation

Within the code there are two momentum balances performed during forced flow conditions. The primary loop flow model determines the total primary mass flow rate through the loop at each time step. The core flow split model determines how the flow is distributed among fuel elements in the core.

3.3.1 Primary Loop Momentum Balance

The overall momentum balance around the primary loop is given by summing over the N nodes in the loop,

$$\sum_{j=1}^{N} \frac{L_j}{A_j} \frac{dm_p}{dt} = \Delta P_{pump} - F_{system} \tag{3}$$

where, L_j = Length of node j (m),

A_j = Flow area of node j (m^2),

m_p = Mass flow rate in primary loop (kg/s),

ΔP_{pump} = Pump applied pressure (Pa),

(Given by user-supplied pump head-flow curve)

F_{system} = Net pressure drop through primary loop (Pa),

The loop mass flow rate, m_p, is assumed to be constant within the loop at each time step.

For the steady-state calculation, the initial mass flow rate is given by the user, and the applied pump pressure is set equal to the net pressure drop, F_{system}.. Because the pressure loss through the primary loop changes during the transient calculation (primarily due to density changes in the fluid), the mass flow rate through the loop changes according to Equation (3) until a new steady-state flow is established. The system tends to resist changes in flow because as the mass flow rate rises, the pump applied pressure tends to drop according to its characteristic curve (this is true for the normal operating point of most centrifugal pumps). This forces the flow back down towards its original value.

The losses through each node i in the primary system are made up of four components: friction (F_f), gravity (F_g), spatial acceleration (F_a), and form (F_k). For all nodes except the heated fuel region, these terms have the following form:

$$F_{f,j} = \frac{f(Re_j) L_j m_p^2}{2\rho_j D_{Hj} A_{fj}^2} \tag{4}$$

$$F_{g,j} = \rho_j g(z_{out_j} - z_{in_j}) \tag{5}$$

$$F_{a,j} = m_p^2\left(\frac{1}{A_{fj}^2\rho_j} - \frac{1}{A_{fj-1}^2\rho_{j-1}}\right) \tag{6}$$

$$F_{k,j} = \frac{K_j m_p^2}{2\rho_j A_{fj}^2} \tag{7}$$

where, $f(Re_j)$ = Darcy-Weisbach friction factor for flow at Reynold's Number Re,

ρ_j = Density of fluid in node j (kg/m^3),

D_{Hj} = Equivalent hydraulic diameter for node j (m),

g = Acceleration due to gravity (m/s^2),

z_{outj} = Outlet elevation of node j (m),

z_{inj} = Inlet elevation of node j (m),

K_j = Form loss coefficient for transition from node j-1 to node j.

In regions where heat is neither added nor removed the acceleration term is negligible, but it is important in the core and in the heat exchangers even for single phase flow. The pressure loss terms above are evaluated based on local values of temperature and pressure in each node. Inlet and outlet elevations are relative heights above any fixed reference point. All K-loss coefficients are supplied by the user. The K-loss term for flow leaving the pumps and entering the hot leg is modified during the steady-state calculations to include a "valve loss" term in the pumps. The inclusion of this term is essentially done to adjust the system model to the user-supplied pump head curve based on the steady-state value of mass flow rate. Because of this, the code will allow primary flow rates that are not within the true operating range of the MITR pumps, and the user must ensure that reliable input is being given to the code. The equivalent hydraulic diameter is equal to the diameter of the pipes for the hot leg and cold leg because these pipes are round. For flow in the core tank the equivalent hydraulic diameter is assumed to be equal to its conventional definition,

$$D_{Hj} = \frac{4A_{fj}}{P_{wj}} \tag{8}$$

where, P_{wj} = Wetted perimeter of node j (m).

The friction factor, f, in Equation (4) is a function of Reynolds number, Re. Under turbulent flow conditions the friction factor is given by the Blasius relation,

$$f = 0.316\,Re^{-.25} \tag{9}$$

for 10000<Re<49818, and the McAdams relation,

$$f = 0.184\,Re^{-.2} \tag{10}$$

for Re>49818. The choice of transition point from the Blasius to the McAdams correlations (Re = 49818) is made to ensure that f is a continuous function. When the flow is laminar (Re<2100) then product of the friction factor and the Reynolds Number is equal to a constant. For flow inside a rectangular channel with an aspect ratio of 25 [7,8],

$$f = \frac{91.5}{Re} \tag{11}$$

In the transition region where 2100<Re<10000, the friction factor is determined by finding the weighted average of the laminar and turbulent values,

$$F_T = \frac{Re - 2100}{7900} \tag{12}$$

$$f = (1 - F_T)\left(\frac{91.5}{Re}\right) + F_T\left(0.316 Re^{-.25}\right) \tag{13}$$

Figure 3.3.1 shows the variation of friction factor with Reynolds Number as calculated by Equations (9) through (13).

The total pressure loss term in Equation (3) is given by the algebraic sum of the four components in each node,

$$F_{system} = \sum_{j=1}^{N}\left(F_{f,j} + F_{g,j} + F_{a,j} + F_{k,j}\right) \tag{14}$$

Because of the slow rate of change of the primary flow rate with respect to time and the small time steps used in transient problems, a first order numerical solution of Equation (3) is acceptable. The mass flow rate is assumed to be the same throughout the loop at each time step. The primary mass flow rate at time step n+1 is given by,

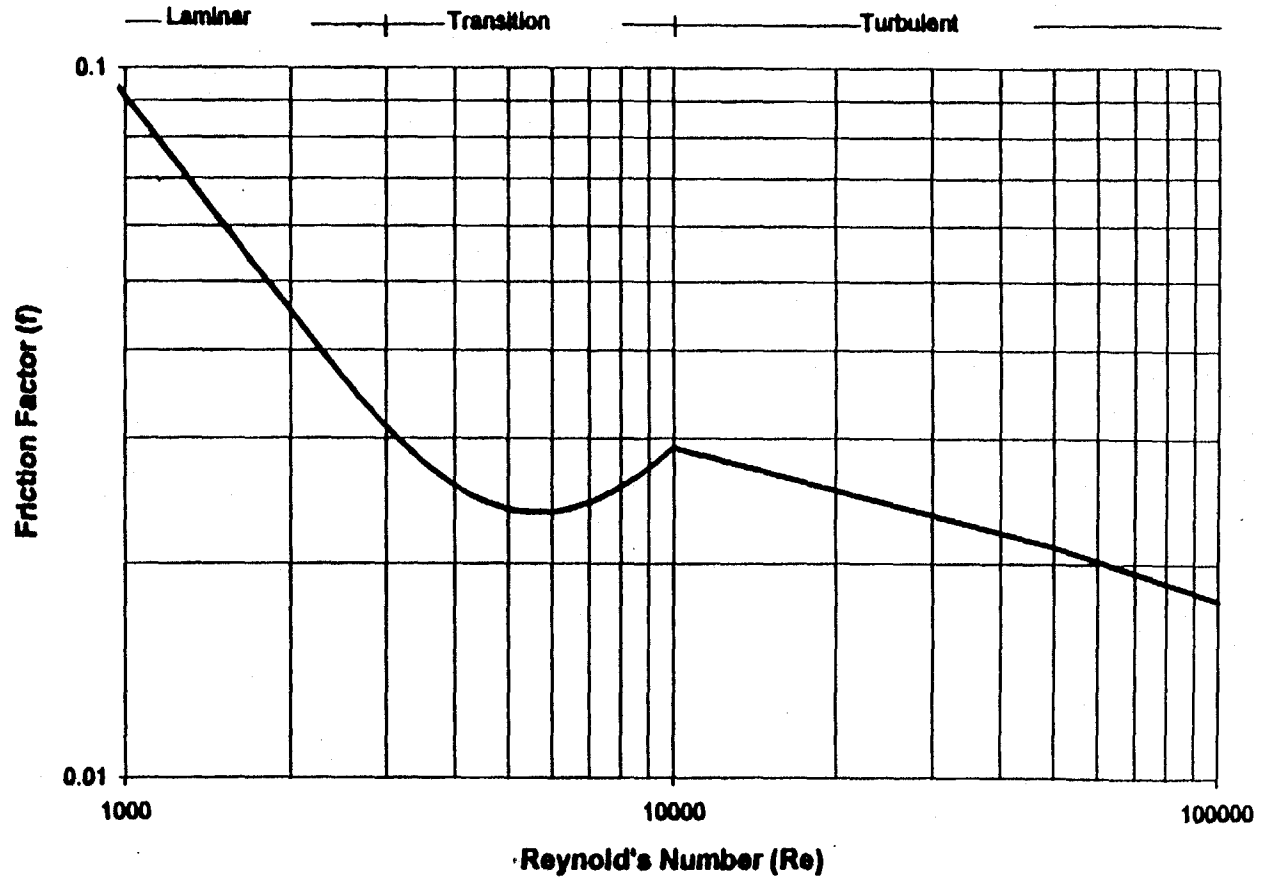

Figure 3.3.1. Friction factor versus Reynolds Number in an MITR channel. In the transition region, a weighted average of the laminar and turbulent friction factors is used to maintain continuity. Under nominal conditions, the Reynolds Number in an MITR coolant channel is between 10000 and 15000.

$$m_p^{n+1} = m_p^n + \frac{1}{\sum_{j=1}^{N} \frac{L_j}{A_{fj}}} \left(\Delta P_{pump} - F_{system} \right) \Delta t \qquad (15)$$

where,

Δt = Time step for transient calculations (s)

There are three junctions in the primary loop where the flow is split into two or more flow paths. A momentum balance requires that the pressure change through each flow path be the same, and the flow rate to each path will vary to accomplish this. As discussed earlier, the flow is split in the lower plenum and the various flow paths through the core are treated explicitly. The flow also splits to go to the heat exchangers (usually two are on-line). Variations between heat exchangers, that are the result of differences in design, obstruction of flow, piping flanges, or maintenance cycles, could lead to different pressure drops for each heat exchanger at a given flow rate. Trosman examined the flow split among heat exchangers and determined that the effect was small, but present in the current MITR-II heat exchangers due to differences in design [4]. The net effect on the core inlet temperature, however, was negligible. The analysis in this report assumes that the new heat exchangers installed for MITR-III will be identical. Therefore, the heat exchangers are lumped together into one unit, requiring an equal flow split among primary-side flow paths. The flow also divides at the exit of the hot leg to enter the two primary pumps. These pumps are assumed to be identical, and the flow through each is assumed to be equal to one-half of the total loop flow.

3.3.2 Core Flow Momentum Balance

The limiting criteria for MITR-III are ONB for the LSSS, and CHF for the Safety Limits. Both of these are localized phenomena, although they do depend to some extent on the heat input history of the channel. The mass flux in each channel is a critical parameter in determining wall temperatures and single-phase heat transfer coefficients. These in turn determine whether or not ONB occurs in a particular node. The mass flux is also a key determinant in the occurrence of CHF in a particular channel. The accurate calculation of mass flux in each channel at each time step is essential to predicting the limits of the MITR-III.

The amount of flow entering each channel at steady-state is governed by the stipulation that the pressure drop over each channel be equal. The bulk flow entering the bottom plenum is at a single pressure, P_{in}. The flow then splits into the individual flow channels and then comes together again in the flow shroud region at a single pressure, P_{out}. In order for this to be true, the integral pressure loss over each channel must be equal to $P_{in} - P_{out}$.

This condition requires only that the integral pressure change be equal in each channel. The pressure gradient, dP/dz, in each channel may be different at each axial position because the flow channels do not communicate along the heated length of the fuel element. This may result in different pressures in each channel at the same height. Figure 3.3.2 shows this effect. The single phase channel has a relatively constant pressure gradient along its length. The hotter channel shows a sudden jump in pressure gradient at the boiling boundary because of the effects of the two-phase friction multiplier and the acceleration term. The different pressure gradients result in the same net pressure loss when the pressure gradients are integrated over the channel length. The result is that the pressure distribution along the channel lengths may be different. Pressures at the same axial plane can vary among channels, as long as the pressure at the inlet and the outlet are equal. The different pressure gradients are a result of variations in heat flux, coolant temperature, and void fraction. Differences in geometry will also lead to different pressure gradients.

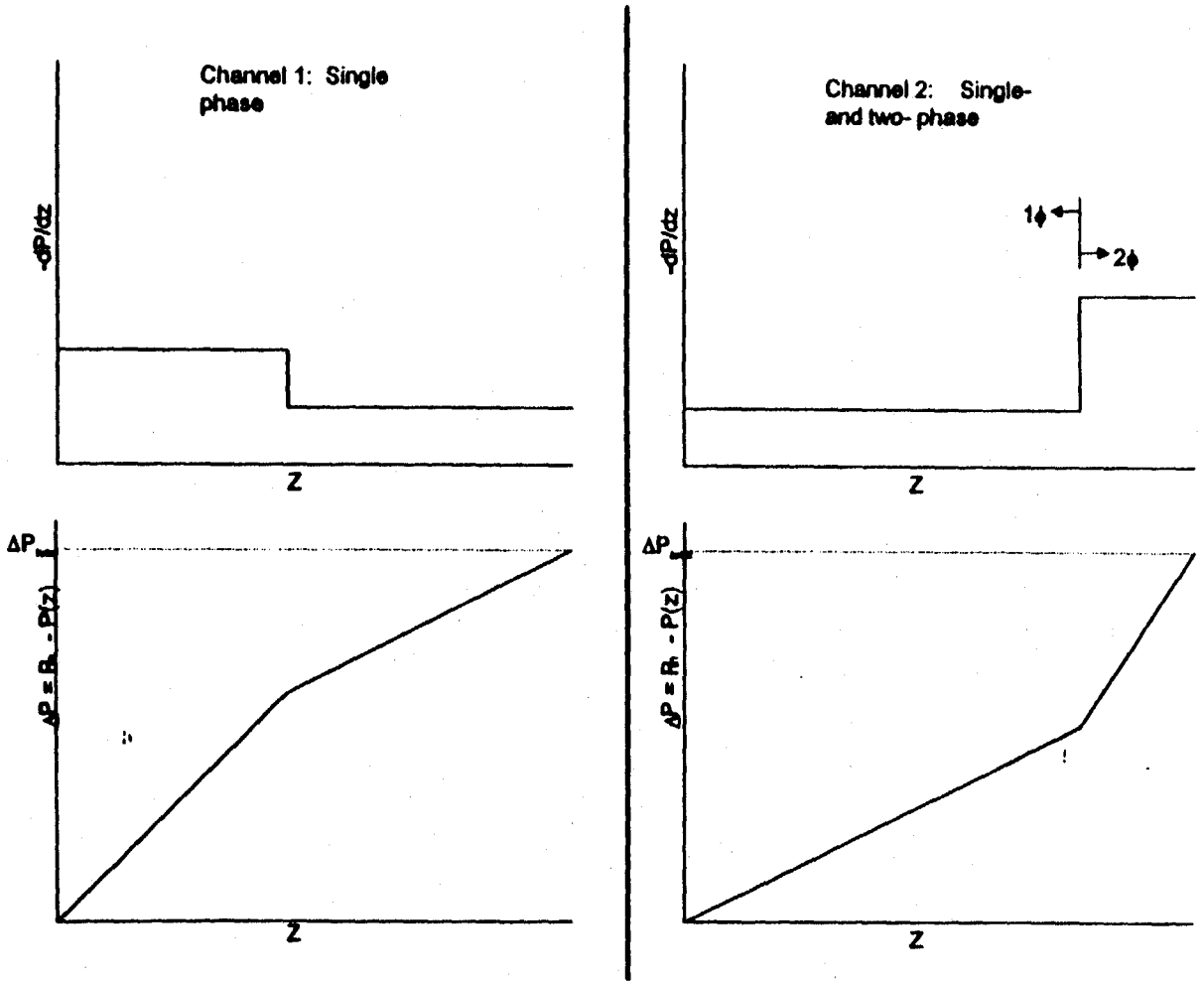

Figure 3.3.2. Constant integral pressure drop condition applied to MITR channels. Channel 1 and Channel 2 both have the same total pressure drop. However, channel two has a lower pressure gradient in its single phase region, and a higher pressure gradient in the two-phase region. Channel 1 receives more flow than Channel 2 in order to maintain equal integral pressure drops.

In addition to pressure gradients within the coolant channels, the shape of the inlet plenum also plays a role in determining the flow distribution among fuel elements. Studies done by Allen measured the flow disparity in coolant channels using a pitot tube inserted in the outlet nozzle of the fuel elements [7]. Flow disparity is defined as,

$$D_{fi} = \frac{m_i N_{ch}}{m_{core}} \tag{16}$$

where, D_{fi} = Flow disparity for channel i,
m_i = Mass flow rate in channel i (kg/s),
N = Number of channels in parallel,
m_{core} = Mass flow rate through the core (kg/s),
G_i = Mass flux in channel i (kg/m^2s),
G_{core} = Average mass flux in core (kg/m^2s).

A flow disparity of 1.0 means that channel i receives an amount of flow equal to the core average. A flow disparity of less than 1.0 implies that a channel is receiving less flow than the average. This means that its pressure gradient per unit flow is higher than the average channel due to one of the reasons discussed above.

Figure 3.3.3 shows the results of Allen's measurements for an MITR-II core during startup tests. Because the tests are conducted at zero power the flow disparities are the result of differences in flow channel geometry (a small effect at zero power due to strict manufacturing tolerances) and the effect of the inlet plenum shape. Prior to the tests, a plate was installed at the bottom of the plenum in order to even out the otherwise irregular distribution of flow to the fuel elements.

The impact of the plenum shape is included in the Multi-Channel Analysis Code by the introduction of plenum flow disparity factors. The user supplies the flow disparity for each channel that results from the plenum shape (i.e., the zero-power flow disparity found by Allen). A plenum flow disparity factor, K_{Pi}, is found for each channel from the following,

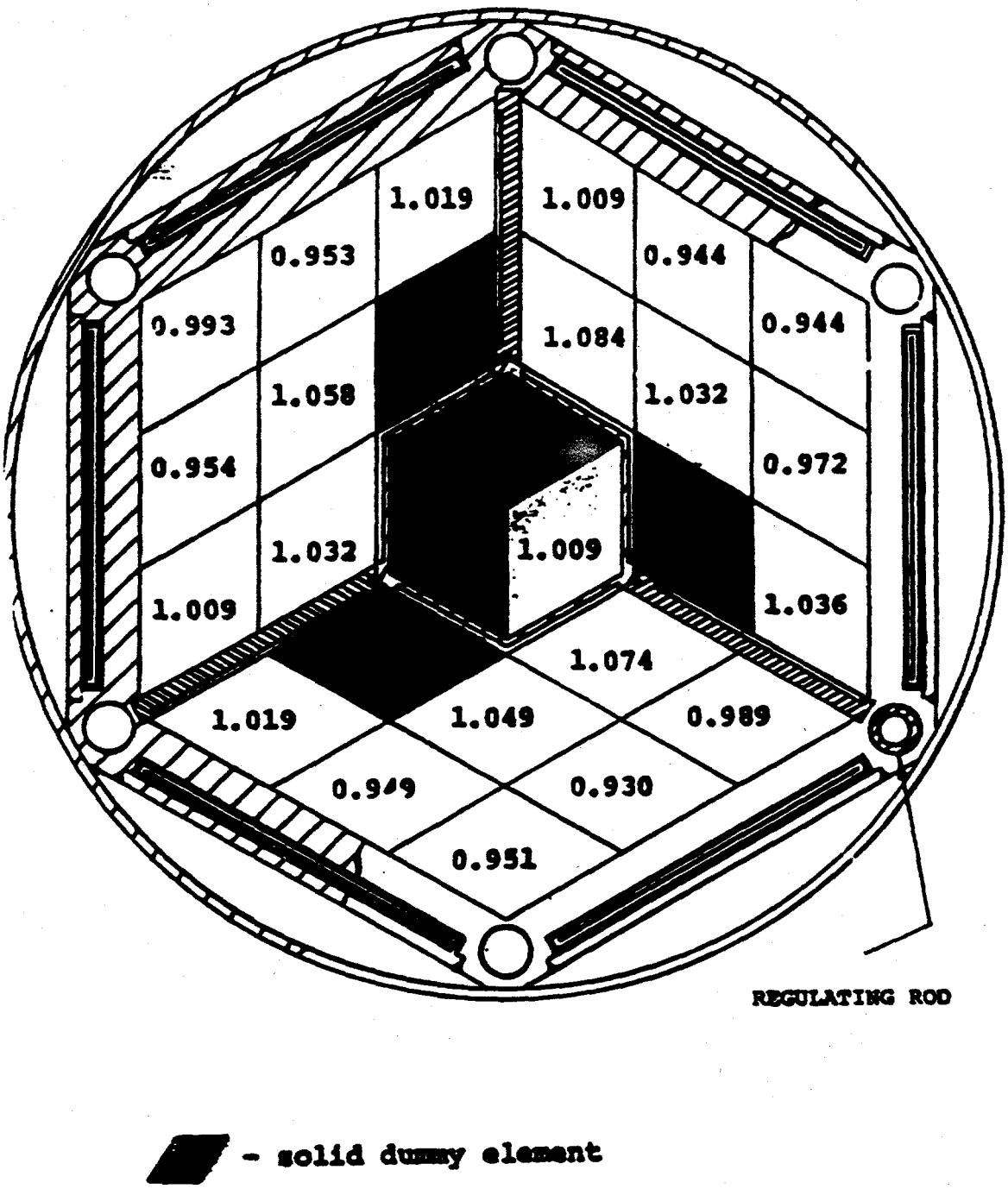

Figure 3.3.3. Plenum flow disparities for the MITR-II. The plenum flow disparities are for MITR-II, Core II (22 fuel elements). These values were experimentally measured by Allen [7].

$$K_{Pi} = \frac{2\rho_{in}}{G_i^2}\left(\Delta P_{core} - F_i(m_i)\right) \qquad (17)$$

with,

$$m_i = \left(\frac{m_{core}}{N}\right) D_{fi} \qquad (18)$$

where, ρ_{in} = Coolant density at fuel element inlet (kg/m^3),

$F_i(m_i)$ = Total losses in fuel element i with a flow equal to m_i (Pa),

m_i = Steady-state flow rate into channel i.

The value of K_{Pi} may be either positive or negative. The physical interpretation of the plenum disparity factors is that they account for a pressure gradient present in the water flowing up from the bottom of the plenum towards the inlets the fuel elements. Figure 3.3.4 illustrates the meaning of the plenum disparity factors. There exists some planar area-averaged pressure, P_0, at the bottom of the plenum. The shape of the bottom of the core tank causes some mal-distribution of pressure within the plenum. The fluid entering the A-ring elements, for example, has further to travel from the downcomer outlet to the fuel element inlet nozzle. On the other hand, the curved shape of the plenum plate reduces the frictional losses that these coolant streams experience. The net result is that the stream heading towards the A ring elements may have a different fuel element inlet pressure than the streams heading towards the B or C ring elements. In effect, the plenum disparity factors impose a pressure "gain" or "loss" on the coolant streams before they actually enter the fuel elements. Because ΔP_{core} is the same for each channel i in Equation (17), the sum of all plenum disparity losses F_{Pi}

$$F_{Pi} = \left(\frac{K_{Pi} G_i^2}{2\rho_{in}}\right) \qquad (19)$$

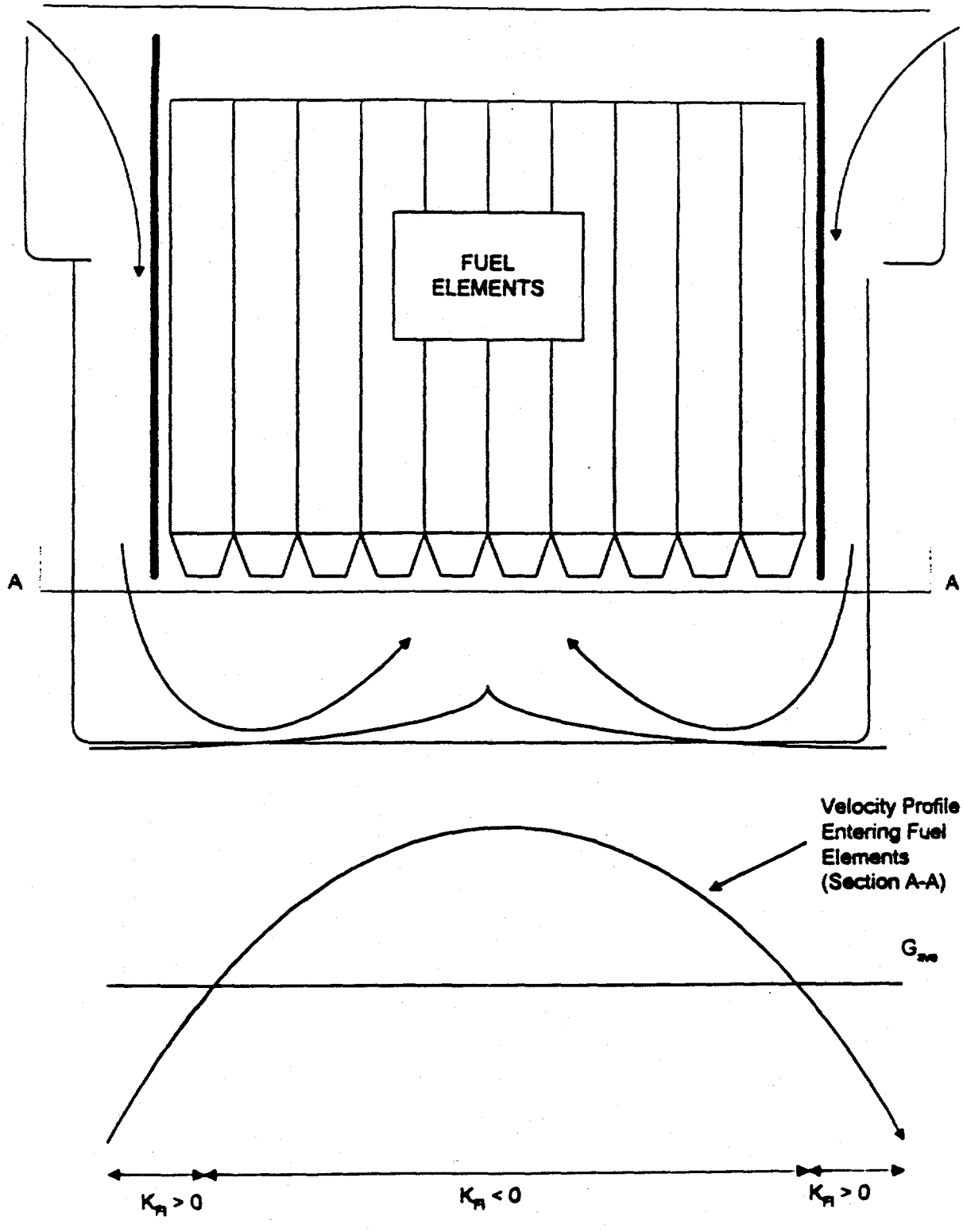

Figure 3.3.4. Source of MITR plenum disparity factors.

is zero. The plenum pressure distribution now contains a radial gradient that is forced to match experimental measurements, while the radially averaged pressure remains unchanged.

Another factor that affects the distribution of flow to the fuel elements is the presence of non-fueled dummy elements in the core. Allen examined the effect of dummy element positions on the flow distribution to the fueled elements [7]. His results show that when a dummy element replaces a fuel element in a given region of the core, the flow to the surrounding fuel elements increases. The increased flow to the surrounding elements occurs because a dummy element has a smaller cross-sectional area for flow than a fuel element. During steady-state operation, the fuel elements in a 22-element core receive an average of 5.42 kg/s, while the dummy element receives only 1.55 kg/s [3,7]. The presence of dummy elements and in-core experiments can be accounted for in one of two ways. The unfueled elements can be modeled exactly like the fuel elements, but with different geometric parameters (flow area, wetted perimeter, etc.) and zero power. The other approach would be to ignore the dummy elements and set the core flow rate equal to the flow rate through the fuel elements only.

Two-Phase Flow in the Core

When severe transients lead to two-phase flow in the core, the pressure drops described in Equations (4) through (7) above are replaced by the following:

$$F_{f,z} = \frac{f(Re_{lo,z})L_z m_p^2}{2\rho_{f,z}D_{H,z}A_{f,z}^2}\phi_{lo,z}^2 \qquad (4a)$$

$$F_{g,z} = \rho_{m,z}g(z_{out,z} - z_{in,z}) \qquad (5a)$$

$$F_{a,z} = m_p^2\left[\left(\frac{(1-x_z)^2}{A_{f,z}^2(1-\alpha_z)\rho_{f,z}} + \frac{x^2{}_z}{A_{f,z}^2\alpha_z\rho_{g,z}}\right) - \left(\frac{(1-x_{z-1})^2}{A_{f,z-1}^2(1-\alpha_{z-1})\rho_{f,z-1}} + \frac{x^2{}_{z-1}}{A_{f,z-1}^2\alpha_{z-1}\rho_{g,z-1}}\right)\right] \tag{6a}$$

$$F_{k,z} = \frac{K_z m_p^2}{2\rho_{m,z}A_{f,z}^2} \tag{7a}$$

where, for each channel i (the subscript i has been dropped for simplicity),

$\phi^2{}_{lo,z}$	=	Two-phase friction multiplier in node z,
$f(Re_{lo,z})$	=	Moody friction factor for liquid only flow at Reynold's Number Re_{lo},
$\rho_{m,z}$	=	Two-phase density of fluid in node z (kg/m^3),
$\rho_{f,z}$	=	Saturated liquid density in node z (kg/m^3),
$\rho_{g,z}$	=	Saturated vapor density in node z (kg/m^3),
x_z	=	Flow quality in node z (mass fraction),
α_z	=	Void fraction in node z (volume fraction).

The two-phase friction multiplier, $\phi^2{}_{lo}$, is generally a function of system pressure and flow quality. In addition, the flow regime is an important factor because many of the two-phase friction models are based on an assumed flow regime. The Homogenous Equilibrium Model (HEM) is based on the assumptions of thermodynamic and mechanical equilibrium between the two phases. The two-phase friction multiplier based on the HEM assumptions is [9],

$$\phi_{lo}^2 = \left[1 + x\left(\frac{\rho_f}{\rho_g} - 1\right)\right]\left[1 + x\left(\frac{\mu_f}{\mu_g} - 1\right)\right]^{-n} \tag{20}$$

where, μ_f = Viscosity of saturated liquid (Ns/m^2),

μ_g = Viscosity of saturated vapor (Ns/m^2),

n = Function of Reynold's Number.

The exponent, n, in the above equation appears because the assumption is made that the two-phase friction factor has the same Reynold's Number dependence as the single phase friction factor. The exponent, n, is the same as the exponent in friction factor relations of the form,

$$f = a\,Re^n \tag{21}$$

The value of n depends on whether the flow is laminar or turbulent. In order to preserve continuity in the transition region between laminar and turbulent flow, the following expression for n is used,

(22)

$n = -1.0$ For $Re < 2100$

$$n = \left(\frac{Re-2100}{7900}\right)(-.25) + \left(1-\left(\frac{Re-2100}{7900}\right)\right)(-1.0)$$ For $2100<Re<10000$

$n = -.25$ For $10000<Re<49818$

$n = -.20$ For $Re>49818$

The Martinelli-Nelson two-phase multiplier is based on a separated flow assumption. It can be expressed in analytic form as,

$$\phi_{lo}^2 = 1.2\left(\frac{\rho_f}{\rho_g}-1\right)x^{0.824}+1 \tag{23}$$

Because of the assumptions used in their formulations, these two models for ϕ^2_{lo} are appropriate for different flow conditions. In low void fraction and high flow rate conditions where bubbly flow is likely to be present, the HEM model is the most accurate. Under conditions of low mass flux ($500 < G < 1000$ kg/m^{2}s) or high void fraction ($\alpha >$ 25%) where annular flow dominates, the Martinelli-Nelson correlation gives better results [9].

The two-phase density term, ρ_m, represents the mixed density of the liquid and vapor phases. The value of ρ_m is given by,

$$\rho_m = \alpha\rho_g + (1-\alpha)\rho_f \tag{24}$$

The values of x and α are determined from the void fraction model outlined in Section 3.5.

Equations (4,5,6,7) (or 4a,5a,6a,7a) are added together to give the total pressure loss in each axial node of each channel. Knowledge of the pressure loss in each axial node gives a discretized axial pressure distribution within each channel. Because the pressure at the top of the mixing area is known to be at atmospheric pressure, and the pressure difference between the top of the mixing area and the fuel element exit nozzle is known, it is possible to determine the pressure at each axial node of each fuel element. This pressure is used to evaluate physical properties.

The losses in each axial node are added to give the total pressure loss in each channel.

3.3.3 Core Flow Split

Once the pressure loss in each channel is determined as outlined above, it is possible to calculate the redistribution of core flow. At steady-state the flow to each fuel element is found such that the pressure loss in each flow path is equal. Changes in power level, total core flow, or other parameters can create a difference in pressure losses among the core channels during each subsequent time step.

The change in flow rate to a given channel, i, is given by,

$$\frac{1}{C_i}\frac{\partial m_i}{\partial t} = \Delta P_{core} - F_i \tag{25}$$

with,

$$C_i = \frac{1}{\sum_{z=1}^{Z}\frac{L_z}{A_z}} \tag{26}$$

where, m_i = Mass flow rate to channel i (kg/s),

t = Time (s),

ΔP_{core} = Pressure difference between core inlet and outlet (Pa),

F_i = Pressure loss in channel i (Pa),

L_z = Length of axial node z in channel i (m),

A_z = Area for flow of axial node z in channel i (m^2).

Equation (25) can be written for each of the N channels being considered. In the resulting system of equations there are N+1 unknowns: $\frac{\partial m_i}{\partial t}$ for each of the N channels, and ΔP_{core}. The rate of change of the total loop flow rate is governed by Equation (3). After any redistribution of flow among the fuel elements, the sum of the flow rate through the fuel elements must equal the total loop flow. Because this was true at steady-state, for each subsequent time step this constraint can be expressed by,

$$\frac{\partial m_P}{\partial t} = \sum_{i=1}^{N} \frac{\partial m_i}{\partial t} \tag{27}$$

Equation (27) provides the necessary equation to form a closed system of N+1 equations. Solving Equation (20) for $\frac{\partial m_P}{\partial t}$ for each channel and substituting into Equation (27) gives the following result for the core pressure drop,

$$\Delta P_{core} = \frac{\left(\frac{\partial m_p}{\partial t}\right) + \sum_{i=1}^{N} C_i F_i}{\sum_{i=1}^{N} C_i} \tag{28}$$

With the core pressure drop known, Equation (25) can be solved using standard numerical methods to give the mass flow rate to each channel for each subsequent time step. It is evident from the above equations that the primary loop momentum equation and the core momentum equation are linked by two variables: m_P and ΔP_{core}. Because of this interdependence, both momentum equations are solved using the same time step size.

During pump coastdown transients, Equation (3) is replaced by a mass flow rate versus time forcing function provided by the user. In this case, the pressure loss around the primary loop is not computed because the primary flow is independent of system pressure losses.

Another exception to the method outlined above is the case of natural circulation in the core. When the natural circulation valves open (thereby creating an additional flow path from the lower plenum to the mixing area), the momentum equation is modified to reflect this change in flow configuration. Natural circulation flow in MITR and the governing momentum equation are discussed in Section 3.9.

3.4 Energy Conservation

3.4.1 Heat Generation and Transfer in the Fuel Elements

Heat generated from fission in the fuel is made up of several components. Most of the kinetic energy of the fission fragments, as well as beta and gamma decay energy, is deposited in the fuel and the adjacent cladding. Some of the energy (including the fission neutrons) is deposited directly into the flowing coolant, or into the shielding and moderator outside of the core. The percentage of energy deposited in each location is determined by the mean free path of the particles and the geometry of the system. Experimental studies by Allen on the MITR-II core determined the fraction of fission energy that is deposited within the core, the reflector, and the shielding. Table 3.4.1 shows that 96.67% of the fission energy is deposited into the core, while the remaining 3.33% is absorbed in the reflector or shielding. Parra used the Monte Carlo Neutron Photon (MCNP) code to determine the fraction of core fission energy that is deposited in the fuel plates, coolant, and core structural material. Energy deposited in these three in-core regions must be eventually transported to the primary coolant, and therefore this heat serves as the basis for thermal-hydraulic design. Table 3.4.1 shows the results of the MCNP calculations for the current MITR fuel.

Table 3.4.1. Distribution of fission energy in MITR [3,7]

Location	Percentage
Core	(96.67)
Fuel	90.97
Coolant	4.60
Structural Material	1.10
Reflector	2.05
Shielding	1.28
TOTAL	100.00

The heat generated in the fuel is transported by conduction to the cladding that covers both sides of the fuel matrix. Because the fuel is in an aluminide matrix of high thermal conductivity, and the thickness of the fuel plates is so small, heat transfer from the fuel to the clad is very good. This results in fuel temperatures that are only a few degrees above the clad temperature. From the clad, the heat is passed by convection to the flowing primary coolant. The presence of the longitudinal fins on the cladding aid in the transfer of heat by increasing the surface area for convection. Figure 3.4.1 shows the relationship between the various heat fluxes. The heat transfer scheme outlined here uses half of a fuel plate as a unit cell. Therefore, all properties represent half of each fuel plate. With the volumetric heat generation rate in the fuel, q_f''' known from neutronic calculations, the heat flux at the fuel-clad interface during steady-state is given by,

$$q_f'' = \frac{q_f''' V_f}{2A_f} \tag{29}$$

where, q_f'' = Heat flux in fuel plate (W/m^2),

q_f''' = Volumetric heat generation rate in fuel (W/m^3),

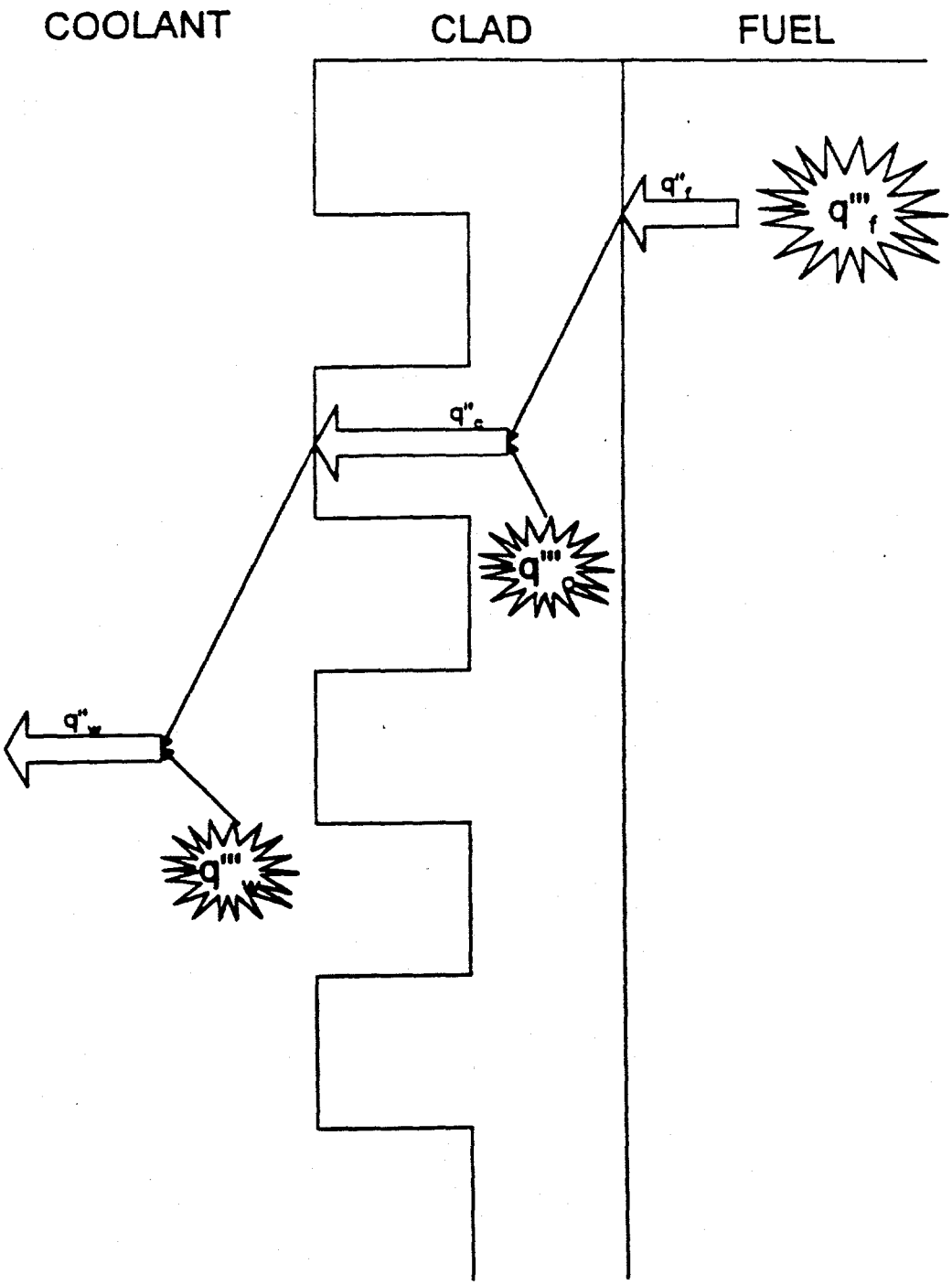

Figure 3.4.1. Heat flux from fuel tocoolant. Heat is generated in the fuel, the clad, and the coolant (shown as q'''). The area used to define the heat flux changes as the heat passes from the fuel into the finned cladding.

V_f = Volume of fuel (m^3),

A_f = Area for heat transfer in fuel (m^3).

This represents the heat flux being transported from fuel to the clad at the fuel-clad interface on each side. The volumetric heat generation rate, q_f''', is equal to the fission energy generated in the fuel times the fraction of fission energy deposited in the fuel. Therefore, it varies with both time and spatial dimensions. The heat flux, q_f'', is the average heat flux at the fuel-clad interface. After crossing the fuel-clad interface, the heat flux begins to rise with the addition of the heat generated from fission energy that is deposited directly in the cladding. The heat flux at the clad-coolant interface is,

$$q_c'' = \frac{q_f'' A_f}{A_c} + \frac{q_c''' V_c}{2A_c} \tag{30}$$

where, q_c'' = Heat flux in clad (W/m^2) [based on finned surface area],

q_c''' = Volumetric heat generation rate in clad (W/m^3),

V_c = Volume of clad (m^3),

A_c = Area for heat transfer in clad (m^2) [including fins].

In the MITR fuel plates, the area for heat transfer in the fuel is approximately equal to the area for heat transfer in the clad at the fuel-clad interface. A short distance into the clad, however, the presence of the fins nearly doubles the available area for heat transfer to the coolant. Equation (30) is based on the clad heat transfer area that includes the fins.

Previous studies have accounted for the presence of the fins by defining the clad-to-coolant heat flux based on a flat (unfinned) surface area. The "flat" surface has approximately half the area as the finned surface. A surface effectiveness factor is included to account for the fins. Parra calculated the surface effectiveness due to fins to be approximately equal to two. He found that the surface effectiveness approaches the ratio of the finned to unfinned surface areas [3]. This method maintains the energy balance because the amount of energy being transferred to the coolant per unit time is the same as it would be for the finned surface. However, the heat flux based on the flat surface approximation is roughly twice the value of the average heat flux defined using the finned surface area. In ONB and CHF calculations, the unreasonably high heat flux based on the flat plate approximation leads to inaccurate predictions of these phenomena. In addition, the flat plate approximation predicts surface temperatures that are eight to ten degrees higher than those observed on the finned surfaces [3]. Using the flat plate approximation, the heat flux at the fin tips and the heat flux between fins are both substantially below the flat "surface average" heat flux. With the average heat flux defined based on the finned surface area, the heat flux from the tips is found to be slightly above the surface average, while the heat flux between fins is slightly below the surface average. This situation provides a more physically correct definition of a surface-average heat flux. Although both approaches (finned surface, flat plate) result in an average heat flux that maintains the energy balance, the finned surface approach is used here because it most accurately represents the true heat flux along the surface of the fuel plate.

After passing through the clad, the heat is transferred by convection to the coolant. The heat flux passing from the clad to the coolant depends on the choice of area for heat transfer at the clad-coolant interface. In a one-dimensional heat transfer model there is no way to explicitly model the heat flux distribution resulting from the longitudinal fins. A choice must be made on how to define the heat flux at the clad-coolant interface.

Knowledge of the clad heat flux serves two purposes. First, it determines the rate of heat addition to the flowing coolant (at steady-state and during transients). In order for an energy balance to be correct over the entire core, the heat flux out of the clad must equal the wall heat flux entering the coolant. Therefore, the heat transfer area from the clad must be the same as the heat transfer area into the coolant. For this purpose, it is sufficient to assume that the heat flux at every point in the clad (in a given channel and axial node) is equal to the average heat flux in that node. This eliminates all differences between the heat flux at fin tips and at the grooves between fins, and maintains the overall energy balance.

Second, the heat flux at the clad-coolant interface is used to predict the clad temperature, the onset of nucleate boiling (ONB), and the point of critical heat flux (CHF). These calculations are very dependent upon local conditions. Several factors cause the heat flux within a given node to vary. These factors, as shown in Figure 3.4.2, include:

1) Power difference between fuel plates (x-direction peaking). The fifteen fuel plates in each fuel element are operating at different power levels. Depending on the location and orientation of the fuel element in the core, and the fuel burnup, one fuel plate will be hotter than the others.

2) Power shape across each fuel plate (y-direction peaking). In a given individual fuel plate, there is a power gradient across the plate width. Depending on the location and orientation of the fuel plate, and the fuel burnup, one spot will be hotter than the others.

3) Axial power shape (z-direction peaking). The axial power shape is imposed on each fuel elements based on a measured or calculated axial heat flux distribution. When the channel is divided into nodes to perform discretized calculations, some of the sharp peaks are lost. Within a node, some axial plane will have a higher heat flux than others.

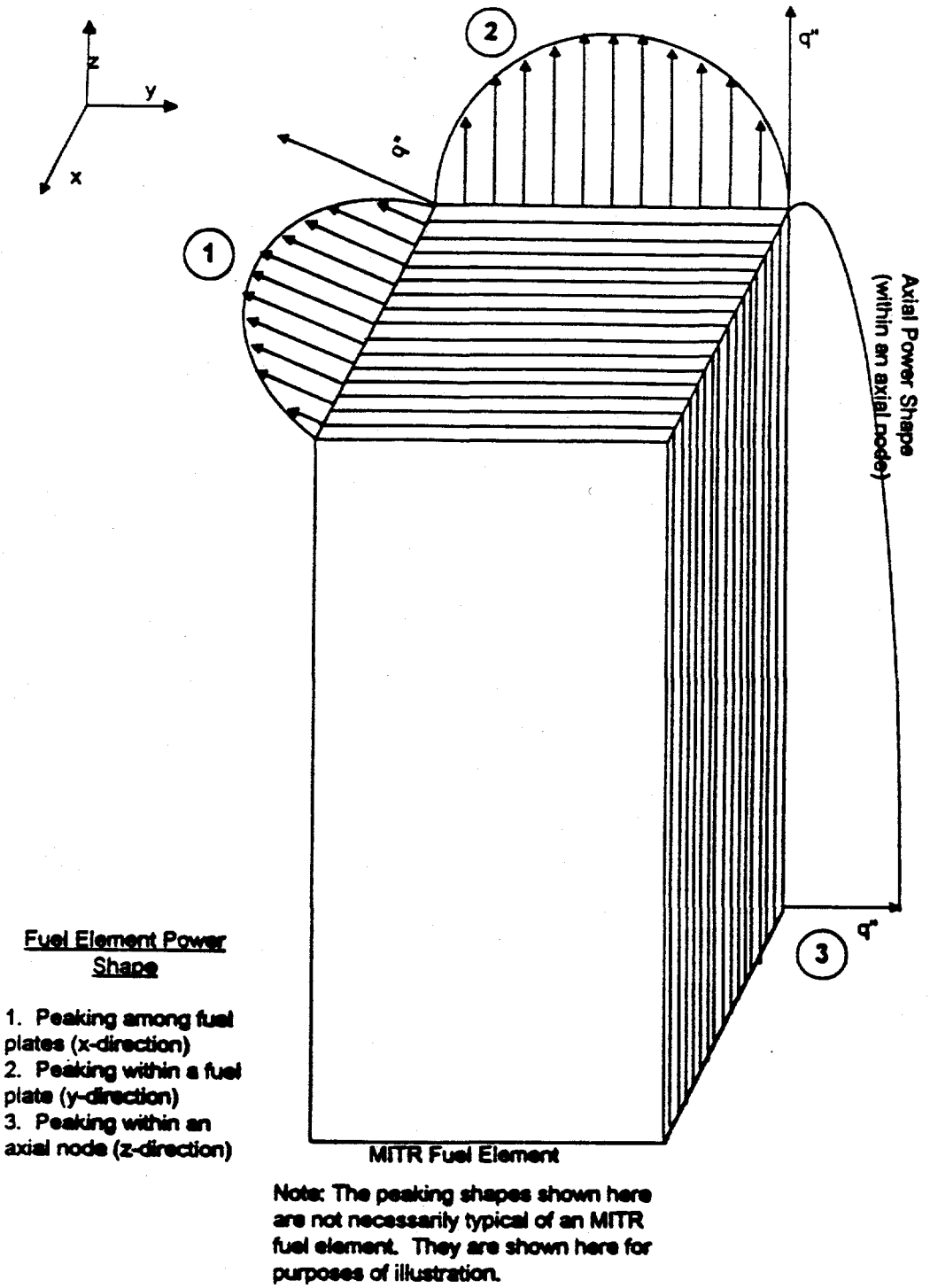

Figure 3.4.2. Heat flux peaking factors. The heat flux peaking factors in the x, y, and z directions used to determine the ratio of the maximum local heat flux within a given node to the node-average heat flux.

These three factors combine to give a three-dimensional power shape to the fuel element. The single point in the node where these three factors peak will be the hot spot. Thermal-hydraulic analyses in nuclear systems often use hot-channel, hot-stripe, or hot-spot calculations to determine the conditions at the hottest point in the core. Treating the entire node as if it were at the hot-spot conditions violates the overall energy balance and causes this error to propagate through subsequent time steps. In order to maintain the overall energy balance, while at the same time predicting the occurrence of localized phenomena (ONB, CHF), the following approach is used:

1) The area for heat transfer is defined to include the entire finned area.

2) For the calculation of the heat transfer to the coolant, the heat flux at each point in the node is assumed to be equal to the surface area-averaged heat flux.

3) For calculation of localized phenomena (ONB, CHF) a heat flux profile within the node is imposed by compensating for the three factors shown above. This is discussed in detail in Section 3.10.

During transients the energy balances discussed above are not applicable. The transient heat conduction equation must solved in the fuel and the clad. The general form of the time-dependent heat transfer equation from the fuel to the adjacent cladding is,

$$M_f c_{p,f} \frac{\partial T_f}{\partial t} = q''_f A_f - U_f A_f (T_f - T_c) \qquad (31)$$

with,

$$q_f'' = \frac{q_f''' V_f}{2A_f}$$

where, M_f = Mass of fuel (kg),

$c_{p,f}$ = Temperature dependent specific heat capacity of fuel (J/kgK),

T_f = Fuel temperature (°C),

T_c = Clad temperature (°C),

U_f = Overall heat transfer coefficient (W/m^2K).

For conduction between the fuel and the clad with no gap, the overall heat transfer coefficient is given by,

$$U_f = \frac{k_f}{\delta_f} \tag{32}$$

where, k_f = Temperature dependent fuel conductivity (W/mK),

δ_f = Thickness of fuel (m).

Equation (31) can be rearranged into the following form,

$$\frac{\partial T_f}{\partial t} = \frac{q''_f A_f}{m_f c_{p,f}} - \frac{(T_f - T_c)}{\tau_f} \tag{33}$$

with the fuel plate time constant given by,

$$\tau_f = \frac{M_f c_{pf}}{U_f A_f} \tag{34}$$

Equation (33) can be written in discrete form as [4],

$$\Delta T^{+}_{f} = \frac{\left[\frac{\Delta t q''_{f} A_{f}}{M_{f} c_{pf}} - \frac{\Delta t (T^{0}_{f} - T^{0}_{c})}{\tau_{f}}\right]}{1 + \frac{\Delta t}{\tau_{f}}} \qquad (35)$$

where, ΔT^{+}_{f} = Change in fuel temperature during time step (°C),

Δt = Time step size (s),

^{0} = Value at last time step (superscript),

$^{+}$ = Value at next time step (superscript).

This semi-implicit solution scheme gives the fuel temperature at the new time step.

Equation (31) shows that some of the heat flux, q''_{f}, goes into raising the temperature of the fuel, while the remainder is conducted to the cladding. The heat flux being transported from the fuel to the clad is given by,

$$q''_{f \to c} = \frac{q''_{f} A_{f}}{A_{c}} - \frac{M_{f} c_{pf}}{A_{c}} \frac{\partial T_{f}}{\partial t} = \frac{U_{f} A_{f}}{A_{c}} (T_{f} - T_{c}) \qquad (36)$$

where the subscript c represents clad quantities.

The ratio of heat transfer areas that appears in Equation (36) is included because the clad heat flux is defined based on the finned surface area, while the heat flux in the fuel was based on the fuel surface area (which has no fins). This heat flux may appear to be somewhat artificial because in reality the clad has approximately the same heat transfer area as the fuel at the fuel-clad interface. However, the this heat transfer scheme is used to determine the heat flux and temperature at the clad-coolant interface. Therefore, the heat flux throughout the clad must be based on the finned surface area in order to be consistent.

In the cladding, the heat generation rate due to fission energy deposited directly into the cladding must be added to the heat flux passing from the fuel to the clad. The total heat flux at the clad-coolant interface is now given by,

$$q''_c = q''_{f\to c} + \frac{q'''_c V_c}{A_c} \tag{37}$$

The procedure used to compute the clad temperature is similar to that described above for the fuel temperature. Conduction through the clad is limited by the conductivity of the cladding.

Axial conduction along the fuel plate, and conduction from one plate to another are not considered in this analysis. Previous studies indicate that axial conduction reduces the heat flux near the bottom of the fuel by 32% or more [3]. However, the effect of axial conduction out of the fuel plate is only felt in the first 10 mm of the plate. The entrance effects that result from the developing thermal and hydraulic boundary layers are also not considered in this analysis. The heat transfer coefficient near the inlet can be significantly higher than the fully-developed heat transfer coefficient. The entrance effects can be felt up to 50-100 mm into the fuel elements. Both axial conduction and the entrance effects tend to reduce the wall temperature near the inlet to the fuel elements. The onset of nucleate boiling is most likely to occur near the exit of the fuel elements. Therefore, neglecting axial conduction and entrance effects will not have a significant impact on the prediction of the LSSS.

Heat transfer from the clad to the coolant is governed by the convective heat transfer coefficient, h. In the absence of any other resistances to heat transfer from clad to coolant, the overall heat transfer coefficient for this process, U_c, is made up of conduction through the clad and convection to the coolant,

$$\frac{1}{U_c} = \frac{1}{h} + \frac{\delta_{cl}}{k_{cl}} \tag{38}$$

where, k_{cl} = Temperature-dependent conductivity of clad (W/mK),

δ_{cl} = Thickness of clad (m).

3.4.2 Heat Transfer to the Coolant

Convective heat transfer from the clad to the coolant is determined using the Chen correlation for h. Chen's correlation is chosen because it can be modified to be applicable over all boiling regimes from single-phase flow to bulk boiling. This eliminates any discontinuities associated with changing correlations each time the heat transfer regime changes. During single-phase flow the dominant heat transfer mechanism is convection. When nucleate boiling begins, heat transfer via nucleate boiling is introduced. Following the onset of nucleate boiling, nucleation quickly becomes the dominant heat transfer mechanism. Chen's correlation is made up of a nucleate boiling term and a convection term with a factor included to weight the relative contribution of each term based on the heat transfer regime. The overall heat transfer coefficient is expressed as,

$$h = h_{NB} + h_C \tag{39}$$

where, h_{NB} = Nucleate boiling heat transfer coefficient (W/m^2K),

h_C = Convective heat transfer coefficient (W/m^2K).

The convective term is the Dittus-Boelter correlation, with convection to the liquid phase only. It also contains a factor to account empirically for the contribution of vapor to the convective heat transfer.

$$h_C = 0.023\left[\frac{G(1-x)D_e}{\mu_f}\right]^{0.8} Pr_f^{0.4}\frac{k_{l,s}}{D_e}F \tag{40}$$

with the factor F given by,

$$F = 1 \qquad \text{For } 1/X_{tt} < 0.1$$

$$F = 2.35\left(0.213 + \frac{1}{X_{tt}}\right)^{0.736} \qquad \text{For } 1/X_{tt} > 0.1 \tag{41}$$

with,

$$\frac{1}{X_{tt}} = \left(\frac{x}{1-x}\right)^{0.9}\left(\frac{\rho_f}{\rho_g}\right)^{0.5}\left(\frac{\mu_g}{\mu_f}\right)^{0.1} \tag{42}$$

where, G = Mass flux (kg/m^2s),

x = Vapor flow quality,

D_e = Equivalent heated diameter (m),

μ_f = Saturated liquid viscosity (Ns/m^2),

μ_g = Saturated vapor viscosity (Ns/m^2),

$k_{l,s}$ = Saturated liquid conductivity (W/mK),

Pr_f = Saturated liquid Prandtl Number,

ρ_f = Saturated liquid density (kg/m^3),

ρ_g = Saturated vapor density (kg/m^3).

The Chen correlation reduces to the standard Dittus-Boelter correlation during single-phase flow, where $x = 0$ and $F = 1$. The nucleate boiling term has the same form as the Forster-Zuber correlation for nucleate boiling heat transfer, but contains a factor, S, to suppress it during low-quality flow.

$$h_{NB} = S(0.00122)\left[\frac{k_{l,s}^{0.79} c_{pl,s}^{0.45} \rho_f^{0.49}}{\sigma^{0.5} \mu_f^{0.29} h_{fg}^{0.24} \rho_g^{0.24}}\right] \Delta T_{sat}^{0.24} \Delta P_{sat}^{0.75} \tag{43}$$

with,

$$S = \frac{1}{1 + 2.53 \times 10^{-6} \left(\frac{G(1-x)D_e}{\mu_f} \right)^{1.17} F^{2.42}} \tag{44}$$

where, $c_{pl,s}$ = Specific heat capacity of saturated liquid (J/kgK),

σ = Surface tension of liquid (N/m),

h_{fg} = Latent heat of vaporization (J/kg),

ΔT_{sat} = $T_c - T_{sat}$ (°C),

ΔP_{sat} = $P_{sat}(T_c) - P_{sat}(T_{sat})$ (Pa),

T_{wall} = Wall temperature (°C),

T_{sat} = Saturation temperature (°C),

P_{sat} = Saturation pressure (Pa).

In the subcooled boiling regime, where bubbles may nucleate along the wall but collapse in the bulk of the fluid (which is still below saturation temperature), Collier proposed that the heat flux from the wall to the coolant is made up of convective and nucleation terms weighted by temperature differences,

$$q'' = h_{NB}(T_C - T_{sat}) + h_C(T_C - T_B) \tag{45}$$

where, T_B = Mixed mean temperature of coolant (°C).

This can be combined with a steady-state form of Equation (31),

$$q_c'' = h(T_C - T_B) \tag{46}$$

and Equation (39) to give the following expression for the overall heat transfer coefficient during subcooled boiling,

$$h = h_C + \frac{h_{NB}(T_C - T_{sat})}{(T_C - T_B)} \tag{47}$$

With the overall heat transfer coefficient from clad to coolant now known, the transient heat transfer equations for the clad-coolant interface can be solved. Analogous to Equation (33), the time-dependent clad temperature is given by,

$$\frac{\partial T_c}{\partial t} = \frac{q''_c A_c}{M_c c_{p,c}} - \frac{(T_c - T_B)}{\tau_c} \tag{48}$$

with,

$$\tau_c = \frac{M_c c_{p,c}}{U_c A_c} \tag{49}$$

where, M_c = Mass of clad (kg),

c_{pcl} = Temperature-dependent specific heat of clad (J/kgK).

This equation is discretized and solved semi-explicitly to give,

$$\Delta T^{+}_C = \frac{\left[\frac{\Delta t q''_c A_c}{M_c c_{p,c}} - \frac{\Delta t(T_C^0 - T_B^0)}{\tau_c}\right]}{1 + \frac{\Delta t}{\tau_c}} \tag{50}$$

Equation (50) gives the magnitude of the temperature change resulting from the fraction of the heat flux that stays in the clad. The remaining heat given by,

$$q''_{c\to w} = q''_c - \frac{M_c c_{p,c}}{A_c}\frac{\partial T_c}{\partial t} = U_c(T_c - T_B) \tag{51}$$

is transferred to the coolant. In addition to the heat transferred from the clad, a fraction of the fission energy is deposited directly to the coolant. This fraction does not contribute to the surface heat flux, but it is a heat generation rate that must be added in to give a proper energy balance on the coolant.

In addition, the fission energy that is deposited in the core structural materials is added to the coolant. A transient energy balance is not solved on the core structural materials because the heat deposited there is small, and the temperature in the structural materials is not of concern. Therefore, it is assumed that the fission energy deposited there is immediately transferred to the coolant.

3.4.3 Coolant Enthalpy Rise

The equations outlined above give the total heat flux added by convection from the cladding. The volumetric heat generation rate from fission energy deposited directly in the coolant, q_w''', is normalized to the clad heat transfer area and added to the clad heat flux to give an artificial heat flux. This total "heat flux" (q''_o) represents the total amount of heat added to the coolant per unit of heat transfer area in each node.

$$q_o'' = q_{c\to w}'' + q_w''' \left(\frac{A_f}{P_h}\right) \tag{52}$$

where, q'''_w = Volumetric heat generation rate in coolant and structural materials (W/m^3),

A_f = Channel flow area (m^2),

P_h = Channel heated perimeter for heat transfer (m) [including fins].

The addition of heat to the coolant is expressed in terms of fluid enthalpy. The enthalpy at a given height, z, in a channel can be expressed using an energy balance,

$$h(z) = h(0) + \frac{1}{\dot{m}} \int_0^z q''(z) P_h dz \qquad (53)$$

In discrete form, each core channel is divided into Z axial control volumes. The following notation is used to describe the properties in each control volume:

Δt	=	Time step size (s)
Δz	=	Length of axial node (m)
h_z^n	=	Enthalpy in node z at time step n (J/kg)
m	=	Channel mass flow rate (kg/s)

A modified donor-cell approach is used to determine the enthalpy in each control volume at each time step. The recipient cell in this approach is one of the Z control volumes that is fixed in location. The donor cell, however, is allowed to vary in location.

The enthalpy in each axial node is equal to the enthalpy entering the node at time step n+1, plus the amount of specific heat added during time Δt. During this time interval, a volume of coolant will move c nodes, where,

$$c = v \frac{\Delta t}{\Delta z} \qquad (54)$$

where, v = average velocity of coolant (m/s).

In calculating the enthalpy in node z at time n+1, the recipient cell is node z and the donor is node z-c. A discretized energy balance gives,

$$h_z^{n+1} = h_{z-c}^n + \frac{1}{\dot{m}} \sum_{i=z-c}^{z} q_{0i}'' P_{hi} \Delta z \qquad (55)$$

where, q''_{oi} = Artificial heat flux into node i (W/m^2) (See Equation 52),

P_{hi} = Heated perimeter in node i (m).

Because the recipient nodes are fixed in space, the parameter c will not necessarily be an integer. Therefore, the donor node will not coincide with any of the fixed nodes in the channel. Figure 3.4.3 diagrams the enthalpy transport scheme described here. The enthalpy of the donor node, h_{z-c}^{n+1} is found by averaging the enthalpies of the fixed nodes that make up the donor node.

In Figure 3.4.3 the recipient node is z = 4 and c = 1.7. The donor node is z = 2.3 which overlaps both node 2 and node 3 in the fixed node scheme. The donor enthalpy is then a mixed enthalpy containing 30% of coolant at h_3 and 70% of coolant at h_2. Note that end-point enthalpies are used to calculate fluid properties. The enthalpy within a control volume is an average of the endpoint enthalpy of the nodes above and below it.

The summation term in Equation (55) represents the total amount of heat added to the coolant while it moves from node z-c to node z. As discussed above for the donor enthalpy, the heat flux in some nodes will be only a fraction of the total heat flux of that node. Because the heat flux within a node is considered to be constant, the heat flux contributed by a fractional node is equal to the total heat flux in that node times the fraction of the node through which the coolant travels. In Figure 3.4.3, the total heat flux added is 70% of the heat flux from node 3 and all of the heat flux from node 4 (the recipient node).

When the donor cell is identified to be below the channel inlet (z-c < 0), the inlet enthalpy is taken to be equal to the core inlet enthalpy.

This enthalpy transport scheme is essentially a discretized form of the method of characteristics. The axial position of a packet of fluid is taken as one dimension, and time is the other. The amount of heat added to the packet is found by integrating along the path traveled by the fluid during a given time step.

During short time steps,

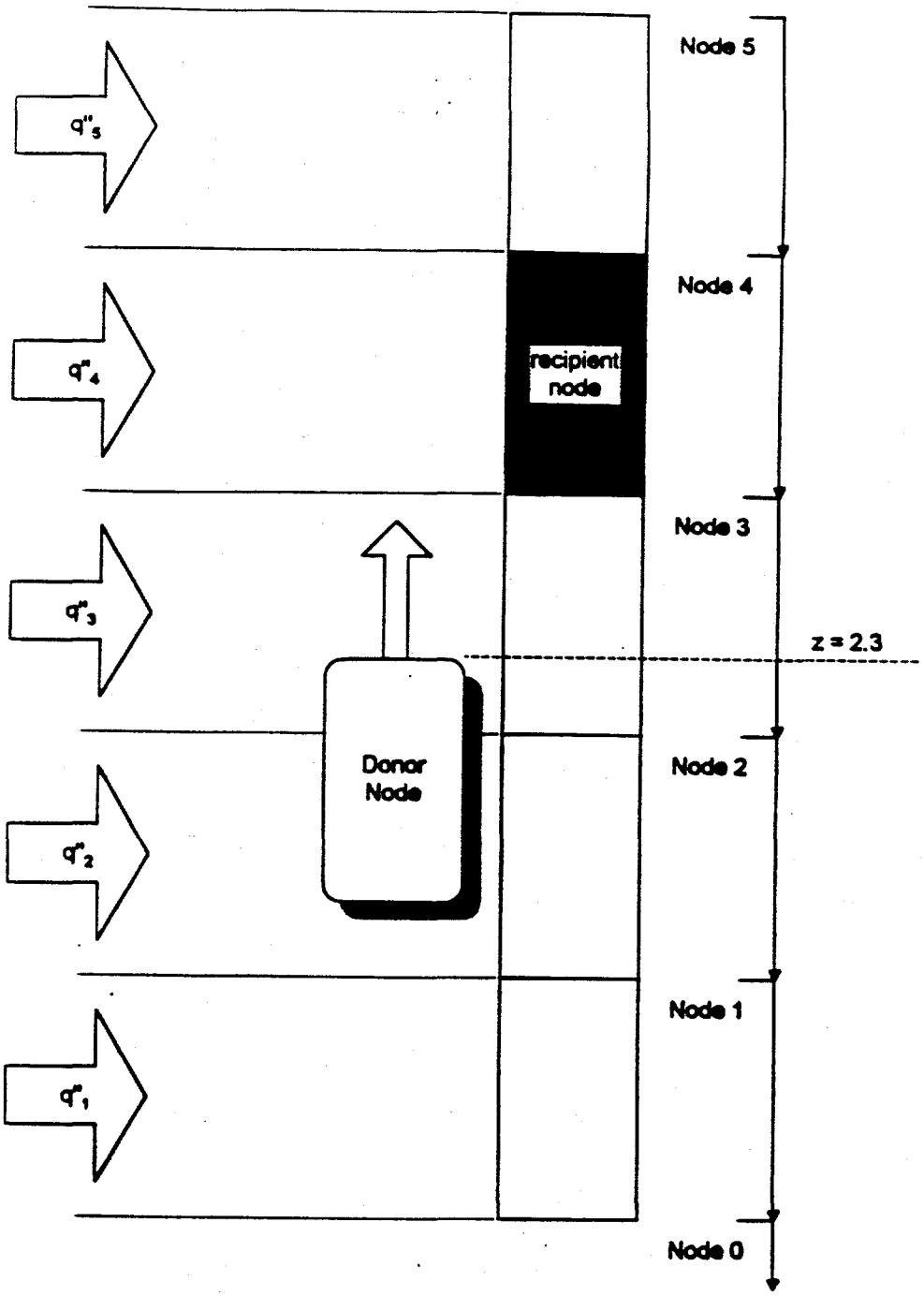

Figure 3.4.3. Enthalpy transport model. The enthalpy transport model used in the MITR Multi-Channel Analysis Code used fixed control volumes as recipient nodes. For short time steps, the model reduces to the donor cell approach. For larger time steps, the enthalpy transport model is similar to the method of characteristics.

$$\Delta t < \frac{\Delta z}{v} \tag{56}$$

and the modified donor-call scheme outlined above reduces down to the conventional donor cell scheme in which the fluid entering each node comes from the node immediately below it. The time constraint shown in Equation (56) does not need to be followed in order to obtain accurate knowledge of coolant temperature. However, the same time step is used to calculate quantities such as core power, mass flow rates, and both clad and fuel temperatures. Accurate calculation of these quantities generally requires smaller time steps than for the coolant enthalpy calculations, and therefore may limit the time step to within the constraint of Equation (56).

3.5 *Void Fraction Model*

In the event of a severe transient, the MITR core may experience two-phase flow. The formation of vapor in the core has a significant impact on the momentum and energy equations, as outlined in sections 3.3 and 3.4 above. Mass conservation will also be affected by the rapid formation of vapor. It is possible that sudden vaporization of liquid could force coolant out of both ends of the coolant channel. This phenomenon is not modeled in this analysis. Because of the low pressure of the MITR primary system, accurate prediction of the mass vapor fraction (x) (also called the flow quality) and void fraction (α) shortly after the onset of nucleate boiling (ONB) is necessary to model flow excursion instabilities.

If there was no temperature gradient within the coolant at a given axial plane, the mass fraction of vapor would be equal to the equilibrium quality, x_{eq},

$$x_{eq} = \frac{h - h_f}{h_g - h_f} \tag{57}$$

where, h = Enthalpy of coolant (J/kg),

h_f = Saturation enthalpy of liquid (J/kg),

h_g = Saturation enthalpy of vapor (J/kg).

The equilibrium quality represents the fraction of mass of the coolant existing in the vapor phase under static and thermal equilibrium conditions.

In reality a temperature gradient exists between the temperature of the coolant adjacent to the clad and the temperature of the coolant in the middle of the channel. It is possible for the coolant near the wall to be above the saturation temperature, while the remainder of the coolant is still subcooled. Under these circumstances, there would be some vapor formed. However, the equilibrium quality, x_{eq}, would still be less than zero. This condition, known as subcooled boiling, marks the first phase of boiling in the MITR system. Figure 3.5.1 shows the progression of boiling regimes encountered in the MITR.

Subcooled boiling is further subdivided into two regimes. At the onset of nucleate boiling (ONB) the first bubbles begin to nucleate along the wall of the heated channel. In the highly subcooled boiling region, the bulk of the coolant is still subcooled enough so that the bubbles do not move far from the wall. As the bulk coolant temperature is increased (as indicated by movement in the positive x-direction of Figure 3.5.1) the bubbles may begin to move away from the wall without collapsing. The point in Figure 3.5.1 where the bubbles leave the wall is called the onset of significant void (OSV). At OSV the bubbles leave their nucleation sites and new bubbles may begin to nucleate in their place. This leads to a rapid increase in void fraction. The slightly subcooled region is identified by OSV and the accompanying jump in void fraction. Because the bulk of the fluid is still subcooled, the bubbles that leave the wall in the slightly subcooled region still collapse upon approaching the middle of the channel.

Bulk boiling begins when the mixed-mean enthalpy of the coolant exceeds the saturation enthalpy (i.e., $x_{eq} > 0.0$).

The mass of vapor flowing at a given axial plane is identified by flow quality, x, defined by,

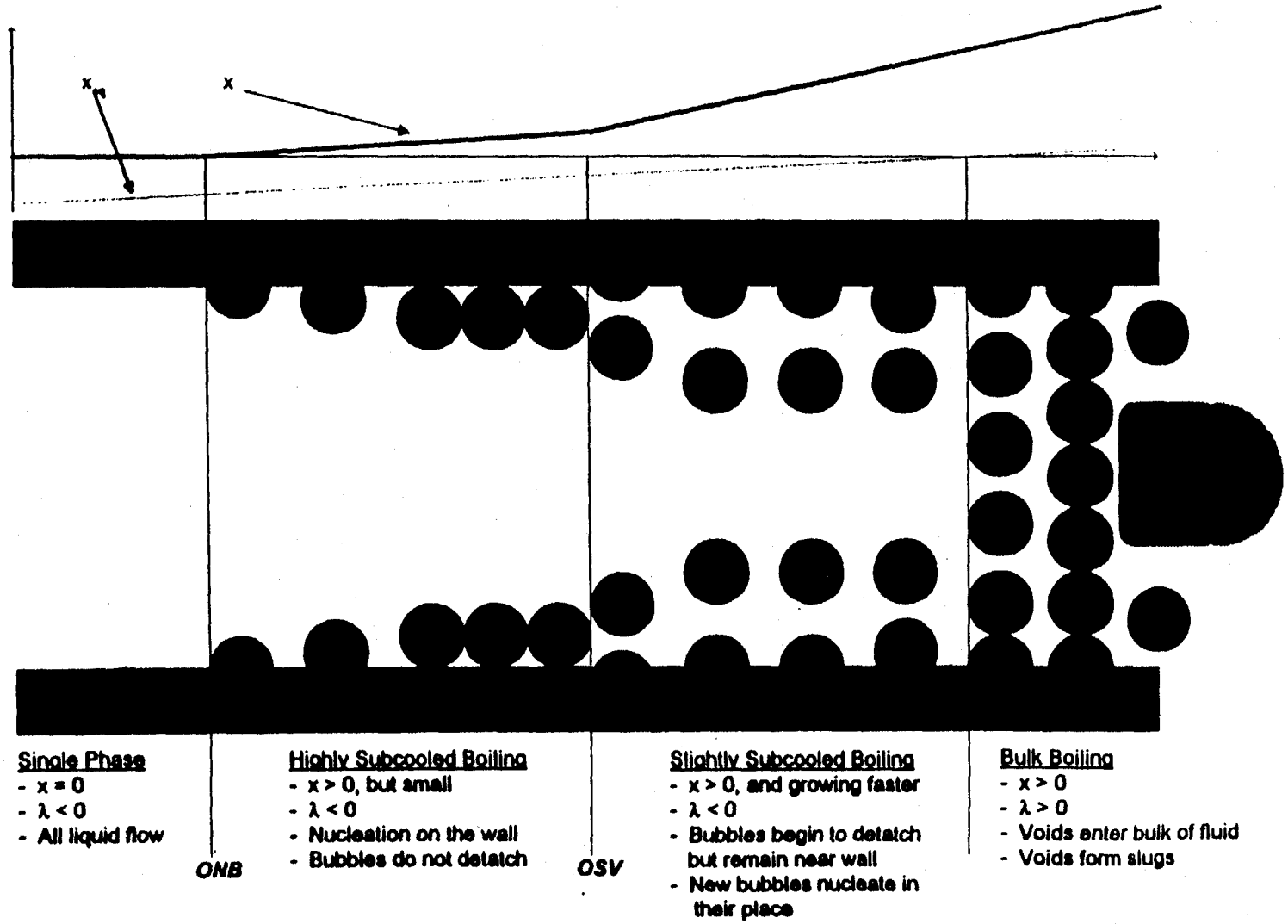

Figure 3.5.1. Boiling regimes in an MITR channel. Heat is added along the walls as the coolant flows from left to right. The profiles of equilibrium quality and flow quality are shown above the diagram.

$$x = \frac{\dot{m}_v}{\dot{m}} = \frac{1 - \dot{m}_l}{\dot{m}} \tag{58}$$

where, m_v = Mass flow rate of vapor (kg/s),

m_l = Mass flow rate of liquid (kg/s),

m = Total coolant mass flow rate [$m = m_l + m_v$] (kg/s).

Figure 3.5.2 shows the flow quality as a function of the equilibrium quality. During highly subcooled boiling, the flow quality is small because the only vapor that exists is present in nucleation sites along the clad. In the slightly subcooled region, the flow quality rises as bubbles begin to detach and move away from the clad. The flow quality shown in Figure 3.5.2 is small during subcooled boiling, but in low-pressure systems small flow qualities can lead to large volumes of vapor.

Drift Flux Model

The volume of vapor flowing through a channel at a given axial plane is measured by the void fraction, α. Various models have been proposed to relate the void fraction to the flow quality. The drift-flux model is used in this analysis for the following reasons:

1) It allows for mechanical non-equilibrium. Vapor and liquid velocities are allowed to be unequal by including an effective drift velocity term.

2) The nonuniform profile of void production and fluid flow can be accounted for with a distribution parameter.

3) The model includes the effect of mass velocity on the value of the void fraction.

The void fraction can be expressed as,

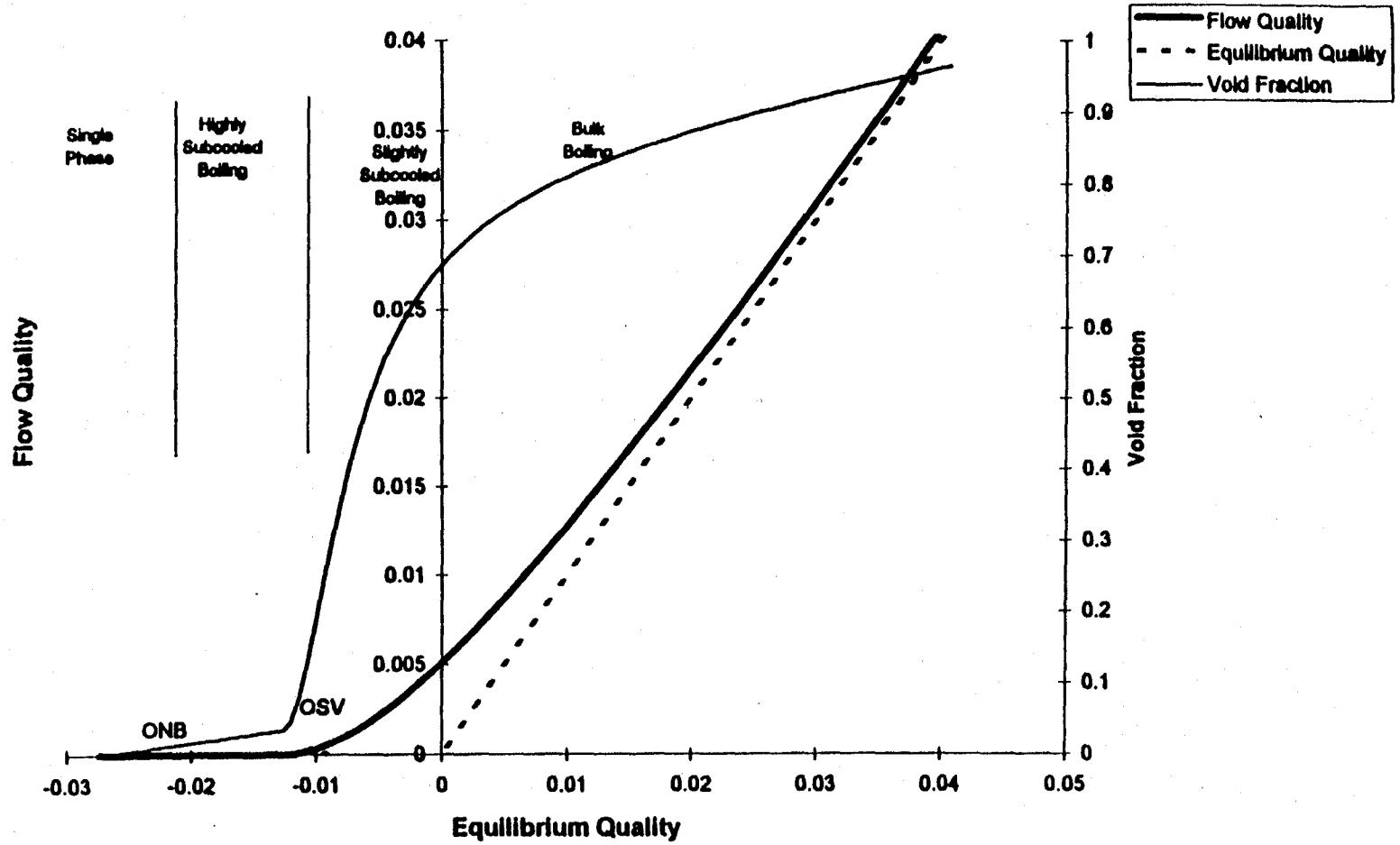

Figure 3.5.2. Flow quality and void fraction in an MITR channel. The MITR Multi-Channel Analysis Code determines the void fraction as a function of true quality in four continuous regions: single phase liquid, highly subcooled boiling, slightly subcooled boiling, and bulk boiling.

$$\alpha = \frac{1}{C_0\left(1+\frac{1-x}{x}\frac{\rho_v}{\rho_l}\right)+\frac{V_{vj}\rho_v}{xG}} \tag{59}$$

where, G = Mass Flux (kg/m^2s),

C_0 = Distribution parameter,

V_{vj} = Effective drift velocity (m/s)

The two parameters, C_0 and V_{vj}, change as the flow regime changes. Figure 3.5.3 shows a flow regime map drawn for typical MITR conditions at the top of a fuel element. The boundaries between flow regimes are based on Taitel and Dukler's analysis of the physical mechanisms responsible for flow regime transitions at atmospheric pressure [10]. The axes are superficial phase velocities defined as,

$$\{j_l\} = \frac{G(1-x)}{\rho_l} \tag{60}$$

$$\{j_v\} = \frac{Gx}{\rho_v} \tag{61}$$

The dotted lines represent the path of the coolant in an MITR channel during the beginning of two-phase flow. The endpoint of each dotted line represents the value at a flow quality of 0.001, and the arrow represents the value at a flow quality of 0.02. Although regions of bubbly flow are shown on the regime map in Figure 3.5.3, experimental work indicates that for small-diameter channels, the bubbles will rapidly coalesce into slugs. [10]. A semi-mechanical model can be used to give the following criterion for the absence of a bubbly flow regime [9]:

$$\text{If} \quad \left[\frac{\rho_l^2 g D_e^2}{(\rho_l-\rho_v)\sigma}\right] \le 4.36 \quad \text{then no bubbly flow regime exists.} \tag{62}$$

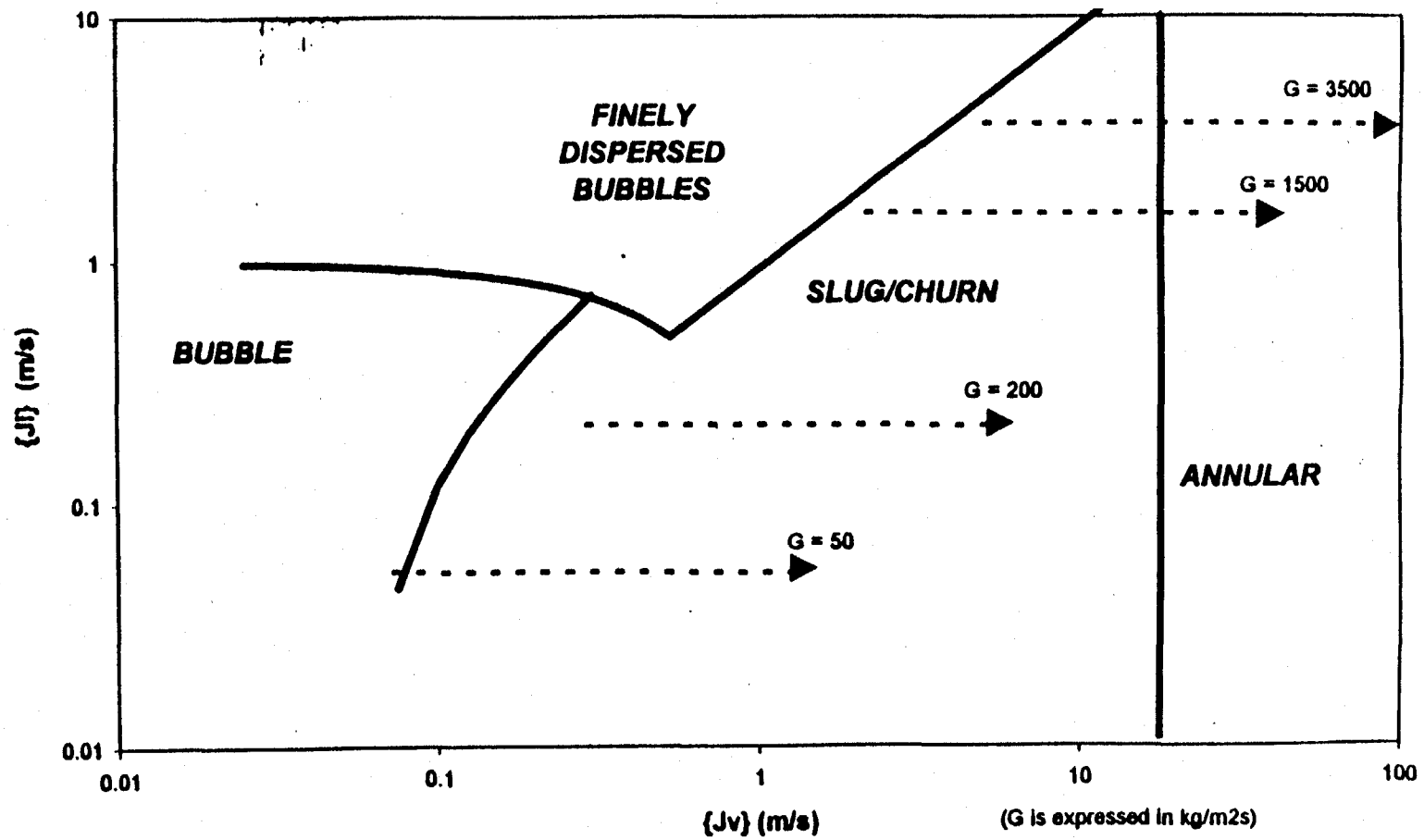

Figure 3.5.3. Flow regime map for MITR conditions. The boiling regime transition boundaries are based on the work of Taitel, Bornea, and Dukler [10]. The dotted lines represent the trajectories of MITR coolant during two-phase transients

This inequality is true for all conditions that can be expected for steady-state and transient conditions in the MITR. The dotted lines in Figure 3.5.3 show that if bubbly flow does occur during a two-phase transient, it occurs very briefly and only for small flow qualities ($x < 0.001$).

Two-phase transients in the MITR core can be considered to pass through two flow regimes. As soon as the first vapor appears, slug or churn flow develops in the channel. Taitel suggests that slug flow is merely a developing phase of churn flow. The region marked "Slug/Churn" in Figure 3.5.3 may represent either flow regime depending on where in the coolant channel it occurs.

As the flow quality rises, the flow approaches the annular flow boundary. Annular flow is predicted to occur when [9]

$$\frac{\{j_v\}\rho_v^{1/2}}{[\sigma g(\rho_l - \rho_v)]^{1/4}} = 3.1 \tag{63}$$

Using Equation (61), this condition for transition to annular flow can be expressed as,

$$x_{tr} = \frac{3.1[\sigma g(\rho_l - \rho_v)]^{1/4}\rho_v^{1/2}}{G} \tag{64}$$

The distribution parameter, C_0, is assumed to be equal to 1.2 at the beginning of two-phase flow in the slug/churn flow regime, and drops to 1.0 when annular flow develops [11]. The value of C_0 is assumed to vary linearly from the onset of two-phase flow to the annular flow transition point. Therefore,

$$C_0 = 1 + 0.2\left(1 - \frac{x}{x_{tr}}\right) \qquad x \le x_{tr}$$

$$C_0 = 1 \qquad x > x_{tr} \tag{65}$$

The effective drift velocity, V_{vj}, can be expressed in the slug/churn regime as [12],

$$V_{vj_0} = 1.41\left[\frac{(\rho_l - \rho_v)g\sigma}{\rho_l^2}\right]^{1/4} \tag{66}$$

When annular flow dominates, the void fractions are so high that the vapor volumetric flow rate is almost equal to the total volumetric flow rate. Therefore, the effective drift velocity is negligible. As described above for the distribution parameter, the effective drift velocity is forced to be a linearly decreasing function between the onset of two-phase flow and the transition to annular flow. The effective drift velocity is found from,

$$V_{vj} = \left(1 - \frac{x}{x_{tr}}\right)V_{vj_0} \qquad x \le x_{tr}$$

$$V_{vj} = 0 \qquad x > x_{tr} \tag{67}$$

The drift flux relation given in Equation (59), is used to find the void fraction for all values of flow quality. Figure 3.5.4 shows the variation of void fraction with flow quality for various mass fluxes. The transition to annular flow is evident in the two high flow cases ($G = 1500$ kg/m^{2}s and $G = 3500$ kg/m^{2}s) as a change of slope. The effect of coolant velocity disappears as the flow regime becomes annular because the drift flux term goes to zero at this point. Figure 3.5.4 shows that low-pressure systems can generate very high void fractions with relatively little mass of vapor.

Solution of Equation (59) requires that the true quality, x, be known throughout the full range of boiling regimes. It is convenient to relate the flow quality, x, to the equilibrium quality, x_{eq}. Several observations can be made concerning the two qualities:

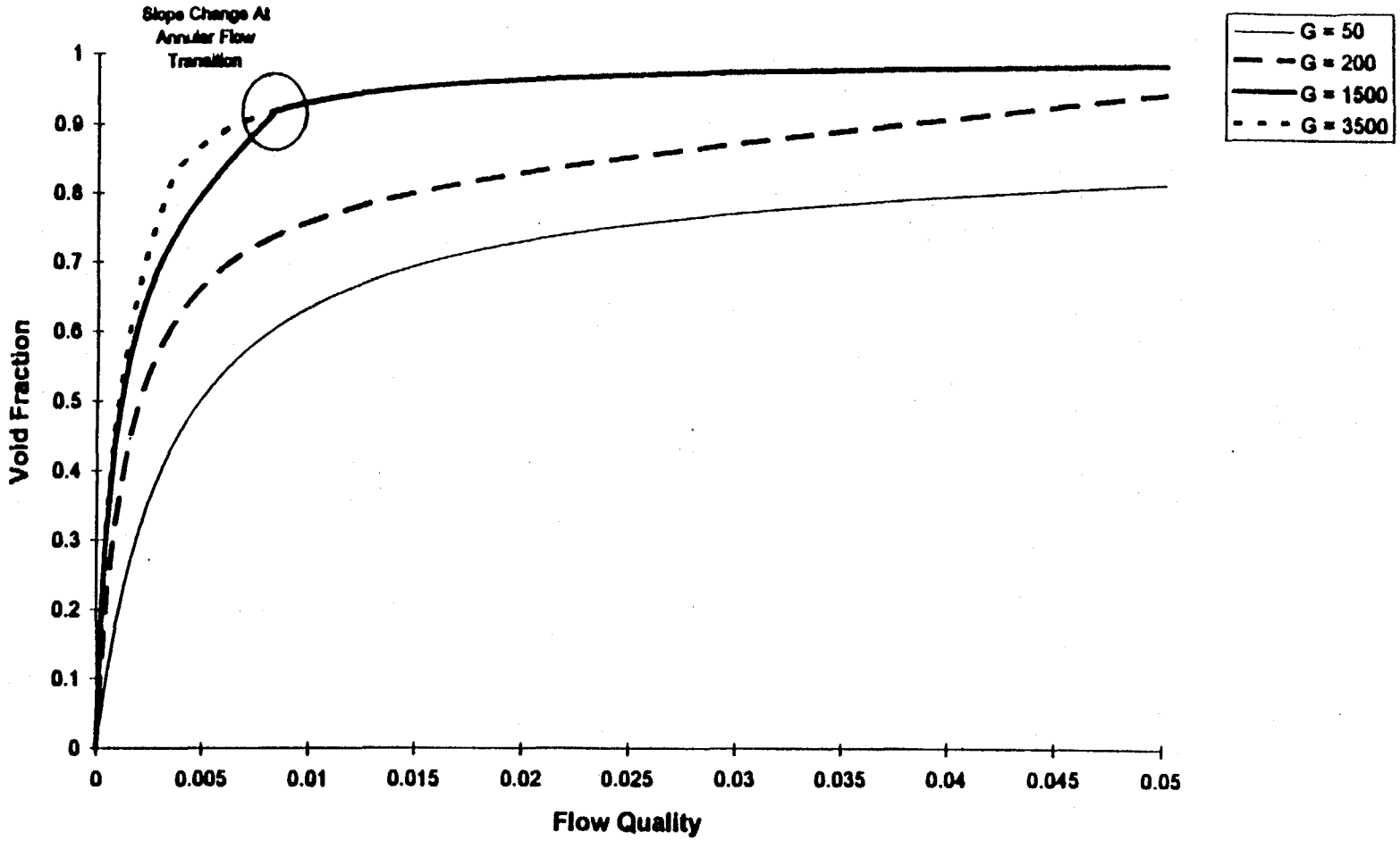

Figure 3.5.4. MITR void fraction at various mass fluxes. The dependence of the void fraction on the channel mass flux is shown. At higher mass fluxes, the transition to annular flow is predicted to occur at lower flow qualities. The nominal mass flux in an MITR channel is between 2400 and 3700 kg/m^{2}s.

1) Prior to ONB the flow quality is zero and the equilibrium quality is less than zero.

2) Between ONB and OSV the flow quality rises from zero to some small value representing the amount of vapor at the point of bubble detachment.

3) When bulk boiling is well established and the equilibrium quality is high, the flow quality should approach the equilibrium quality.

These observations suggest that a plot of x versus x_{eq} (Figure 3.5.2) could be made by considering three distinct regions:

1)	Single-Phase Region	$x_{eq} < (x_{eq})_{ONB}$
2)	Highly Subcooled Boiling	$(x_{eq})_{ONB} < x_{eq} < (x_{eq})_{OSV}$
3)	Slightly Subcooled Boiling/Bulk Boiling	$x_{eq} > (x_{eq})_{OSV}$

where, $(x_{eq})_{ONB}$ = Equilibrium quality at ONB,

$(x_{eq})_{OSV}$ = Equilibrium quality at OSV.

In the single-phase region, the flow quality is zero for all values of equilibrium quality. The boundary between the single-phase and highly subcooled regions is given by correlations for ONB. The difference between the wall temperature required for bubble nucleation, and the coolant saturation temperature is found by the Davis and Anderson correlation, with the constant (C = 12.5) found by experiments on finned fuel plates [13,14],

$$T_{w,ONB} - T_{sat} = \left[\frac{12.5 q'' \sigma T^{*}_{sat}}{h_{fg} k_l (\rho_l - \rho_v)} \right]^{1/2} \qquad (68)$$

where, $T_{w,ONB}$ = Wall temperature required for nucleation (°C)

T^{*}_{sat} = Coolant saturation absolute temperature (K)

k_l = Saturated coolant conductivity (W/mK).

Equation 46 can be rewritten as,

$$T_{w,ONB} - T_{b,ONB} = \frac{q''}{U} \tag{69}$$

where, $T_{b,ONB}$ = Bulk coolant temperature at ONB (°C),

U = Wall-to-coolant heat transfer coefficient (W/m^2K).

An equation for the equilibrium quality at ONB can now be written by combining Equations (68) and (69) with the definition of equilibrium quality given in Equation (57),

$$(x_{eq})_{ONB} = \frac{h_{b,ONB} - h_{sat}}{h_{fg}} = \frac{(T_{b,ONB} - T_{sat})c_p}{h_{fg}} = \frac{\left(T_{w,ONB} - \frac{q''}{U} - T_{sat}\right)c_p}{h_{fg}} \tag{70}$$

where, $h_{b,ONB}$ = Bulk coolant enthalpy at ONB (J/kg)

h_{sat} = Liquid saturation enthalpy (J/kg)

c_p = Specific heat capacity of liquid (J/kgK)

Because subcooled boiling begins when the wall is hot enough to initiate bubble nucleation in the hot water near the wall-coolant interface, the bulk of the coolant will still be subcooled. As a result, $(x_{eq})_{ONB}$ is less than zero.

The boundary between the highly subcooled and the slightly subcooled boiling regions is the onset of significant voids (OSV). The Saha and Zuber correlation is based on plots of experimentally observed occurrences of OSV. They present their results in a plot of dimensionless groups (Stanton Number versus Peclet Number), showing the effects of mass velocity and subcooling on the point of OSV [15]. Similar experiments have been performed for finned surfaces under roughly the same conditions as MITR coolant channels. These experiments led to the following correlation for OSV [14],

$$St = 0.0446 Pe^{-0.18} \tag{71}$$

with,

$$St = \frac{q''}{G c_p (T_{sat} - T_{b,OSV})} \tag{72}$$

and,

$$Pe = \frac{G D_e c_p}{k_l} \tag{73}$$

Equations (71), (72), (73), and (57) can be combined to give the equilibrium quality at OSV,

$$(x_{eq})_{OSV} = \frac{(T_{b,OSV} - T_{sat}) c_p}{h_{fg}} = \frac{-q''}{0.0446 Pe^{-0.18} G h_{fg}} \tag{74}$$

The above relationship gives no information about what the flow quality is at OSV. However, several empirical and semi-empirical models for the void fraction at OSV can be found in the literature [16,17,18]. The method used here is based on the dynamics of bubble growth, as described by Levy [18]. It is assumed that immediately prior to bubble detachment, the bubbles growing along the heated perimeter are packed together in a square array. For spherical bubbles, the void fraction under these conditions is,

$$\alpha_{osv} = \frac{\pi Y_b}{6D_e} \tag{75}$$

where, α_{osv} = Void fraction at OSV

Y_b = Bubble diameter at OSV (m)

The bubble diameter is found from a force balance on the growing bubble. Levy predicts the bubble diameter to be,

$$Y_b = 0.015\left(\frac{\sigma D_e}{\tau_w}\right)^{1/2} \tag{76}$$

with the wall shear stress, τ_w, expressed as,

$$\tau_w = \frac{fG^2}{8\rho_l} \tag{77}$$

The flow quality at OSV is related to the void fraction at OSV through the drift flux equation (Equation (59). Solving Equation (59) for x, and substituting Equations (65) and (61) for the drift velocity and distribution parameter gives an equation for flow quality as a function of void fraction. The true quality at OSV is then,

$$x_{OSV} = \frac{V_{vj_0}\rho_v x_{tr}}{\frac{x_{tr}G}{\alpha_{OSV}} + V_{vj_0}\rho_v - G} \tag{78}$$

In region 1, between ONB and OSV, the flow quality is assumed to vary linearly from zero up to x_{OSV}. In region 2 the flow quality follows an asymptotic curve, approaching the equilibrium quality. The flow quality is known for all values of equilibrium quality,

$$x = 0 \qquad x_{eq} < (x_{eq})_{ONB}$$

$$x = x_{OSV}\left(\frac{(x_{eq})_{OSV} - (x_{eq})_{ONB}}{(x_{eq})_{OSV} - (x_{eq})_{ONB}}\right) \qquad (x_{eq})_{ONB} < x_{eq} < (x_{eq})_{OSV}$$

$$x = (x_{eq}) + \left(x_{OSV} - (x_{eq})_{OSV}\right)\exp\left[\frac{(x_{eq})_{OSV} - (x_{eq})}{x_{OSV} - (x_{eq})_{OSV}}\right] \quad (x_{eq})_{OSV} < x_{eq} < 1 \tag{79}$$

The variation of flow quality with equilibrium quality is shown in Figure 3.5.2.

3.6 *Heat Exchanger Model*

Three main heat exchangers are available to transfer heat from the primary coolant to the secondary coolant. Normally, two of the three heat exchangers are on line. Under steady-state conditions, the heat transferred by the heat exchangers is equal to the heat deposited in the primary coolant. When a transient causes the rate of heat generation or the rate of core heat transfer to change, the effects of the change will not be seen until some time later. In the event of a loss of primary or secondary flow, however, the heat transfer rate in the heat exchangers is immediately affected. The rate of heat transfer in the heat exchangers, Q_{hx} (W), is given by,

$$Q_{hx} = U_{hx} A_{hx} \Delta T_{lm} \tag{80}$$

where, U_{hx} = Heat exchanger overall heat transfer coefficient ($W/m^{2o}C$)

A_{hx} = Area for heat transfer in heat exchanger (m^2)

ΔT_{lm} = Log-mean temperature difference (°C)

The log-mean temperature difference is a representation of the difference between the average temperatures of the primary and secondary loops throughout the length of the heat exchanger. The log-mean temperature difference is defined as,

$$\Delta T_{lm} = \frac{(T_{1I} - T_{2O}) - (T_{1O} - T_{2I})}{\ln\left[\frac{(T_{1I} - T_{2O})}{(T_{1O} - T_{2I})}\right]} \tag{81}$$

where, T_{1I} = Primary inlet temperature (°C)

T_{1O} = Primary outlet temperature (°C)

T_{2I} = Secondary inlet temperature (°C)

T_{2O} = Secondary outlet temperature (°C)

Heat balances on the primary and secondary side are used to give two more equations,

$$Q_{hx} = m_1 c_{p1} (T_{1I} - T_{1O}) \tag{82}$$

and,

$$Q_{hx} = m_2 c_{p2} (T_{2O} - T_{2I}) \tag{83}$$

where, m_1 = Primary mass flow rate (kg/s)

m_2 = Secondary mass flow rate (kg/s)

c_{p1} = Specific heat of water at average primary temperature (J/kgK)

c_{p2} = Specific heat of water at average secondary temperature (J/kgK)

From previous calculations, the temperatures going into the heat exchanger are known (T_{1I}, T_{2I}). The two outlet temperatures and the heat exchanger power (Q_{hx}) are the three unknowns. Equations (81), (82), and (83) can be combined to give the following expression for the heat exchanger power,

$$Q_{hx} = \frac{(T_{1I} - T_{2I})(1 - e^{F})}{\frac{e^{F}}{m_1 c_{p1}} - \frac{1}{m_2 c_{p2}}} \tag{84}$$

with,

$$F = U_{hx} A_{hx} \left(\frac{1}{m_1 c_{p1}} - \frac{1}{m_2 c_{p2}} \right) \tag{85}$$

The overall heat transfer coefficient, U_{hx}, is made up of several conductances in series. For a shell-and-tube heat exchanger, where the primary fluid flows through the small tubes, the overall heat transfer coefficient is expressed as,

$$\frac{1}{U_{hx}} = \frac{r_o}{h_1 r_i} + \frac{r_o \ln\left(\frac{r_o}{r_i}\right)}{k_t} + \frac{1}{h_2} + \frac{1}{h_F} \tag{86}$$

where, A_o = Total outside surface area of primary tubes (m^2)

A_i = Total inside surface area of primary tubes (m^2)

r_0 = Outer radius of a primary tube (m)

r_i = Inner radius of a primary tube (m)

k_t = Thermal conductivity of tubes (W/mK)

h_1 = Convective heat transfer coefficient on primary side (W/m^2K)

h_2 = Convective heat transfer coefficient on secondary side (W/m^2K)

h_F = Fouling heat transfer coefficient (W/m^2K) [Calculated using A_o]

For a lamellar heat exchanger, with primary and secondary coolant flow in separate, rectangular channels, Equation (86) is replaced by [4],

$$\frac{1}{U_{hx}} = \frac{A_o}{h_1 A_i} + \frac{d}{k_t} + \frac{1}{h_2} + \frac{1}{h_F} \qquad (87)$$

where, d = Thickness of lamellar plate (m)

k_t = Thermal conductivity of plate (W/mK)

A_o = Total outside surface area on secondary side (m^2)

A_i = Total inside surface area on primary side (m^2)

The fouling factor represents the resistance to heat transfer resulting from the buildup of deposits on the heat transfer surfaces. Its value can be found by comparison with experimental results, or from estimates of deposit resistances [19]. The standard Seider and Tate correlation is used to find the heat transfer coefficients in Equations (86) and (87).

3.7 Secondary Loop Model

The main components of the secondary loop, as shown in Figure 1.2.2, are the heat exchangers, the hot leg, the cold leg, the secondary pumps, and the cooling towers. The heat exchanger model is described in Section 3.6.

No momentum balance is done on the secondary side. The secondary loop flow is provided as a time-dependent forcing function. The pressure loss through the secondary side, and its impact on the secondary loop flow, is not important to this analysis for the following reasons:

1) The losses in the secondary loop are relatively constant for a given flow rate because the occurrence of two-phase flow is extremely unlikely.

2) Changes in the secondary system are not critical to predicting the response of the core to rapid transients (such as reactivity insertions and loss of primary flow).

3) A loss of flow in the secondary side (the limiting loss of heat sink transient) is modeled through the use of a flow coastdown curve. The coastdown curve is a function of time only.

The conservation of energy within the loop is maintained by the addition of energy in the heat exchangers, and the loss of energy at the cooling towers. Heat is transported between the source (heat exchangers) and sink (cooling towers) by the flow of coolant between the two locations.

Cooling towers dissipate heat to the environment by using direct contact heat transfer to cool the secondary water. A schematic of a cooling tower is shown in Figure 3.7.1. The loss of heat from the secondary coolant is accomplished by a combination of convection and evaporation that occurs as the ambient air is forced past the water. A number of variables influence the rate of heat transfer in a cooling tower:

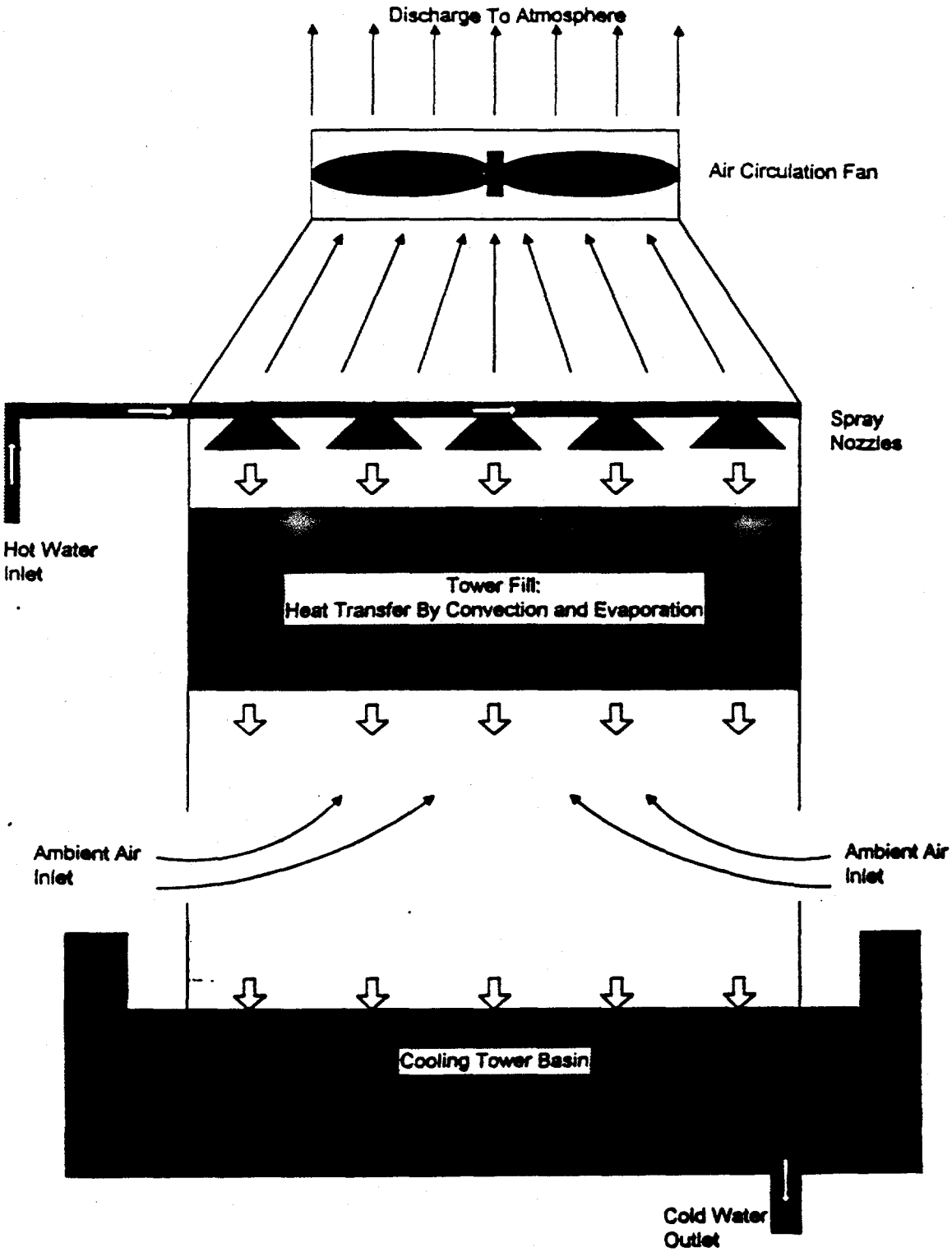

Figure 3.7.1. Diagram of a cooling tower. The cooling tower above is similar to the induced-draft heat exchangers used to remove heat from the MITR-II secondary system. A fan is used to draw ambient air past the warm secondary coolant in order to transfer heat to the environment.

1) The temperature of the incoming water. Similar to heat exchangers, the rate of heat transfer is proportional to a temperature difference that acts as a driving force. The general expression for the heat transfer rate given in Equations (82) and (83) can be used to represent the energy balance in a cooling tower.

2) The temperature of the ambient air. Because direct contact cooling involves both convection and evaporation, the wet-bulb temperature is a more useful quantity for expressing the temperature of the ambient air. The wet-bulb temperature takes into account the humidity of the air, and its capacity to absorb evaporating coolant.

3) The area for heat transfer. Figure 3.7.1 shows that the incoming secondary coolant is forced to the top of the cooling tower. From there it flows by gravity through a layer of "fill." The fill is a means of increasing the area for heat transfer when a given tower height is available. A fill is often a packed bed where the falling coolant is forced to travel within the voids.

4) The flow rate of the air. The air is drawn up (or, in some designs, forced down) through the fill. There is no physical barrier between the water and the air. The size of the fans used to move the air is an indication of the air flow rate. A higher air flow rate will increase the heat transfer coefficient for convection and decrease the exit temperature of the water.

5) The flow rate of the water. The water is the source of the heat in the direct cooling process. A lower flow rate will naturally decrease the heat transfer coefficient in the cooling tower. However, if less water is coming in, then there is less heat to be dissipated. The net result is that the water leaves the cooling tower at a lower temperature.

Many other design parameters and operational variables play a part in determining the heat transfer rate in the cooling towers, but the five listed above are the major factors. The temperature of the incoming air is determined by the ambient conditions, while the water temperature is determined by the operating state of the reactor.

The difference between the cooling tower outlet temperature (T_1) and the ambient wet bulb temperature (T_0) is referred to as the approach temperature. For an ideal direct heat exchanger the approach temperature would be zero. However, because not all of the coolant can be cooled to the ambient wet bulb temperature in a finite distance, an approach temperature exists. Note that because the tower cools by evaporation as well as by convection, it is possible to cool the water to below the standard dry-bulb temperature of the ambient air [20]. As the coolant temperature approaches the wet-bulb temperature, however, the driving force for heat transfer approaches zero. The approach temperature is a function of cooling tower design and ambient conditions. Cooling tower manufacturers have plots of approach temperature versus ambient temperature for each specific design. For the MITR Multi-Channel Analysis code, the approach temperature is provided by the user based on information obtained from the cooling tower manufacturer [21].

The heat transfer rate in the cooling tower can be found from,

$$Q_{ct} = h_{ct} A_{ct} \frac{(T_2 - T_1)}{\ln\left[\frac{T_2 - T_0}{T_1 - T_0}\right]} \tag{88}$$

where, h_{ct} = Heat transfer coefficient in cooling tower (W/m^2K)

A_{ct} = Area for heat transfer in cooling tower (m^2)

T_2 = Cooling tower inlet temperature (°C)

T_1 = Cooling tower outlet temperature (°C)

T_0 = Ambient wet bulb temperature (°C)

Note that Equation (88) contains a term similar to the log-mean temperature difference in Equation (81). The mixed air temperature at the inlet and the outlet is assumed to be equal to the wet bulb temperature, T_0. The cooling tower power, Q_{ct}, is also equal to the enthalpy lost by the water,

$$Q_{ct} = m_s c_{ps}(T_2 - T_1) \tag{89}$$

where, m_s = Secondary loop flow rate (kg/s)

c_{ps} = Specific heat at average secondary temperature (J/kgK)

The temperature of the water entering the cooling tower, T_2, is known from the energy balances around the heat exchangers. Equation (89) can be used to eliminate Q_{ct} in Equation (88). This gives the following equation for the temperature of the water exiting the cooling tower,

$$T_1 = T_0 + (T_2 - T_0)\exp\left[-\frac{h_{ct}A_{ct}}{m_s c_{ps}}\right] \tag{90}$$

The heat transfer coefficient in a direct-contact process is closely linked with the mass transfer coefficient. The ratio of the heat transfer to mass transfer coefficients is described by the Lewis Number, Le,

$$Le = \frac{h_{ct}}{K_{ct} c_{ps}} \tag{91}$$

where, K_{ct} = Mass transfer coefficient in cooling tower (kg/m^2s)

Studies show that the Lewis number is approximately equal to one for air-water systems [20]. An analysis of the transfer of heat from the water to the air by simultaneous diffusion and convection yields a dimensionless quantity, n_d, that represents the ability of the system to remove heat,

$$n_d = \frac{K_{ct} A_{ct}}{m_s} \tag{92}$$

Cooling tower performance curves are generally expressed as a relationship between n_d and the ratio of water-to-air flow rates. The Performance and Technology Committee of the Cooling Tower Institute, which publishes the standard cooling tower performance curves, recommends the following relationship [22],

$$\frac{K_{ct} A_{ct}}{m_s} \propto \left(\frac{m_s}{m_{air}} \right)^{-.6} \tag{93}$$

where, m_{air} = Mass flow rate of air through tower (kg/s)

The Lewis relation in Equation (91) can be used to express Equation (93) in terms of the heat transfer coefficient,

$$\frac{h_{ct} A_{ct}}{m_s c_{ps}} \propto \left(\frac{m_s}{m_{air}} \right)^{-.6} \tag{94}$$

or,

$$h_{ct} \propto m_s^{0.4} \left[\frac{m_{air}^{0.6} c_{ps}}{A_{ct}} \right] \tag{95}$$

During a loss of secondary pumps the secondary mass flow rate will drop from its initial value, m_{s0}, in accordance with its coastdown curve. The terms in the brackets in Equation (95) represent quantities that do not vary significantly during operation, and can be treated as constants. The air flow is set by the speed of the electric fans used to draw air into the cooling towers. The area for heat transfer, A_{ct}, is not a well defined quantity because heat transfer is taking place by direct contact. At steady state the value of the heat transfer coefficient can be found by solving Equation (88) for h_{ct} and setting Q_{ct} equal to Q_{hx}, which is in turn equal to the steady state heat deposition rate in the primary coolant. Using the proportionality in Equation (95), the heat transfer coefficient during a secondary pump coastdown is given by,

$$h_{ct} = h_{ct0}\left(\frac{m_s}{m_{s0}}\right)^{0.4} \tag{96}$$

where, h_{ct0} = Cooling tower heat transfer coefficient at flow rate m_{s0} (W/m^2K)

m_{s0} = Secondary mass flow rate at steady state (kg/s)

According to this model the heat transfer coefficient will go to zero when the secondary flow rate goes to zero. In reality, there will still be some heat transfer taking place within the cooling towers. In the absence of any secondary flow, the secondary loop will be effectively cut off from its ultimate heat sink (the atmosphere). Therefore, it is fair to assume that the cooling tower heat transfer rate approaches zero as the secondary flow rate goes to zero.

3.8 *Kinetics and Decay Heat*

The total fission power of the MITR is found by solving the point kinetics equations. The distribution of this power within the reactor is determined by axial and radial power shapes supplied by the user.

The point kinetics equations are written in their standard form as,

$$\frac{dT}{dt} = \frac{\rho - \beta}{\Lambda} + \sum_{i=1}^{6} \lambda_i \chi_i \tag{97}$$

and,

$$\frac{d\chi_i}{dt} = \frac{\beta_i}{\Lambda} T - \lambda_i \chi_i \tag{98}$$

where, T = Amplitude function,

χ_i = Concentration of neutron precursor i,

ρ = Reactivity,

Λ = Prompt neutron lifetime (s),

λ_i = Decay constant for precursor group i (s^{-1}),

β_i = Effective delayed neutron fraction for precursor group i,

β = Sum of all β_i.

It is convenient to express the kinetics equations in a normalized form. The normalized point kinetics equations can be written as,

$$\frac{dP_F}{dt} = \left(\frac{\rho - \beta}{\Lambda}\right) P_F + \sum_{i=1}^{6} \frac{C_i \beta_i}{\Lambda} \tag{97a}$$

and,

$$\frac{dC_i}{dt} = \lambda_i (P_F - C_i) \tag{98a}$$

where, P_F = Normalized core power,

C_i = Normalized concentration of delayed neutron precursor i,

The derivation of the normalized kinetics equations is presented in Appendix C. The use of normalized power and precursor concentration requires that the initial values of power and precursor concentrations be supplied by the user. A normalized value of 1.0 means that the variable is equal to its steady-state value.

The total power generated in the core is made up of the sum of the fission power and the contribution of the decay of all of the decay precursors that have been formed as a result of previous operation. During steady-state operation the decay precursors contribute approximately 6.1% of the total power. The remaining 93.9% is fission power which is found from the kinetics equations. The decay heat is found from [23],

$$P_D = \sum_{i=1}^{7} \beta_{Di} C_{Di} \tag{99}$$

and,

$$\frac{dC_{Di}}{dt} = \lambda_{Di} (P_F - C_{Di}) \tag{100}$$

where, P_D = Normalized decay heat,

C_{Di} = Normalized concentration of decay heat fission products i,

λ_{Di} = Decay constant for decay heat fission products group i (s^{-1}),

β_{Di} = Effective fraction of decay heat fission product group i,

The total normalized power generated is then the weighted average of the fission and decay heat,

$$P = P_F(1 - f_D) + P_D f_D \tag{101}$$

where, P = Total normalized core power

f_D = Fraction of power from decay heat ($f_D = 0.061$)

The fractions and decay constants for the delayed and decay groups are given in Tables 3.8.1 and 3.8.2, respectively.

Table 3.8.1 Delayed neutron group constants [4,23]

Group (i)	β_i	λ_i (s^{-1})
1	0.0124	0.000248
2	0.0305	0.001643
3	0.1110	0.001470
4	0.3010	0.002962
5	1.1400	0.000863
6	3.0100	0.000315

Table 3.8.2 Decay heat fission product group constants [4,23]

Group (i)	β_{Di}	λ_{Di} (s^{-1})
1	0.097	1.280
2	0.220	0.152
3	0.237	1.93×10^{-2}
4	0.187	1.88×10^{-3}
5	0.132	1.43×10^{-4}
6	0.072	1.25×10^{-4}
7	0.055	2.20×10^{-7}

When a positive reactivity insertion occurs, the fission power begins to rise in accordance with Equations (97a) and (99). This causes the inventory of delayed neutron precursors and decay heat fission products to begin to rise. When the fission power levels off, the precursor concentrations will eventually establish new equilibrium values.

In the event of a large, negative insertion of reactivity (such as a reactor scram), the fission power will rapidly drop to zero. The delayed neutrons prevent the fission power from dropping instantly to zero. The decay heat, however, begins to drop very slowly as the fission products decay away.

The decay heat model shown above is accurate for short time periods following a reactor scram. For long time periods, however, it may underpredict the decay heat [24]. For this reason the decay heat found by Equation (99) is compared to the following empirical relation for decay heat [25],

$$P_D = 0.1P_0\left[(t+10)^{-0.2} - (t+\tau+10)^{-0.2} + 0.87(t+\tau+2E7)^{-0.2} - 0.87(t+\tau+2E7)^{-0.2}\right] \tag{102}$$

where, P_0 = Total normalized power prior to scram,

t = Time elapsed since scram (s),

τ = Operating time at P_0 prior to scram (s)

The elapsed operating time in Equation (102) is set to infinity to represent a long operating history. Empirical equations such as Equation (102) are not reliable during the first few seconds following a scram, but they are more reliable than summation methods such as Equation (99) for long-term decay heat [24]. To avoid, the decay heat is assumed to be equal to the larger of Equation (99) or Equation (102).

When a scram condition is detected, a signal is sent to deenergize the magnets that hold the control blades. When the magnetic field has disappeared, the blades begin to drop into the core by gravity. The instrumentation delay time and the time needed to deenergize the magnets have been measured and analyzed [1,26]. This delay time is included in the scram model. When a trip limit is exceeded, nothing happens until the delay time has expired. After the delay, the blades begin to drop by gravity. The drop of the blades is hindered by the presence of water in their channels. This creates buoyancy and drag that causes the blades to accelerate at a rate less than the gravitational acceleration. The effective resistance to acceleration was estimated in blade drop studies conducted by Terry and Sardy [1,26]. The amount of negative reactivity inserted during the scram is found by using an integral blade worth curve.

3.9 *Natural Circulation in MITR*

During normal operation the natural circulation valves shown in Figure 3.2.1 are kept closed by the pressure of the coolant flowing under them. The natural circulation valve, shown in Figure 3.9.1, consists of a metal ball that is free to move within a cylindrical shaft. There are four such valves located outside the flow shroud of the MITR. The valve is shut when the ball is forced to the top of the shaft, thereby blocking the top aperture of the valve. When the conditions are such that the ball begins to drop, the natural circulation valve is open.

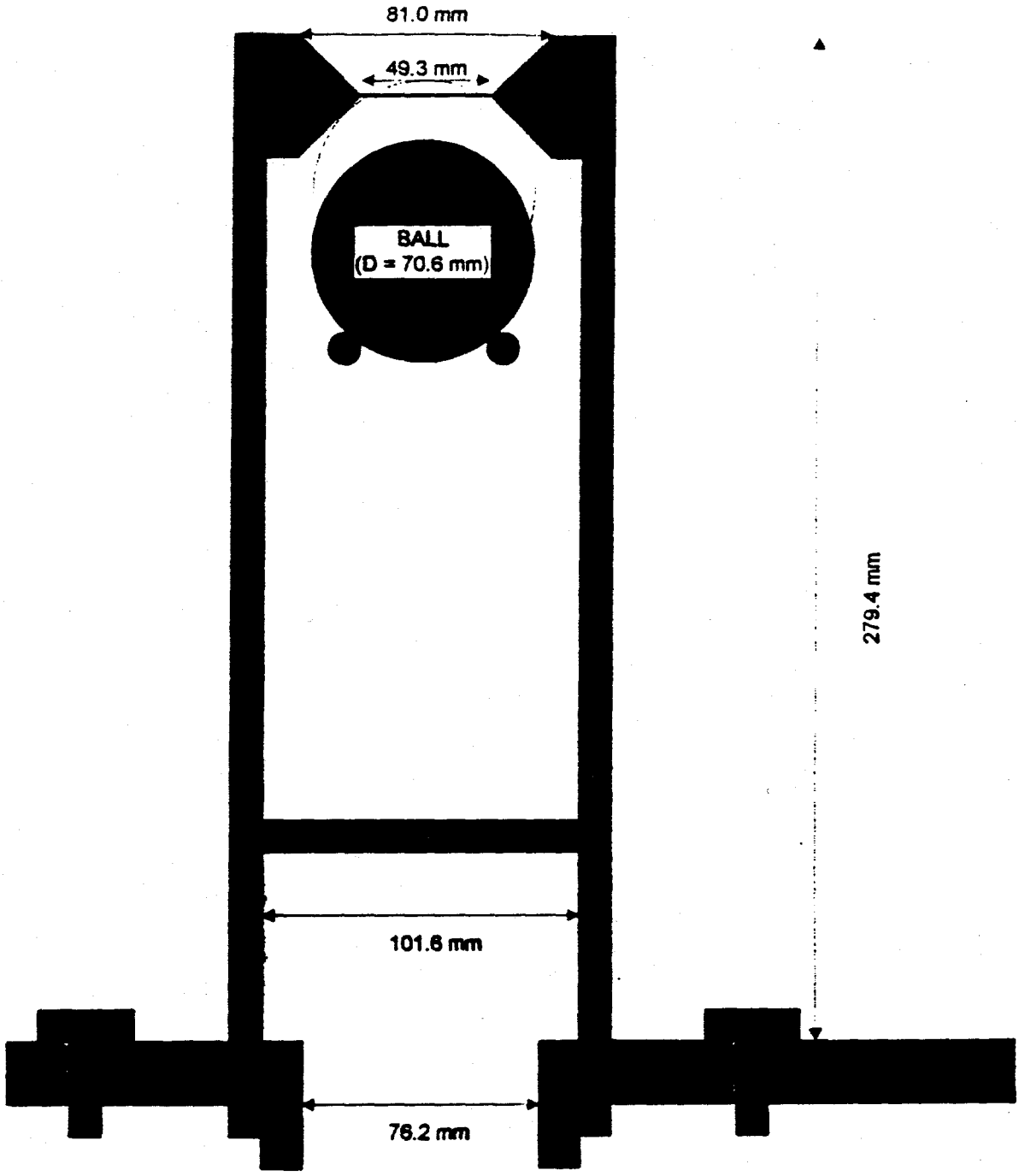

Figure 3.9.1. Drawing of an MITR natural circulation valve. The valve is shown in its "open" position, permitting coolant to flow between the downcomer and the mixing area (adapted from [27]).

A pressure balance on the ball gives the following criteria for the ball to begin dropping,

$$(P_A - P_B) < \frac{(\rho_{ball} - \rho_{dc})gV_{ball}}{A_{nc}} \qquad (103)$$

where, P_A = Pressure below natural circulation ball (Pa),

P_B = Pressure above natural circulation ball (Pa),

ρ_{ball} = Density of metal ball (kg/m^3),

ρ_{dc} = Density of coolant in downcomer (kg/m^3),

V_{ball} = Volume of ball (m^3),

A_{nc} = Average flow area of natural circulation valve (m^2).

The static pressure difference between the top and bottom of the natural circulation ball is negligible. When the primary flow rate is high, the kinetic head of the coolant flowing below the natural circulation valve is sufficient to keep the ball up. The kinetic head of the coolant in the mixing area above the natural circulation valve is nearly zero. During a flow coastdown the natural circulation valves will open when the kinetic head in the downcomer drops to the point where Equation (103) is true.

When the inequality in Equation (103) is true, the ball will begin to drop. The pressure below the valve is still greater than the pressure above, however. The opening of the natural circulation valves has effectively created an additional flow path for the coolant to follow. This additional flow path bypasses the core, thereby reducing the core flow rate. Figure 3.9.2 shows the core flow path when the natural circulation valves open. Initially the flow through the natural circulation valves (m_{NC}) is positive. There is still some forced flow (m_{pump}) coming in the cold leg and leaving out the hot leg. Conservation of mass requires that the sum of the flow through all flow paths equals the net flow provided by the pumps,

$$m_{pump} = m_{NC} + m_{core} \qquad (104)$$

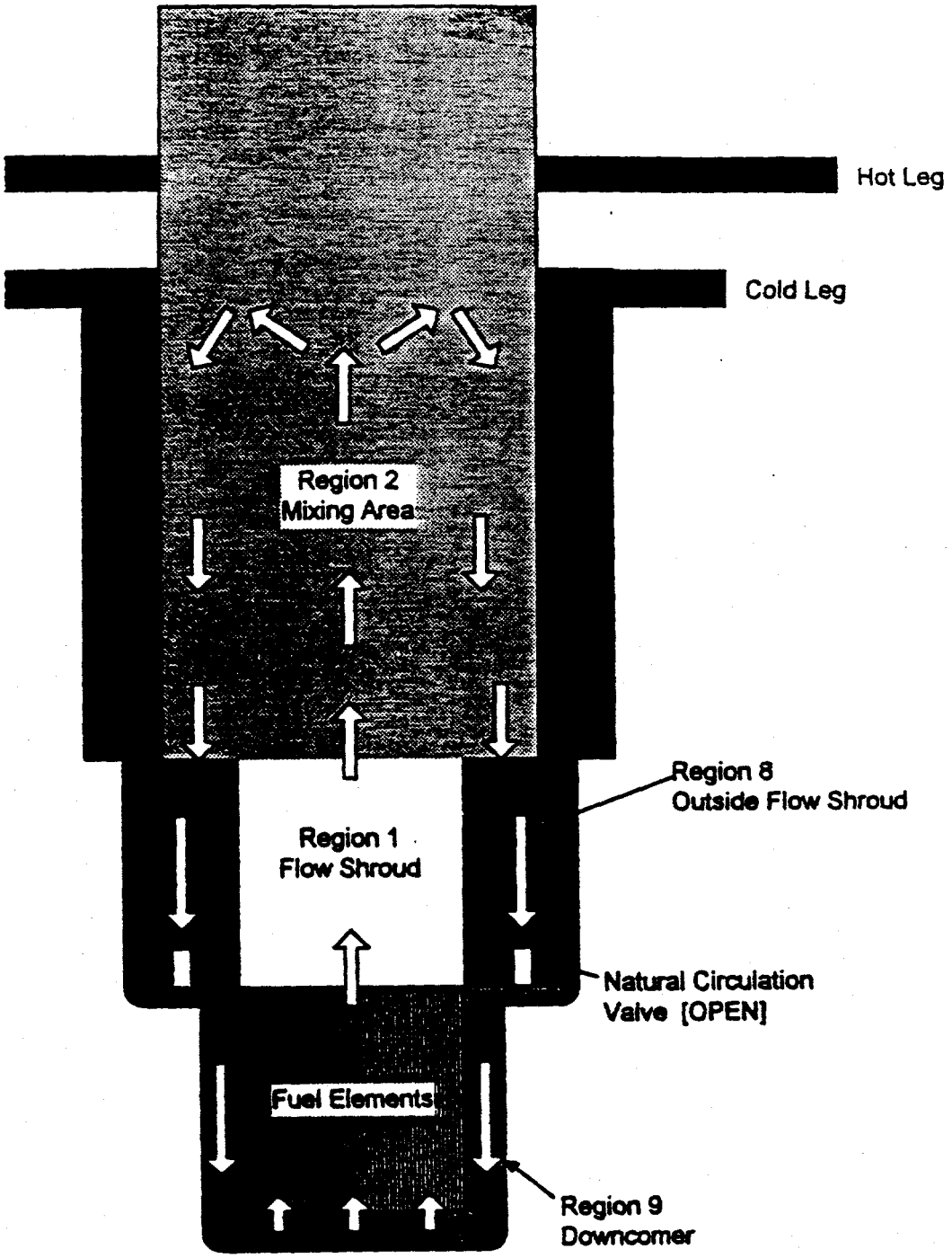

Figure 3.9.2. Core control volumes used for natural circulation calculations. When the natural circulation valves open, control volume 8 is moved from the downcomer to the region outside the flow shroud in order to provide more precise information about the conditions above the core.

The fraction of the forced flow bypassing the core is found by a momentum balance on the two flow paths. The pressure difference (pressure losses plus buoyancy) is required to be the same for each flow path. In Figure 3.9.2, the core flow path includes passage through the downcomer (Region 9), the core, and the flow shroud (Region 1). While the natural circulation loop in being established, some flow will bypass the core by flowing *upwards* through the natural circulation valves and Region 8. Bypass flow is defined as the rate of flwo passing up (in the positive direction) through the natural circulation valves. The regions shown in Figure 3.9.2 are different from those used to analyze the core during forced flow (shown in Figure 3.2.1). The main difference is that one region is redifined to provide more detail in the mixing area. Region 8 in Figure 3.9.2 is outside the flow guide because the enthalpy entering this region from the natural circulation valves may be quite different from the enthalpy in the rest of the mixing area.

The amount of bypass flow will quickly begin to decrease as: 1) the forced flow from the pump drops; and 2) the form losses through the natural circulation valve cause a high pressure loss. During this time, the low core flow rate leads to high temperature coolant exiting the core and entering the flow shroud. The hotter fluid has a lower density, and therefore represents a lower buoyancy head than an equal column of cooler water (such as the water in the mixing area above the natural circulation valve). The result of the density difference between the coolant in the two flow paths is that the flow through the natural circulation valves will drop below zero, indicating a flow reversal through the valves. The conservation of mass given in Equation (104) is still required to hold true. When the forced flow drops to zero, the flow through the natural circulation valve will be equal to the flow through the core, and opposite in sign. Flow will travel upwards through the core, and down through the natural circulation valves (as shown in Figure 3.9.2). This is a natural circulation loop driven by the density differences between the two flow paths.

3.9.1 Natural Circulation Momentum Balance

When the natural circulation valves open, a momentum balance is used to determine the flow split between the core and the bypass. The change in mass flow rate to each flow path is given by,

$$\frac{1}{C_i}\frac{\partial m_i}{\partial t} = \Delta P_{total} - F_i \tag{105}$$

with,

$$C_i = \frac{1}{\sum_{z=1}^{Z}\frac{L_z}{A_z}} \tag{106}$$

where, i = Flow path index (1 = core; 2 = bypass)

m_i = Mass flow rate flow path i (kg/s),

t = Time (s),

ΔP_{total} = Pressure difference between bottom of natural circulation valve and top of flow shroud (Pa),

F_i = Pressure loss in flow path i (Pa),

L_z = Length of Region z in flow path i (m),

A_z = Area for flow of Region z in flow path i (m^2).

The pressure loss for each path (F_i) is found using the momentum equations outlined in Section 3.3. There is an additional form loss term for flow passing through the natural circulation valves. Because the valves have a smaller flow area than the regions above and below them, there are losses associated with entrance contraction and exit expansion. The inner structure of the natural circulation valves also introduce form losses. The value of the form loss coefficient has been calculated by Bamdad [27] for both upflow and down flow. New values have been derived by Hu based on computational fluid dynamics (CFD) code models of the natural circulation valves [5].

During natural circulation flow, the core is treated the same as described for forced flow. The fraction of flow that is determined by Equation (105) to enter the core is further divided among the core flow channels as outlined in Section 3.3.

The solution of ΔP_{total} is analogous to the method described for ΔP_{core} in Section 3.3. The differential form of Equation (104) can be expressed as,

$$\frac{dm_{pump}}{dt} = \frac{dm_{core}}{dt} + \frac{dm_{NC}}{dt} \tag{107}$$

Combining Equation (105) with Equation (107) gives an expression for the total pressure drop,

$$\Delta P_{total} = \frac{\left(\frac{dm_{pump}}{dt}\right) + \sum_{i=1}^{N} C_i F_i}{\sum_{i=1}^{N} C_i} \tag{108}$$

At the instant that the natural circulation valve opens the bypass flow rate is zero and the frictional losses are also zero. This leads to a rapid rise in positive bypass flow by Equation (105). When the natural circulation flow loop is well established, the flow rate through the loop represents a balance between the buoyancy driving force and the friction and form losses.

3.9.2 Natural Circulation Energy Equation

Figure 3.9.3 shows a block diagram of the flow through the MITR core during three stages of the transition to natural circulation flow. During the first phase, labeled "Forced Convection," the flow path through the MITR system is as described in Section 3.3.

The transition to "Mixed Convection" is marked by the opening of the four natural circulation valves in response to a reduction in primary loop flow such that Equation (103) is satisfied. During this phase there is still some net flow of primary coolant through the entire primary loop during the pump coastdown. Immediately after the natural circulation valves open, the control volumes within the core change to include an extra control volume outside the flow shroud. When the natural circulation valves open, the core is nearly cut off from the remainder of the primary loop, including the heat exchangers, hot leg, and cold leg. Within ten seconds following the opening of the natural circulation valves, all forced flow will be lost. The pressure difference across the natural circulation valves is still high enough that flow through the valves is in the positive (upward) direction. Coolant enters the downcomer at a mass flow rate, m_{pump}, corresponding to the forced flow from the pump coastdown. This coolant has an enthalpy equal to the cold leg enthalpy leaving the heat exchangers. The enthalpy in each node is calculated by a mass and energy balance over each control volume at each time step. The enthalpy at each time step is found from,

$$h_i^+ = \frac{h_i^0 V_i + \sum_{j=1}^{J} m_j h_j^0 \Delta t - \sum_{k=1}^{K} m_k h_i^0 \Delta t}{V_i} \qquad (109)$$

where, h_i = Enthalpy in node i (J/kg)

m_i = Mass flow rate in node i (kg/s)

V_i = Volume of node i (m^3)

Δt = Time step size (s)

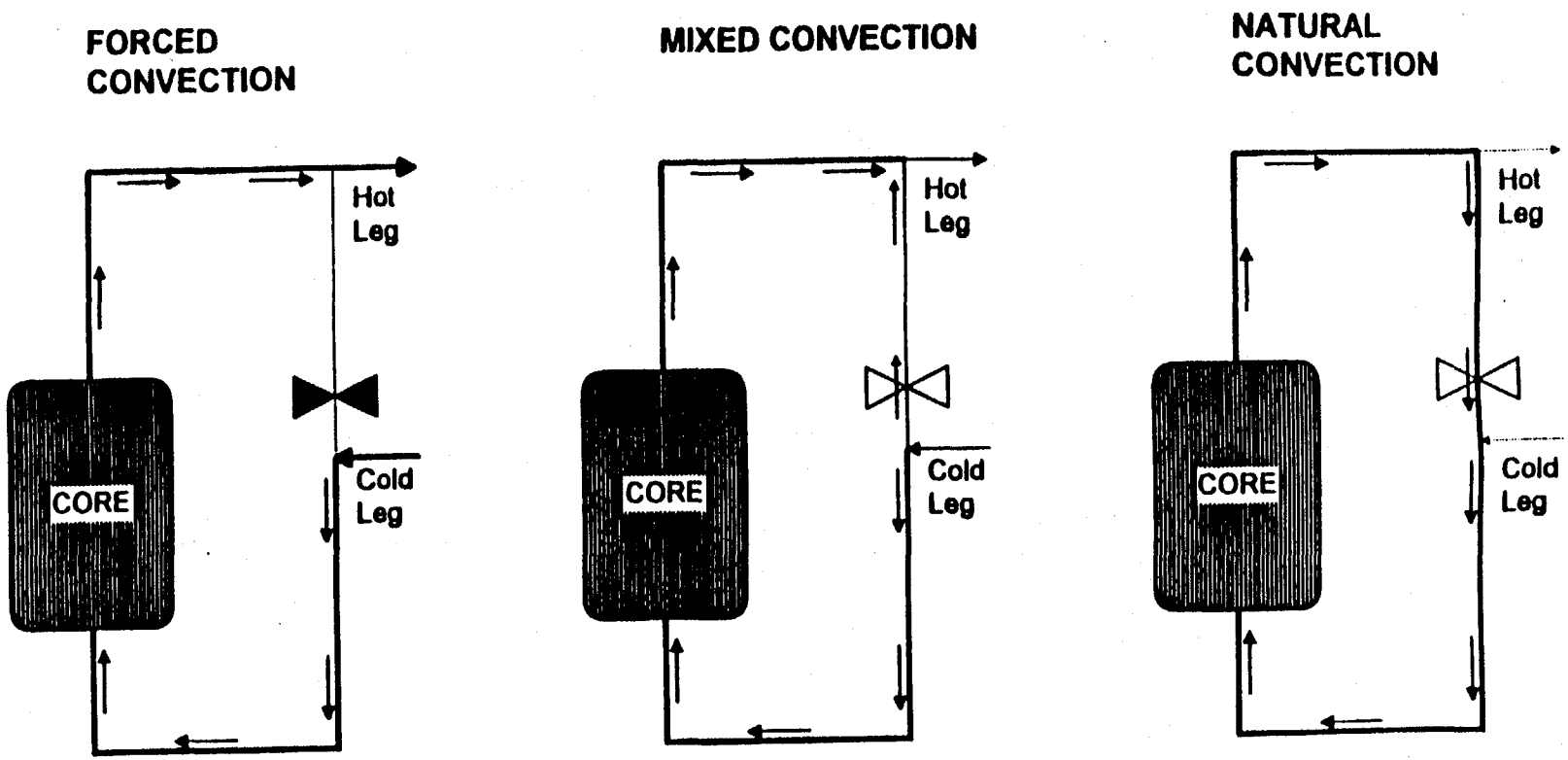

Natural Circulation Valve:	Closed	Open	Open
Flow Through Valve:	None	Upward	Downward
Pump Forced Flow:	High	Low	Very Low

Figure 3.9.3. Core flow paths during mixed and natural circulation. The diagram shows the three phases of core flow during a loss of primary flow in MITR.

and the indices j and k represent flow streams into and out of node i, respectively.

When the momentum balance described above indicates a flow reversal through the natural circulation valves, the core enters the "Natural Circulation" phase in Figure 3.9.3. The enthalpy in each node is calculated using Equation (109). Because the flows entering and exiting some nodes change when the flow is reversed, the inlet and exit streams change. Table 3.9.1 shows the inlet and exit streams for each control volume during the "Mixed Convection" and "Natural Circulation" phases. The flow rates represent the mass of coolant crossing the control volume each second. Mass conservation for incompressible flow implies that the mass entering each volume must equal the mass leaving each volume.

Tables 3.9.1. Mass transfer following the opening of the natural circulation valves.

Control Volume	Mixed Convection		Natural Convection*	
	Inlet Streams	**Exit Streams**	**Inlet Streams**	**Exit Streams**
9 (Downcomer)	Cold Leg (m_{pump})	Node 8 (m_{NC}) Node 0 (m_{core})	Cold Leg (m_{pump}) Node 8 ($-m_{NC}$)	Node 0 (m_{core})
0 (Core)	Node 9 (m_{core})	Node 1 (m_{core})	Node 9 (m_{core})	Node 1 (m_{core})
1 (Flow Shroud)	Node 0 (m_{core})	Node 2 (m_{core})	Node 0 (m_{core})	Node 2 (m_{core})
2 (Mixing Area)	Node 1(m_{core}) Node 8 (m_{NC})	Hot Leg (m_{pump})	Node 1(m_{core})	Hot Leg (m_{pump}) Node 8 ($-m_{NC}$)
8 (Outside Flow Shroud)	Node 9 (m_{NC})	Node 2 (m_{NC})	Node 2 ($-m_{NC}$)	Node 9 ($-m_{NC}$)

* The natural circulation flow rate, m_{NC}, is algebraically negative during this phase because the flow is downward through the valves.

A short time into the natural convection phase the forced flow from the pump will equal zero. At this time Equation (104) reduces to,

$$m_{core} = -m_{NC} \tag{110}$$

During normal operation the hot leg temperature sensor is relied upon to give information about the temperature of the coolant leaving the core. As the primary flow rate drops during a flow coastdown, the usefulness of this sensor decreases. At low flow rates the delay between a temperature rise at the core exit and a temperature rise at the hot leg inlet can be on the order of minutes [5]. When the pump flow rate reaches zero, and all flow through the core is driven by natural convection, the temperature sensors at the core exit (MTS-1, MTS-1A) fail to provide reliable information.

3.10 Limit Criteria

3.10.1 Heat Flux Shape

The heat flux passing from the clad to the coolant varies spatially within the core. The discretization scheme used in this analysis explicitly models each of the twenty-seven element positions. Each element is further subdivided into axial nodes. The smallest unit used in this analysis represents one axial section of one fuel element. All variables (including surface heat flux, fluid enthalpy, pressure, clad temperature, fuel temperature, void fraction, flow quality) are assumed to be the same within each of these nodes. In reality, however, these values vary from place to place within a node. The node-average values are adequate to calculate macroscopic quantities such as pressure loss and coolant temperature. The node-average values are based on the axial and radial power shape in the MITR core. It would be inaccurate (and non-conservative) to use the node-average heat flux to locate the first occurrence of localized ONB or CHF within the core during a transient.

The power shape is made up of an axial and a radial shape factor for each node. The radial shape factor relates the fission power in fuel element i to the average power in the core. The axial shape factor relates the fission power in axial node z of element i to the average power in element i. These shape factors are defined as,

$$P_{R,i} = \frac{q'''_i}{\overline{q}'''_{core}} \tag{111}$$

and,

$$P_{A,z} = \frac{q'''_z}{q'''_i} \tag{112}$$

where, $P_{R,i}$ = Radial power shape factor for element i,

$P_{A,z}$ = Axial power shape factor for axial node z,

q'''_{core} = Core average volumetric heat generation rate (W/m^3),

q'''_i = Average volumetric heat generation rate in element i (W/m^3),

q'''_z = Average volumetric heat generation rate at axial plane z (W/m^3).

It is apparent from the definitions above that,

$$\sum_{i=1}^{N} P_{R,i} = \sum_{z=1}^{Z} P_{A,z} = 1 \tag{113}$$

where, N = Number of fuel elements,

Z = Number of axial nodes in each element.

The axial and radial power shape factors are multiplied together to give the power shape factor for axial node z in element i. The product of the shape factor and the core average volumetric heat generation rate is the average volumetric heat generation rate in axial node z of element i. This heat generation rate is used to determine the node-average properties and for all balance equations described in Sections 3.3 and 3.4 of this report. One axial power distribution is used to describe the axial power shape in each fuel element.

The remainder of this section describes the method used to account for the variation of heat flux within a node to predict ONB and CHF. The variation in heat flux within an axial segment of a single fuel element can be attributed to three peaking factors. These three peaking factors are described qualitatively in Section 3.4 of this report. The approach taken here is to define a peaking factor that relates the highest heat flux within a node to the node-average heat flux that is used in the macroscopic energy balance. This peaking factor, P_T, is the product of three independent peaking factors that describe the heat flux shape within a node,

$$P_T = P_X P_Y P_Z \tag{114}$$

where, P_X = Peaking among fuel plates in a fuel element (x direction),
P_Y = Peaking within a fuel plate (y direction),
P_Z = Axial peaking due to discretization (z direction),

These three factors are combined non-stochiastically (multiplied together) because they are assumed to be independent of each other. In other words, there will be a single point in a given node where all three factors combine to give the peak heat flux. The important distinction between the peaking factors and the power shape factors is that the peaking factors are only used to check for the occurrence of ONB or CHF. The peaking factors are not used in the energy or momentum balances.

X-Direction Peaking

The x direction is defined as the direction perpendicular to the fuel plates within the fuel element. Because the orientation of the fuel elements varies within the core, the axis system used here is defined separately for each fuel element. Peaking in the x-direction is discrete because it is a measure of the heat flux within one of the fifteen fuel plates in a fuel element. The x-direction peaking factor is defined as,

$$P_X = \left.\frac{\text{Heat flux in the hottest fuel plate in a fuel element}}{\text{Average heat flux in a fuel element}}\right|_{y,z} \qquad (115)$$

Recall that the avergae heat flux in a fuel element is determined by the core power level and the radial power shape factor for that fuel element.

Y-Direction Peaking

The y-direction refers to the variation within a given fuel plate at a given axial location. The orientation of the fuel element and its location within the core causes a variation in heat flux within a given fuel plate. The y-direction peaking factor is defined as,

$$P_Y = \left.\frac{\text{Heat flux at the hottest spot on a fuel plate}}{\text{Average heat flux in a fuel plate}}\right|_{x,z} \qquad (116)$$

The product of P_X and P_Y gives the peak heat flux found in a given fuel element at a given axial node. This corresponds to the location on the hottest of the fifteen fuel plates with the highest heat flux.

Z-Direction Peaking

The z-direction refers to the axial direction.

Each channel is discretized into Z axial nodes in order to find a numerical solution to the conservation equations. The axial power shape factor serves to discretize the continuous axial power shape that is observed in MITR fuel elements. Figure 3.10.1 shows a typical MITR axial power shape and the discretized power shape corresponding to ten axial nodes. Because of the sharp peaking observed at the top and bottom of the fuel element, the act of discretizing the power shape results in lost information about the true magnitude of the sharp power peaks.

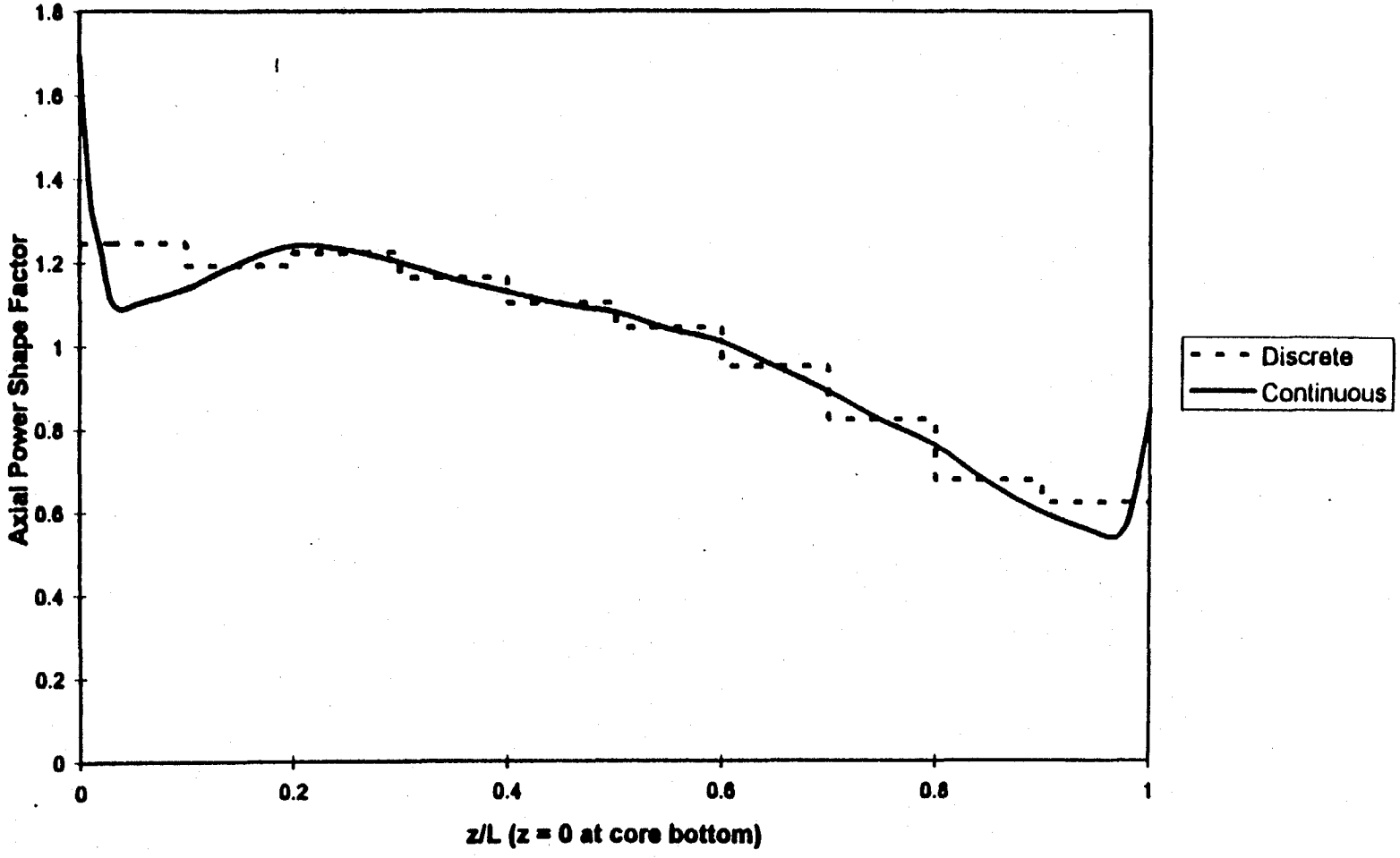

Figure 3.10.1. Average axial power shape in the MITR core. The axial power distribution is discretized into ten nodes for the analyses in this report. The continuous axial shape represents and average power shape based on MCNP calculations [3].

In addition, the assumption that a core-averaged axial power shape is applicable to all elements in the core introduces some error. The z-direction peaking factor is defined to recover information about the axial peaking within a discrete axial node. It is defined as,

$$P_Z = \left. \frac{\text{Peak heat flux in an axial node}}{\text{Axial node average heat flux}} \right|_{x,y} \tag{117}$$

Figure 3.10.1 shows how this peaking factor is defined for a typical MITR axial power shape. As stated for the other peaking factors, the largest value of P_Z observed in the core is used for all axial nodes in all fuel elements. The z-direction peaking factor essentially compensates for information about the axial shape that was lost when the continuous shape was discretized. The magnitude of P_Z can be reduced by using more axial nodes in the core. In this case, more information is retained in the axial power shape factor.

Because MITR fuel elements show more severe power peaks at the beginning of life (immediately after the fuel element is placed in the core), the value of P_Z must be evaluated for a fresh core.

The definitions of P_X, P_Y, and P_Z require detailed information about the power shape within a fuel element. The distribution of power within an element is determined by several factors, including,

1) Location of the fuel element within the core.

2) Presence of dummy elements or experimental assemblies.

3) Orientation of the fuel element.

4) Fuel element burnup.

It is not practical to calculate P_X, P_Y, and P_Z for each fuel element in the core. The approach used in this analysis is to use information from experimental measurements and CITATION computer calculations to determine the power shape factors [7]. The peaking factors are obtained from MCNP calculations of the power shape and power peaking within each element in a 22 element core [3]. The total peaking factor, P_T, is then found for each node as the ratio of the peak power (from MCNP calculations) to the node-average power.

3.10.2 Prediction of Hot Spot Clad Temperature

The hot spot clad temperature is calculated at the peak heat flux within each node. In addition, hot channel factors are used to find the bulk coolant temperature and heat transfer coefficient at the hot spot. The power shape factors and the power peaking factors give best estimate predictions of the heat flux in the core. The hot channel factors, however, account for *possible* variations in properties within the core. The use of hot channel factors allows the peak clad temperature to be calculated under worst-case conditions of bulk coolant temperature rise and heat transfer coefficient. The two hot channel factors are given in Table 3.10.1.

Table 3.10.1. Summary of engineering hot channel factors for MITR [3].

Hot Channel Factor	Value
Bulk Water Temperature Rise	
Reactor power measurement	1.05
Power density measurement	1.10
Fuel density tolerances	1.027
Fuel plate eccentricity	1.001
Flow measurement	1.02
Bulk Water Temperature Rise Factor (F_B)	1.210 (1.146)*
Heat Transfer Coefficent	
Reactor power measurement	1.05
Power density measurement	1.10
Fuel density tolerances	1.10
Flow measurement	1.02
Heat transfer coefficient	1.20
Heat Transfer Coefficient Factor (F_H)	1.550 (1.527)*

* Total in parentheses represents semi-statistical combination of subfactors.

The heat flux at the hottest spot in each axial node z in element i is given by (the subscripts have been dropped for clarity),

$$q''_{HOT} = q'' P_T \tag{118}$$

where, q'' = Average clad-to-coolant heat flux (W/m^2)

q''_{HOT} = Peak clad-to-coolant heat flux (W/m^2)

The higher heat flux at the hot spot results in a higher clad surface temperature at the hot spot. The highest possible bulk coolant temperature at each node is found using the bulk water temperature rise hot channel factor, F_B,

$$T_{B,HOT} = (T_B - T_{in})F_B + T_{in} \tag{119}$$

where for each axial node z in element i,

T_B = Bulk coolant temperature in node from energy balance (°C),

T_{in} = Core inlet temperature (°C),

$T_{B,HOT}$ = Highest possible bulk temperature in node (°C).

The lowest possible heat transfer coefficient is given by,

$$h_{HOT} = \frac{h}{F_H} \tag{120}$$

where for each axial node z in element i,

h_{HOT} = Lowest possible heat transfer coefficient in node (W/m^2K),

h = Average heat transfer coefficient in node (W/m^2K).

The clad temperature and the heat flux are related by the convective heat transfer relation,

$$q'' = h(T_C - T_B) \tag{121}$$

where for each axial node z in element i,

T_C = Clad temperature based on nodal average heat flux, q'' (°C)

Similarly, the clad temperature at the hot spot is related to the hot spot heat flux by,

$$q''_{HOT} = h_{HOT}\left(T_{C,HOT} - T_{B,HOT}\right) \tag{122}$$

Equations (118), (119), (120) and (122) are combined to give the temperature at the hot spot in each node,

$$T_{C,HOT} = \frac{q''_{HOT}}{h_{HOT}} + T_{B,HOT} = \left(T_C - T_B\right)P_T F_H + \left(T_B - T_{in}\right)F_B + T_{in} \tag{123}$$

For each axial node in each fuel element, two heat fluxes are computed. The nodal average heat flux, q", is based on power shape factors only. It is used for all macroscopic balances. The hot spot heat flux, q''_{HOT}, is based on shape factors and peaking factors. It represents the highest heat flux found anywhere in the node. The hot spot heat flux is used to determine whether or not ONB or CHF has occurred anywhere in the node. Likewise, two clad surface temperatures are computed, T_C and $T_{C,HOT}$. The peak clad temperature is used to predict the first occurrence of ONB in a node. The peak clad temperature is calculated with hot channel factors to account for the possible changes in the bulk coolant temperature rise and heat transfer coefficient within a channel.

Thus far no mention has been made of the impact of the fins on the heat flux and surface temperature within a node. The effect of the fins must be treated empirically because the heat transfer characteristics of the fins are not explicitly modeled.

Studies of the heat flux distribution over the finned surface of the MITR fuel elements were carried out by Parra and Szymczak [3,28]. Parra found that the heat flux at the fin tips is higher than in the valleys between fins. Furthermore, he found that the surface temperature between fins is higher than the surface temperature at the tips of the fins. These factors cause ONB to occur first in the valleys between the longitudinal fins. The lower heat flux occurs in between fins despite the higher surface temperature for three reasons. First, the heat transfer coefficient will be lower between the fins because of the fluid velocity profile. Second, the coolant in the valleys is hotter than the coolant that is adjacent to the fin tips. Third, the conduction distance from the fuel centerline to the clad base is less than the distance to the fin tips.

3.10.3 Predicion of ONB At Hot Spot

The hot spot found by combining the peaking factors may represent either a fin or a valley. Which of these two locations is most important depends on the event that is being studied. For predicting ONB, the valley is the most important because the heat flux is lower and the clad temperature is higher. Figure 3.10.2 shows the position of the clad base and the fin tips with respect to the Davis and Anderson correlation for ONB. The conditions at the clad base will cause it to experience ONB before the fin tip.

To check for ONB in the valley between fins at the hot spot, the Davis and Anderson Correlation is used to predict the ONB heat flux for a wall temperature of $T_{C,HOT,V}$,

$$q''_{ONB} = \frac{h_{fg} k_l (\rho_l - \rho_v)(T_{C,HOT,V} - T_{sat})^2}{12.5 T^*_{sat} \sigma} \qquad (124)$$

where, $T_{C,HOT,V}$ = Temperature in valley between fins at hot spot (°C)

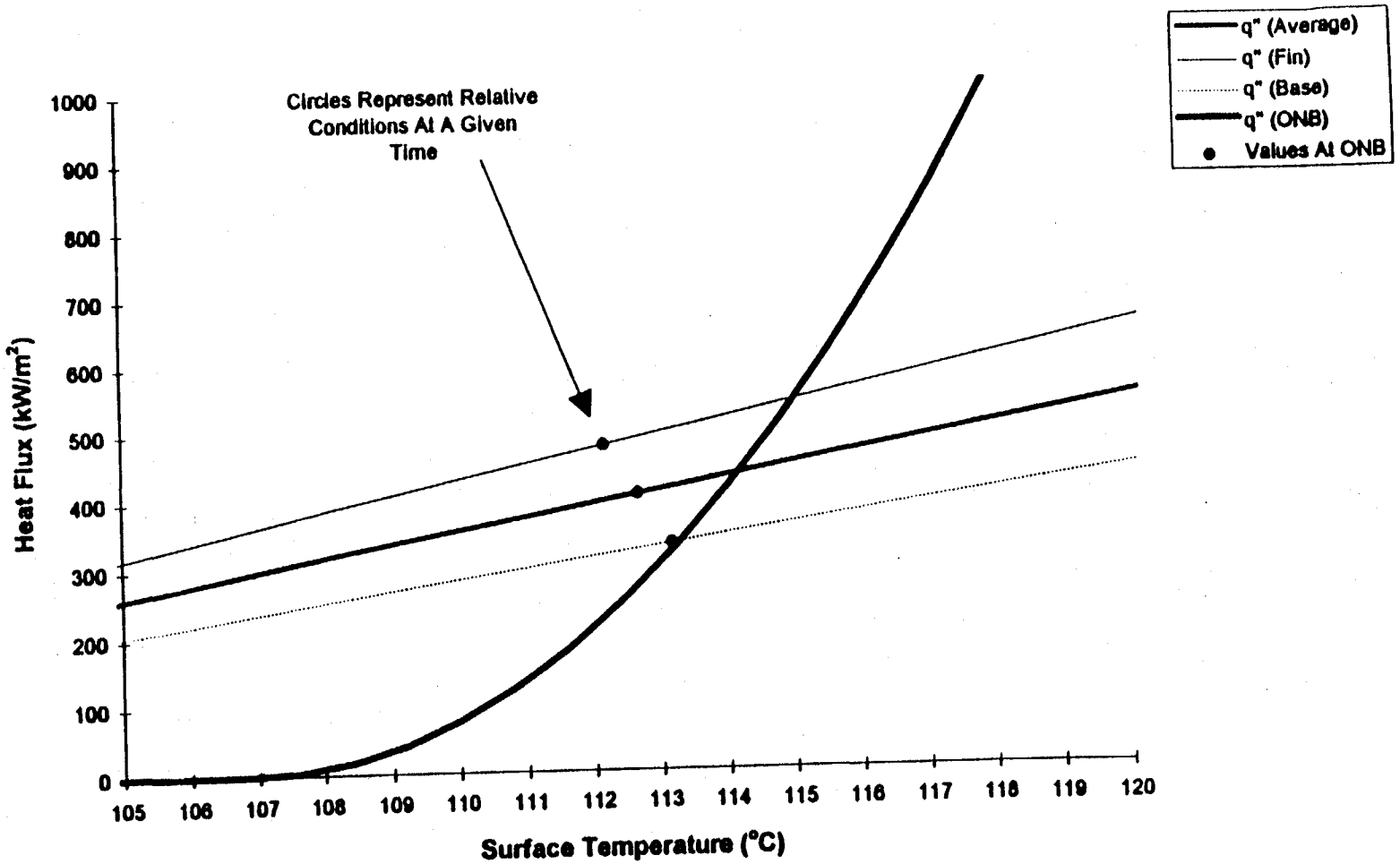

Figure 3.10.2. Approach to ONB in an MITR channel. At any given time, the clad base has a lower heat flux and a higher surface temperature than the fin tip. Therefore, it is expected to reach ONB before the fin sides or tip. In this example, when ONB begins at the clad base, the fin tip temperature is 3.5°C below the temperature required for nucleation.

The difference between the hot spot temperature and the temperature in the valley at the hot spot must be determined experimentally or by numerical simulation (see [3]). If the wall temperature in the valley is above the wall temperature required to nucleate at the local heat flux, then nucleate boiling is predicted to occur at the hot spot. The difference between the hot spot heat flux and the heat flux in the valley must be determined experimentally or by numerical simulation (see [3]). When ONB is predicted to occur at the hot spot, and the reactor has not yet scrammed, the LSSS criteria has been exceeded. This fact is noted by the code, and the calculation continues.

For the prediction of CHF, it is the fin tip that is of the most concern. Critical heat flux will occur in an MITR channel following the initiation of a flow excursion in one or more coolant channels. At the low coolant mass flux that will result from the flow instability, circulation-limited burnout is expected to be the dominant mechanism of CHF in MITR channels [3]. An annular flow pattern will be present in the channel, as the void fraction approaches 100%. The small amount of liquid that is present will flow through the valleys between fins. Based on Parra's studies, the fin tips will have a higher heat flux than the valleys. Therefore, the higher heat flux and poorer heat transfer at the fin tips will cause a departure from nucleate boiling CHF to occur there before it occurs in the valleys.

3.10.4 Critical Heat Flux Correlation For MITR Conditions

The critical heat flux is a complex function of channel geometry, surface heat flux, and pressure. It is also dependent upon the flow regime and two-phase flow conditions in the channel [9]. Various theoretical models have been proposed to model the heat transfer conditions in order to predict the onset of CHF in a given system. In general, these theoretical models are helpful in understanding the mechanism responsible for CHF, but they are relatively inaccurate and are applicable only over a narrow set of conditions. The most accurate estimates of CHF come from experimental or semi-empirical correlations based on a large number of observations. A number of well-tested correlations are available for the conditions found in power reactors. Choices for CHF correlations in low pressure systems are more limited. The unique geometry of the MITR fuel channels (narrow, rectangular channels with longitudinal fins) further limits the number of choices for an appropriate CHF correlation.

Experimental CHF studies carried out by the Japan Atomic Energy Research Institute on the JRR-3 research reactor are applicable to the MITR[29,30]. The conditions of a typical MITR channel are shown in Table 3.10.2, along with the conditions of the Japanese studies.

Table 3.10.2 Comparison of MITR conditions with conditions in JRR-3 [29,30]

Variable	JRR-3 Experiments	MITR Channel
Pressure (MPa)	0.1 - 0.6	0.13*
Mass Flux (kg/m^2s)	0 - 600	0 - 3500**
Inlet Temperature (°C)	19 - 80	20 - 50
Channel Width (mm)	50.0	58.67
Channel Depth (mm)	2.25	2.24
Heat Flux (W/m^2)	$0 - 3.5 \times 10^5$	2.3×10^5 ***

* This is the pressure at the core outlet.

** The mass flux during a flow excursion (which precedes CHF) will be substantially lower.

*** This is an average heat flux for 10 MW operation with 22 fuel elements, based on a finned surface area.

The Japanese studies were focused on the prediction of CHF at low flow conditions approaching a flow reversal. A flow excursion in an MITR channel will cause a rapid and severe drop in the flow of coolant to the affected channel. For this CHF mechanism, the JRR-3 CHF correlation would be appropriate for predicting CHF in an MITR channel for low flow conditions.

A large insertion of reactivity could lead to CHF at full flow before a flow excursion could take place. Although this form of CHF is far less likely than the circulation-limited case studied for JRR-3, it must still be considered. For mass fluxes above 1400 kg/m^{2}s, the Gambill correlation is useful for predicting the critical heat flux in rectangular channels at atmospheric pressure. → Bambill ?

The circulation limited CHF correlation includes two equations for CHF. The first is a flooding limit critical heat flux. This is the critical heat flux when the mass flux in a channel is zero or slightly negative (indicating a flow reversal). Regardless of the mass flux, the critical heat flux will not be below this value. The second equation includes the effect of the mass flux on the critical heat flux. The critical heat flux is the greater of the two equations. The circulation limited CHF correlation is [29,30],

$$q''_{CHF,f} = \frac{0.40 A_F h_{fg} \sqrt{2\rho_g(\rho_f - \rho_g)gW}}{A_H\left[1+\left(\frac{\rho_g}{\rho_f}\right)^{\frac{1}{4}}\right]^2} \tag{125}$$

and,

$$q''_{CHF,M} = 0.005 h_{fg} \sqrt{\lambda\rho_g(\rho_f - \rho_g)g}\left[\frac{G}{\sqrt{\lambda\rho_g(\rho_f - \rho_g)g}}\right]^{0.611} \tag{126}$$

where the characteristic length, λ, is,

$$\lambda = \left[\frac{\sigma}{(\rho_f - \rho_g)g}\right]^{\frac{1}{2}} \tag{127}$$

with, h_{fg} = Heat of vaporization of coolant (J/kg),

G = Mass flux (kg/m^{2}s),

g = Gravitational acceleration (m/s^2),

σ = Coolant surface tension (N/m)

W = Width of channel (m)

The Gambill correlation for CHF at higher flow rates consists of a sum of two terms. The first term represents boiling heat transfer, and the second term is a convective (non-boiling) term. Gambill's correlation for CHF is,

$$q''_{CHF,G} = K_1 h_{fg} \rho_g \left(\frac{\sigma g(\rho_f - \rho_g)}{\rho_g^2}\right)^{0.25} \left[1 + \left(\frac{\rho_f}{\rho_g}\right)^{0.923} \left(\frac{c_p(T_{sat} - T_B)}{25 h_{fg}}\right)\right] + K_2 \left(\frac{k_l}{D_e}\right) Re^{0.8} Pr^{0.4} (T_C - T_B) \tag{128}$$

where, K_1 = Boiling term constant ($K_1 = 0.12$)

K_2 = Convective term constant ($K_2 = .018$)

Equations (125), (126), and (128) are shown in Figure 3.10.3. It is apparent that the Gambill correlation predicts a higher critical heat flux than the correlations developed for JRR-3. The CHF criteria used in this study is the lowest CHF predicted by either Equation (126) or Equation (128). For mass fluxes in the range of interest for MITR, the lowest CHF is given by the JRR-3 correlation. Although the JRR-3 correlation is extrapolated beyond its mass flux envelope ($G > 600$ kg/m^{2}s), it is still used because it gives a lower CHF than the Gambill correlation.

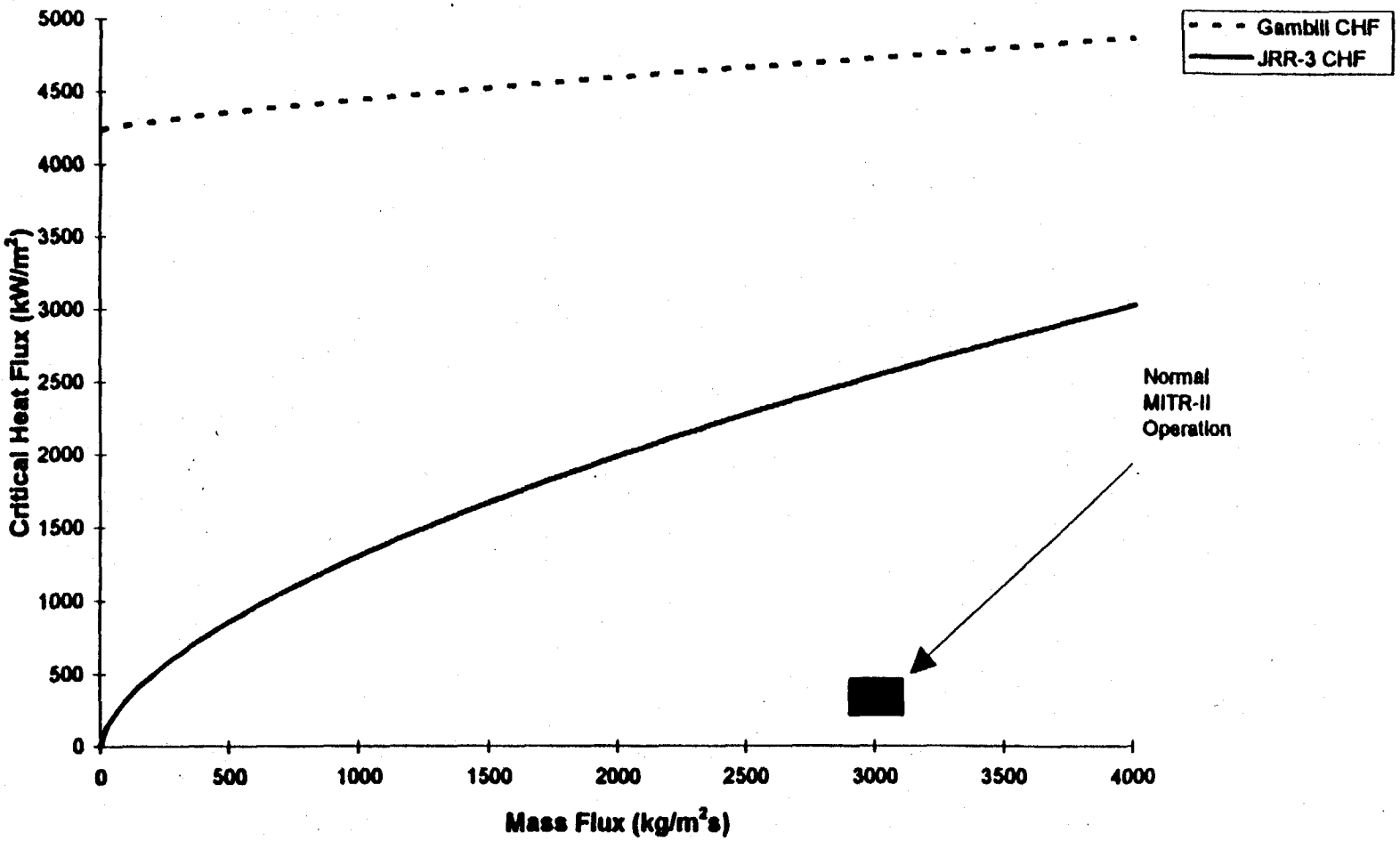

Figure 3.10.3. Critical heat flux correlations for MITR channels. The JRR-3 correlation is recommended for low mass fluxes where CHF is expected to occur by flooding. The Gambill CHF limit is expected to be reached only during a transient that does not lead to a flow excursion.

The predicted value of the critical heat flux is calculated in each node of the core. The predicted CHF is compared with the heat flux out of the fin tips at the hot spot in each node. If the hot spot heat flux exceeds the predicted critical heat flux, CHF is assumed to occur. At this point the safety limit criteria has been exceeded and no further calculations are made.

Nearly all correlations for CHF are based on experiments run at steady-state or near steady-state operating conditions. During a transient in the MITR that leads to a flow excursion, the flow rate in the affected channel may be changing rapidly. The sudden formation of vapor in the channels also leads to a dynamic system that cannot be considered to be near steady-state. Several studies have been performed on the applicability of steady-state CHF correlations to the transient conditions found in a reactor during an accident. Tong reports that these studies have all found that the transient CHF values lie at or above those predicted by the steady state correlations [31]. Collier cites several studies that indicate that steady-state correlations are appropriate for analyzing transient problems provided that the instantaneous conditions are used in the correlations (i.e., the local, time-dependent enthalpies and temperatures must be used in the correlations) [12]. This is the approach that is used in this analysis.

3.11 Summary

The models described in Chapter 3 are incorporated into the MITR Multi-Channel Analysis Code as subroutines. A steady-state solution is found based on the input power, flow rate, and characteristic temperature. At each time step, the equations presented above are solved to give the transient behavior of the coolant, clad, and fuel at each axial node in each coolant channel. The behavior of the primary and secondary systems is also modeled at ech time step.

Correlations for ONB, OSV, and CHF are found in the literature. The correlations are chosen from experiments that closely match the geometry, pressure, and flow conditions in an MITR coolant channel. When several correlations were applicable, the more conservative one is used.

In most calculations, a best-estimate result is calculated. However, when predicting whether or not a limit criteria has been exceeded, peaking factors and hot channel factors are used to examine the conditions at the hottest point in each node.

The models presented in Chapter 3 are developed to be used to predict limits for MITR operation. They are applicable to studying a variety of possible MITR transients. Several limitations must be noted:

1) The models presented here are not valid beyond critical heat flux.

2) A point kinetics model with a user-supplied power shape is used. The power shape is constant throughout the transient.

3) MITR auxilliary systems are not included in the code.

4) The mixing are above the core is assumed to be fully mixed at each time step.

4. Validation of MITR Multi-Channel Analysis Code

4.1 Objectives

The objective of this chapter is to validate the models described in Section 3 of this report. Because this code is used to predict the LSSS and Safety Limits for MITR-III, it is necessary to investigate the capability of the code to predict quantities of interest during steady-state and transient operation of the MITR. The process of validation points out the limitations of the code and identifies shortcomings in the mathematical models used. Validation also identifies the events that can be accurately modeled, and provides confidence in the applicability of the code to these problems.

As discussed in Section 1.3, many choices must be made in modeling a complex physical system. The effort in this analysis has been to produce best-estimate predictions of the response of the reactor core to the limiting transients described in Section 2.2. Less emphasis is placed on the response of components, such as the cooling towers and the secondary loop, that have a less critical impact on the approach to thermal-hydraulic limits. Several auxiliary systems are not included at all in this analysis because they will not affect the conditions in the core until the reactor has shut down following a transient (such as the shield coolant system, the D_2O reflector, the primary coolant purification system, and others). Special attention is given to the validation of new mathematical models of the MITR that were developed for this study. These new models include the core momentum model, the core energy model, the void fraction model, the determination of the onset of flow instability, and the natural circulation model.

Figure 4.1.1 shows the relative importance of the systems and components that make up the MITR. Because the reactor limits investigated here are based on thermal-hydraulic conditions in the core, the models that determine the thermal-hydraulic state of the reactor core are the most essential. The validation procedure is based on verifying that these key models are capable of accurately predicting the response of the MITR system to the limiting transients.

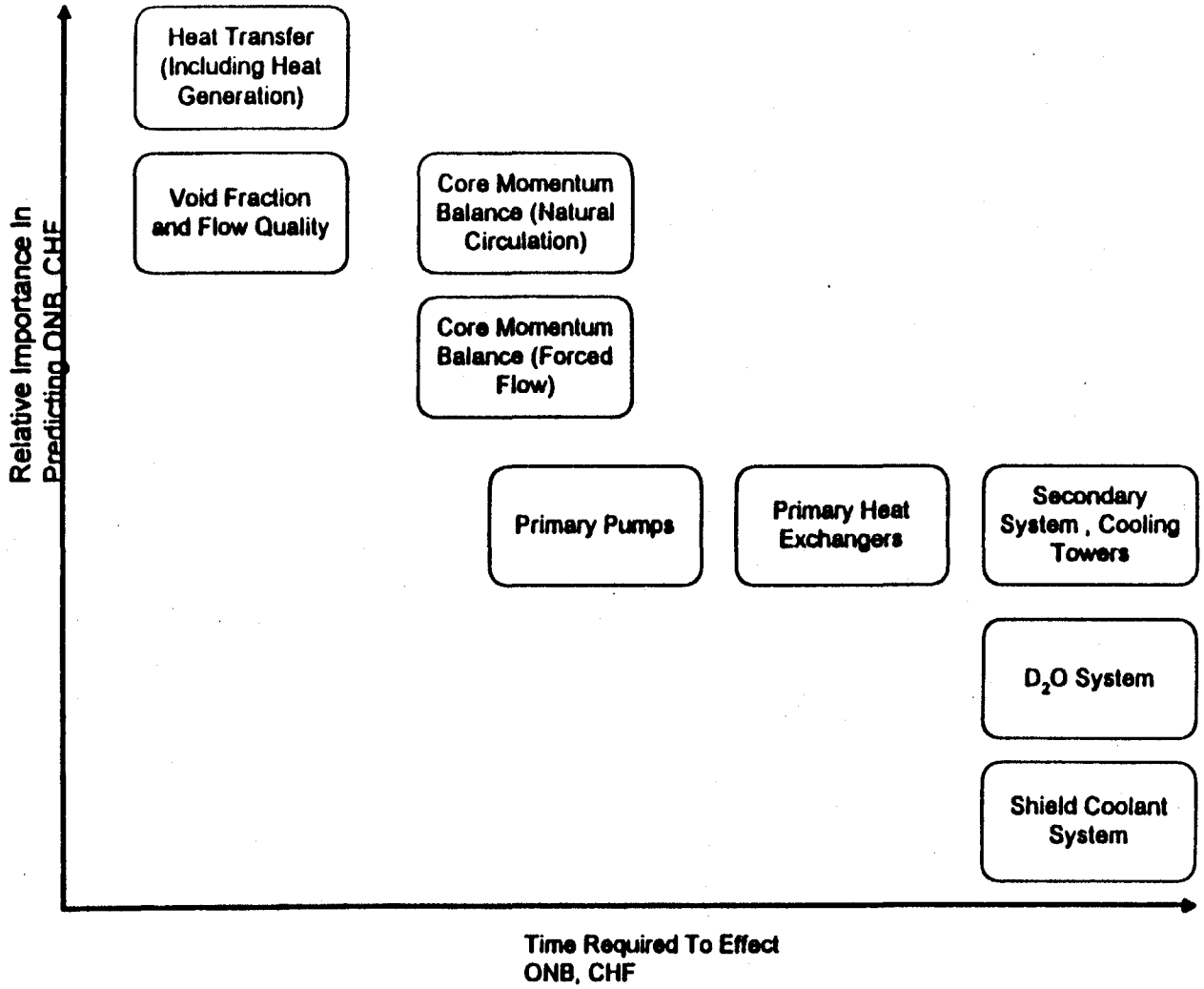

Figure 4.1.1 Relative importance of MITR system models. The void fraction model is a key model because it is closely linked to both the momentum and the energy equations during two-phase transients. The cooling tower performance is important during long transients, but it has a minimal impact on the core conditions during the first 30 seconds of a transient.

If the models of secondary importance are too inaccurate, the values of the key core variables will reflect this. In this event, it would be necessary to revise these secondary models. Likewise, if the omission of any of the auxiliary system models causes the key core variables in the code to deviate from their measured values, then attention should be given to including auxiliary systems. During the development of the MITR Multi-Channel Analysis Code, these criteria have led to the addition of some models, and to the refinement of others.

The code is validated by comparing the computed values of core temperatures to experimentally measured values. Core temperatures are used to for these comparisons because,

1) Temperatures are the most directly measured quantities in the core. Temperatures measured by thermocouples are typically within one or two degrees of the true temperature.

2) Coolant and clad temperatures play a major role in determining the LSSS and Safety Limits.

3) Temperatures quickly and accurately reflect changes in other core variables that cannot be so easily measured (such as the surface heat flux and the heat transfer coefficient).

Experimental data from MITR-II is available for both slow and rapid transients. However, no data is available for two-phase flow in the MITR. The two-phase flow models in the MITR Multi-Channel Analysis code must be validated by comparison with experimental data taken on other systems under conditions similar to those of MITR-II.

4.2 MITR-II Startup

Data from the power ascension of the MITR-II was recorded by Hu in 1993 [5]. This data was also used by Trosman to validate his code [4]. The power ascension procedure consisted of raising the reactor power from a critical state at 500 kW to the target power of 4.9 MW in a series of steps. The control blades were used to make six step changes in power during a one hour period, as shown in Figure 4.2.1 During this time interval, the outlet temperature of the cooling towers varied as shown in Figure 4.2.2. A sudden drop in cooling tower outlet temperature occurred when the fans were turned on.

The core power and the cooling tower outlet temperatures were used as forcing functions in the MITR Multi-Channel Analysis Code. Because the data was taken at 90 second intervals, the values were linearly interpolated between consecutive measurements. At t = 0, the core inlet temperature was set to equal the measured value of 25°C.

Figure 4.2.3 shows the measured and predicted values of the hot leg and cold leg during the one hour transient. The predicted temperatures lie within an experimental uncertainty of 2° measured values. This relatively slow transient demonstrates that the overall energy and momentum balances used in the code are acceptable during steady-state and slow transients.

One area of concern in the energy balance is the mixing area above the reactor core. The coolant exiting the fuel elements and entering the MITR-II mixing area undergoes a complex mixing process. Studies are currently underway to model the turbulent mixing in the region above the core [5]. The model employed in this analysis uses two fixed control volumes to represent the mixing area during forced flow, and three control volumes during natural circulation. Each region is assumed to be fully mixed at each time step. The step power changes in the startup transient can be used to check the validity of this assumption. The predicted values match the measured values closely during this relatively slow power rise, indicating that the two-region, fully mixed model of the MITR-II mixing area is appropriate for slow changes in core outlet temperature. For faster transients, plume effects cause the temperature at the hot leg to rise sooner the fully-mixed model would predict.

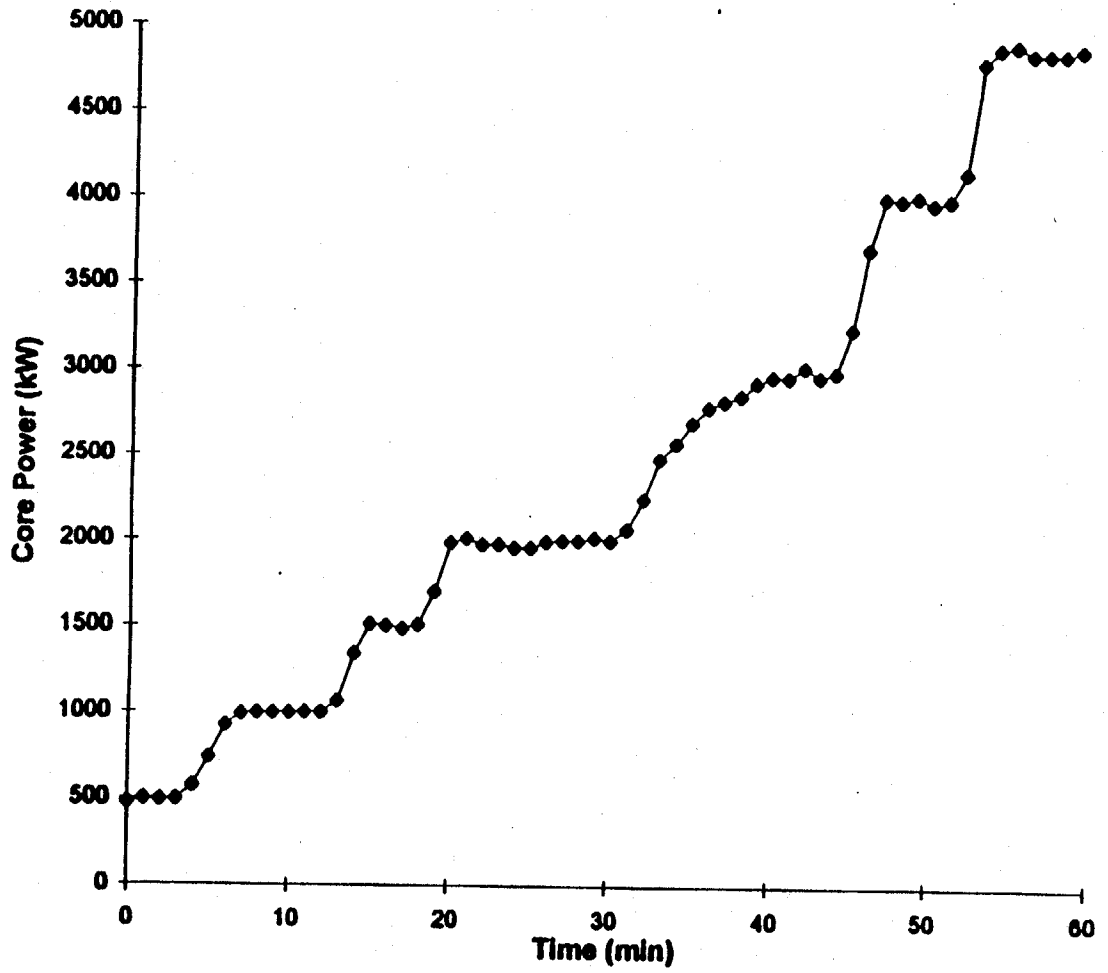

Figure 4.2.1 Core power in MITR-II power ascension transient. The core power is raised from 500 kW to 5 MW during a one-hour period (data from [4]).

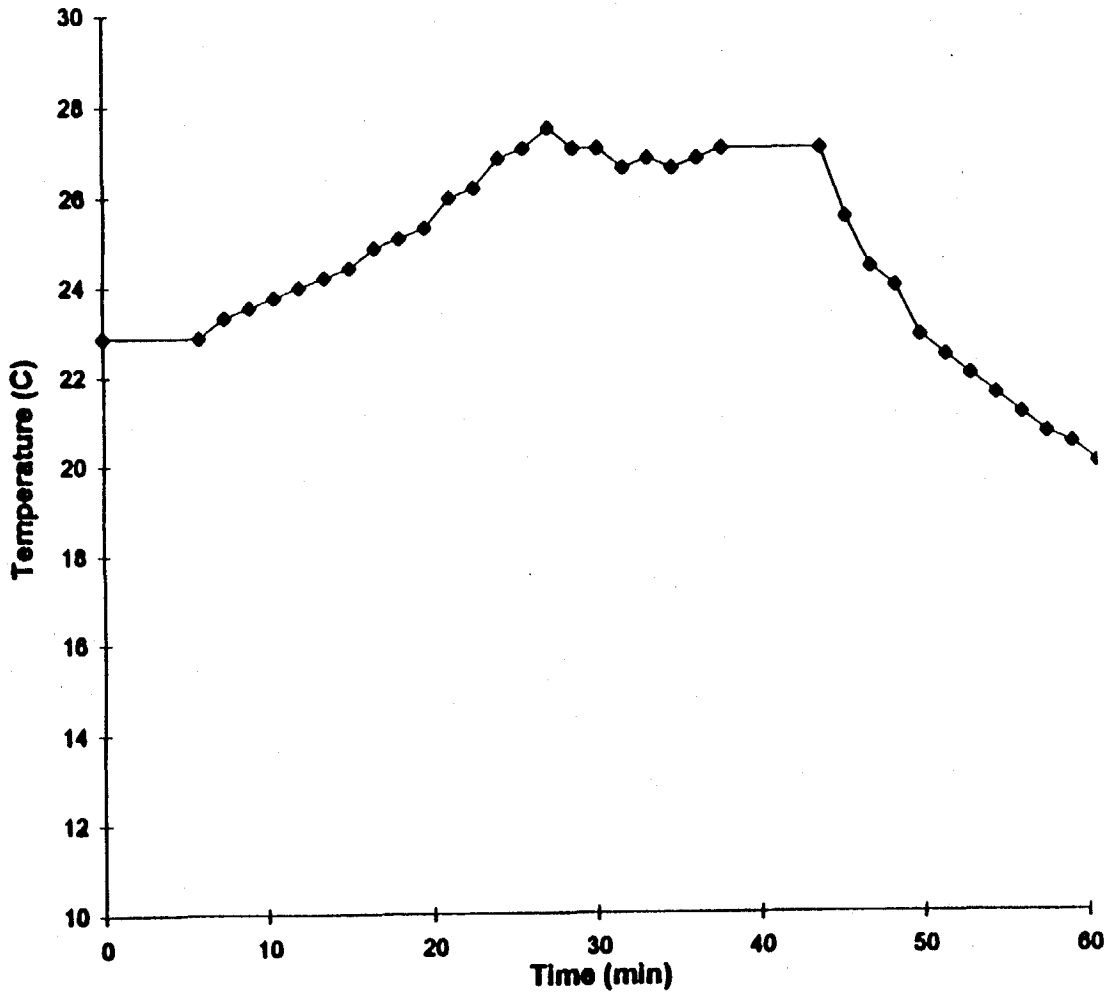

Figure 4.2.2 Cooling tower outlet temperature in MITR-II power ascension transient. During the power ascension transient, the cooling tower outlet temperature rises until the fans are turned on (data from [4]).

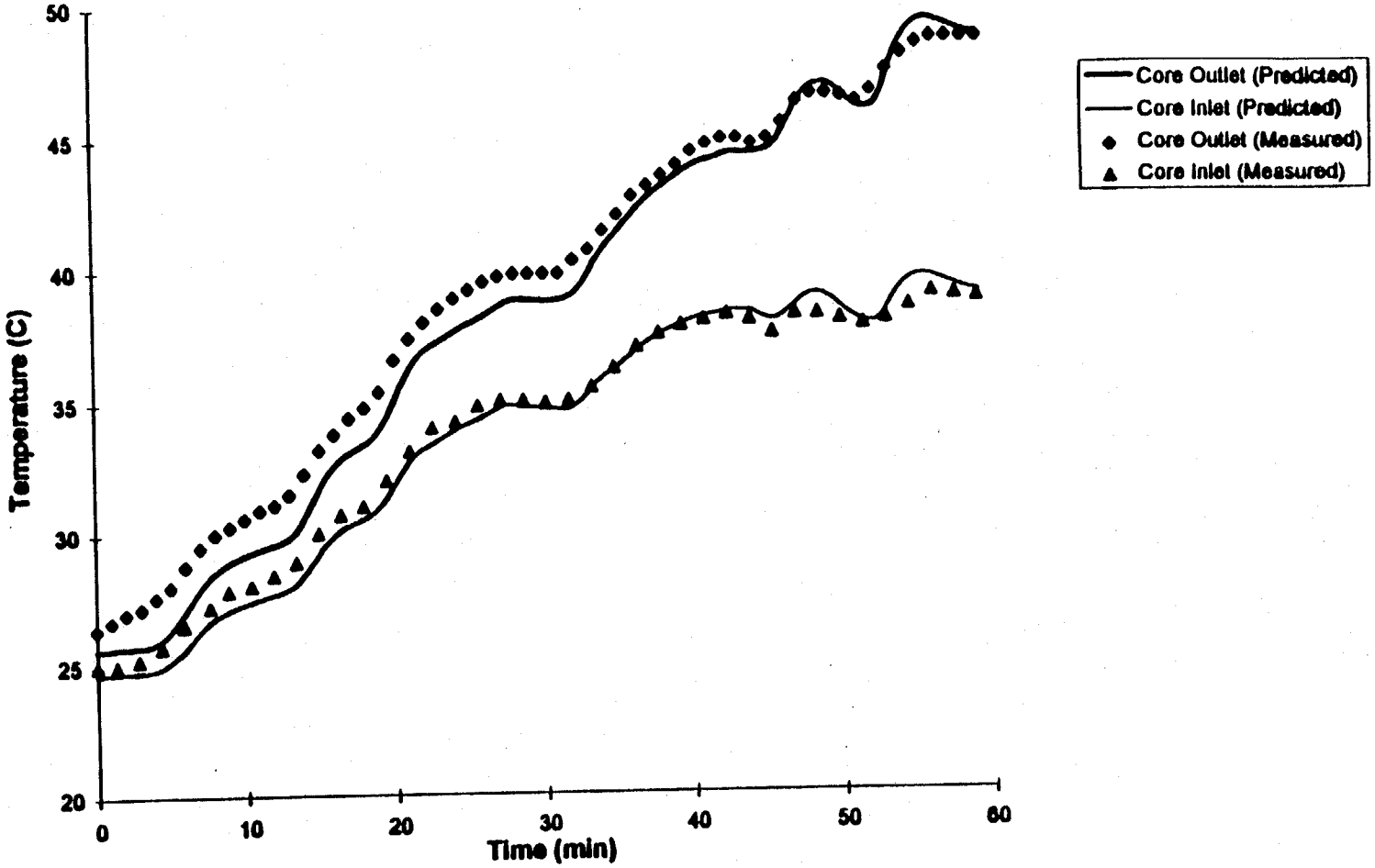

Figure 4.2.3 Core inlet and outlet temperatures in MITR-II power ascension transient. The temperatures predicted by the MITR Multi-Channel Analysis Code are compared to experimental measurements (measured data from [4]).

4.3 MITR-II Loss of Flow

The loss of primary flow in MITR-II has been studied in detail by Bamdad [27]. He took experimental data during a series of loss of flow transients (see Table 4.3.1). For each transient, the outlet temperatures from two or three fuel elements were measured every fifteen to thirty seconds. Figures 4.3.1 through 4.3.4 show comparisons between measured and predicted core mixed mean outlet temperatures.

Table 4.3.1. Experimental measurements of core temperatures during a loss of flow in MITR-II.

Figure Number	Steady State Power (MW)	Operating Time Prior To Transient (H:M)	Fuel Element
4.3.1	3.5	6:37	B-6
4.3.2	4.0	11:30	B-6
4.3.3	4.83	18:00	B-6
4.3.4	5.0	Not Available	Not Available

The experimental points shown in Figures 4.3.1 through 4.3.4 represent the values measured by the thermocouple in fuel element B-6. The other fuel elements that had thermocouples installed (C-13 and C-15) recorded lower temperatures during each transient. The predicted core outlet temperatures shown in Figures 4.3.1 through 4.3.4 are shown for both the hottest fuel element and the core mixed-mean outlet temperature. The hottest fuel element is the one with the maximum ratio of radial power shape factor to flow disparity factor,

$$\left.\frac{P_{Ri}}{D_{Fi}}\right|_{Max}$$

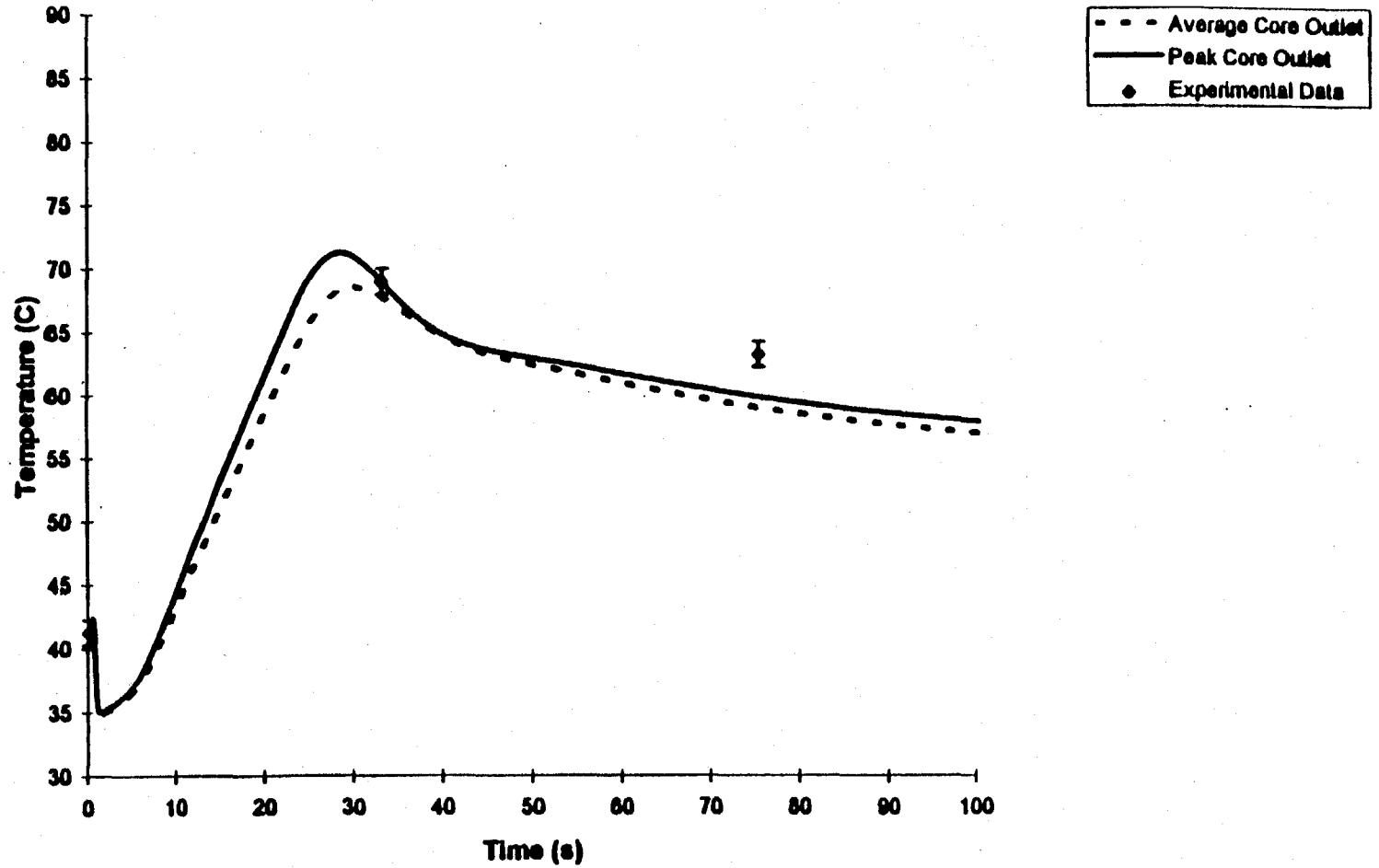

Figure 4.3.1 Core outlet temperatures in MITR-II flow coastdown at 3.5 MW.

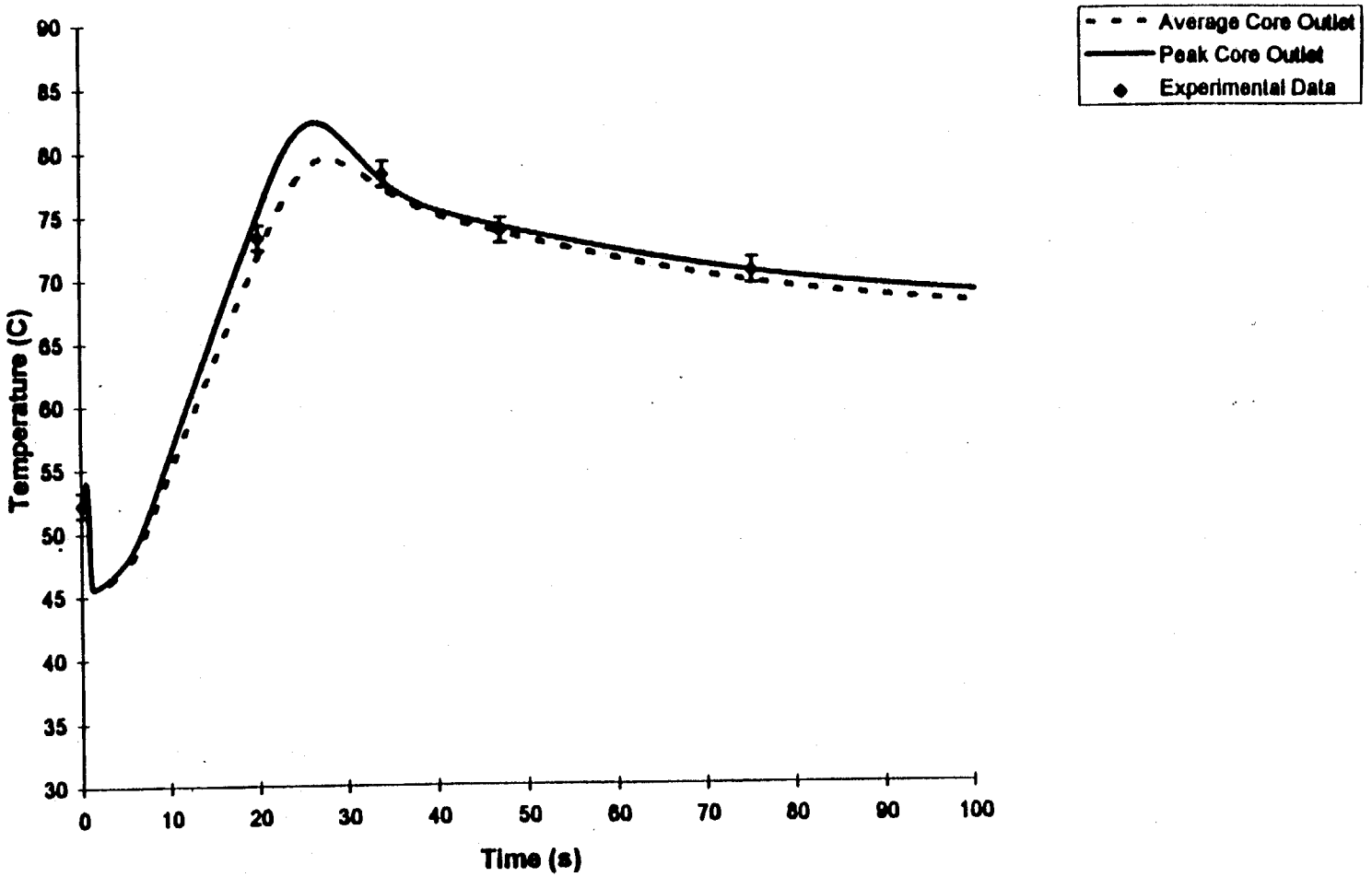

Figure 4.3.2 Core outlet temperatures in MITR-II flow coastdown at 4.0 MW.

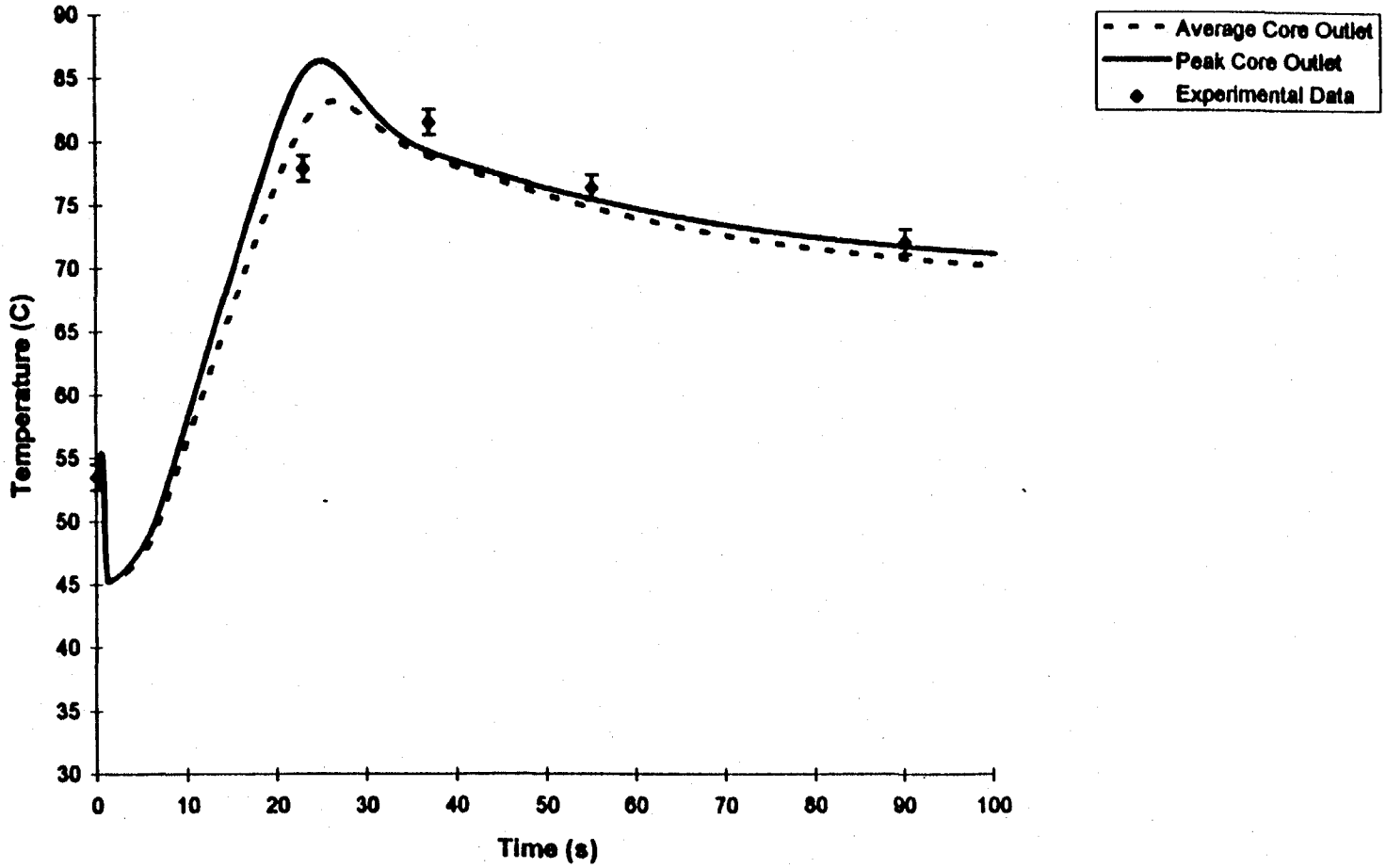

Figure 4.3.3 Core outlet temperatures in MITR-II flow coastdown at 4.83 MW.

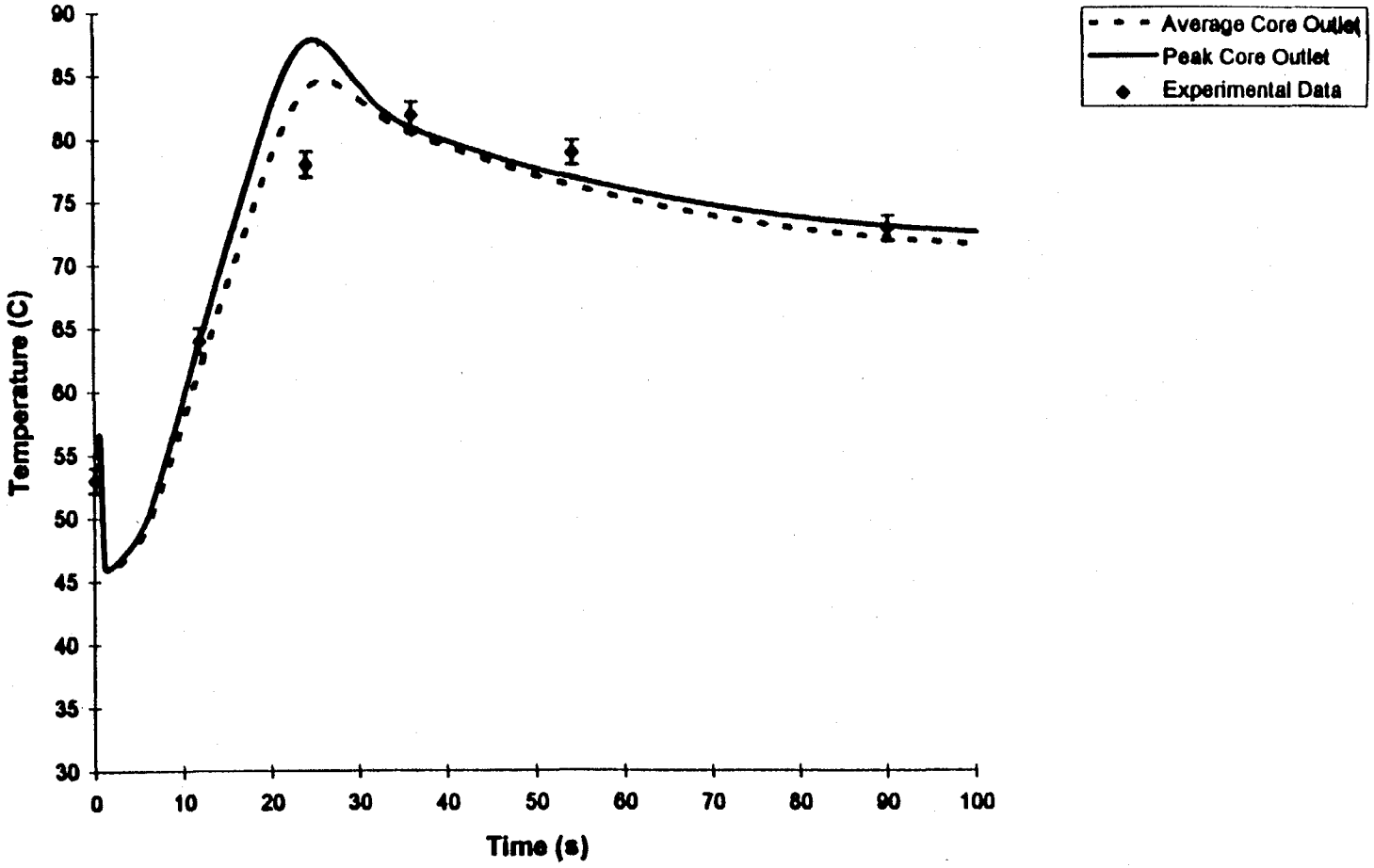

Figure 4.3.4 Core outlet temperatures in MITR-II flow coastdown at 5.0 MW.

and therefore the highest coolant outlet temperature. The mixed-mean outlet temperature is the mass-averaged core outlet temperature at each time step. It is expected that the measured temperature from fuel element B-6 would fall between the predicted average and peak temperatures (within experimental error). This behavior is shown well in Figure 4.3.2. In the other cases, however, the predicted values lie above and below the measured values. There are two sources for the difference between measured and predicted values of outlet temperature.

In the early phases of the transient, ($10 < t < 50$ seconds) a broad temperature peak is evident in both the measured and predicted values. The predicted power peak appears to be shifted to the left of the measured peak (i.e., it is predicted to occur sooner). This may be because conduction from the core to the downcomer was neglected in the calculations.

The longer-term temperatures reflect the decay heat generation rate in the core. The calculated decay heat generation rate is a function of the decay precursor concentrations, which are related to the operating history of the reactor prior to the experiments. The predicted temperatures were based on the assumption that the reactor had been operating infinitely at the power level used for each experiment. This is included in the MITR Multi-Channel Analysis Code by setting all initial decay precursors to their saturated values. In Bamdad's study of the effect of operation history on the decay heat generation rate, he concluded that three hours of operation was sufficient to simulate infinite operation. During the experiment represented in Figure 4.3.1, the reactor had been operating at 3.5 MW for only six and a half hours, while the other runs had operating histories of at least ten hours. Because the predicted long-term outlet temperatures are accurate for the runs with longer operating histories, the difference between the measured and predicted long-term outlet temperatures in Figure 4.3.1 are assumed to be due to the short operating history prior to the experiment.

Comparison of predicted values with Bamdad's data show that the MITR Multi-Channel Analysis code predicts core outlet temperatures that are with the range of thermocouple experimental error for cases when the reactor had been at power for ten hours or more. The predicted peak in the outlet temperature is higher than the observed temperature, and it is predicted to occur earlier than the experimental data indicates. Both of these inaccuracies in the calculated results are tolerable, and they lead to conservative conclusions.

The core outlet temperature during a loss of flow transient is a function of many parameters, and it is therefore a good indicator of the validity of several mathematical models used in the code. To understand what factors contribute to determining the core outlet temperature, Figures 4.3.5 through 4.3.8 show the predicted values of several core variables during the first 100 seconds following the loss of applied torque to the pumps.

The reactor is initially operating at a steady state power of 5 MW with a core inlet temperature of 44°C and a hot leg (average core exit temperature) of 54°C. The steady-state primary flow rate is 127 kg/s (2050 gpm). The analysis is performed for a 22 fuel element core with 5 dummy elements present. At t = 0, the applied toque to both primary pumps is cut off, simulating a loss of electrical power to the pumps. The forced mass flow rate immediately begins to drop exponentially as shown in Figure 4.3.7. The pump coastdown curve is based on the coastdown shape measured by Terry and Sardy [1,26]. When the flow rate drops below 112 kg/s (1800 gpm), a reactor trip signal is initiated due to low primary flow. The core outlet and maximum clad temperatures rise briefly as the flow rate drops while the core power stays at 5 MW.

Following an instrument delay time of 0.41 seconds, the control blades are released and begin to drop into the core. The reactor power, shown in 4.3.6, quickly drops as negative reactivity is inserted from the scram. The core outlet and peak clad temperatures show a significant drop in response to the reduced heat flux, as shown in Figure 4.3.5.

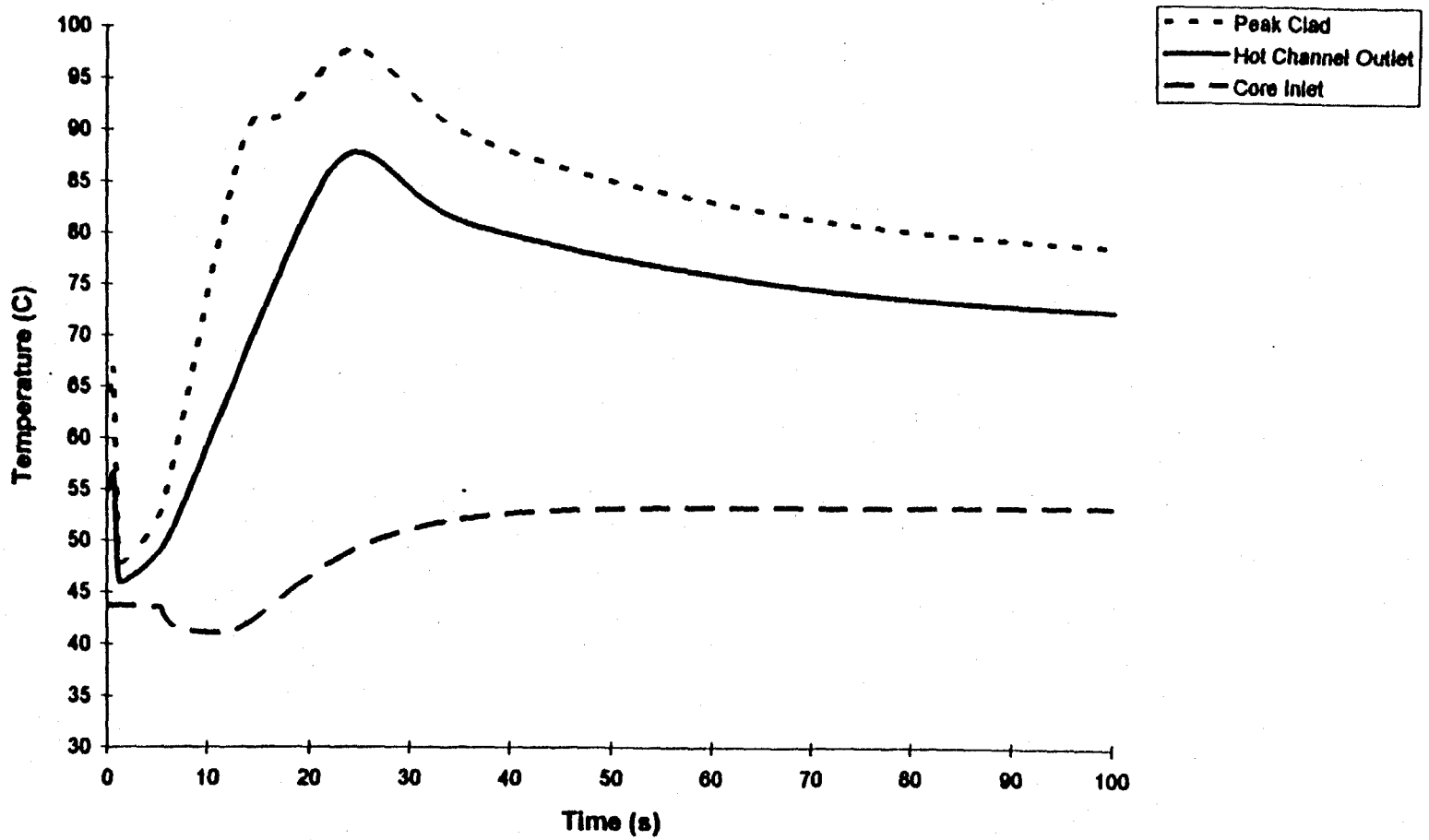

Figure 4.3.5 Temperature in MITR-II flow coastdown at 5 MW.

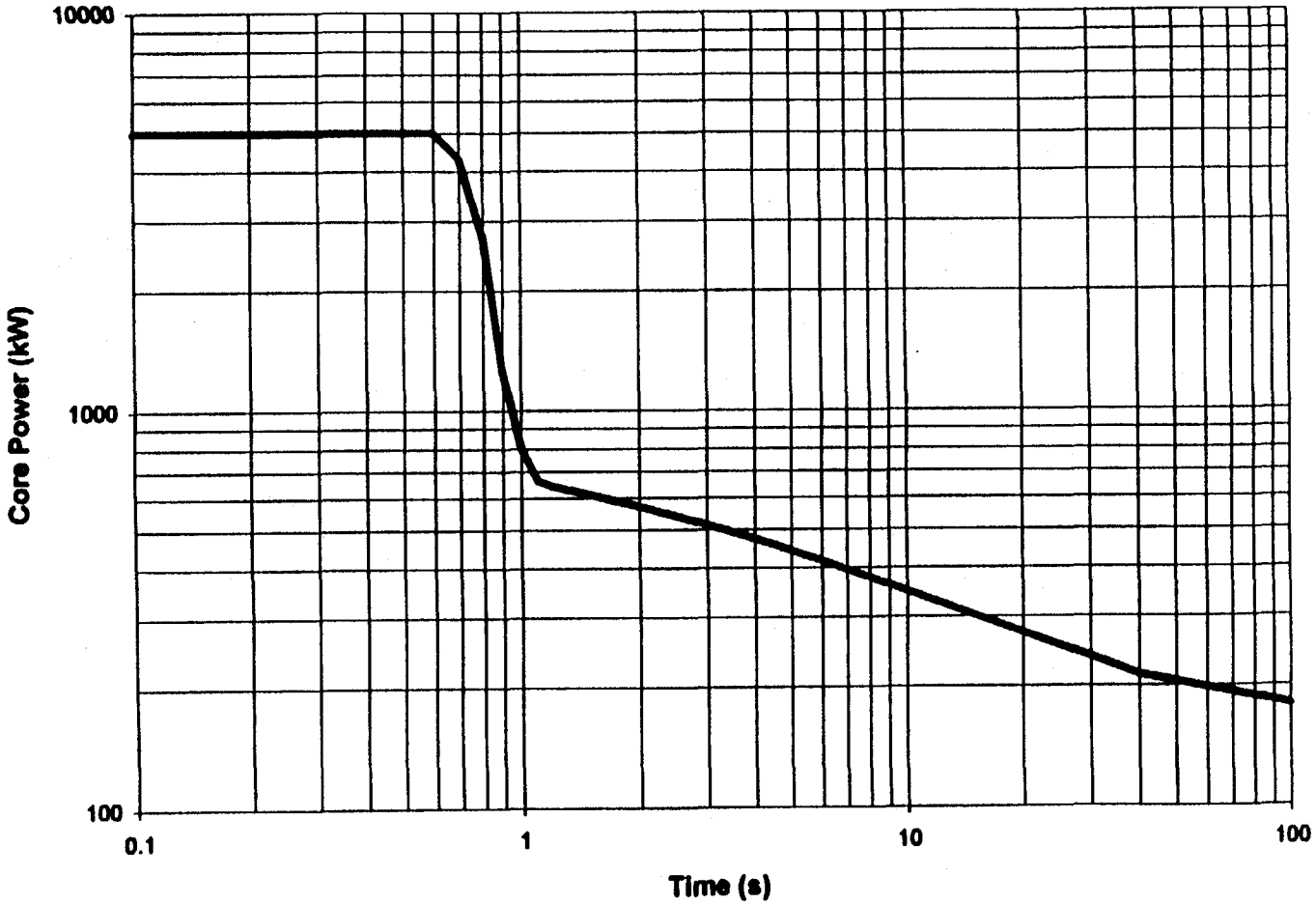

Figure 4.3.6 Core power in MITR-II flow coastdown at 5 MW.

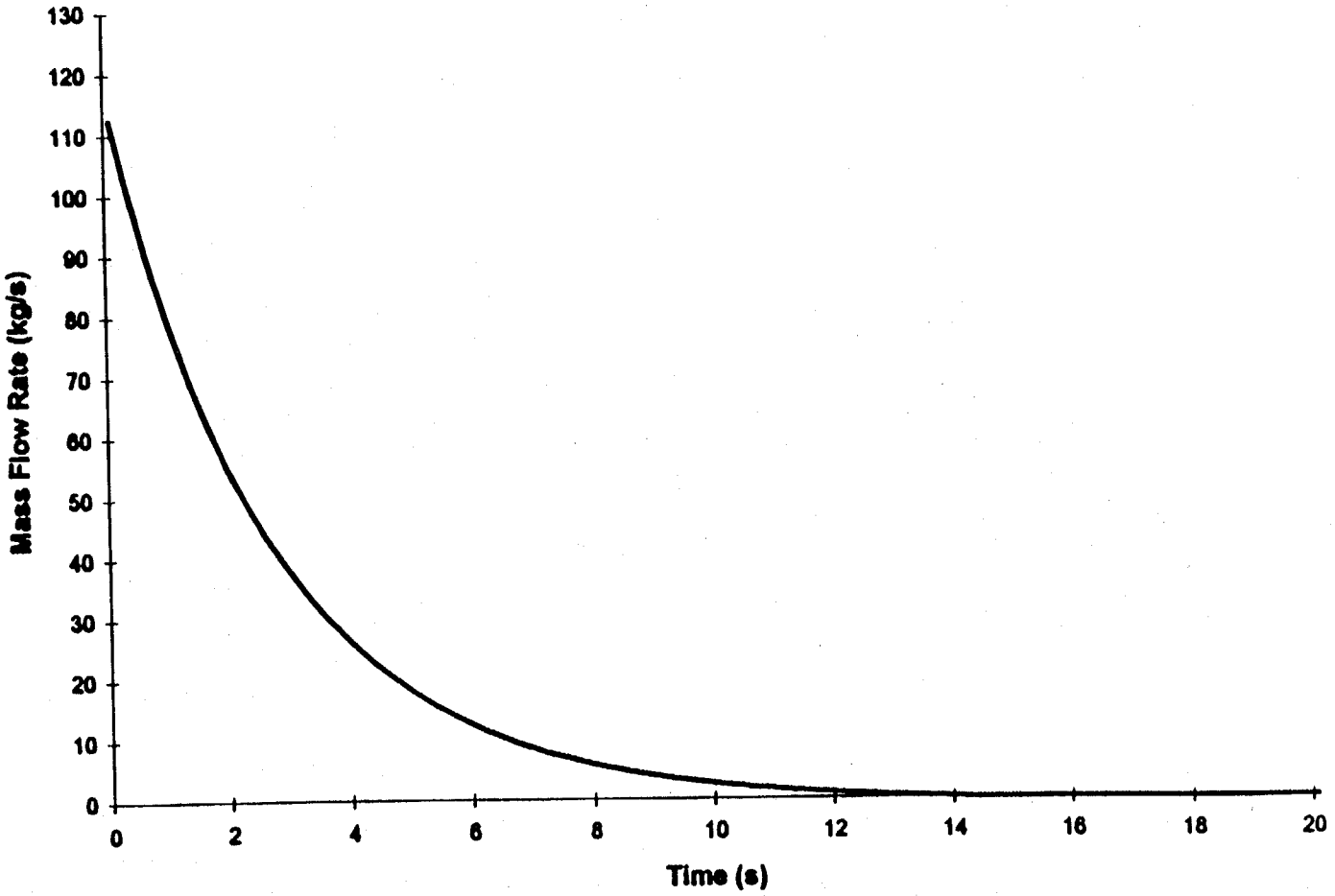

Figure 4.3.7 Forced flow rate in MITR-II flow coastdown at 5 MW. The pump coastdown curve is based on experimental measurements of the mass flow rate following a trip of both primary pumps [26].

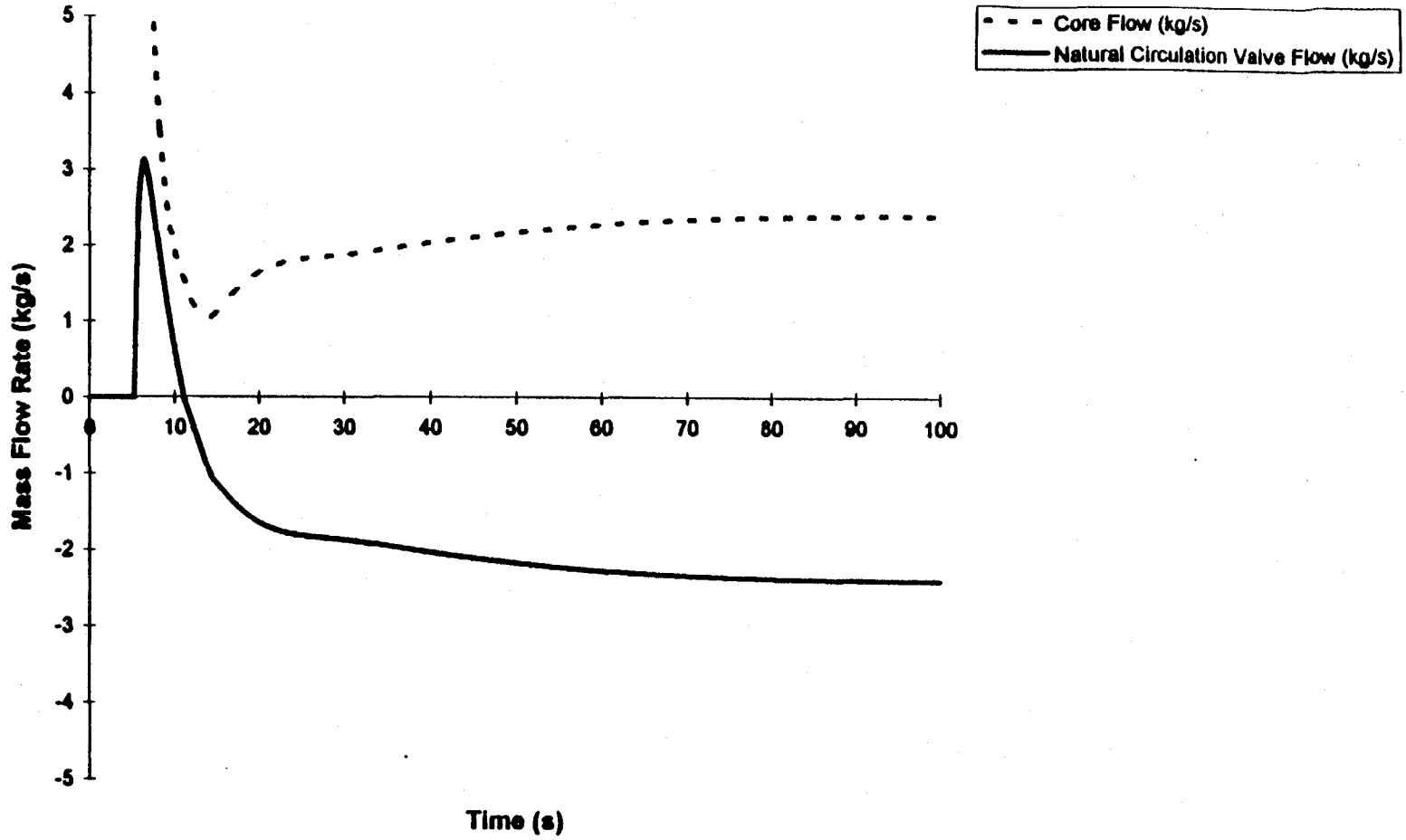

Figure 4.3.8 Core and bypass flow in MITR-II flow coastdown at 5 MW. A positive flow through the natural circulation valves indicates flow in the upwards direction (i.e., bypassing the core).

Heat continues to be added to the coolant as decay precursors deposit their decay energy in the fuel, clad, and coolant. At the same time, the coolant flow rate through the core continues to drop. When the flow rate is low enough, the natural circulation valves open and an alternate route for coolant to enter the core is created. Figure 4.3.8 shows the flow through the core and the bypass flow up through the natural circulation valves. When the valves first open, there is a rapid increase in bypass flow. Within several seconds, however, the pressure losses through the natural circulation valve and the pressure gradient across the valve have forced a flow reversal. The transition between forced flow and natural circulation (the mixed convection phase) leads to a minimum in core flow rate, and a corresponding local maximum in the peak clad temperature.

Following the minimum in core flow, the natural circulation loop becomes well established. When the forced flow from the pumps reaches zero, the core is essentially isolated from the rest of the loop. The coolant surrounding the flow shroud passes down through the natural circulation valves and becomes the source of the core inlet stream. The increased core flow from natural circulation and the continuous drop in decay heat cause the core temperatures to begin to drop 22 seconds into the transient.

In the long term, the decay heat continues to decay exponentially. Because the decay heat provides the driving force for the natural circulation loop, the natural circulation flow rate will begin to decrease.

If no action is taken to restore flow in the core, boiling is predicted to occur approximately 58 minutes following the pump trip [27]. This prediction ignores the possibility of heat transfer to the D_2O reflector or to other potential heat sinks. The margin of nearly one hour allows plenty of time to restore forced flow using backup power supplies (batteries) or alternate methods to restore some forced circulation.

Although there are no reliable ways to measure the flow of coolant through the natural circulation valves during a loss of primary flow at 5 MW, the core outlet temperature responds quickly to changes core flow. Accurate prediction of the core outlet temperature then implies that the correct primary flow rate is being used in the core energy balance calculations.

The flow coastdown experiments analyzed here do not provide any data to validate the two-phase flow models used in the MITR Multi-Channel Analysis Code. Such experiments are not permitted to be done on MITR-II for obvious safety reasons. Therefore, two-phase experiments performed under conditions similar to those found in the MITR must be relied upon to validate the void fraction model.

4.4 *Void Fraction Model Validation*

The void fraction model developed for the MITR Multi-Channel Analysis Code is used to predict the amount of vapor present in MITR channels during subcooled and bulk boiling between ONB and CHF.

As described in Section 3.5, the flow quality is related to the equilibrium quality based on calculated transitions between boiling regimes. The void fraction is then related to the flow quality by the drift flux model. The parameters of the drift flux model are modified based on the flow regime.

An acceptable void fraction model then requires the following predictions to be accurate:

1) The wall superheat required for nucleation [found from Equation (68)].
2) The coolant subcooling at the onset of significant voids [Equation (74)].
3) The void fraction at bubble departure [Equation (75)].
4) The flow quality at the annular flow transition [Equation (64)].

Under conditions similar to the MITR channels (including the presence of fins), Equation (68) was found to give wall superheats within +/- 7% of the experimentally observed values [14]. Another study that closely matched the conditions in an MITR channel (except the presence of the fins) found that superheats predicted by Equation (68) are within 1°C of observed values [32].

The correlation used to predict OSV was derived from Kowalski's studies of flow through finned, rectangular channels. His correlation, shown here as Equation (73), is found to match experimental results to within +/- 8%.

The void fraction at bubble departure and the flow quality at the annular flow transition are more difficult to measure experimentally. However, these predictions can be verified by examining the void fraction profile found by experiment.

Firstenberg and Neal measured the subcooled void fraction in a rectangular test section at atmospheric pressure (as reported in [33]). The conditions of the experiment are shown in Table 4.4.1.

Table 4.4.1. Conditions of Firstenberg and Neal void fraction measurements (reported in [33]).

Experimental Parameter	**Value**
Fluid	Water
Pressure (Pa)	1.013×10^5 (1 atm)
Channel Cross-Section (mm x mm)	21.1 x 2.95
Channel Heated Length (mm)	625.0
Mass Flux (kg/m^2s)	451.0
Heat Flux (W/m^2)	2.65×10^4
Inlet Subcooling (°C)	3.3

The results of this experiment are presented in Figure 4.4.1, along with several common void fraction models. All of the void fraction models are based on a flow quality profile that is found as described in Section 3.5 of this report. This common basis allows the relationships between the void fraction and the flow quality to be compared for each model.

The Homogeneous Equilibrium Model (HEM) overpredicts the void fraction along the entire range of equilibrium qualities found in the test section. The HEM model is generally applicable only when the flow is near thermal and mechanical equilibrium (high pressure, high mass flux, or high flow quality). Details of the HEM model are found in Reference [9].

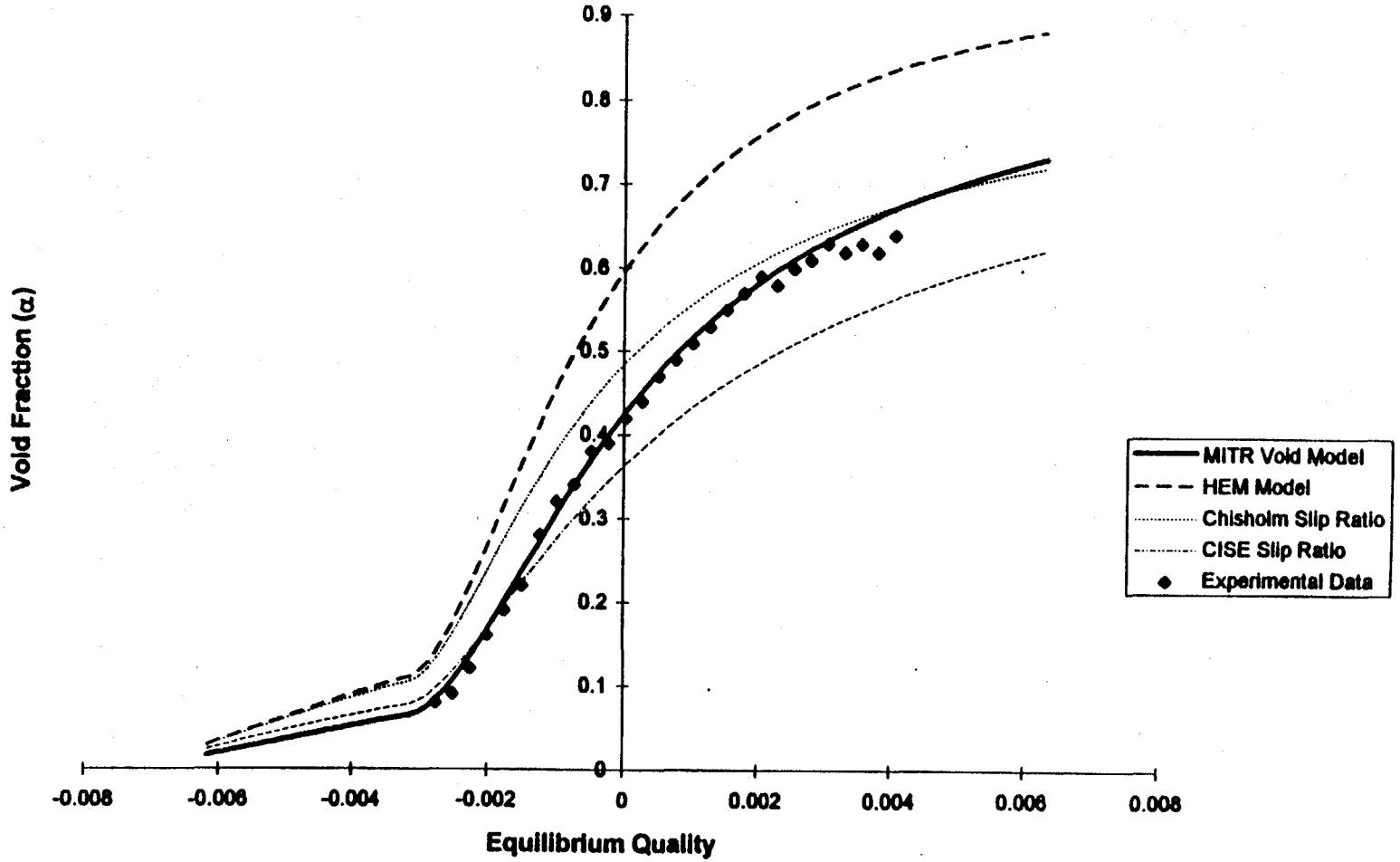

Figure 4.4.1 Comparison of MITR void fraction model with experiment. The MITR void fraction model is compared to void fraction predictions by other models, and to experimental data (data from [33]).

The CISE correlation is a complex empirical relation for the slip ratio in two-phase flow. It is widely applicable and considered to be among the most accurate separated flow models [34]. It underpredicted the void fraction for the test results shown in Figure 4.4.1.

The Chisholm correlation is a theoretical, and relatively simple, relation for the slip ratio in a separated flow model. Unlike the CISE correlation, the Chisholm slip ratio has no dependence on the mass flux. This fact makes it undesirable for use in analyzing loss of flow transients and flow excursions in the MITR. It does, however, predict the void fraction in the test section quite accurately. The MITR model maintains a dependence upon mass flux through a drift flux relation, and is therefore capable of predicting the void fraction during flow rate transients.

The MITR model gives the closest fit to the experimental data. The calculated point of OSV, visible as a slope change in the void fraction curve in Figure 4.4.1, appears to coincide well with the data. However, there are not enough experimental points in the highly subcooled boiling region to make any definitive conclusions. The MITR void fraction relation appears to deviate from the measured data at void fractions above 65%. This could be the result of one or more of the following:

1) A transition to annular flow sooner than predicted by Equation (64).

2) Over-prediction of the flow quality at high qualities. This could be the result of the presence of superheated vapor and subcooled liquid in the bulk boiling region. This type of thermal non-equilibrium is not included in the MITR void fraction model.

3) Reduced accuracy in void fraction measurements at higher void fractions. The data indicates a greater scatter at higher void fractions.

The MITR void fraction model accurately predicts the void fraction under conditions similar to those found in the MITR coolant channels. Any deviations from measured void fractions appear only at high void fractions. Moreover, these errors predict higher void fractions, and are therefore conservative.

The void fraction model determines the flow quality and the void fraction in each node at each time step. This information is used in the two-phase momentum and energy models to predict the two-phase multiplier and heat transfer coefficient in each node. Therefore, any error in the void fraction model is propagated into the momentum and energy models. Studies of various two-phase multipliers show relative errors between predicted and observed results of 20% for the HEM model and 32% for the Martinelli-Nelson model [35]. However, these errors are for data covering a wide range of conditions (all at pressures above 1.7×10^6 Pa). Additionally, the method used to determine the flow quality is not stated. As described above, an inaccurate prediction of flow quality can lead to a large discrepancy in the value of the two-phase friction multiplier. The errors reported in Reference [35] are greatly reduced by minimizing the error in flow quality calculations, and by using the two-phase multiplier correlations only under the conditions where they are most reliable.

Similarly, the Chen correlation used in the two-phase heat transfer model has a mean error of 11% [9]. This error includes errors introduced in determining both the flow quality and the void fraction.

The reliability of the two-phase momentum model can be evaluated by comparing the predicted occurrence of flow excursions to experimental values.

4.5 *Analysis of Flow Instability Predictions*

The MITR is susceptible to the form of static instability known as flow excursion (or Ledinegg) instability. Flow excursion instability is a static instability because there is a range of mass fluxes where steady state operation is not possible. If the system is perturbed into this unstable region, the flow rate undergoes a rapid excursion to a new steady state value that may be far from the original operating point. In low-pressure systems the new flow rate is likely to lead directly to critical heat flux.

Flow excursion instability is best explained by examining a plot of pressure drop versus mass flow rate, as shown in Figure 4.5.1. Each point on the S-shaped curve in Figure 4.5.1 represents a steady state point. The S-shaped curve represents the internal characteristic of the channel. The pressure drop at each point can be found by summing the appropriate pressure loss terms given in Equations 4-7 (or Equations 4a-7a, for the two-phase portions of the curve). The external characteristic is also shown in Figure 4.5.1. The external characteristic is determined by the pump head curve for the pump that is driving flow through the channel. The external characteristic shown in the figure is equal to a constant ΔP for all values of mass flow rate. This represents the situation where many parallel channels share a common inlet and outlet header (and therefore experience the same pressure drop) [36]. The intersection of the internal and external characteristics gives the possible operating points of the system. In Figure 4.5.1, the external curve is tangent to the internal curve at Point A. Thus, Point A is the only possible operating point for this system. At Point A the slope of the external curve is equal to the slope of the internal curve.

The same internal characteristic is shown in Figure 4.5.2. The external characteristic line in Figure 4.5.2 intersects the internal curve at three points (Point B, Point C, and Point D). If the system is initially operating at Point B, and the flow is perturbed, the system will restabilize itself at Point B. For example, if the mass flow rate is increased from Point B, the pressure loss will also increase. The higher pressure loss will result in less flow into that channel until the mass flow rate corresponding to Point B is reached. A similar situation exists at Point D, where the flow is nearly all vapor. Although Point D represents a mathematically stable operating point, it is likely that this point would be beyond the conditions for CHF, and excessive clad temperatures would result.

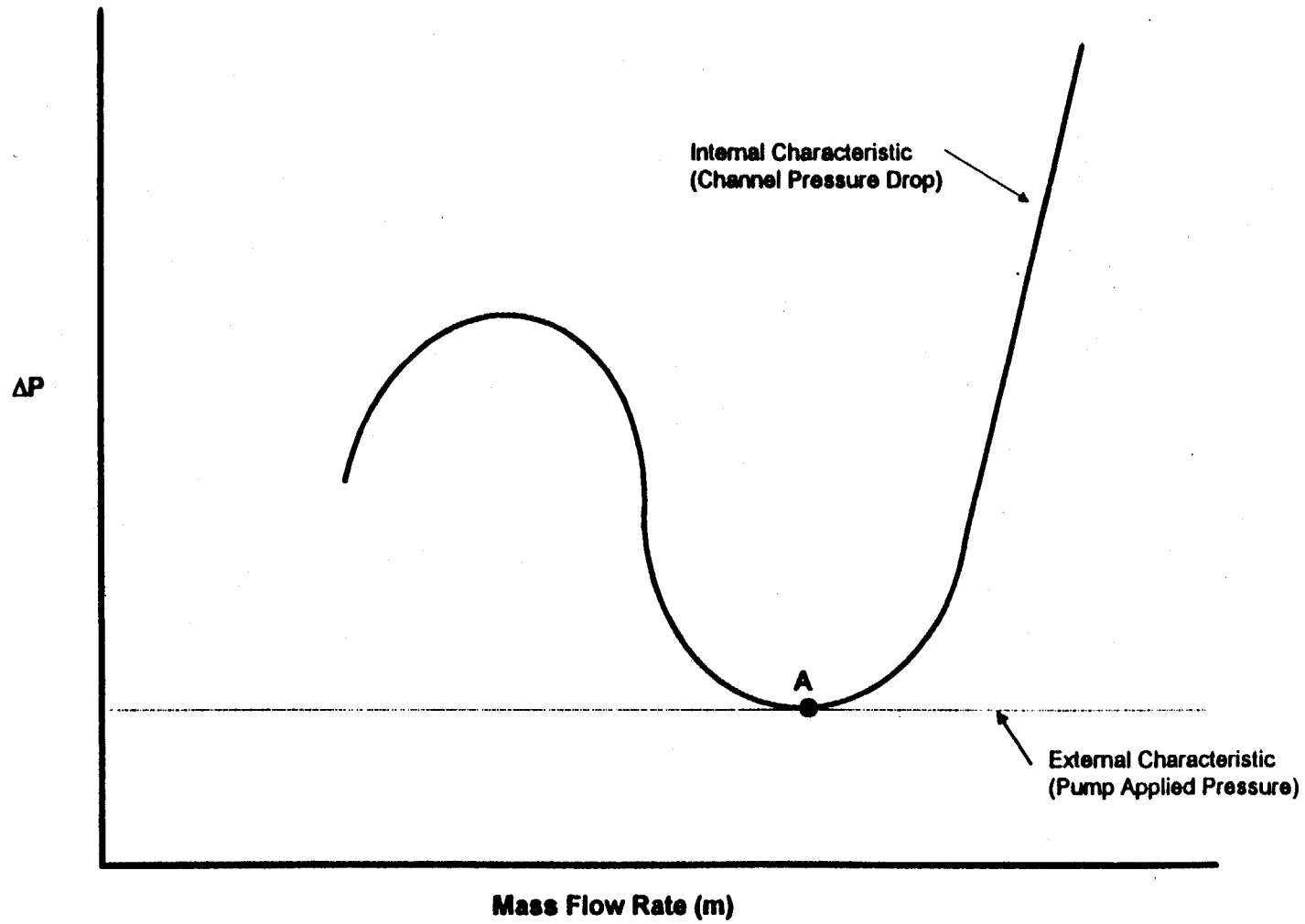

Figure 4.5.1 Condition required for the onset of flow instability. A flow instability is expected to occur when the slope of the external characteristic exceeds the slope of the internal characteristic.

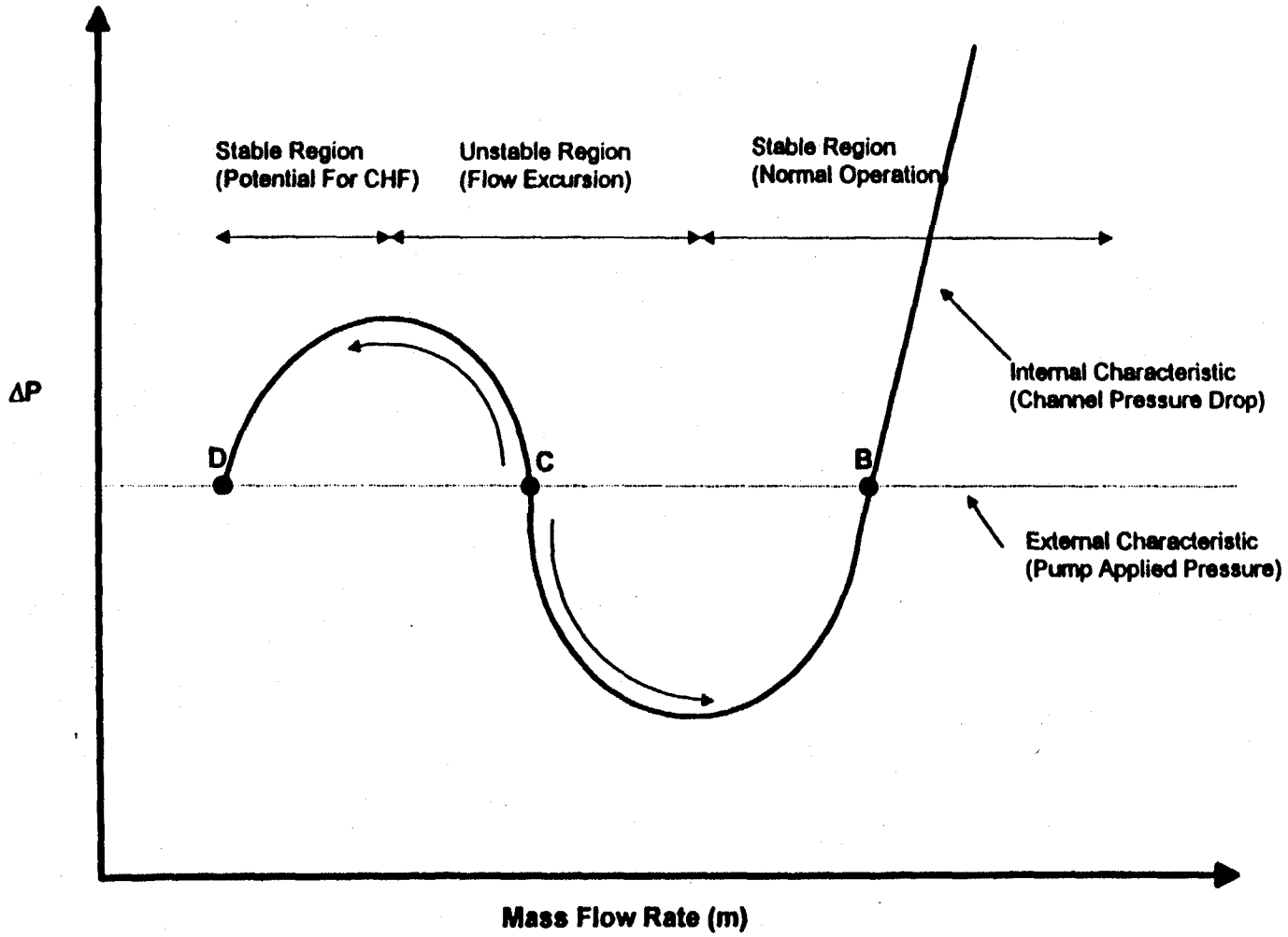

Figure 4.5.2 Stable operating regions. The stable region with a high flow rate is the only acceptable, steady-state operating region.

The situation is very different at Point C. Point C is an unstable operating point where steady state operation is not possible in multi-channel systems (without the use of special techniques such as inlet throttling). If a system was artificially placed at Point C and subjected to a perturbation in flow, a flow excursion would occur. An increase in mass flow rate from Point C would lead to a lower drop across the channel. The lower pressure drop would cause the flow rate to rise again in order to keep the pressure drop equal in all of the parallel channels. This excursive behavior would continue until stable operation was achieved at Point B. A decrease in mass flow rate from Point C would lead to an excursion to Point D.

The general criterion for stability is that the slope of the internal characteristic must be greater than the slope of the external characteristic [37],

$$\left.\frac{\partial \Delta P}{\partial m}\right|_{Internal} > \left.\frac{\partial \Delta P}{\partial m}\right|_{External} \tag{129}$$

For systems of many parallel channels, where the slope of the external characteristic is zero, the stability criterion reduces to,

$$\text{If} \quad \left.\frac{\partial \Delta P}{\partial m}\right|_{Internal} > 0 \quad \text{then the operating point is stable.} \tag{130}$$

The task of predicting when a flow excursion will occur is now reduced to finding the value of mass flow rate that gives the minimum in the internal characteristic. This is the approach that has been taken in most flow instability studies. The minimum in the channel characteristic is given by the value of mass flow rate where,

$$\frac{\partial\left(F_{f,i} + F_{g,i} + F_{a,i} + F_{k,i}\right)}{\partial m_i} = 0 \tag{131}$$

where, m_i = Mass flow rate in channel i (kg/s),

$F_{f,i}$ = Friction pressure drop in channel i (Pa),

$F_{g,i}$ = Gravity pressure drop in channel i (Pa),

$F_{a,i}$ = Spatial acceleration pressure drop in channel i (Pa),

$F_{k,i}$ = Form pressure drop in channel i (Pa).

Each component of pressure loss is given by the sum of the contribution from each axial node, as given in Equations (4a-7a). Because Equation (131) is difficult to solve, the minimum in the internal characteristic is often found by running a series of steady state experiments to construct the ΔP versus m curve for a particular channel. The minimum in this internal characteristic is the onset of flow instability (OFI). The point of OFI is expressed as a ratio of the temperature rise in the channel to the inlet subcooling,

$$R = \frac{T_{out} - T_{in}}{T_{sat} - T_{in}} \tag{132}$$

where, T_{out} = Channel exit temperature at OFI (°C),

T_{in} = Channel inlet temperature (°C),

T_{sat} = Saturation temperature at channel exit (°C).

For a low pressure system, upper and lower bounds can be placed on the exit temperature at OFI. The system conditions must be such that some vapor is present (i.e., ONB must have occurred). Without any vapor present, the pressure drop would not rise as the flow rate is decreased. Also, the outlet temperature will usually be less than saturation. Several authors have proposed that OFI in low pressure systems coincides with the onset of significant voids (OSV) [38,39]. The OFI ratio, R, can be expressed in terms of a parameter that represents the conditions necessary for OSV,

$$R = \frac{1}{1 + \eta \frac{D_E}{L_H}} \tag{133}$$

with,

$$\eta = \frac{\rho c_p V_c (T_{sat} - T_{out})}{4q''} \tag{134}$$

where, η = Constant representing OSV,

D_E = Equivalent heated diameter (m),

L_H = Heated length (m),

q'' = Average heat flux (W/m^2),

V_c = Coolant velocity at OSV (m/s).

The minimum in the internal characteristic can be estimated by one of several approaches,

1) Determine the value of η by experiment,

2) Find R by experiment,

3) Predict the location of OSV (assuming that this is where the minimum in the internal characteristic lies for a low pressure system),

4) Plot the internal characteristic and locate the minimum.

The following empirical relations for the onset of flow instability are available in the literature,

$$\eta = 25 \qquad [39] \tag{135}$$

$$R = 0.21 \ln\left(\frac{L_H}{D_E}\right) - 0.258 \qquad 70 < L_H/D_E < 250 \text{ ([40] as reported in [3])} \tag{136}$$

$$R = 0.697 + 0.00063\left(\frac{L_H}{D_E}\right) \qquad 100 < L_H/D_E < 200 \text{ [39]} \tag{137}$$

In the above equations, the equivalent heated diameter is based on the full heated perimeter of the fuel channel, including the fins. Experimental studies have shown that the flat plate approximation is not valid for predicting the onset of flow instability [3,41]. The correlations are determined from experiments conducted on thin, rectangular channels with a uniform axial heat flux profile.

In addition to the empirical correlations for η and R, the OSV correlation given in Equation (71) can be used to give a transcendental equation for the mass flow rate at which OSV occurs for a given rate of heat addition,

$$\frac{Q}{m_{osv}c_p\left(T_{sat} - T_{in} - \frac{Q}{m_{osv}c_p}\right)} = .0446\left(\frac{P_H L_H k_l}{m_{osv}c_p D_E}\right)^{0.18} \tag{138}$$

where, Q = Rate of heat addition to coolant (W),

m_{osv} = Mass flow rate in channel at OSV (kg/s),

P_H = Channel heated perimeter (m),

k_l = Coolant conductivity (W/mK).

Equation (132) can be used to express the mass flow rate in the channel at which OFI is predicted to occur for a value of R calculated by the above relations,

$$m_{OFI} = \frac{Q}{Rc_p(T_{sat} - T_{in})} \tag{139}$$

In the MITR Multi-Channel Analysis code, the mass flow rate at OFI is not specifically identified by any of the methods above. The core momentum equations outlined in Section 3.3 are solved at each time step. If one channel contains enough vapor to cause its pressure loss to be greater than the others, the momentum balance will require that this channel receives less flow than the others. This is unstable operation and the flow rate in the channel will quickly move to a new (lower) steady state value.

The MITR Multi-Channel Analysis code can be modified to determine the pressure drop in a single MITR channel at several steady-state flow rates in order to identify the minimum in the internal characteristic. Figure 4.5.3 shows portions of five internal characteristics for five different power levels. The inlet temperature for each case is 50°C. For the three highest powers (Q = 454 kW, Q = 227 kW, and Q = 113.5 kW), the minima are clearly visible. For the Q = 56.75 case, there is a drop in the characteristic caused by the reduced gravity head at the onset of subcooled boiling. When the void fraction is high enough (during saturated boiling), the acceleration and friction terms dominate, and the curve begins to rise again.

The mass flow rates at which OFI is predicted to occur by Equations (135), (136), (137), (138) for each power level are given in Table 3.5.1. Also shown in Table 4.5.1 is the mass flow rate at which OFI was observed to occur in the characteristic curve generated by the MITR Multi-Channel Analysis Code.

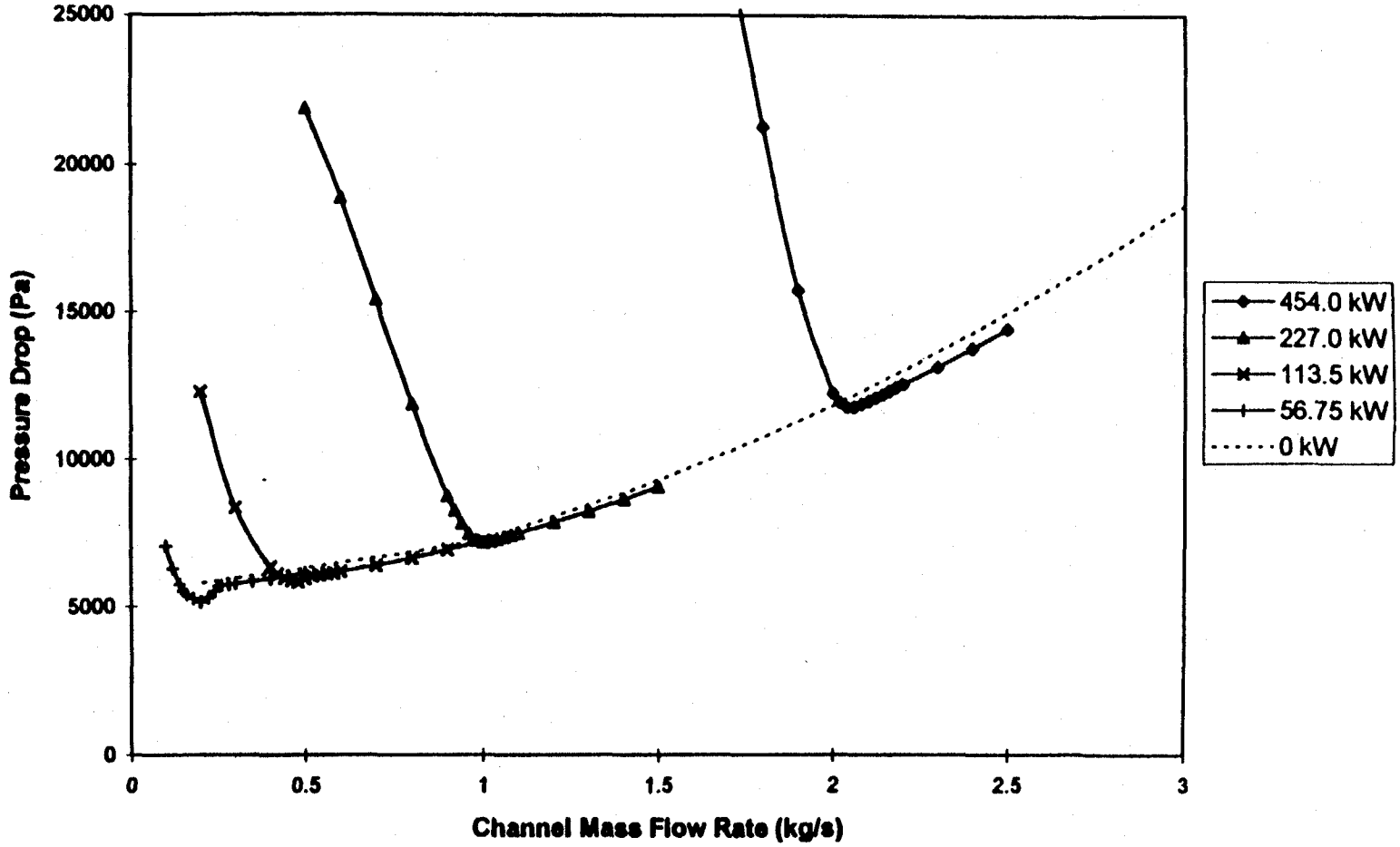

Figure 4.5.3 Onset of flow instability in MITR channels. The minima in the curves represents the point where a flow instability is predicted to begin. The curves are calculated with the MITR Multi-Channel Analysis Code.

Table 4.5.1. Mass flow rate at OFI in MITR channel (kg/s).

Power Level (W)	Equation (135)	Equation (136)	Equation (137)	Equation (138)*	MITR Code
4.54×10^5	2.08	2.09	2.21	2.13	2.05
2.27×10^5	1.04	1.05	1.11	1.05	0.98
1.13×10^5	0.52	0.52	0.55	0.52	0.47
5.68×10^4	0.26	0.26	0.28	0.26	0.18

* Equation (137) is only valid up to L/D ratios of 200. The L/D ratio of an MITR channel is 253.

The empirical relations for OFI used in Table 4.5.1 are functions of the hydraulic diameter of the channel. None of the correlations are based on experiments on finned channels similar to the MITR channels.

A uniform axial heat flux shape was used to generate the curves in Figure 4.5.3. Experimental evidence suggests that the axial flux shape affects the point of flow instability [42]. In these experiments, a cosine-shaped flux distribution was found to give an 11% higher R value than a uniform distribution with the same total power. Additionally, exit-peaked and double-peaked distributions showed larger R values than the uniform shape.

Using the MITR Multi-Channel Analysis Code, three different axial flux shapes were analyzed. The three shapes were: uniform profile, cosine-shaped profile, and a characteristic MITR profile (see Figure 4.5.4). The total power for all three cases was 454 kW, and the inlet temperature was 50°C. Table 4.5.2 shows that the computer simulation results show the same trends as the experimental evidence.

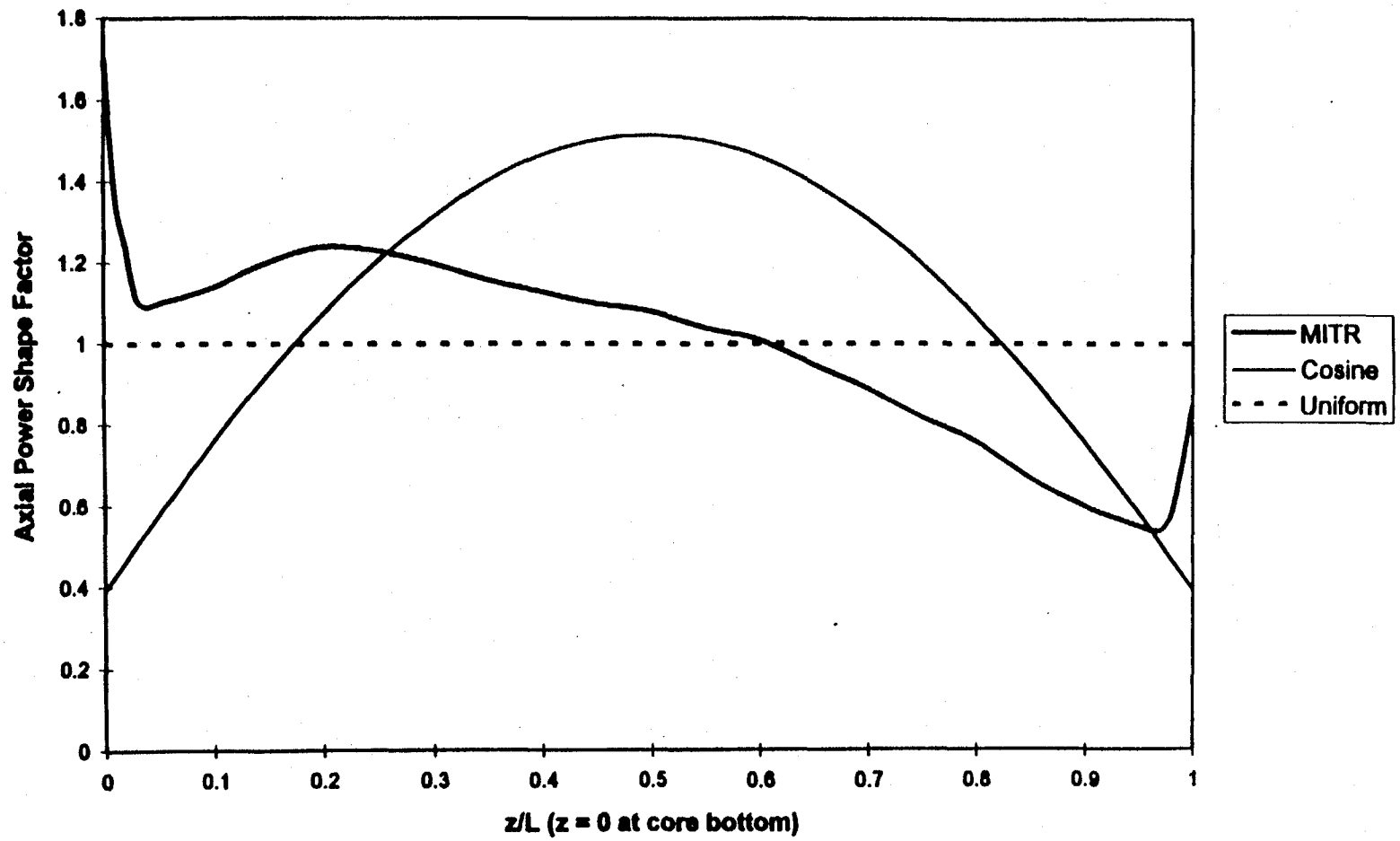

Figure 4.5.4 Three axial flux shapes used to predict the onset of flow instability.

Table 4.5.2 Effect of flux shape on OFI in MITR channels.

Flux Shape	Flow Rate at OFI (kg/s)	R
Uniform Shape	2.05	0.923
MITR Shape	1.96	0.965
Cosine Shape	1.92	0.985

4.6 Summary

The MITR Multi-Channel Analysis Code has been benchmarked by comparison with experimental data from MITR-II. Because the experimental data is limited to single-phase transients, it is necessary to use out-of-core results to validate the void fraction and flow excursion predictions of the code.

The MITR Multi-Channel Analysis Code accurately reproduces experimental results from MITR transients including slow power increases at startup, and loss of primary flow transients. The two-phase flow model matches vapor fraction measurements taken under conditions similar to those found in MITR channels.

The code has been used to predict the onset of flow instability in MITR channels at various heat fluxes, and with several axial power shapes.

5. Calculation of Limiting Safety System Settings and Safety Limits

5.1 MITR Limit Diagram

Figure 5.1.1 shows an MITR Limit Diagram for a primary mass flow rate of 127 kg/s (2050 gpm). This configuration represents MITR-II with its current heat removal system. The core power is shown on the y-axis, and the hot leg outlet temperature is shown on the x-axis. Because this is a two-dimensional presentation of a three-dimensional state-space, the mass flow rate is not shown. The mass flow rate boundary of the steady-state operating envelope is shown below the figure.

As described in Chapter 2, the LSSS and Safety Limits are artificial reactor trip points that are necessary to avoid reaching the limit criteria. The limits are based on a series of transients initiated from within an acceptable, steady-state operating envelope. In Figure 5.1.1, the operating envelope is enclosed by thick lines. If a proposed operating point can be plotted within this operating envelope, then the limits shown on the diagram will be applicable. For a steady-state operating point that lies outside this envelope, it is not possible to set LSSS that will prevent nucleate boiling in severe transients.

The set of nine parallel, diagonal lines represent a range of cooling tower outlet temperatures. The top line, representing 0°C (32°F), is the lowest cooling tower outlet temperature included in this study. Because the cooling tower basin must be kept above freezing, this lower limit is not expected to be exceeded. Based on the cooling tower characteristics, this outlet temperature may be 5 - 15 degrees above the ambient wet-bulb temperature. The constant outlet temperature lines are shown in 5°C increments. The bottom line represents a cooling tower outlet temperature of 40°C (104°F). This is above the maximum expected cooling outlet temperature.

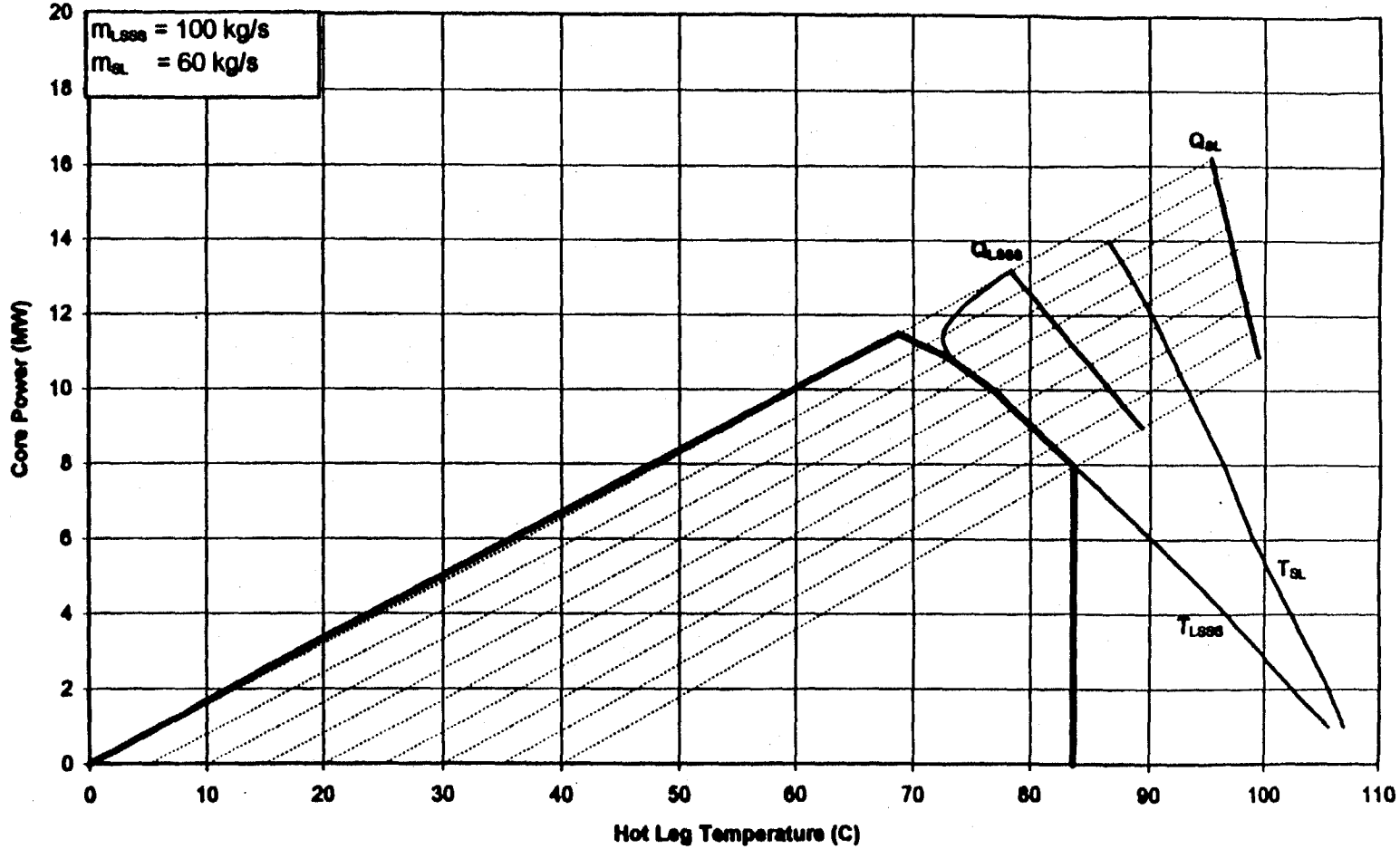

Figure 5.1.1 MITR Limit Diagram for a primary flow rate of 127 kg/s (2050 gpm). The secondary flow rate is 103 kg/s (1660 gpm). This represents the MITR-II in its current configuration. The parameters used to generate the limit diagram are given in Appendix D.

In Figure 5.1.1 there are two LSSS limit lines shown on the diagram. T_{LSSS} line follows the operating envelope boundary until it reaches the 40°C cooling tower outlet line, and the line diverges. This line gives the hot leg temperature at which the trip signal must be initiated to avoid ONB. To find the temperature LSSS, follow a constant power line from the steady-state operating point until the LSSS Temperature line is met. This temperature is the LSSS temperature. In a loss of heat sink transient initiated from within the operating envelope, the core outlet temperature will continue to rise after the reactor trip signal is initiated. This temperature "overshoot" is included in the LSSS. The edge of the steady-state operating envelope coincides with the LSSS temperature. When the reactor is operating at the edge of the steady-state envelope, there is no margin between the operating conditions and the LSSS. Operating limits should be used to prevent this situation.

The Q_{LSSS} line gives the core power level at which a trip signal must be initiated to avoid ONB resulting from excessive core power. The core power LSSS is found by following a constant cooling tower outlet temperature line from the steady-state operating point until it intersects the LSSS Power line. The power at this intersection is the power LSSS. If a signal is initiated when this power is reached, then the reactor will scram before ONB occurs.

The LSSS for primary mass flow rate (m_{LSSS}) is written on Figure 5.1.1. During a pump coastdown, a reactor trip signal must be initiated when the primary loop flow rate reaches the flow LSSS. The steady-state operating envelope is found for a primary mass flow rate of 127 kg/s. If the true flow rate is above 127 kg/s, then the chart will be conservative. If the true flow rate is less then 127 kg/s, then the chart should not be used.

There are two Safety Limit (SL) lines shown in Figure 5.1.1. The T_{SL} line gives the hot leg temperature at which a trip signal must be initiated to avoid CHF in the core. If the transient is not halted by the time the LSSS temperature is reached, boiling may begin in the hottest channels. The voiding may lead to the beginning of a flow excursion in one or more coolant channels. If a trip signal is initiated by the time the hot leg temperature reaches the temperature SL, the flow excursion will be reversed and the reactor will scram before CHF is reached.

The Q_{SL} line represents the core power level at which a trip must be initiated to avoid CHF resulting from a reactivity insertion. The power SL is found by following a constant cooling tower outlet temperature line from the steady-state operating point until it intersects the SL Power line. The power at this intersection is the power SL.

The flow Safety Limit (m_{SL}) is written on Figure 5.1.1. In order to avoid CHF from a pump coastdown, a trip signal must be initiated when the primary mass flow rate reaches the flow Safety Limit.

When a proposed steady-state operating point is determined, the LSSS and Safety Limits can be read from a Limit Diagram similar to Figure 5.1.1. The LSSS should provide the reactor operations staff with an upper limit to their operating limits. The operating limits, which will correspond to the true reactor trip points, should be chosen to provide a margin between operation and the LSSS.

If the reactor is moved from its initial steady-state point to a new steady state point that is less restrictive (i.e., lower power, higher flow rate, or lower core outlet temperature), then there is no need to redetermine the LSSS and Safety Limits. If the new steady state operating point is more restrictive (for example, if the wet-bulb temperature went up overnight), then the limits must be re-examined.

A Limit Diagram, similar to Figure 5.1.1, is specific to a given reactor configuration. Important characteristics include:

1) Primary mass flow rate. The operating mass flow rate should be equal to or greater than the mass flow rate given on the diagram.

2) Secondary mass flow rate. The operating secondary mass flow rate should be equal to or greater than the secondary flow rate used to construct the diagram.

3) Cooling tower parameters. Replacement of the cooling tower will change the approach temperature. A better cooling tower will expand the steady-state operating envelope.

4) Heat exchanger parameters. New heat exchangers will expand the steady-state operating envelope and the margin to the temperature limits.

5) Core configuration. The number of fuel elements and dummy elements will affect the flow disparity, bypass flow, and radial power shape. The burnup of the core will change the radial and axial power shapes.

6) Fuel characteristics. Any changes in fuel composition, loading, or shape will impact the fuel and clad heat transfer properties, as well as alter the neutronic characteristics of the core.

If any of these parameters are changed in a manner that would reduce the limit margins, a new Limit Diagram should be constructed.

5.2 *MITR Limit Diagrams For Three Flow Rates*

The Limit Diagram described above was generated for three different heat removal system configurations. Table 5.2.1 shows the primary and secondary loop flow rates used to calculate the Limit Diagrams included in this report. The three cases represent the current MITR-II, and two different options for upgrading the current MITR-II heat removal system to accommodate 10 MW operation.

Table 5.2.1. MITR Limit Diagrams included in this report.

	MITR-II	**Upgrade 1**	**Upgrade 2**
Figure	5.1.1	5.2.1	5.2.2
Primary Flow (kg/s)	127.0	154.0	172.0
(gpm)	(2050)	(2500)	(2800)
Secondary Flow (kg/s)	103.0	103.0	142.0
(gpm)	(1660)	(1660)	(2300)

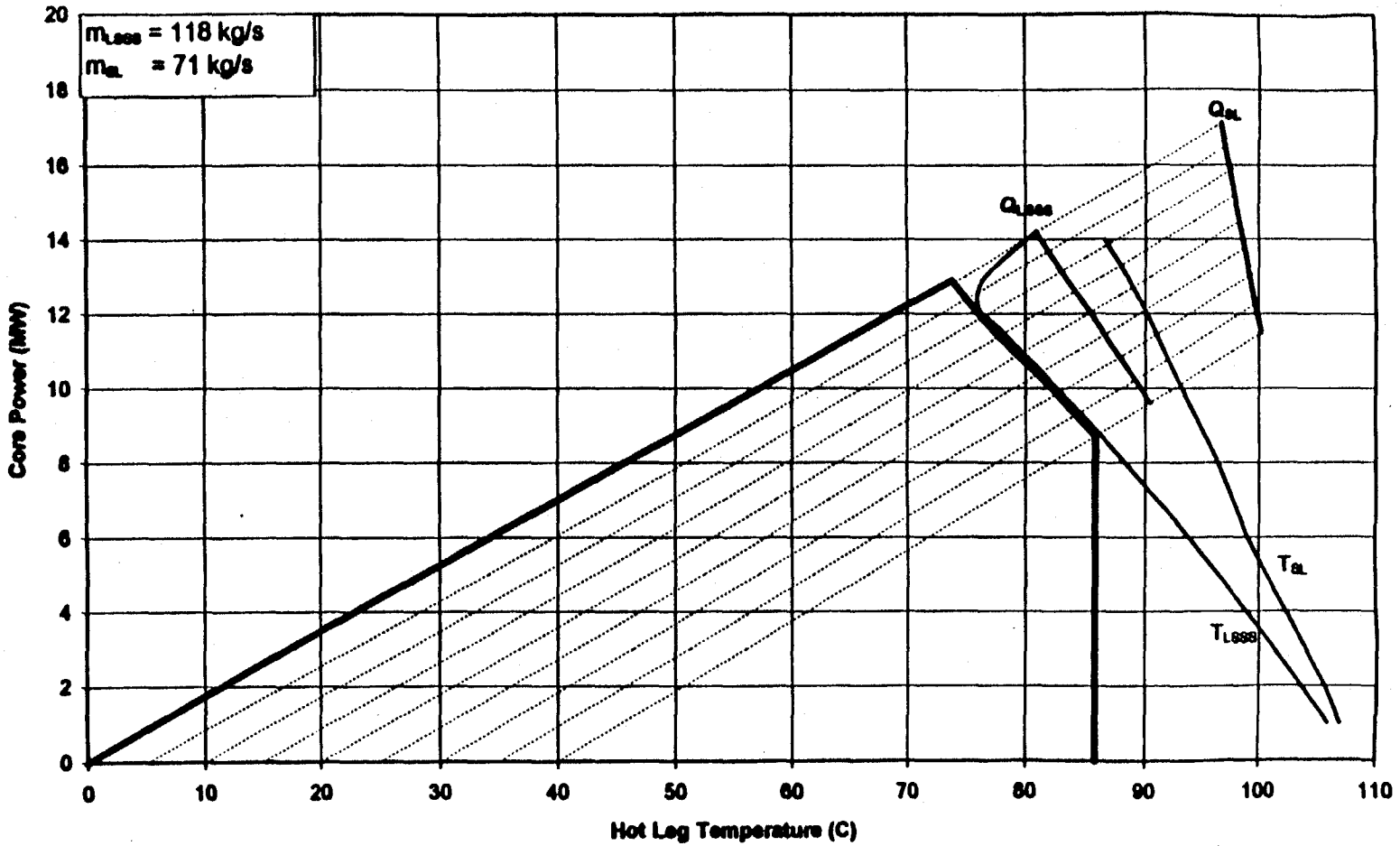

Figure 5.2.1 MITR Limit Diagram for a primary flow rate of 154 kg/s (2500 gpm). The secondary flow rate is 103 kg/s (1660 gpm). This represents MITR-III with larger pumps on the primary side. The parameters used to generate the limit diagram are given in Appendix D.

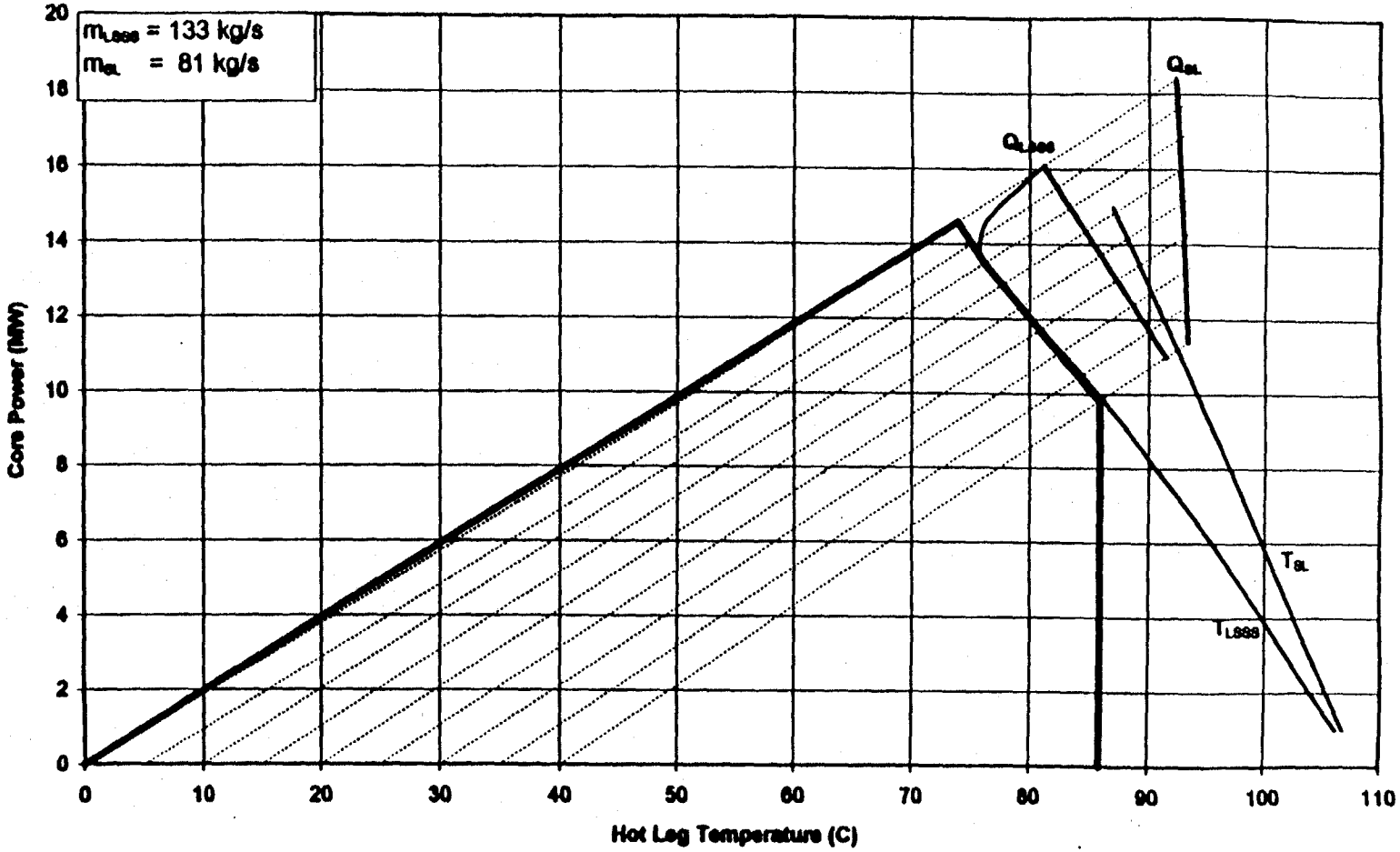

Figure 5.2.2 MITR Limit Diagram for a primary flow rate of 172 kg/s (2800 gpm). The secondary flow rate is 142 kg/s (2300 gpm). This represents MITR-III with larger pumps on both the primary and secondary sides. The parameters used to generate the limit diagram are given in Appendix D.

The input data used to generate the Limit Diagrams is described in Appendix D. The core configuration is a five-dummy core. This configuration was selected because the core is not operated with fewer than 22 fuel elements. If more fuel elements are included at the same power, the surface average heat flux will be less, and more flow will be available for the fuel elements. The flow disparities and power shapes for the 22-element core analyzed in this report are from previous studies of Core-II from MITR-II [3,7].

The primary pump flow coastdown curve and control blade drop times are based on experimental measurements and statistical analyses performed by Sardy and Terry [1,26]. Much of the geometry, and properties of the fuel and clad are taken from previous studies [3,4,5,6].

The three Limit Diagrams shown in Figures 5.1.1, 5.2.1, and 5.2.2 share the same basic features. As expected, the operating envelope increases as the loop flow rates increase. The LSSS increase with the operating envelope, resulting in a comparable margin between operation and the LSSS in the three cases.

The margin between the LSSS and the Safety Limits decreases as the flow rates are increased. For example, in the high flow rate case (Figure 5.2.2) it is seen that the LSSS temperature closely approaches the Safety Limit temperature. The high primary flow rate provides a strong driving force for a flow excursion. Therefore, when a small amount of void is present, a rapid flow excursion develops which quickly leads to CHF. In the lower flow rate cases, a larger amount of void is needed to generate a flow excursion. This results in a larger margin between the LSSS and Safety Limits at lower power.

As a means of comparison, Table 5.2.2 shows the LSSS and Safety Limits associated with operating at 10 MW and a cooling tower outlet temperature of 20°C in each Limit Diagram.

Table 5.2.2. LSSS and Safety Limits for 10 MW operation with a cooling tower outlet temperature of 20°C.

	127 kg/s	154 kg/s	172 kg/s
Steady-State Hot Leg Temperature (°C)	76	74	68
LSSS			
Power (MW)	11.2	12.1	13.7
Temperature (°C)	76	83	86
Mass Flow Rate (kg/s)	70	93	113
Safety Limits			
Power (MW)	13.8	14.5	15.2
Temperature (°C)	93	93	94
Mass Flow Rate (kg/s)	30	45	54

Table 5.2.2 shows that with the current heat removal system (primary mass flow rate of 127 kg/s), the operating point lies at the edge of the steady-state operating envelope. The steady-state core outlet temperature is at the LSSS temperature. This system could not operate at 10 MW with a cooling tower outlet temperature greater than 20°C. The second case (primary mass flow rate of 154 kg/s) has a 9°C margin between its steady state operating temperature and the LSSS temperature, and a 2.1 MW power margin. An upgraded MITR-III in this configuration could operate at 10 MW with cooling tower outlet temperatures up to 28°C. The third system (primary mass flow rate of 172 kg/s and secondary flow rate of 142 kg/s) could operate at 10 MW with cooling tower outlet temperatures as high as 38°C.

The maximum cooling tower outlet temperature at which 10 MW operation is permitted is important to reactor operations because it indicates how often it will be necessary to reduce the reactor power. On days when the wet-bulb temperature is high, the current cooling towers operate with an approach temperature of approximately 5 - 6 °C (the approach temperature is the difference between the cooling tower outlet temperature and the ambient wet-bulb temperature). In Boston, MA, a wet-bulb temperature of 25.6°C (78°F) is exceeded on only one percent of the days. The current heat removal system would be capable of operating at 10 MW during only a fraction of the year. The upgraded MITR-III with a primary flow rate of 172 kg/s and a secondary flow rate of 142 kg/s could operate year-round at 10 MW with a margin of 10°C or greater between the operating point and the LSSS temperature. The intermediate option, with a primary flow rate of 154 kg/s, would be forced to reduce power to below 10 MW approximately 120 days per year in order to maintain a 7°C margin between the operating point and the LSSS temperature on the hottest days (weather data from [43]).

The performance of the low flow rate options can be improved by upgrading the cooling towers and heat exchangers. New heat exchangers will reduce the log-mean temperature difference between the primary and secondary loop temperatures. With more effective heat exchangers, the primary loop will operate at a lower temperature for a given cooling tower outlet temperature. The current shell-and-tube heat exchangers can be replaced by more effective lamellar heat exchangers to reduce the log-mean temperature difference. The effectiveness of the cooling towers determines the approach temperature that can be attained for a given ambient wet-bulb temperature. Replacing the current cooling towers will not offer any great reduction in the operating approach temperature at the present power level. However, the current cooling towers will be unable to accommodate an increased thermal load without a significant decrease in effectiveness.

In summary, the steady-state operating envelope can be expanded to allow year-round operation at 10 MW by increasing the primary and secondary flow rates, and by replacing the heat exchangers and cooling towers with new components that offer improved efficiency and the capability to handle an increased heat load. Maintenance and cost analyses will determine what combination of these upgrades is the optimum course of action. When a new heat removal system configuration is selected, a new MITR Limit Diagram can be constructed.

5.3 Construction of MITR Limit Diagrams

This section outlines the procedure used to generate the MITR Limit Diagrams shown in Figures 5.1.1, 5.2.1, and 5.2.2. In each step in the process, the objective is to determine a trip point that will cause the system to avoid reaching a limit criteria. Figure 5.3.1 shows the clad temperature during a loss of heat sink transient (secondary pump trip). The response of the system to the transient is shown for three different trip points. In the LSSS curve, the trip signal is initiated at the hot leg temperature LSSS, allowing the system to scram prior to the onset of nucleate boiling at the hottest spot in the core. The Safety Limit curve shows the clad temperature when the trip point is at the Safety Limit. Boiling is predicted to occur, but the reactor scrams immediately prior to the CHF limit. The top curve, labeled "No Trip" shows the clad temperature when no scram signal is sent and the system reaches CHF as a result of a flow excursion.

Figure 5.3.2 shows the mass flow rate in the channel that is most susceptible to a flow excursion instability. When the trip point is at the LSSS, the channel mass flow rate remains constant because no boiling occurs. When the trip point is at the Safety Limit, some boiling occurs and a flow excursion begins. The reactor trips immediately prior to the predicted onset of CHF in the hottest spot. When the transient is allowed to proceed beyond the Safety Limit, the flow excursion continues until the surface heat flux exceeds the predicted critical heat flux. At this point the heat transfer from the clad to the coolant drops significantly and the clad temperature will rises rapidly.

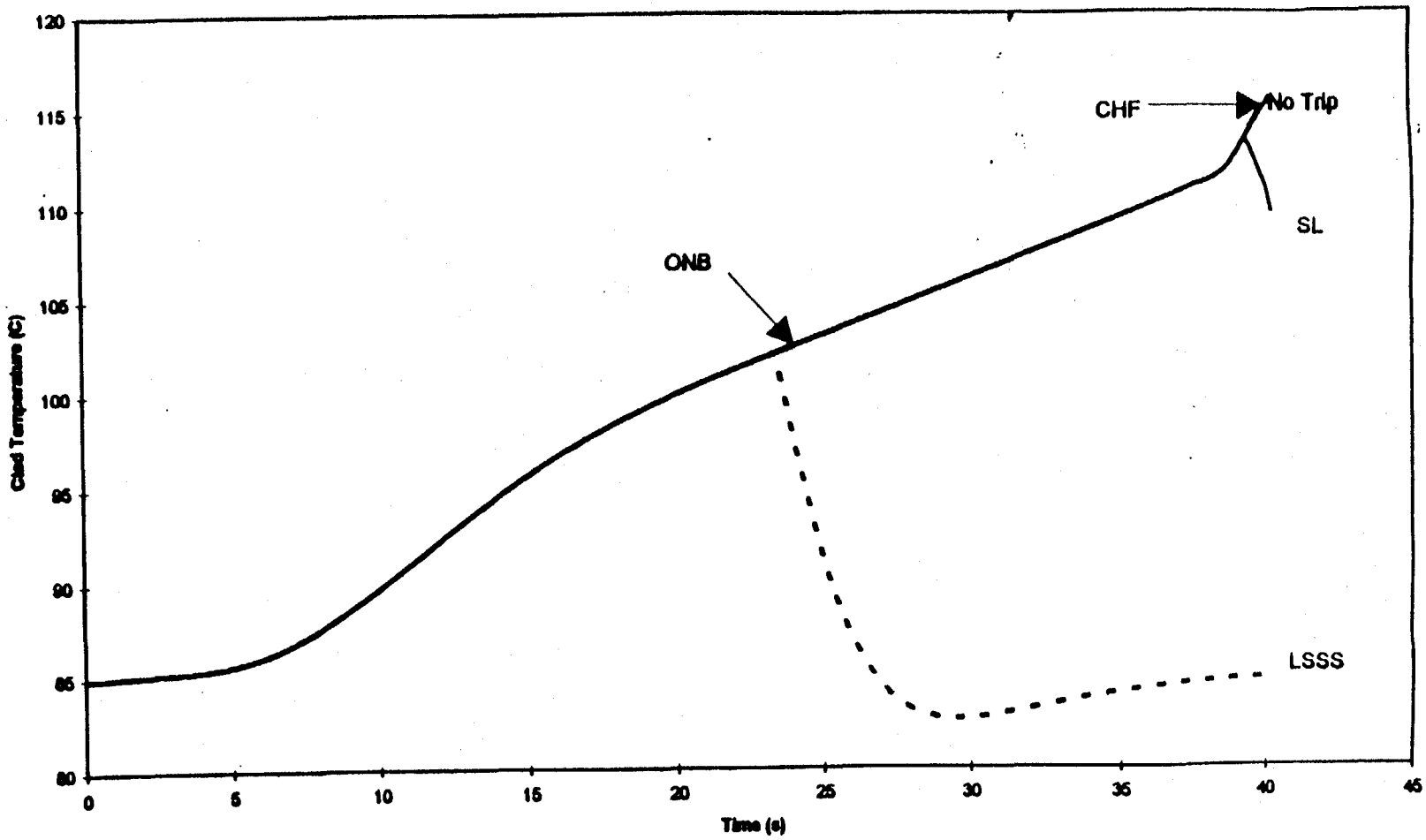

Figure 5.3.1 Clad temperatures in loss of heat sink transients. Node-average clad temperatures are shown. The peak clad temperature at the hot spot and between the fins is approximately 10°C above the average.

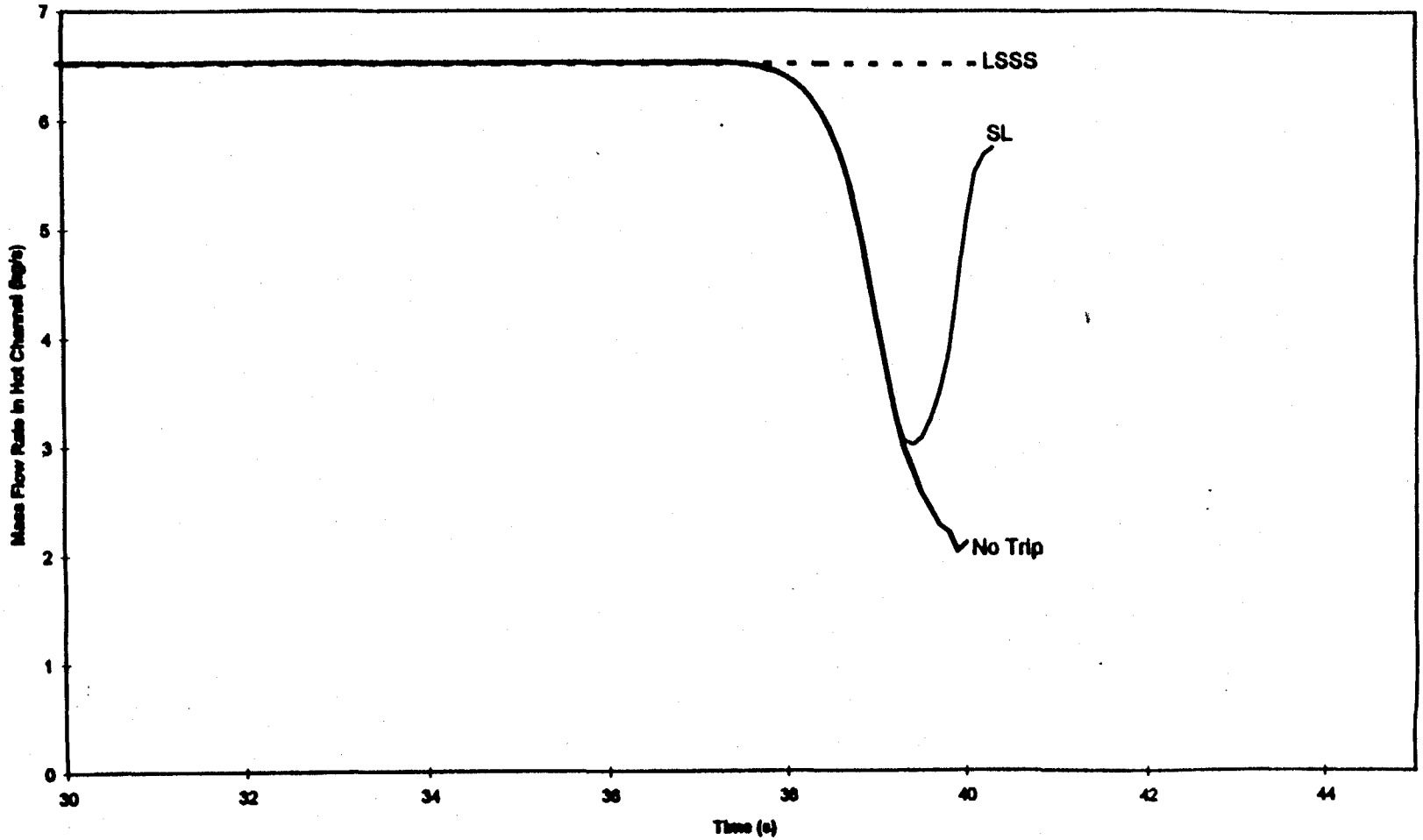

Figure 5.3.2 Channel flow rate in loss of heat sink transients. The onset of a flow instability can be prevented if the reactor trip signal is sent before the LSSS is reached. If a trip signal is sent at the Safety Limit, the flow excursion can be reversed and CHF will be avoided. If the trip signal is not sent by the time the Safety Limit is reached, the hot channel will dry out and clad temperatures will rise rapidly.

For a given heat removal system, the first step in setting the LSSS is to establish an acceptable steady-state operating envelope. For each value of cooling tower outlet temperature there exists a maximum core power level that can be maintained without any nucleate boiling in the core. These points make up line AB in Figure 5.3.3. During an infinitely slow power increase, the operating point will move up from its steady-value along a line of constant cooling tower outlet temperature. At each point in the transient a new steady-state will be established. This small reactivity insertion transient was found to lead to ONB at lower power levels than a large reactivity insertion.

During a large reactivity insertion, the operating point will move up in power at a relatively constant hot leg temperature because the core temperatures do not have time to reach their equilibrium values associated with the rising power. For this reason, the surface heat fluxes are high, but the flowing coolant keeps wall temperatures low and nucleation is not predicted to occur. A large reactivity insertion, when initiated from a low power level, can result in a large "power overshoot" during the instrumentation delay time between the scram signal and the insertion of the control blades. The power limits shown by line AB represent the small reactivity insertion limits. A maximum reactivity insertion transient from low power was simulated for comparison. For the conditions studied in this report, the small reactivity insertion was found to be the more limiting event. Therefore, line AB represents the power LSSS.

The steady-state operating envelope is further restricted by the condition that a loss of heat sink transient initiated within the envelope must not lead to ONB prior to a scram. During a secondary system pump coastdown, the core inlet temperature begins to rise as the heat transfer rate in the heat exchangers drops. When the secondary flow rate has gone to zero, the core inlet temperature is rising at its maximum rate. The rate of temperature rise is important because the temperature will continue to rise during the instrumentation delay time. A high rate of temperature increase causes a high temperature overshoot. Therefore, the most limiting loss of heat sink transient is the one that is initiated at a low system temperature, such that the rate of temperature rise is a maximum.

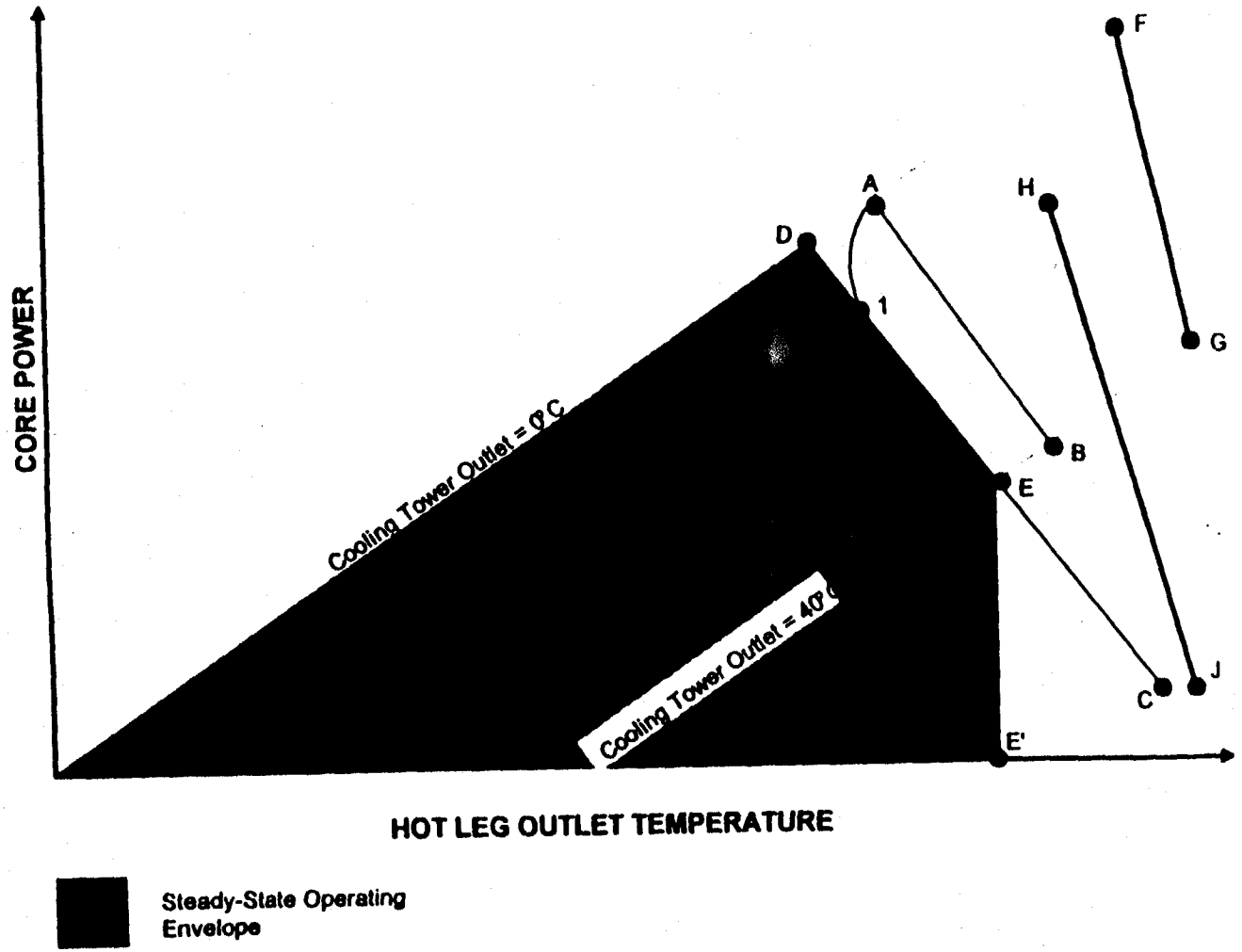

Figure 5.3.3 Construction of an MITR Limit Diagram. The lines shown are: LSSS Temperature (Line DC), LSSS Power (Line AB), Safety Limit Temperature (Line HJ), Safety Limit Power (Line FG). Steady-state operation is permitted in the shaded region to the left of Line DEE'.

For each power level, there is a hot leg temperature at which a trip signal must be initiated in order to avoid ONB prior to a scram. This limiting temperature is lowest for a transient that is initiated from a cooling tower outlet temperature of 0°C (shown by the dotted line in Figure 5.3.3). The collection of these limiting temperatures is plotted as line AC.

The last LSSS to be determined is the mass flow rate limit. Due to the hot leg temperature limit, steady state operation is not permitted to the right of line AC. At each point along line AC there exists a mass flow rate at which a trip signal must be initiated in order to avoid ONB. The flow rate trip point required to avoid ONB from operation at Point A is nearly equal to the steady-state flow rate because Point A lies on the LSSS power limit line. The flow rate trip point required to avoid ONB during a transient initiated from Point A is lower. The loss of heat sink transient has already limited the steady-state operating envelope to the temperature at Point 1. Therefore, the mass flow rate LSSS is chosen to be the flow rate trip point that avoids ONB during a loss of flow transient initiated from Point 1. Line DE represents the maximum operating envelope that can be achieved with this flow rate LSSS.

As discussed aerlier, three type of loss of flow transients were considered: a double pump trip, a single pump trip, and a gradual loss of forced flow. Although it is the least likely of the three, the gradual loss of flow is found to be the most limiting because the coolant is allowed to reach higher temperatures. The mass flow rate LSSS is based on a gradual loss of flow transient.

The Safety Limits are found by initiating transients from within the steady-state operating envelope and allowing the transients to proceed past the LSSS. Line FG in Figure 5.3.3 represents the maximum steady-state power at which the reactor can operate at for each value of cooling tower outlet temperature. Attempting to operate at a higher power level would cause the initiation of a flow excursion. For the same reasons as discussed above for the power LSSS, line FG represents the limiting power for a small reactivity insertion. For all power levels, the CHF was induced by a flow excursion. During a maximum reactivity insertion, the coolant does not have time to boil and cause a flow excursion.

Line HJ is found in the same manner as line AC. A loss of heat sink transient is initiated from the 0°C cooling tower outlet temperature line. Line HJ is the maximum hot leg temperature at which a scram can be initiated to avoid CHF.

To determine the Safety Limit for the mass flow rate, one further restriction on the operating envelope is needed. For operation at cooling tower outlet temperatures above 40°C, the maximum hot leg temperature is required to remain constant (Line EE'). This does not place any practical limitations on reactor operations because cooling tower outlet temperatures approaching 40°C are not expected to occur. With the operating envelope now fully defined, the Safety Limit is found by initiating loss of flow transients from steady-state points along line DEE' and finding the lowest trip point that avoids CHF.

6. Conclusions and Recommendations

6.1 Summary and Conclusions

6.1.1 Definitions of Limiting Safety System Settings and Safety Limits

New definitions of the Limiting Safety System Settings (LSSS) and Safety Limits are proposed. The reactor operating envelope and the limits are defined in terms of three fundamental variables: core power, primary loop mass flow rate, and hot leg temperature. The new limits represent reactor trip points that are necessary to avoid exceeding the limit criteria.

If a reactor trip signal is sent before any of the Limiting Safety System Settings are exceeded, there will be no nucleate boiling in the core prior to the scram. Similarly, if the trip signal is sent before the Safety Limits are exceeded, critical heat flux will be prevented.

The LSSS represent the extreme values of the reactor trip points, and may be used to help set the operating limits. The Safety Limits do not have a direct impact on reactor operation. The purpose of the Safety Limits is to demonstrate that a significant margin exists between the normal operating regime of the reactor and the point at which the safety of the reactor core is in jeopardy. The Safety Limits are defined such that the margin between the operating envelope and the Safety Limits cannot be exceeded by any of the plausible transients examined in this report. The transients studied in this report represent the most severe events that are plausible in the MITR system, including loss of primary flow, loss of heat sink, and reactivity insertion events.

The new definitions of the LSSS and Safety Limits are appropriate to describe the safety margins associated with MITR operation. The two sets of limits are defined analogously, allowing the margin between them to be easily determined. Because the limits are based on hypothetical trip points, a physical meaning has been assigned to each set of limits.

For each permissible steady-state operating point defined, a set of Limiting Safety System Settings and Safety Limits can be found. These limits are found by computer simulation. The MITR Multi-Channel Analysis Code was written to analyze the response of the MITR system to each of the transients.

6.1.2 MITR Multi-Channel Analysis Code

The MITR is a unique system with several features that require special attention. The MITR Multi-Channel Analysis Code was written specifically to predict the behavior of the MITR system during the transients described above. Although emphasis is placed on calculating the thermal-hydraulic conditions in the core, models of the primary loop, heat exchangers, secondary loop, and cooling towers are included.

The Safety Limit Criteria for the MITR is the prevention of critical heat flux and the resulting excessive clad temperatures. In most cases, critical heat flux is preceded by the onset of a parallel channel flow instability in the core. Therefore, prediction of the Safety Limits requires a core model that explicitly models multiple coolant flow paths and two-phase flow. During two-phase flow, the momentum and energy equations are closely linked by the value of the volumetric void fraction. An atmospheric pressure void fraction model was developed that accurately predicts the void fraction in the subcooled and bulk boiling regimes.

The reactor core is divided into axial and radial nodes for all thermal-hydraulic calculations. Overall conditions within each node are determined based on best-estimate calculations. To monitor the approach to the limit criteria, heat flux peaking factors and engineering hot-channel factors are used to ensure conservative results.

The MITR Multi-Channel Analysis Code is validated by comparison with experimental data from the MITR-II and from several out-of-core experiments. Because the MITR-II has not operated under two-phase conditions, the results of two-phase experiments on similar systems must be relied upon to verify the two-phase models in the code. The models in the code have been used to predict the behavior of a multi-channel system under abnormal conditions including two-phase flow and heat transfer, flow excursion instability, and natural circulation. The onset of flow instability in MITR channels requires accurate prediction of the void fraction and appropriate two-phase momentum and energy models. The MITR Multi-Channel Analysis Code can be used to analyze the behavior of the MITR system during all phases of a Ledinegg flow instability.

The computer model of the MITR and the limit definitions are used to generate Limit Diagrams that define permissible operating envelopes, Limiting Safety System settings, and Safety Limits for various configurations of the MITR.

6.1.3 MITR Limit Diagrams

The MITR Limit Diagrams are two-dimensional projections of a three dimensional state-space. The core power is plotted as a function of hot leg temperature for a given mass flow rate. The MITR Multi-Channel Analysis Code is used as a tool to calculate the trip points that are required to avoid exceeding the limit criteria. The collection of these points is represented by the limit lines on the Limit Diagram. A permissible steady-state operating envelope is defined. For operation within this envelope, the LSSS and Safety Limits can be read from the diagram.

At a given power level, the most limiting loss of heat sink accident was found to be a secondary pump trip at a low operating temperature. When a loss of heat sink is initiated from a low system temperature, the rate of temperature rise in the system is at a maximum. The temperature continues to rise at this rate during the instrmentation delay time, resulting in a high temperature overshoot. At higher temperatures, when the operating point is near the limit line, the system temperature is rising more slowly during the instrumentation delay time between the trip signal and the insertion of the blades.

Several reactivity transients were examined. A large reactivity insertion causes a rapid increase in surface heat flux. However, the coolant temperature is slower to respond. The net result is that nucleate boiling is slow to develop. During a small reactivity increase, the coolant temperature rises with the heat flux. This leads to a higher clad temperature and a closer approach to nucleate boiling. For a given system temperature, the most limiting reactivity insertion is an infinitely small rate of power increase, such that a steady-state condition is established at each new power level.

Three types of loss of flow transients were considered: a double pump trip, a single pump trip, and a gradual loss of flow. The gradual loss of flow required the most limiting flow rate trip because the primary coolant had time to heat up, thereby raising the clad temperature. The higher coolant temperature also promotes the onset of flow instabilities.

Under nominal flow conditions, there is a large margin to critical heat flux in the MITR core. Because the value of the critical heat flux is a function of the flow rate through each channel, a flow excursion is a likely path to critical heat flux. All of the transients examined in this report have the potential to cause a flow instability shortly following the onset of significant voids in a given coolant channel.

At higher flow rates, the driving force for a flow instability is greater. Therefore, the Limit Diagrams for high mass flow rates show smaller margins between the operating envelope and the Safety Limits. The advantage of the higher flow rate is that it expands the available operating envelope.

On days when the ambient wet-bulb temperature is high, it may be necessary to reduce the reactor power level in order to remain within the steady-state operating envelope. With the current heat removal system in place, operation at 10 MW is predicted to be acceptable when the cooling tower outlet temperature is below 20°C (this corresponds to a wet-bulb temperature of approximately 15°C). If the primary pumps are replaced and the primary flow rate is raised to 154 kg/s (2500 gpm) the reactor could operate at 10 MW with cooling tower outlet temperatures up to 28°C (ambient wet-bulb temperature below 23°C).

The operating envelope can be expanded to permit 10 MW operation at cooling tower outlet temperatures of up to 38°C (wet bulb temperatures up to 33°C) by raising the primary flow rate to 172 kg/s (2800 gpm) and the secondary flow rate to 142 kg/s (2300 gpm). This will allow for year-round operation at 10 MW with a 10°C margin between the peak operating temperature and the LSSS temperature.

The operating envelope is sensitive to changes in the heat removal system. Larger pumps and more efficient heat exchangers will expand the operating envelope and permit full-power operation at higher wet-bulb temperatures. The methods outlined in this report, and the MITR Multi-Channel Analysis Code, can be used to generate new Limit Diagrams as the heat removal system evolves.

6.2 *Recommendations For Future Work*

6.2.1 Space Kinetics Model

The current point-kinetics model used to predict the reactor power during reactivity transients could be replaced by a space kinetics model. An accurate space kinetics model of the MITR would eliminate the need for power shape factors and power peaking factors because the fission power in each node would be calculated at each time step. The current model does not allow the power shape to change with time.

With a space kinetics model, the MITR Multi-Channel Analysis Code could be used to simulate transient and accident scenarios that result in large changes in the core power shape. For example, the effects of uneven shim bank heights, and the impact of a reactivity insertion from an experimental assembly could be predicted. A space kinetics model would alow the effects of fuel temperature and void fraction reactivity feedback to be accurately modeled. The current limits could be reexamined with the effects of reactivity feedback included to reveal an increased margin between the LSSS and the Safety Limits.

The use of a space kinetics model would significantly increase the computing time required at each time step. Its use should be limited to transients involving localized power changes or alterations in the core power shape.

Research is currently underway in the MIT Nuclear Engineering Department to develop a three-dimensional, space-time diffusion code model of the MITR using triangular geometry [44].

6.2.2 Analysis of the Mixing Area

The region above the core serves as a mixing cup and a thermal reservoir for the fluid exiting the core. This volume of water separates the hot leg temperature detector from the exit of the core. When the hot leg temperature is relied upon to understand the conditions in the heated region of the core, the mixing area introduces an element of uncertainty.

For the calculations in this report, the two control volumes used to represent the mixing area during forced flow are assumed to be fully mixed at each time step. In reality, the coolant exiting the core is likely to form a plume above the core. This would cause information from the core exit to reach the hot leg temperature sooner than predicted by the fully-mixed condition.

A detailed analysis of the mixing area would yield valuable information about the flow of coolant between the core and the hot leg thermocouple. The behavior of the coolant in the mixing area is currently being investigated [5]. Information from this study can be used to suggest new control volumes or boundary conditions that can be applied in the mixing area.

6.2.3 Thermal Hydraulic Experiments On An MITR Fuel Element

The best available correlations for the onset of nucleate boiling (ONB), onset of significant voids (OSV), critical heat flux (CHF), friction factors, and heat transfer coefficients were used to analyze the MITR coolant channels. The MITR fuel elements have several features that require special attention. The presence of the longitudinal fins, the narrow rectangular channels, and the low pressure of the system result in a unique set of conditions. Correlations based on experiments in similar geometries can often be generalized, but without experimental validation in an MITR fuel element, some uncertainty will exist.

A non-fueled MITR fuel element could be instrumented and tested in an out-of-core loop to determine the proper choices of friction factor, hydraulic diameter, and form loss coefficients. An electrically heated fuel element could be instrumented to provide heat transfer data. It may be possible to obtain much-needed information on two-phase flow regimes in the MITR. When a reliable experiment is not possible, a computational fluid dynamics code could be used to obtain information about three-dimensional fluid flow and heat transfer in an MITR coolant channel. Experimental studies of MITR fuel elements were completed in 1976, but much could be gained by continuing this work [28,45].

6.2.4 MITR Auxiliary Systems

This study was limited to analyzing only the major systems involved with the removal of heat from the MITR. Possible malfunctions in other systems should be investigated. Based on these investigations, some limits may be required on such systems as: the shield coolant system, the D_2O system, fuel transfer/storage systems, and experimental facilities.

This report considered only three reactor variables in setting the limits. The results of this report indicate that these variables are sufficient to prevent the limiting criteria from being exceeded. Other reactor variables should be monitored and used to detect abnormal operation and to trip the reactor if necessary. For 10 MW operation and a new heat removal system, suitable trip points should be found for the reactor period, secondary flow rate, core tank level, and auxiliary system variables.

6.2.5 Determination of Operating Limits For MITR-III

Once a new set of heat removal system components (pumps, heat exchangers, cooling towers) has been selected, a Limit Diagram can be constructed to set the Limiting Safety System Settings and Safety Limits. The Limit Diagram will also outline the maximum steady-state operating envelope.

The operating limits will lie somewhere between the operating point and the edge of the steady-state operating envelope. The choice of the operating limits should be guided by two considerations:

1) The operating limits should be slightly beyond the chosen operating point. This choice of trip points limits allow a reactor scram to be initiated as soon as a reactor variable deviates from its nominal value. Enough margin should be present between the operating point and the trip points (operating limits) to prevent a reactor trip signal from initiating during anticipated fluctuations from nominal power.

2) The operating limits should be placed below the LSSS by a sufficient margin to account for uncertainties in the correlations used in this study (see Section 4.4). Any changes in reactor system parameters, such as power shapes and flow disparities, must also be considered. The use of engineering hot channel factors accounts for uncertainties in enthalpy rise and heat transfer coefficients (see Section 3.10.2).

When it is not possible to include a sufficient margin between the operating limits and the LSSS, the maximum operating power should be reduced.

Appendix A

Nomanclature

General Notation

A	Area (m^2)
A_f	Flow area (m^2)
C	Normalized concentration
C_0	Distribution parameter
c	Number of nodes moved during a single time step
c_p	Specific heat capacity (J/kgK)
D_e	Equivalent heated diameter (m)
D_f	Flow disparity
D_H	Equivalent hydraulic diameter (m)
d	Plate thickness (m)
F	Chen correlation Reynolds number factor
F	Net pressure loss (Pa)
F_B	Bulk coolant enthalpy rise hot channel factor
F_H	Heat transfer coefficient hot channel factor
F_a	Spatial acceleration pressure loss (Pa)
F_f	Friction pressure loss (Pa)
F_g	Gravity pressure loss (Pa)
F_k	Form pressure loss (Pa)
f(Re)	Friction factor
f_D	Decay power fraction
G	Mass flux (kg/m^2s)
g	Gravitational acceleration (m/s^2)
h	Enthalpy (J/kg)
h	Heat transfer coefficient (W/m^2s)
h_{fg}	Latent heat of vaporization (J/kg)
K	Form loss coefficient
K	Mass transfer coefficient (kg/m^2s)
k	Thermal conductivity (W/mK)
L	Length (m)
Le	Lewis number
M	Mass (kg)
m	Mass flow rate (kg/s)
N	Number of flow channels
n	Cooling tower diffusion units
n	Friction factor-Reynolds number exponent
P	Normalized power
P	Pressure (Pa)
P_A	Axial power shape factor
P_h	Heated perimeter (m)

P_R	Radial power shape factor
Pr	Prandtl number
P_T	Total peaking factor
P_w	Wetted perimeter (m)
P_X	Peaking factor in x-direction
P_Y	Peaking factor in y-direction
P_Z	Peaking factor in z-direction
Q	Rate of heat transfer (W)
q''	Heat flux (W/m^2)
q_0''	Artificial heat flux (W/m^2)
R	Ratio of temperature rise to inlet subcooling
Re	Reynolds number
r	Radius (m)
S	Chen correlation suppression factor
T	Temperature (°C)
T*	Absolute temperature (K)
T_0	Ambient wet bulb temperature (°C)
t	Time (s)
U	Overall heat transfer coefficient (W/m^2s)
V_{vj}	Effective drift flux (m/s)
v	Velocity (m/s)
X_{tt}	Flow quality parameter
x	Flow quality
x_{eq}	Equilibrium quality
Y_b	Bubble diameter at OSV
Z	Number of axial nodes
z	Elevation (m)

Greek Letters

α	Void fraction
β	Effective fraction
ΔP	Pressure difference (Pa)
ΔT	Temperature difference (°C)
ΔT_{lm}	Log-mean temperature difference (°C)
Δt	Time step size (s)
Δz	Axial node length (m)
δ	Thickness (m)
ϕ^2_{lo}	Two-phase friction multiplier (liquid only)
η	OSV constant
Λ	Prompt neutron lifetime (s)
λ	Characteristic length (m)
λ	Decay constant (s^{-1})
μ	Viscocity ($Ns/m^{2)}$

ρ	Density (kg/m^3)
ρ	Reactivity
σ	Surface tension (N/m)
τ	Operating time
τ	Time constant (s)
τ_w	Wall shear stress (N/m^2)

Subscripts

0	Ambient
0	Initial value
1	Primary
1I	Primary inlet
1O	Primary outlet
2	Secondary
2I	Secondary inlet
2O	Secondary outlet
air	Air
B	Bulk
ball	Natural circulation valve ball
C	Convection
CHF	Critical heat flux
c	Clad
cl	Clad
core	Core
ct	Cooling tower
D	Decay heat
dc	Downcomer
e	Equivalent (heated)
eq	Equilibrium
F	Fission
F	Fouling
f	Fuel
f	Saturated liquid
G	Gambill correlation
g	Saturated vapor
HOT	Hot spot
h	Heated
hx	Heat exchanger
i	Channel index
i	Decay precursor group index
i	Delay precursor group index
i	Inside
in	Inlet

j	Inlet flow stream index
j	Node index in primary loop
k	Outlet flow stream index
l	Liquid
lm	Log-mean
lo	Liquid only
m	Mixed
NB	Nucleate boiling
nc	Natural circulation valve
OFI	Onset of flow instability
ONB	Onset of nucleate boiling
OSV	Onset of significant voids
o	Outside
out	Outlet
p	Primary loop
pump	Pump
s	Saturated
s	Secondary
sat	Saturation
system	System
T	Total
t	Heat exchanger tube
V	Valley between fins
v	Vapor
W	Channel width
w	Wall
w	Wetted
wall	Wall
x	X direction
y	Y direction
z	Axial node index
z	Z direction

Superscripts

+	At new time step
0	At old time step
*	Absolute temperature

Units

C	Celcius degree
J	Joule
K	Kelvin degree
kg	Kilogram
m	Meter
mm	Millimeter
N	Newton
Pa	Pascal
s	Second
W	Watt

Acronyms

CHF	Critical heat flux
HX	Heat exchangers
LSSS	Limiting Safety System Settings
MIT	Massachusetts Institute of Technology
MITR	Massachusetts Institute of Technology Reactor
MITR-II	The current Massachusetts Institute of Technology
MITR-III	Proposed MITR to begin operation in 1999
NRL	MIT Nuclear Reactor Laboratory
OFI	Onset of flow instability
ONB	Onset of nucleate boiling
OSV	Onset of significant voids
SL	Safety Limits

Appendix B
Physical Properties

Physical properties of water are determined in the MITR Multi-Channel Analysis Code by the following polynomial fits to tabulated data. Each property is a function of enthalpy or pressure.

Each property is expressed as a series of five constants representing the coefficients of a fourth order polynomial of the form,

$$P(X) = C_1X^4 + C_2X^3 + C_3X^2 + C_4X + C_5$$

where, $P(X)$ = Physical Property,
X = Enthalpy, temperature, or pressure
C_i = Constant

Because a high order polynomial fit is used for the physical properties, it is important that the domain of the independent variable is not exceeded during any calculations. In the MITR Multi-Channel Analysis Code, when the domain is exceeded, a constant property value is used. The correlation parameter, r, is included for each property.

Saturation Pressure $P_{sat}(T)$ [kPa]

C_1 = 1.830965
C_2 = -0.000449
C_3 = 0.088117
C_4 = -7.684060
C_5 = 241.310501
r = 0.999996

Domain: $50 < T < 400$ °C

Saturation Temperature T_{sat} (P) [°C]

C_1 = -4.073472
C_2 = 9.023727
C_3 = -0.000777
C_4 = 0.379212
C_5 = 68.842368
r = 0.999972

Domain: $100 < P < 800$ kPa

Saturation Enthalpy, Liquid $h_f(P)$ [kJ/kg]

C_1	=	-1.488186E-8
C_2	=	1.714575E-5
C_3	=	-8.072093E-3
C_4	=	2.315689
C_5	=	251.069334
r	=	1.000000

Domain: $100 < P < 400$ kPa

Saturation Enthalpy, Vapor $h_g(P)$ [kJ/kg]

C_1	=	-6.273926E-10
C_2	=	2.162076E-6
C_3	=	-1.761328E-3
C_4	=	0.695185
C_5	=	2621.460462
r	=	1.000000

Domain: $100 < P < 400$ kPa

Subcooled Liquid Density $\rho_l(T)$ [kg/m^3]

C_1	=	0
C_2	=	0
C_3	=	-0.002746
C_4	=	-0.162252
C_5	=	1002.482222
r	=	0.999725

Domain: $0 < T < 150$ °C

Saturated Liquid Density ρ_f (P) [kg/m^3]

C_1	=	3.1557E-9
C_2	=	-4.5268E-6
C_3	=	2.2881E-3
C_4	=	-5.7310E-1
C_5	=	996.08
r	=	0.999

Domain: $100 < P < 400$ °C

Saturated Vapor Density ρ_g (P) [kg/m^3]

C_1	=	0
C_2	=	0
C_3	=	0
C_4	=	5.257089E-3
C_5	=	0.071712
r	=	0.999944

Domain: $100 < P < 400$ °C

Liquid Viscosity μ_l (h) [Ns/m^2]

C_1	=	5.381740E-14
C_2	=	-7.445486E-11
C_3	=	4.048806E-8
C_4	=	1.126196E-5
C_5	=	0.001708
r	=	0.999952

Domain: $50 < h < 450$ kJ/kg

Vapor Viscosity μ_v (P) [Ns/m^2]

C_1	=	-1.450417E-16
C_2	=	1.714234E-13
C_3	=	-8.155063E-11
C_4	=	2.257002E-8
C_5	=	1.044731E-5
r	=	1.000000

Domain: $100 < P < 400$ kPa

Surface Tension σ_l (h) [N/m]

C_1	=	0
C_2	=	0
C_3	=	-0.014368
C_4	=	-34.484129
C_5	=	7.575844E+4
r	=	0.999988

Domain: $50 < h < 450$ kJ/kg

Liquid Thermal Conductivity k_l (h) [Ns/m^2]

C_1	=	-4.803269E-16
C_2	=	4.914226E-13
C_3	=	-5.716419E-10
C_4	=	4.562090E-7
C_5	=	5.687472E-4
r	=	1.000000

Domain: $50 < h < 450$ kJ/kg

Liquid Specific Heat Capacity $c_{p,l}$ (h) [kJ/kgK]

C_1	=	4.585342E-12
C_2	=	-5.499936E-9
C_3	=	2.812709E-6
C_4	=	-5.362758E-4
C_5	=	4.211440
r	=	0.999952

Domain: $50 < P < 450$ kJ/kg

Appendix C

Derivation of Normalized Point Kinetics Equations

Normalized equations for fission power and precursor concentration can be derived from the standard point kinetics equations. The normalized power is defined as the ratio of the fission power at time t to the steady-state fission power. Likewise, the normalized precursor concentration is defined to be the ratio of the current concentration to the steady-state concentration. Therefore, prior to the initiation of a transient the normalized fission power is equal to 1.0. The normalized precursor concentrations are equal to 1.0 if it is assumed that the precursors have reached their equilibrium levels for the steady-state power level.

The standard point kinetics equations are:

$$\frac{dT}{dt} = \frac{\rho - \beta}{\Lambda} + \sum_{i=1}^{6} \lambda_i \chi_i \qquad \text{(B-1)}$$

and,

$$\frac{d\chi_i}{dt} = \frac{\beta_i}{\Lambda} T - \lambda_i \chi_i \qquad \text{(B-2)}$$

where, T = Amplitude function,
ρ = Reactivity,
β_i = Delayed neutron fraction for precursor i,
β = Sum of all b_i,
Λ = Prompt neutron lifetime (s),
λ_i = Decay constant for precursor group i (s^{-1}),
χ_i = Concentration of neutron precursor group i,

The normalized power and concentrations are defined as,

$$P_F = \frac{T}{T_0} \qquad \text{(B-3)}$$

and,

$$C_i = \frac{\chi_i}{\chi_{i0}} \qquad \text{(B-4)}$$

where, P_F = Normalized core power,
C_i = Normalized concentration of neutron precursor i,
T_0 = Amplitude function at steady state,

χ_{i0} = Concentration of neutron precursor group i at steady-state [χ_{i0} corresponds to infinite, steady-state operation at T_0],

To solve for χ_{i0}, set the time derivative in Equation (B-2) to zero to find the steady-state precursor concentration,

$$\chi_{i0} = \frac{\beta_i T_0}{\Lambda \lambda_i} \tag{B-5}$$

Equation (B-5) is substituted into (B-4) to find the normalized concentration of precursor group i,

$$C_i = \frac{\chi_i}{\chi_{i0}} = \frac{\chi_i \lambda_i \Lambda}{\beta_i T_0} \tag{B-6}$$

Rearrange Equation (B-6) to express χ_i in terms of C_i,

$$\chi_i = \frac{C_i \beta_i T_0}{\lambda_i \Lambda} \tag{B-7}$$

Substitute Equation (B-7) into the time-dependent concentration expression, Equation (B-2),

$$\frac{d\left(\frac{C_i \beta_i T_0}{\lambda_i \Lambda}\right)}{dt} = \frac{\beta_i}{\Lambda} T - \lambda_i \left(\frac{C_i \beta_i T_0}{\lambda_i \Lambda}\right) \tag{B-8}$$

Note that only C_i is a function of time in Equation (B-8). When the constants are taken out of the derivative, Equation (B-8) can be expressed as,

$$\frac{dC_i}{dt} = \lambda_i \frac{T}{T_0} - \lambda_i \chi_i \tag{B-9}$$

Using the definition of normalized power in Equation (B-3), the normalized precursor concentration equation is obtained:

$$\frac{dC_i}{dt} = \lambda_i (P_F - C_i) \tag{B-10}$$

The normalized power equation can be found by substituting $T = P_F T_0$ into Equation (B-1), and replacing χ_i with Equation (B-7),

$$\frac{d(P_F T_0)}{dt} = \left(\frac{\rho - \beta}{\Lambda}\right) P_F T_0 + \sum_{i=1}^{6} \lambda_i \left(\frac{C_i \beta_i T_0}{\lambda_i \Lambda}\right) \qquad \text{(B-11)}$$

The constant, T_0, can be removed from the derivative and the summation,

$$T_0 \frac{dP_F}{dt} = \left(\frac{\rho - \beta}{\Lambda}\right) P_F T_0 + T_0 \sum_{i=1}^{6} \left(\frac{C_i \beta_i}{\Lambda}\right) \qquad \text{(B-11)}$$

Dividing through by the steady-state amplitude gives the normalized power equation,

$$\frac{dP_F}{dt} = \left(\frac{\rho - \beta}{\Lambda}\right) P_F + \sum_{i=1}^{6} \frac{C_i \beta_i}{\Lambda} \qquad \text{(B-12)}$$

Appendix D
MITR Multi-Channel Analysis Code Parameters

D.1 General Information

The MITR Multi-Channel Analysis Code uses input files to set the physical parameters of the MITR, and to set the operational characteristics of the reactor for steady-state and transient simulations.

Appendix D gives the values used to generate the limit diagrams in this report. The structure of the input deck, as well as the capabilities of the MITR Multi-Channel Analysis Code, are subject to change as the code is updated. The user should refer to the MITR Multi-Channel Analysis Code User's Guide for more information.

D.2 Input Data Description

Table D.2.1 gives the information needed to put together the input file MITR.DAT. The data in Table D.2.1 represents the MITR in its current configuration, with experimental data taken during startup testing on Core II [7].

Additional data needed to generate an input data file for a transient simulation is shown in Table D.2.6. The variables in Table D.2.6 will vary depending on the configuration of the MITR and the operating point.

Table D.2.1 MITR parameters used in MITR Multi-Channel Analysis Code input deck.

Parameter	Value	Comments
Number of channels	22	Five-dummy core, 22 fuel elements
Number of time steps	9999	Run will end when CHF is reached
Number of core axial nodes	10	
Steady-state time step size	0.05 s	Sufficient for precise steady-state solution
Transient time step size	0.10 s	
Core axial node length	0.05683 m	Core height is 0.5683 m

Parameter	Value	Comments
Coolant temperature tolerance	0.05 kJ/kg	Maximum change in steady-state coolant enthalpy in any node during one steady-state time step
Mass flux tolerance	0.01 kg/m^2s	Maximum change in steady-state mass flux to any channel during one steady-state time step
Fuel temperature tolerance	0.05 K	Maximum change in steady-state fuel temperature in any node during one steady-state time step
Water Height	3.05 m	Height of water above core exit
Fuel element flow area	0.00196 m^2	Total flow area in one 15-plate fuel element
Fuel element wetted perimeter	3.503 m	Includes finned surface
Fuel element heated perimeter	3.394 m	Includes finned surface
Plenum flow disparity	Figure 3.3.3	Flow disparity depends on core loading. Figure 3.3.3 determined by experiment [7].
Radial power shape	Table D.2.2	Table D.2.2 based on measured values [7].
Axial Power shape	Table D.2.3	Table D.2.3 based on MCNP calculations [3].
Peaking factors	Table D.2.4	Table D.2.4 based on MCNP calculations and experimental measurements [3, 7].
Number of fuel plates	15	Number of plates in each fuel element
Mass of fuel per plate	0.08312 kg	
Heat transfer area per fuel plate	0.00391 m^2	Finned heat transfer area for one side of a fuel plate
Fuel plate thickness	0.000762 m	Half-thickness of a single fuel plate
Fuel density	3675.0 kg/m^3	Density at operating temperature.
Thermal conductivity of fuel (may be temperature dependent)	C1 = 0 C2 = 0 C3 = 41.2 C4 = 0	$k_{fuel} = C_1T^2 + C_2T + C_3 + C_4T^{-1}$ T = Fuel temperature (°C) k_{fuel} = Conductivity (W/m°C)
Specific heat capacity of fuel (may be temperature dependent)	C1 = 0 C2 = 1120.9 C3 = 2.22E6 C4 = 0	$c_{p,fuel} = (C_1T^2 + C_2T + C_3 + C_4T^{-1})/\rho_{fuel}$ ρ_{fuel} = Fuel density (kg/m^3) T = Fuel temperature (°C) $c_{p,fuel}$ = Conductivity (J/kg°C)
Mass of clad per fuel plate	0.09619 kg	
Thickness of clad	0.000508 m	Average half-thickness of cladding.
Clad density	2712.6 kg/m^3	Density at operating temperature.

Parameter	Value	Comments
Thermal conductivity of clad (may be temperature dependent)	C1 = 0 C2 = 0 C3 = 186.0 C4 = 0	$k_{clad} = C_1T^2 + C_2T + C_3 + C_4T^{-1}$ T = Clad temperature (°C) k_{clad} = Conductivity (W/m°C)
Specific heat capacity of clad (may be temperature dependent)	C1 = 0 C2 = 1187.0 C3 = 2.41E6 C4 = 0	$c_{p,clad} = (C_1T^2 + C_2T + C_3 + C_4T^{-1})/\rho_{clad}$ ρ_{clad} = Clad density (kg/m^3) T = Clad temperature (°C) $c_{p,clad}$ = Conductivity (J/kg°C)
Fraction of fission energy deposited in fuel	0.3867	MCNP calculations give 0.9207 deposited in fuel and clad together[3]. It is assumed that the fission energy is proportional to volume of fuel.
Fraction of fission energy deposited in clad	0.5340	MCNP calculations give 0.9207 deposited in fuel and clad together [3]. It is assumed that the fission energy is proportional to volume of clad.
Fraction of fission energy deposited in coolant	0.0460	From MCNP calculations [3].
Primary loop parameters	Table 3.2.1	Dimensions from [4,6].
Density of natural circulation ball	7833.0 kg/m^3	
Volume of natural circulation ball	2.039E-4 m^3	Volume of a single ball
Area of natural circulation valves	0.007628 m^2	Sum of the flow areas of all four valves
Natural circulation valve form loss factor (upflow)	0.254	Based on natural circulation valve area. Various estimates are available [5,27]
Natural circulation valve form loss factor (upflow)	0.830	Based on natural circulation valve area. Various estimates are available [5,27]
Heat exchanger length	4.32 m	
HX tube inner diameter	0.007035 m	
HX tube outer diameter	0.009525 m	
Number of HX tubes	1770	All heat exchangers are lumped together.
Form loss factor on primary side of HX	0.017	

Parameter	Value	Comments
Equivalent diameter of secondary side	0.00550 m	Flow is across bundles of primary tubes.
Hydraulic diameter of secondary side of HX	0.005475 m	Flow is across bundles of primary tubes.
Area for flow on secondary side of HX	0.0442 m^2	Flow is across bundles of primary tubes.
Fouling factor for HX	0.433 (kW/m^2K)	Based on outside area of HX tubes.
Primary Pump Head Curve	$C_1 = -2.556$ $C_2 = 14.247$ $C_3 = -15.306$ $C_4 = 4.596$	$H = H_R(C_1 + C_2X + C_3X^2 + C_4X^3)$ $X = (M/M_R)(\rho/\rho_R)$ Pump model from [4]
Primary Pump Rated Head (H_R)	241300.0 Pa	Pump model from [4]
Primary Pump Rated Density (ρ_R)	992.2 kg/m^3	Pump model from [4]
Primary Pump Rated Flow Rate (M_R)	128.6 kg/s	Pump model from [4]
Primary pump coastdown curve	$A_1 = -1.87$ $A_2 = 0.41$ $A_3 = 2.95$ $A_4 = -0.68$ $A_5 = 0.5136$ $A_6 = 1.492$	$m = \frac{m_0\left[A_1 + A_2\tau + A_3e^{-\tau} + A_4e^{-\tau^2} - A_5\right]}{A_6 - A_5}$ m = Primary flow rate (kg/s) m_0 = Steady-state primary flow rate (kg/s) τ = Time since primary pump trip (Pump coastdown data from [1,26])
Secondary pump coastdown curve	$A_1 = -1.87$ $A_2 = 0.41$ $A_3 = 2.95$ $A_4 = -0.68$ $A_5 = 0.5136$ $A_6 = 1.492$	$m = \frac{m_0\left[A_1 + A_2\tau + A_3e^{-\tau} + A_4e^{-\tau^2} - A_5\right]}{A_6 - A_5}$ m = Secondary flow rate (kg/s) m_0 = Steady-state secondary flow rate (kg/s) τ = Time since secondary pump trip (Secondary pump coastdown is assumed to have the same shape as the primary pump coastdown)
Fraction of flow through the core	0.9205	From experimental measurements on five-dummy core [7]
Scram signal instrumentation delay time	0.53 s	Experimental measurement. A delay of 0.53 s represents one standard deviation above the mean [1,26].

Parameter	Value	Comments
Control blade acceleration during drop	4.53 m/s^2	This is an "effective gravity" that accounts for the presence of water in the blade path. Calculated from experimental measurements in [1,26]
Control blade worth curve	Table D.2.5	From MITR Nuclear Reactor Lab data, as reported in [4]

Table D.2.2 Radial power shape factors for Core II (data from [7])

Fuel Element Number	Fuel Element Location	Radial Shape Factor
1	A-1	1.250
2	B-1	1.137
3	B-2	1.121
4	B-4	1.082
5	B-5	1.081
6	B-7	1.106
7	B-8	0.966
8	C-1	0.929
9	C-2	0.989
10	C-3	0.909
11	C-4	0.952
12	C-5	0.947
13	C-6	0.890
14	C-7	0.945
15	C-8	0.890
16	C-9	0.900
17	C-10	0.947
18	C-11	0.952
19	C-12	0.909
20	C-13	0.989
21	C-14	0.929
22	C-15	0.966

Table D.2.3 MITR axial shape factors for average fuel element (data from [3])

Axial Node	Axial Shape Factor
1	1.247
2	1.193
3	1.223
4	1.163
5	1.103
6	1.043
7	0.950
8	0.823
9	0.677
10	0.623

Table D.2.4 MITR peaking factors for Core II (Data from [3,7])

Fuel	Axial Node									
Element	1	2	3	4	5	6	7	8	9	10
A-1	1.486	1.073	1.112	1.169	1.160	1.150	1.095	1.263	1.419	1.909
B-1	1.468	1.179	1.150	1.210	1.355	1.349	1.389	1.496	1.560	1.959
B-2	1.391	1.121	1.167	1.227	1.294	1.283	1.315	1.409	1.450	1.703
B-4	1.592	1.239	1.209	1.192	1.256	1.329	1.265	1.459	1.502	2.058
B-5	1.603	1.163	1.210	1.352	1.341	1.330	1.363	1.461	1.367	1.913
B-7	1.618	1.212	1.183	1.244	1.311	1.300	1.332	1.318	1.603	2.014
B-8	1.545	1.047	1.167	1.227	1.374	1.283	1.221	1.300	1.318	1.845
C-1	2.322	1.995	1.777	1.335	0.938	1.786	1.852	0.754	0.765	0.823
C-2	2.221	2.075	1.936	1.295	1.463	1.444	1.473	1.438	1.432	1.884
C-3	2.196	1.949	1.901	1.564	1.191	1.163	1.064	0.982	1.046	1.126
C-4	2.151	2.120	1.978	1.229	1.296	1.371	1.390	1.470	1.626	1.750
C-5	2.025	2.025	1.975	1.535	1.333	1.410	1.437	1.531	1.552	2.172
C-6	2.190	2.035	1.899	1.452	1.053	1.012	1.000	1.026	0.936	1.008
C-7	2.269	2.166	1.929	1.449	1.528	1.508	1.419	1.501	1.494	2.145
C-8	2.095	2.040	1.990	1.455	1.247	1.116	1.114	1.157	1.095	1.178
C-9	2.346	1.977	1.837	1.256	1.324	1.400	1.419	1.501	1.494	1.788
C-10	2.096	1.947	1.899	1.362	1.340	1.316	1.445	1.283	1.404	2.016
C-11	2.201	1.937	1.803	1.445	1.047	0.906	0.885	1.021	0.931	0.836
C-12	2.271	2.028	1.888	1.324	1.396	1.476	1.390	1.603	1.626	2.100
C-13	2.076	1.864	1.901	1.564	1.191	1.163	1.064	1.228	1.046	1.126
C-14	2.286	1.984	1.936	1.295	1.366	1.341	1.360	1.438	1.432	1.884
C-15	2.171	1.908	1.862	1.335	1.314	1.389	1.417	1.383	1.530	1.976

Table D.2.5 MITR control blade worth curve [4]

Control Blade Position (m)	Worth ($)
0.0000	0.0
0.0508	-0.9
0.0762	-1.2
0.1016	-1.9
0.1270	-2.7
0.1524	-3.5
0.1778	-4.3
0.2032	-5.1
0.2286	-5.9
0.2540	-6.7
0.2794	-7.4
0.3048	-8.0
0.3300	-8.6
0.3556	-9.2
0.3810	-9.7
0.4064	-10.2
0.4318	-10.6
0.4572	-11.0
0.4826	-11.3
0.5080	-11.5
0.5334	-11.6
0.5683	-11.7

Table D.2.6 Variables used in MITR Multi-Channel Analysis Code input deck.

Variable	Comments
Ambient wet bulb temperature (°C)	
Cooling tower approach temperature (°C)	Available from cooling tower manufacturers
Secondary mass flow rate (kg/s)	103 kg/s for MITR-II
Primary mass flow rate (kg/s)	127 kg/s for MITR-II
Core inlet temperature scram limit (°C)	
Core outlet temperature scram limit (°C)	
Core power scram limit (kW)	
Primary flow scram limit (kg/s)	
Secondary flow scram limit (kg/s)	
Initial control blade height (m)	Control blades are not completely withdrawn at steady-state
Initial core power (kW)	
Reactivity insertion/power forcing function	

References

[1] S. Sardy. *Uncertainty Evaluations For MITR-III Applications.* MITNE-305. Nuclear Engineering Department, Massachusetts Institute of Technology. April, 1994.

[2] MITR Staff. *Safety Analysis Report For the MIT Research Reactor (MITR-II).* MITNE-115. Nuclear Engineering Department, Massachusetts Institute of Technology. October, 1970.

[3] S. A. Parra. *The Physics and Engineering Upgrade of the Massachusetts Institute of Technology Research Reactor.* Ph.D. Thesis, Nuclear Engineering Department, Massachusetts Institute of Technology. April, 1993.

[4] H. Trosman. *Computer Simulation For Transient Analysis of MITR Loop Components.* SM Thesis, Nuclear Engineering Department, Massachusetts Institute of Technology. May, 1994.

[5] L. W. Hu. Ph.D. Thesis In Progress, Nuclear Engineering Department, Massachusetts Institute of Technology, 1995.

[6] C. Kao. *Simulation of MITR-II Primary System in Steady State.* Nuclear Engineering Department, Massachusetts Institute of Technology. Special Project, 1992.

[7] G. C. Allen. *The Reactor Engineering of the MITR-II Construction and Startup.* Ph.D. Thesis, Nuclear Engineering Department, Massachusetts Institute of Technology. June, 1976.

[8] W. M. Kays. *Convective Heat and Mass Transfer.* McGraw-Hill Book Co., New York. 1966.

[9] N. Todreas and M. Kazimi. *Nuclear Systems I: Thermal Hydraulic Fundamentals.* Hemisphere Publishing, New York. 1990.

[10] Y. Taitel, D. Bornea, and A. E. Dukler. "Modeling Flow Pattern Transitions For Steady Upward Gas-Liquid Flow in Vertical Tubes." *AIChE J.*, 26:345, 1980.

[11] N. Zuber and J. A. Findlay. "Average Volumetric Concentration In Two-Phase Flow Systems." *J. Int. Multiphase Flow*, 2:521, 1976.

[12] J. G. Collier. *Convective Boiling and Condensation (Second Edition).* McGraw-Hill Book Co., New York. 1982.

[13] E. J. Davis and G. H. Anderson. "The Incipience of Nucleate Boiling In Forced Convection Flow." *AIChE J.* 12:4:775, 1966.

[14] J. E. Kowlaski, P. J. Mills, and S. Y. Shim. "Onset of Nucleate Boiling and Significant Void On Finned Surfaces." ASME, FED 99:405-411. 1990.

[15] P. Saha and N. Zuber. "Point of Net Vapor Generation and Vapor Void Fraction in Subcooled Boiling." *Proceedings Fifth International Heat Transfer Conference*, pp. 175-179, Tokyo. 1974.

[16] P. S. Larsen and L. S. Tong. "Void Fractions In Subcooled Boiling." *Journal of Heat Transfer*, pp. 471-476. November, 1969.

[17] S. Z. Rouhani. "Calculation of Steam Volume Fraction In Subcooled Boiling." *Journal of Heat Transfer*, pp. 158-164. February, 1968.

[18] S. Levy. "Forced Convection Subcooled Boiling-- Prediction of Vapor Volumetric Fraction." *International Journal of Heat and Mass Transfer*, 10:951-965.

[19] S. Whitaker. *Fundamental Principles of Heat Transfer*. Robert E. Kreiger Publishing Company, Malabar, Florida. 1977.

[20] D. Q. Kern. *Process Heat Transfer*. McGraw-Hill Book Co., New York. 1950.

[21] Marley Cooling Tower Company. UPDATE Computer Code. Mission, KS 1992.

[22] Cooling Tower Institute. *Cooling Tower Institute Performance Curves.* Performance and Technology Committee, Cooling Tower Institute. May, 1967.

[23] S. P. Kao. *A Multi-Loop Primary System Model For Pressurized Water Reactor Plant Sensor Validation*. Sc.D. Thesis, Nuclear Engineering Department, Massachusetts Institute of Technology. 1984.

[24] M. A. Bjerke, et. al. "A Reveiw of Short-Term Fission-Product-Decay Power. *Nuclear Safety*, 18:5:596-616. September, 1977.

[25] S. Glasstone and A. Sesonske. *Nuclear Reactor Engineering (Third Edition)*. Van Nostrand Reinhold, New York. 1981.

[26] K. Terry. *Flow Coastdown and Time To Scram For MITR-II.* Special Report, Nuclear Engineering Department, Massachusetts Institute of Technology. 1993.

[27] F. Bamdad-Haghighi. *Natural Convection Analysis of the MITR-II During Loss of Flow Accident.* Engr. and SM Thesis, Nuclear Engineering Department, Massachusetts Institute of Technology. August, 1977.

[28] W. J. Szymczak, *Experimental Investigation of Heat Transfer Characteristics of MITR-II Fuel Plates, In-Channel Thermocouple Response and Calibration.* SM Thesis, Nuclear Engineering Department, Massachusetts Institute of Technology. February, 1976.

[29] Y. Sudo, et. al. "Experimental Study of Differences In DNB Heat Flux Between Upflow and Downflow in Vertical Reactangualr Channel." *Journal of Nuclear Science and Technology*, 22:8:604-618. August, 1985.

[30] K. Mishima and H. Nishihara. "The Effect of Flow Direction and Magnitude On CHF For Low Pressure Water in Rectangular Channels." *Nuclear Engineering and Design*, 86:165-181. 1985.

[31] L. S. Tong and J. Weisman. *Thermal Analysis of Pressurized Water Reactors.* American Nuclear Society, 1970.

[32] Y. Sudo, et. al. "Experimental Study of Incipient Nucleate Boiling in Narrow Vertical Recatngular Channel Simulating Subchannel of Upgraded JRR-3." *Journal of Nuclear Science and Technology*, 23:1:73-82. January, 1986.

[33] P. G. Kroeger and N. Zuber. "An Analysis of the Effects of Various Parameters On the Average Void Fractions In Subcooled Boiling." *International Journal of Heat and Mass Transfer*, 11:211-213. 1968.

[34] P. B. Whalley. *Boiling, Condensation and Gas-Liquid Flow.* Oxford Science Publications, Clarendon Press, Oxford. 1987.

[35] W. Idsinga, N. Todreas, and R. Bowring. "An Assessment of Two-Phase Pressure Drop Correlations For Steam-Water Systems. *International Journal of Multiphase Flow*, 3:401-413. 1977.

[36] J. H. Rust. *Nuclear Power Plant Engineering.* Haralson Publishing, Buchanan, Georgia. 1979.

[37] J. A. Boure, A. E. Bergles, and L. S. Tong. "Review of Two-Phase Instability." *Nuclear Engineering and Design*, 25:165-192. 1973.

[38] R. W. Bowring. "Physical Model, Based On Bubble Detatchment and Calculation of Voidage In the Subcooled Region of a Heated Channel." *HPR* 10. 1962.

[39] R. H. Whittle and R. Rorgan. "A Correlation For the Minima In the Pressure Drop Versus Flow-Rate Curves For Sub-Cooled Water Flowing In Narrow Heated Channels." *Nuclear Engineering and Design*, 6:89-99. 1967.

[40] T. Dougherty, et. al. "Flow Instability In Vertical Channels." *HTD-Vol 159, Phase Change Heat Transfer.* ASME, 1991.

[41] G. S. H. Lock. *The Thermosyphon: Variations on a Theme.* Oxford University Press, Oxford. 1992.

[42] T. Dougherty, C Fighetti, G. Reddy, B. Yang, E. McAssey. and Z. Qureshi. "Flow Instability in Non-Uniformly Heated Channels," *6th Miami International Symposium on Heat and Mass Transfer.* December, 1990.

[43] J. Hughes. Ph.D. Thesis In Progress, Nuclear Engineering Department, Massachusetts Institute of Technology, 1995.

[44] J. Taborda-Romero, *Design of MITR-II Fuel Plates. Heat Transfer in Longitudinal Finned Narrow Channels.* SM Thesis, Nuclear Engineering Department, Massachusetts Institute of Technology. February, 1976.

[45] National Weather Service, US Department of Commerce. *Local Climatological Data: Monthly Summary for Boston, MA.* January 1993 - December 1993.